Inaugual - Dissertation

zur

Erlangung des akademischen Grades

Doctor rerum naturalium

(Dr. rer. nat.)

der

Naturwissenschaftlich - Mathematischen

Gesamtfakultät

der Ruprecht-Karls-Universität

Heidelberg

vorgelegt von

M.Sc. Lena Spillecke

geboren am 14. April 1995 in Chemnitz

eingereicht am 29. Oktober 2021

High-frequency / High-field Electron Paramagnetic Resonance Investigations on Metal-Organic Molecular Compounds

Erstgutachter: Prof. Dr. Rüdiger Klingeler
Zweitgutachter: Prof. Dr. Maurits Haverkort

Abstract

In this thesis detailed studies of the magnetic properties of different metal-organic molecular compounds are presented. The experimental investigations are mainly performed by high-frequency / high-field electron paramagnetic resonance (HF EPR) spectroscopy in an external magnetic field up to 16 T, accompanied by direct (dc) or alternating current (ac) susceptibility measurements. The results allowed to precisely determine the anisotropy parameters for a set of tetrahe-drally coordinated Co(II) compounds with the general formula $[Co(L_1)_4]X_2$, and thereby deliver a direct experimental proof for the influence of the second coor-dination sphere on the magnetic properties of the respective complexes. On the other hand, strong zero-field splitting induced by a highly axial anisotropy for an octahedrally coordinated mononuclear Co(II) complex was determined by pulsed field magnetisation measurements up to 55.5 T. The influence of the spatial co-ordination geometry on the g-anisotropy and slow relaxation of magnetisation behaviour was studied by the investigation of two isomeric Co(II) low spin (S = 1/2) complexes in a square-pyramidal and trigonal-bipyramidal coordination ge-ometry, respectively. For a pentagonal-bipyramidal coordinated V(III) complex $[V(III)(DAPBH)(CH_3OH)_2]$ Cl·CH_3OH a planar crystal field anisotropy as well as a finite dimer-like intermolecular interaction was quantified by both, HF EPR in-vestigations and low temperature magnetisation measurements. The exploration of small intermolecular coupling pathways is further a comprehensive thread run-ning through the study of all the aforementioned complexes. In a second part $4f$ rare earth metal containing compounds are addressed. The evaluation of ac susceptibility data on the monomeric Dy(III) compound $[Dy^{III}L^1]OTf$ reveal an interesting two step magnetic relaxation. The magnetic relaxation behaviour also motivated a comparative HF EPR study on two novel Er(III) complexes figuring a pentagonal-bipyramidal coordination surrounding. In this context it was found that the differences in magnetic relaxation behaviour can directly be traced back to the changes in electronic structure induced by the crystal field. Beyond the investigation of monomeric $3d$ or $4f$ complexes, the coupling between those two species of magnetic ions is studied and quantified by HF EPR investigations on a Cu(II)-Ln-Cu(II) sample set with Ln = Gd, Tb, Dy and La.

Zusammenfassung

Diese Arbeit behandelt detaillierte Untersuchungen der magnetischen Eingenschaften verschiedener metall-organischer Verbindungen. Als experimentelle Methode wurde dabei überwiegend die Hochfrequenz-/Hochfeld-Elektronenspinresonanz-Spektroskopie (HF-EPR) in externen Magnetfeldern bis zu 16 T genutzt. Die daraus resultierenden Ergebnisse wurden durch Untersuchungen der statischen (DC) und dynamischen (AC) Suszeptibilität ergänzt. Damit konnten für eine Probenreihe tetraedrisch koordinierter Co(II)-Verbindungen mit der Summenformel $[Co(L_1)_4]X_2$ die Anisotropieparameter bestimmt werden, aus welchen ein direkter experimenteller Beweis für den Einfluss der zweiten Koordinationssphäre auf die magnetischen Eingenschaften der jeweiligen Komplexverbindung abgeleitet werden kann. Darüber hinaus konnte eine starke Nullfeldaufspaltung, welche durch die hohe axiale Anisotropie eines oktaedrisch koordinierten Co(II)-Monomers induziert ist, durch Magnetisierungsmessungen in gepulsten Feldern bis 55,5 T quantifiziert werden. Anhand isomerer Co(II)-Komplexe im Spin S = 1/2 Zustand mit jeweils einer quadratisch-pyramidalen und trigonal-bipyramidale Koordinationsgeometrie konnte untersucht werden, welchen Einfluss die geometrische Anordnung der koordinierenden Liganden auf die g-Anisotropie und das magnetische Relaxationsverhalten ausübt. Des Weiteren wurde für einen pentagonal-bipyramidal koordinierten V(III)-Komplex $[V(III)(DAPBH)(CH_3OH)_2]Cl \cdot CH_3OH$ eine planare Kristallfeldanisotropie sowie eine schwache intermolekulare dimer-artige Wechselwirkung festgestellt. Letztere wurde sowohl mittels HF EPR als auch durch Magnetisierungsmessungen bei tiefen Temperaturen bestätigt. Die Quantifizierung von intermolekularen Wechselwirkungen bildet darüber hinaus eine wiederkehrende Untersuchungsthematik für alle zuvor behandelten Komplexe. In einem zweiten Themenschwerpunkt dieser Arbeit liegt der Fokus auf molekularen Verbindungen, welche u.a. aus $4f$ Seltenerdmetalle aufgebaut sind. Anhand von AC-Suszeptibilitätsdaten eines monomeren Dy(III)-Komplexes $[Dy^{III}L^1]OTf$ wird ein interessanter zweistufiger Relaxationsprozess ersichtlich. Die Untersuchung des magnetischen Relaxationsverhaltens motivierte ebenfalls die vergleichenden HF-EPR-Studien zweier Er(III)-Monomerverbindungen, welche jeweils eine pentagonal-bipyramidale Koordinationsumgebung aufweisen. In diesem Zusammenhang konnten die Unterschiede in dem beobachteten Relaxationsverhalten direkt auf die Varianzen der durch das Kristallfeld induzierten elektronischen Struktur zurückgeführt werden. Neben der Betrachtung von mononuklearen $3d$ und $4f$ Komplexen, wurde auch die Kopplung dieser zwei magnetischen Ionenspezies durch HF-EPR-Messungen an einer Cu(II)-Ln-Cu(II)-Probenreihe mit Ln = Gd, Tb, Dy oder La untersucht.

Contents

1. Introduction

In 1941, Konrad Zuse presented the first electromechanically programmable, fully digital computer.[1] This device had an overall memory which was able to record 64 words with the length of 22 bit and, yet, it had a weight of 1 ton and occupied an entire room. Looking back from the present perspective, it is hard to imagine, that this giant machine is the origin of modern computing technology in which a single chip can have a minimal size of 0.1 mm^3.[2] This eighty year journey was accompanied by several ground breaking inventions such as the development of the first transistor by Bardeen, Brattain and Shockley, which superseded the application of electromechanical relays and became a key component of modern electronic devices.[3] The undisputable extensive impact of their work was honoured in 1956 by the Nobel Prize in physics.[4] Another example is the enormous advancement of data storages from the initially used punchcards towards techniques like magnetic data storages in hard drives or field effect transistors, which can be found in USB sticks and other flash drive memories. The discovery of a magnetic moment arising exclusively from an isolated molecule was quickly handled as another potential breakthrough in the development of small sized electronics and established the research field of molecular magnetism.[5, 6] These findings not only presented a new benchmark for the smallest synthesizeable magnetic unit, but also the broad possibilities to chemical engineer these compounds sparked interest in the investigation of this novel materials.[7–10]

The class of molecular magnets is a hypernym for materials figuring a combination of metal centres which are coordinated by an organic ligand environment.[11] These metal centres can appear in the form of single ions or coupled metal clusters which are isolated from each other by the spatial extension and the arrangement of the surrounding ligands, but they can also form correlated systems as chains or two- and three-dimensional frameworks.[12–15] Besides their potential application in novel computing and processor technologies, molecular magnetic materials are also in the focus of fundamental research as synthetic toy models to investigate magnetic properties on the nanoscale, where quantum effects become relevant.[16, 17] Thereby, the limited number of metal ions that contribute to the magnetic centre allow for a comparably easy phenomenological description of experimentally obtained data. However, even though the observed magnetic properties can be framed by the application of phenomenological models, the fundamental origin of the very same, namely the interplay between the magnetic centres with the crystal field induced by the surrounding organic ligands, is still not fully understood. To decipher this mechanism it is crucial to obtain reliable experimental data which allows to precisely quantify the crystal field effect onto the magnetic metal centres.

Tunable high frequency/high field electron paramagnetic resonance (HF EPR) spectroscopy allows for directly obtaining information on the magnetic anisotropy for a given molecular system and, consequently, on the local chemical environment of the metal centres which is formed by the coordinating ligands.[11, 18] Thus, this technique represents an important experimental approach to connect the ligation geometry, which can be manipulated by chemical engineering, and the resulting magnetic properties.[19–23] The measurement principle was discovered in 1944 in the former U.S.S.R. by Zavoisky and is based on the induction of transitions between the m_S states belonging to a given spin S by the irradiation of electro-magnetic waves in the microwave range.[18]

This thesis presents a comprehensive demonstration of the application of HF EPR spectroscopy as powerful tool to evaluate the magnetic properties of various examples from the class of molecular magnet materials. In this context, all of these materials were characterized for the first time using the HF EPR technique. Two primary material groups were investigated within the scope of the here-presented work. Firstly, magnetic properties of different $3d$ transition metal compounds were studied, secondly, spectroscopic investigations on $4f$ containing complexes were performed. In this regard it is noteworthy, that especially the application of HF EPR onto the latter represents a challenging experimental task due to the high single-ion anisotropies of $4f$ compounds, various mixing of state effects and highly forbidden ground state transitions.[24, 25] Beyond this, the advantages of the HF EPR technique is particularly demonstrated in the detection and precise quantification of small dimer-like intermolecular interactions in a Co(II) and V(III) mononuclear complex, which are on an energy scale that is beyond the capabilities of standard measurement techniques like direct current (dc) SQUID[1] magnetometry. To acquire a complete picture not only on the static magnetic properties but also on the dynamic magnetic relaxation, which is a crucial parameter for many applications, the HF EPR and dc SQUID magnetometry investigations are complemented by alternating current (ac) measurements.

After this introductory first chapter, the second chapter will give a brief overview of the theoretical background of magnetism in general which is subsequently extended by the experimental details of the measurement methods presented in chapter three. The fourth and fifth chapter is focused on the detailed investigation of $3d$ monomers containing Co(II) and V(III) centres, respectively. In chapter six this investigation is extended to molecular magnets which are build from $4f$ rare earth metals as well as $3d$-$4f$ coupled systems. To demonstrate the broad variety of molecular magnetic systems, chapter seven discusses molecular compounds, which can not directly be categorized in the prior chapters. The final chapter eighth gives a summarizing conclusion across the discussed topics of this thesis.

---

[1]SQUID = superconducting quantum interference device.

2. Theoretical Background

This chapter provides an introduction into the description of free atoms in a magnetic field (chap. 2.1 and 2.3) as well as the origin of magnetic anisotropy induced by a crystal field (CF) or magnetic interactions (chap. 2.4). Furthermore, the effective spin Hamiltonian approach is introduced (chap. 2.5). The description of the theoretical background is mainly based on the following books of S. Blundell [26], P. Fazekas [27], W. Nolting [28], T. Fließbach and H. Walliser [29] (chap. 2.1, 2.2 and 2.3), A. Abragam and B. Bleaney [18], D. Gatteschi, R. Sessoli and J. Villain [11], C. Benelli and D. Gatteschi [12] (chap. 2.4 and 2.5).

2.1. The free Atom Hamiltonian

The Hamiltonian $\mathcal{H}$ for a free atom consisting of N electrons which are bound to a nucleus can be written in a centre-of-mass system as:

$$\mathcal{H} = \sum_{i=1}^{N} \left(\frac{p_i^2}{2m_\mathrm{e}} - \frac{Ze^2}{r_i} + \sum_{j=1, j \neq i}^{N} \frac{e^2}{2|r_i - r_j|} \right) \tag{2.1}$$

where p_i and $r_{i/j}$ denote the momentum operator and distance from the nucleus for the ith or jth electron and m_e and Z reflect the electron mass and the proton number, respectively. This description takes advantage of the BORN-OPPENHEIMER-approximation which assumes, that the electron mass is much smaller than the nuclear mass and, hence, the movement of the electrons and the nucleus can be treated as decoupled.[30]

The first two terms in eqn. 2.1 describe the kinetic and potential energy of a single electron; the third term considers the interactions between two electrons. To solve the free atom Hamiltonian a mean-field approach can be applied, assuming every electron is subjected to an effective potential induced by the other electrons and the Hamiltonian in eqn. 2.1 can be simplified to:

$$\mathcal{H}_0 = \sum_{i=1}^{N} \left(\frac{p_i^2}{2m_\mathrm{e}} - \frac{Ze^2}{r_i} + V_i(r_i) \right) \tag{2.2}$$

with the central potential V_i. The eigenfunctions ψ of this Hamiltonian consist of a radial part $R_{n,l}$ as well as an angular dependent part which is constructed from the spherical harmonics $Y_l^{m_l}$:

$$\psi_i(r_i, \theta_i, \phi_i)_{n,l,m_l,s,m_s} = R_{nl}(r_i)Y_l^{m_l}(\theta_i, \phi_i)\chi(m_s) \qquad (2.3)$$

with the main quantum numbers $n = 1, 2, ...$ and $l = 0, 1, ..., n\text{-}1$ for a given n and the orbital or spin quantum number $m_{l/s} = \text{-}l/s, \text{-}l/s\text{+}1, ...,l/s\text{-}1, l/s$ for a given l or s quantum number. The function χ incorporates the spin state.

2.2. Spin-Orbit-Coupling

The spin-orbit coupling (SOC) results from an effective magnetic field $\mathbf{B}_n$ which affects the spin of the electron in its rest frame while circulating the nucleus with the velocity $\mathbf{v}$, i.e. it is a relativistic effect. The SOC Hamilton operator for an electron in a Coulomb potential as appearing as third term in equ. 2.1 has the following form:

$$\mathcal{H}_{\mathrm{SOC}} = \frac{\hbar^2}{2m^2c^2}\frac{Ze^2}{r^3}S \cdot L = \lambda S \cdot L \qquad (2.4)$$

with $L = \sum\limits_{i=1}^{l} m_{l(i)}$ and $S = \sum\limits_{i=1}^{s} m_{s(i)}$ being the coupled orbital and spin momenta, respectively and $\lambda > 0$ denotes the SOC constant. Due to the SOC, L and S are no longer separated but only the total angular momentum $J = L + S$ is a conserved quantity which can have values between $|L - S|$ and $|L + S|$. Thus, the resulting magnetic moment $\boldsymbol{\mu}$ can be written as

$$\boldsymbol{\mu} = g_{\mathrm{J}}\mu_{\mathrm{B}}\mathbf{J} \qquad (2.5)$$

with g_{J} being the LANDÉ g-factor as derived e.g. in ref. [26]. To find the L and S values which minimize the energy of a given system HUND's rules can be applied (see ref. [26]) which give an empirical approach to estimate the ground state.

So far the SOC was considered as a small perturbation while the main energy term is defined by the electrostatic interactions between the electrons, i.e. the orbital and spin momenta are summarized separately for each electron which is also called L-S- or RUSSEL-SAUNDERS-coupling. This is a good approach for light or medium heavy elements as e.g. $3d$ transition metals. However, for heavy elements with high atomic numbers Z the spin-orbit interaction becomes the dominant energy. Therefore the so-called j-j-coupling model has to be applied where the orbital and spin momentum of each electron is coupled first and afterwards the resulting momenta are coupled to the total angular momentum J.

2.3. Atom in a Magnetic Field

To introduce a magnetic field $\mathbf{B}$ acting on the many electron system as defined by the SH in eqn. 2.2 the following transformation of the canonical momentum $\mathbf{p}_i$ is

performed:

$$\mathbf{p}'_i \rightarrow \mathbf{p}_i + \frac{e\mathbf{A}(\mathbf{r}_i)}{c} \tag{2.6}$$

with the magnetic vector potential $\mathbf{A} = \frac{1}{2}\mathbf{B} \times \mathbf{r}$. Thus, the kinetic part of the perturbed Hamiltonian can be written as:

$$\mathcal{H}_{kin} = \frac{1}{2m_e} \sum_{i=1}^{N} \left(\mathbf{p}_i + \frac{e}{2c}\mathbf{B} \times \mathbf{r}_i \right)^2 = \sum_{i=1}^{N} \frac{p_i^2}{2m_e} + \mu_B \mathbf{L} \cdot \mathbf{B} + \frac{e^2 B^2}{8m_e c^2} \sum_{i=1}^{N} \left(x_i^2 + y_i^2 \right) \tag{2.7}$$

with the total angular momentum $\hbar\mathbf{L} = \sum_i \mathbf{r}_i \times \mathbf{p}_i$.

The electronic spin $\mathbf{S}$ can be introduced in eqn. 2.7 by considering the energy E of a magnetic spin-moment μ_e interacting with the external magnetic field:

$$E = -\mu_e \cdot \mathbf{B} = g_e \mu_B \mathbf{S} \cdot \mathbf{B} \tag{2.8}$$

A simplified Hamiltonian is thus given by:

$$\mathcal{H} = \mathcal{H}_0 + \mu_B \left(\mathbf{L} + \mathbf{S} \right) \cdot \mathbf{B} + \frac{e^2}{8m_e c^2} \sum_{i=1} \left(x_i^2 + y_i^2 \right). \tag{2.9}$$

The main contribution to the splitting of the energy states is usually given by the second term in eqn. 2.9, which is also known as the paramagnetic- or ZEEMAN-term. The third term corresponds to the diamagnetic contribution which is, however, often several orders smaller than the ZEEMAN-contribution.

2.4. The Origin of Magnetic Anisotropy

The electronic spin itself has a perfect spherical symmetry and by this also isotropic properties. However as already discussed in chap. 2.2, the coupling of the electronic spin to an orbital momentum can induce a splitting of the energy states independently from the application of any external magnetic field, the so-called zero field splitting (ZFS).[12]

2.4.1. The Crystal Field

The crystal field (CF) describes the influence of the neighbouring atoms within a crystalline structure on a given site in terms of an electrostatic field. One approach to describe this additional potential is the application of crystal field theory where the neighbouring orbitals are simplified as point-charges acting on the orbitals of

the central ion. However, it was shown, that in many cases the quantitative results derived from this approach do not describe the experimental data well. On the other hand it turned out, that the qualitative accordance between theory and experiment is quite promising. Hence, the potential produced by ligands around the central metal ion is expressed in terms of the ligation symmetry while the problematic radial integrals are treated as free parameters in the more advanced model of ligand field (LF) theory.[12]

A lot of different notation formalisms and descriptions of the CF Hamiltonian can be found in the literature. Within this work, the STEVENS-notation is used in which the Hamiltonian has the following form:

$$\mathcal{H}_{\mathrm{CF}} = \sum_{k=0}^{k_{\max}} \sum_{q=-k}^{k} B_q^k \hat{C}_q^k \tag{2.10}$$

where B_q^k are real coefficients and $\hat{C}_q^k$ define the extended STEVENS-operator equivalents of rank k. The upper limit of k is defined by $k_{\max} = 2l$ with l being the angular momentum. Even though, k can vary between 0 to $2l$, some terms are cancelled out for specific ligand symmetries. The advantage of the STEVENS-formalism is, that the coefficients are real values which makes them directly comparable to experimentally derived parameters.[31] However, within this scheme, only the energetically lowest multiplets are considered while higher order states and, thus, also their mixing into the ground state are neglected. The coefficients B_q^k can be related to the commonly used axial (D) and transversal (E) second-order zero field splitting parameters (see chap. 2.5) by:

$$D = 3B_0^2; E = B_2^2 \tag{2.11}$$

Orbital quenching

Due to the broad spatial distributions of 3d-orbitals, the CF interaction usually dominates over the SOC in 3d metal containing compounds. Consequently, the effective potential which is seen by the 3d metal ion is in general not spherical and, thus, the components of the orbital momentum are no conserved quantities any more. Due to this influence of the CF, the orbital momentum precesses so that the magnitude is unchanged, but the absolute value of the momentum averages out and the observed orbital contribution becomes zero. This behaviour is called orbital quenching.[26] However, in many cases the orbital contribution is not completely but only partially quenched due to the SOC which leads to spatial preferences of the orbital momentum direction and therefore to a g-value which can be anisotropic and quite different from the spin only value of 2. Especially for cobalt containing compounds which display strong SOC [32] these anisotropies can be relatively strong and may even lead to an alignment of molecules within an external magnetic field exclusively induced by g-anisotropy as shown e.g. in chap. 4.4.

2.4.2. Magnetic Interactions

Magnetic dipolar coupling

The magnetic dipolar coupling, which is sometimes also re-called as "through-space" interaction [11], is the direct interaction between two magnetic dipoles $\boldsymbol{\mu_1}$ and $\boldsymbol{\mu_2}$ which are separated from each other by the distance $\mathbf{r}$. The corresponding coupling energy can be written as: [26]

$$E = \frac{\mu_0}{4\pi r^3} \left[\boldsymbol{\mu_1} \cdot \boldsymbol{\mu_2} - \frac{3}{r^2} \left(\boldsymbol{\mu_1} \cdot \mathrm{r} \right) \left(\boldsymbol{\mu_2} \cdot \mathrm{r} \right) \right] \tag{2.12}$$

The effective dipolar interactions in molecular systems are often either covered by interactions on a higher energy scale like direct exchange or superexchange interactions in multi-core molecules or very weak due to a large separation of the metal centres within the supramolecular structure of a compound. However, even if on a small scale, these interactions can have a significant impact e.g. on the dynamic magnetic relaxation behaviour of a molecular magnetic compound [33–35] or can even induce long range ordering.[36]

Direct Exchange and Superexchange Interactions

Extending an one-electron system to a system with several electrons, the electron-electron interaction or COULOMB-repulsion has to be considered. In the easiest model of two electrons occupying the same shell of an atom, the COULOMB-repulsion effects that the two electrons tend to occupy different orbitals within this shell and thus, according to the second HUND's rule, favour a parallel arrangement of their spins, i.e., a ferromagnetic coupling.

If the two electrons are not on one, but on neighbouring atoms they can save kinetic energy by extending the atomic orbitals to a joined molecular orbital. This molecular orbital can be bonding, i.e. spatially symmetric with a finite probability of presence in between the two atoms, or antibonding (spatially antisymmetric). The antibonding orbital is thereby energetically costlier due to the smaller orbitals and higher kinetic energy. Thus, the reduction in kinetic energy is the binding energy and can be rationalized by the following exchange hamiltonian:

$$\mathcal{H}_{exchange} = -J_{ij}\mathbf{S}_i \cdot \mathbf{S}_j \tag{2.13}$$

where J_{ij} denotes the exchange integral and $\mathbf{S}$ the spin state.

The interaction of electrons of two proximately neighbouring atoms with an orbital overlap is also referred to as direct exchange. However, the orbital overlap between neighbouring atoms is often rather insufficient in real systems. An example deliver $4f$ rare earth materials in which the electronic orbitals are strongly localized around the nuclei and hence the orbital overlap is heavily diminished. Thus, to explain the observed magnetic properties for many materials, indirect or superexchange interac-

tions have to be considered. Thereby, the interaction is mediated via a non-magnetic ion which is placed in between the magnetic ones. Especially for transition metal compounds these non-magnetic species are usually oxygen ions. The exchange interaction itself can be thereby understood as hopping process between the magnetic ions over the orbitals of the non-magnetic one which is described by the hopping-integral t. The energy cost for two electrons situated on the same site, i.e. the cost of placing an electron in an excited state, is given by the COULOMB-energy U. Thus, the over all exchange integral J is proportional to $-t^2/U$. Since the hopping-integral directly depends on the orbital overlap, it is strongly connected to the spatial arrangement of the orbitals in respect to each other, i.e. on binding-angles, but also on hybridisation and degeneracy of the participating electronic orbitals.[26]

2.5. The effective Spin Hamiltonian

To solve a Hamiltonian as described in the previous sections it is mandatory to have knowledge of all position and spin degrees of freedom for each particle involved. However, for the comparison to experimental results acquired, e.g. by spectroscopic investigations, it is often the case that only transitions arising around the ground state are of relevance, while energetically higher lying states can be omitted.[11] Motivated by perturbation theory it is therefore established, to replace the orbital by spin coordinates and take advantage of the symmetry properties to describe the system. With this it is possible to define a Hamiltonian with an effective Spin S:

$$\mathcal{H} = \mu_\mathrm{B} \mathbf{S} \mathbf{g_{eff}} \mathbf{B} + \mathbf{SDS} + \mathbf{S_1 J_{12} S_2} \tag{2.14}$$

including a ZEEMAN-, a CF- and an exchange coupling term. To ensure an isotropic effective spin, the anisotropies are absorbed in the effective g-tensor $\mathbf{g_{eff}}^2$ and the anisotropy tensor $\mathbf{D}$. Both tensors are usually symmetric which is why they can be transformed into their diagonal form if the three orthogonal eigenvectors are chosen along the coordination axes x, y and z. The CF-Hamitonian consequently has the form: [11]

$$\mathcal{H}_\mathrm{CF} = D_{xx} \hat{S}_{xx}^2 + D_{yy} \hat{S}_{yy}^2 + D_{zz} \hat{S}_{zz}^2 \tag{2.15}$$

with $\hat{S}^2$ being the spin operators. Since the addition of a constant to a Hamiltonian does not change the physical properties which are reflected, the parameters in eqn. 2.15 can be reduced by subtracting:

$$\frac{1}{2} \left(D_{xx} + D_{yy} \right) \left(S_x^2 + S_y^2 + S_z^2 \right) = \frac{1}{2} \left(D_{xx} + D_{yy} \right) S(S+1). \tag{2.16}$$

---

[2]In a strict sense, $\mathbf{g}$ is not a real tensor since a tensor always refers to one and the same coordinate system while in the application of the SH in eqn. 2.14 it can be useful to assume separate coordinate systems for the external magnetic field and the electronic spin. Therefore, the $\mathbf{g}$-tensor is often also referred as $\mathbf{g}$-transformation matrix.[11, 18, 37]

With the relations:

$$D = D_{zz} - \frac{1}{2}D_{xx} - \frac{1}{2}D_{yy}; E = \frac{1}{2}(D_{xx} - D_{yy}) \tag{2.17}$$

one finds:

$$\mathcal{H}_{\mathrm{CF}} = DS_z^2 + E\left(S_x^2 - S_y^2\right) \tag{2.18}$$

with the axial and transversal anisotropy parameters E and D, respectively. By further subtracting the constant $DS(S+1)/3$ the CF-Hamiltonian which is used within this work can be written as

$$\mathcal{H}_{\mathrm{CF}} = D\left[S_z^2 - \frac{1}{3}S(S+1)\right] + E\left(S_x^2 - S_y^2\right). \tag{2.19}$$

The last term in eqn. 2.14 describes the interaction between two magnetic moments. This part can be divided into three parts

$$\mathbf{S_1 J_{12} S_2} = -J_{12}\mathbf{S}_1 \cdot \mathbf{S}_2 + \mathbf{S}_1 \cdot \mathbf{D}_{12} \cdot \mathbf{S}_2 + \mathbf{d}_{12} \cdot (\mathbf{S}_1 \times \mathbf{S}_2) \tag{2.20}$$

where the first term describes the isotropic part of the coupling and the second and third term the anisotropic and antisymmetric part, respectively. In general, the isotropic part can be considered as the dominant coupling while the other terms are usually introduced as perturbation.[11]

2.6. Electron Paramagnetic Resonance

Electron paramagnetic resonance (EPR) spectroscopy is a powerful tool to directly investigate transitions between the m states for a given spin multiplet.[11] Fundamentally, it works by exciting the electronic spin through microwave irradiation.

If an external magnetic field $\mathbf{B}$ is applied onto a magnetic dipole moment $\boldsymbol{\mu}$, this moment precesses around the direction of the external field with the angular velocity $\boldsymbol{\nu}_{\mathrm{L}} = -\gamma\mathbf{B}$. This precessing magnetic moment can be disturbed by an oscillating magnetic field perpendicular to the external one with a frequency $\boldsymbol{\nu}$ close to the precession frequency $\boldsymbol{\nu}_{\mathrm{L}}$, i.e., a resonance phenomenom occures if the condition $\boldsymbol{\nu} = \boldsymbol{\nu}_{\mathrm{L}}$ is fulfilled. Thereby, the energy of the dipole moment changes by ΔE. Due to the selection rules for the allowed magnetic dipolar transitions between different energy states Δm_s is restricted to ± 1.[38] Thus, the allowed energetic transitions can be written as

$$\Delta E = h\nu = g_J\mu_{\mathrm{B}}B\Delta m_s \tag{2.21}$$

with $\gamma = -g_J\mu_{\mathrm{B}}$ for electronic dipoles.[18]

In an EPR experiment, the frequency of the microwaves which irradiate the sample is held constant while the external magnetic field is swept over a pre-defined, experiment-specific range. The occurring transitions between the different energy-states can be monitored by absorption peaks in the transmitted EPR spectra. To rationalize the resonance field positions and to evaluate the acquired data in terms of a certain spin model, an energy-level diagram can be used to visualize the theoretically predicted transitions. The upper panel of fig. 2.1 shows an example of a simple energy-level diagram for an S = 3/2 spin. The direction of the external magnetic field is oriented along the anisotropy axis of the molecule which figures a negative sign for D, i.e., at 0 T the $m_S = \pm 3/2$ doublet is lowest in energy while the $m_S = \pm 1/2$ doublet is shifted to higher energies. Red arrows in fig. 2.1 indicate exemplary allowed transitions between the energy states with $\Delta m_S = \pm 1$ which can be monitored as resonance features in the transmitted EPR spectra as indicated by red solid lines in the lower panel of fig. 2.1. The connection between the transitions in the energy-level diagram, the resonance feature in the EPR spectra and the measured data point in the energy (i.e. microwave frequency) vs. external magnetic field diagram is visualized in fig. 2.1 as small dotted lines between the upper and lower panel as well as red dots in the lower panel.
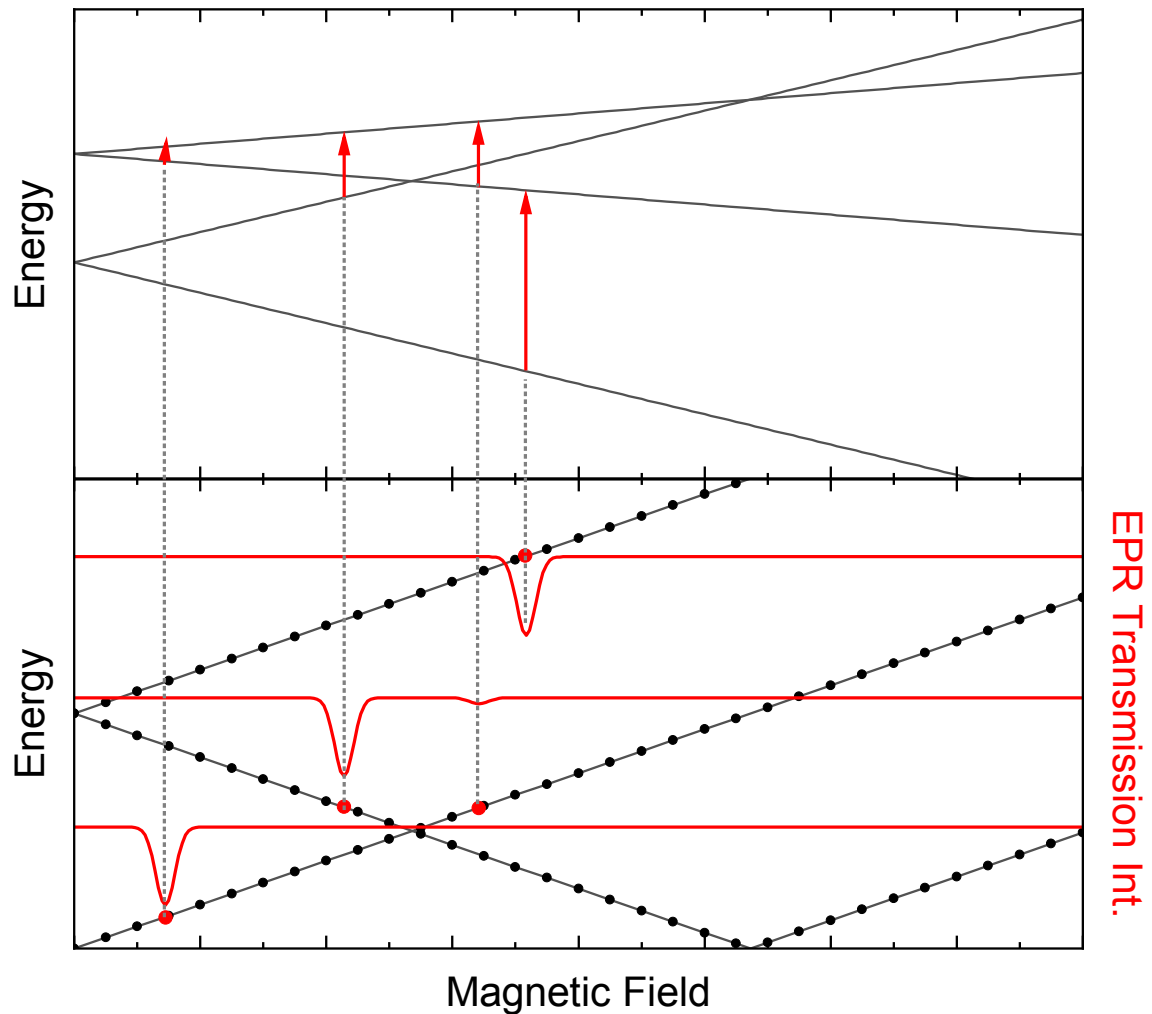
Figure 2.1.: Upper panel: Energy-level diagram for a spin S = 3/2 with the external magnetic field oriented along the anisotropy axis. Red arrows mark allowed transitions between the depicted energy-levels. Lower panel: Black dotted lines show the energy vs. external magnetic field diagram for the allowed transitions shown in the upper panel. Red solid lines display exemplarily EPR resonance spectra for different EPR frequencies (vertically shifted). Small dotted black lines between the upper and lower panel as well as red dots indicate correspondence between the transition in the energy-level diagram, the resonance field position in the EPR spectra and the respective point on the resonance branch in the energy vs. resonance field diagram.

2.7. Magnetic Relaxation Measurements

2.7.1. Theory of AC Susceptibility Measurements

In this section the theoretical concept of the investigation of magnetic relaxation processes in molecular systems based on alternating current (ac) susceptometry is discussed. Thereby, a small oscillating magnetic field in the range of several Oe is applied to a sample and the time-resolved response of the very same is monitored. This small oscillating field can be accompanied by a much stronger external direct current (dc) magnetic field, but does not necessarily have to.

In the most general case, the investigated sample in an ac susceptibility measurement is affected by a static external dc magnetic field H_0 which is superimposed by a small oscillating field h so that the total applied field can be written as:

$$H = H_0 + h cos(\omega t) \tag{2.22}$$

where ω denotes the oscillation frequency of the ac field and t the time.

The ac susceptibility is defined as $\chi_{ac} = \partial M / \partial H$ but can be approximated for small oscillating fields as $\chi_{ac} = \Delta M / \Delta H$. Thus, while the amplitude of the ac signal depends on the change in magnetisation i.e. on $h cos(\omega t)$, it is only indirectly connected to H_0. Due to the saturation behaviour of the magnetisation at higher external magnetic fields for numerous compounds, the ac signal, however, tends to decrease with increasing dc field.

The response of the sample to the ac field can be understood as the transition of the spins between different states. The population of each state m is thereby given by a BOLTZMANN distribution:[11, 26]

$$p_m = \frac{1}{Z} exp \left(\frac{-E_m}{k_B T} \right) \tag{2.23}$$

where $Z = \sum_i exp\left(-E_i/k_B T\right)$ describes the partition function, E_m the energy of the corresponding state and k_B the BOLTZMANN constant. The expectation value of the magnetisation can thus be written as:[11]

$$\langle M \rangle = \sum_m p_m M_m. \tag{2.24}$$

If an oscillating magnetic field as defined in eqn. 2.22 is applied on a system consisting of N spins S $= 1/2$ with the possible states $m_S = \pm 1/2$, the equilibrium population of these two states p_1 and p_2 also oscillates:[11]

$$\frac{p_1}{p_2} = exp \left[\frac{-g\mu_B \left(H_0 + h cos\omega t \right)}{k_B T} \right] \tag{2.25}$$

The time until the equilibrium is established after a change in field direction is measured by τ. If the frequency is very low, i.e., the spin can follow the change in external field without any time dilatation, the measured susceptibility χ_T is called the isothermal susceptibility. In the other limit, were the oscillating field changes much faster than the relaxation time τ, the spins can not follow this change and the measured susceptibility χ_S is called adiabatic susceptibility. The interesting intermediate frequency regime can be described by an interpolation formula as defined by Casimir and Du Pré:[39]

$$\chi(\omega) = \chi_S + \frac{\chi_T - \chi_S}{1 + i\omega\tau}. \tag{2.26}$$

Since χ_T and χ_S are real numbers, the susceptibility can be devided into a real (in-phase) part χ' as well as an imaginary (out-of-phase) part χ'':

$$\chi' = \frac{\chi_T - \chi_S}{1 + \omega^2\tau^2} + \chi_S; \quad \chi'' = \frac{\chi_T - \chi_S\omega\tau}{1 + \omega^2\tau^2}. \tag{2.27}$$
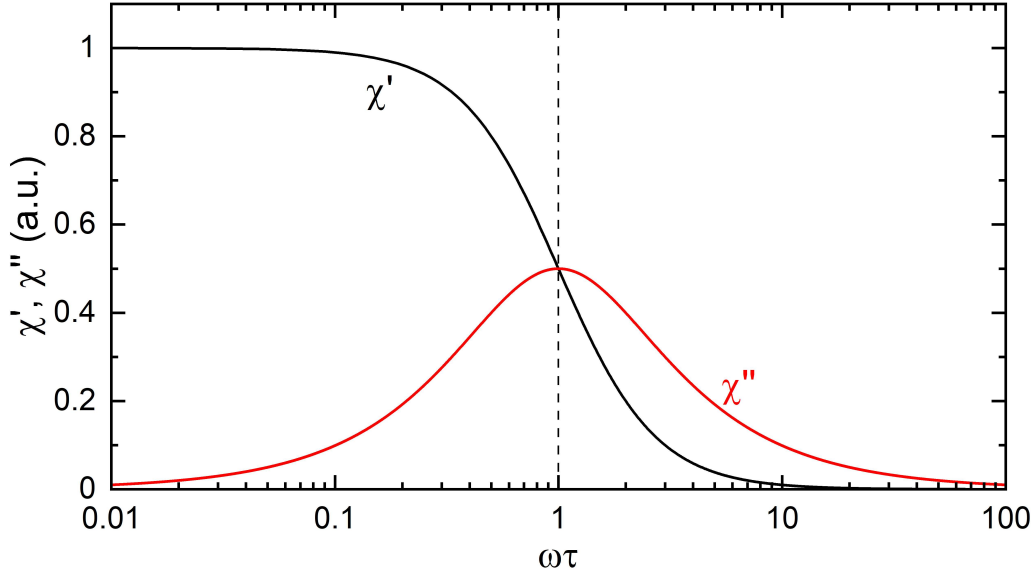
Figure 2.2.: Exemplaric frequency dependence of the in-phase (χ') and out-of-phase (χ'') contribution to the dynamic susceptibility for an arbitrary chosen relaxation time $\tau = 1$.

Fig. 2.2 depicts a generic frequency dependence of the in-phase and out-of-phase susceptibility component for an arbitrary chosen relaxation time $\tau = 1$. As it can be seen, in a semi-logarithmic scaling the in-phase component figures a step were the condition $\omega\tau = 1$ is fulfilled while the out-of-phase component goes through a maximum at this frequency. Thus, from the position of this maximum and the relation $\omega^{-1} = \tau$ the relaxation time of the corresponding relaxation process can be derived.

In a realistic system, the overall magnetic relaxation is in general not defined by just one, but several overlapping processes, i.e. not a single but a distribution of

relaxation times has to be considered. This distribution can be described by an empirical approach which introduces the parameter α:[40]

$$
\begin{aligned}
\chi(\omega) =& \chi_S + \frac{\chi_T - \chi_S}{1 + (i\omega\tau)^{1-\alpha}} \\
\chi'(\omega) =& \chi_S + (\chi_T - \chi_S)\frac{1 + (\omega\tau)^{1-\alpha}sin(\pi\alpha/2)}{1 + 2(\omega\tau)^{1-\alpha}sin(\pi\alpha/2) + (\omega\tau)^{2-2\alpha}} \\
\chi''(\omega) =& (\chi_T - \chi_S)\frac{(\omega\tau)^{1-\alpha}cos(\pi\alpha/2)}{1 + 2(\omega\tau)^{1-\alpha}sin(\pi\alpha/2) + (\omega\tau)^{2-2\alpha}}.
\end{aligned}
\tag{2.28}
$$

2.7.2. Magnetic Relaxation in Molecular Systems

While the previous chapter describes how the magnetic relaxation time of a given spin system can be quantified, this chapter discusses the evaluation of the very same for molecular spin systems. Therefore, the temperature dependence of the relaxation $\tau(T)$ is considered.

Depending on the spin system, $\tau(T)$ can be described by different contributions which effect the overall observed relaxation time. The following equation summarises the, for molecular magnetism, most relevant contributing terms:

$$
\tau^{-1} = \tau_0 exp\left(\frac{-U_{eff}}{k_B T}\right) + AT + BT^n + \tau_{QTM}.
\tag{2.29}
$$

The first term in eqn. 2.29 is also called ORBACH-term and describes the temperature dependence for a relaxation process where an energy barrier of the hight U_{eff} is involved. In the second term, direct relaxation or one-phonon processes are considered which involve phonons of the same energy as the corresponding magnetic transition. The third term is the RAMAN-relaxation term with the prefactor B and the exponent n. It describes strongly temperature dependent two-phonon processes. In the evaluation of ac susceptibility data, n is usually treated as free fit-value. The value of n can give information on the spin system involved in the relaxation process. For a non-KRAMERs system, n is e.g. close to 7 while for a KRAMERs doubled $n \approx 9$. A multiplet with small but finite splittings as e.g. in the case of Co(II) ions in the S = 1/2 low spin state which are splitted by hyperfine interactions with the I = 5/2 nucleus are characterized by $n \approx 5$ (see chap. 4.4).[18] The last term in eqn. 2.29 refers to the contribution from the quantum tunnelling through a potential energy barrier. This tunnelling mechanisms are usually induced by a mixing of states due to transversal anisotropies or small interactions with surrounding ions or nuclear spins.

3. Experimental Methods

3.1. High-frequency / High-field Electron Paramagnetic Resonance

The tunable high-frequency/high-field electron paramagnetic resonance (HF EPR) measurement setup which was used in this work can cover a frequency range between 30 GHz and 1 THz as well as a magnetic field range between 0 and 18 T. The sample temperature can be varied in a range between 1.8 and $\approx$ 270 K. Fig. 3.1 shows a schematic sketch of the experimental setup.

The microwave radiation is generated by a microwave vector network analyser (MVNA) provided by the company *AB millimetre, Paris* and transferred over the harmonic generator (HG) part via circular waveguides (blue parts in fig. 3.1) to the sample (green cuboid in fig. 3.1). After passing the sample, the transmitted radiation is reflected by two gold plated mirrors at the bottom of the sample rod (refer to the pathway of the red dotted line in fig. 3.1) and goes back to the MVNA via the harmonic mixer (HM) part where the microwaves are getting detected. The MVNA can generate frequencies between 8 to 18 GHz by means of two gun-diodes. This ground frequency is multiplied by assembling different Schottky diodes to cover the whole frequency range as implied above. The signal detection of the MVNA is based on the evaluation of the beat signal in the MHz range between output and input signal. To stabilize the measurement frequency an EIP 575B source locking frequency counter is used provided by *Phase Matrix Inc., National Instruments*. In order to gain a higher sensitivity the signal itself is modulated with a frequency of $f = 10.448$ kHz and detected by a lock-in amplifier provided by *Stanford Research Systems*. This detected signal is subsequently read out via a desktop PC by a home-build *NI LabView* measurement program.

The high external magnetic fields are generated by a commercial superconducting magnet (orange ring in fig. 3.1) provided by *Oxford Instruments, plc UK*, which is cooled with liquid helium. The helium flow into the sample space is operated over a needle valve (NV). To control the sample temperature, two thermometer and heater pairs are used: one directly situated at the helium output into the sample space as part of a variable temperature insert (VTI) and one in close proximity to the sample. The respective control devices are provided by *Oxford Instruments, plc UK* and *LakeShore Cryogenics*.

The investigated samples were all provided in a solid powder form. Thereby, two different preparation techniques were used. In both cases the samples were placed
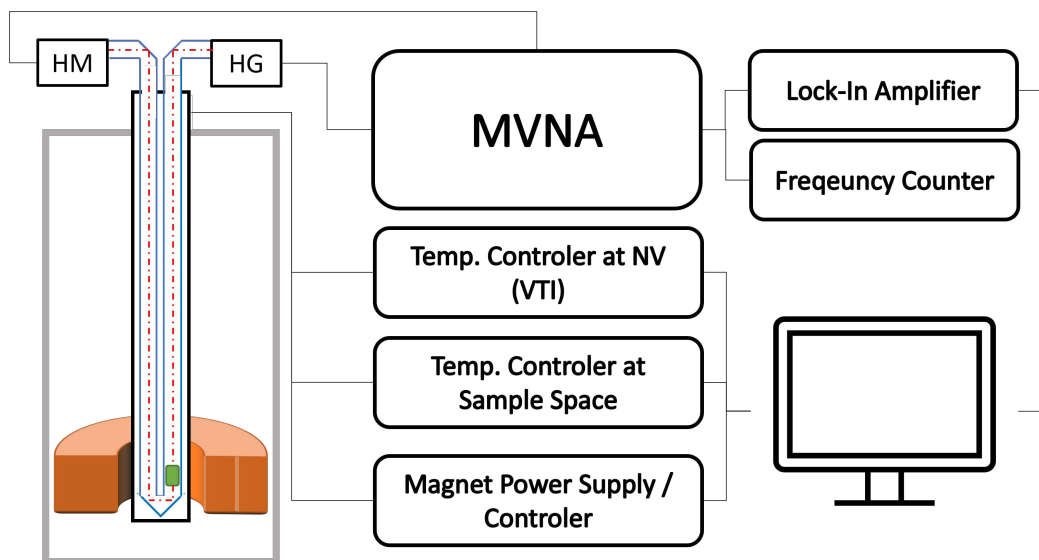
Figure 3.1.: Schematic sketch of the experimental HF EPR spectrometer setup which was used within this work. The superconducting magnet (orange half ring) is located inside a helium cryostat (grey rectangle). The sample (green cuboid) sits inside the waveguides (blue lines) which are surrounded by a vacuum-jacket (black rectangle around waveguides). The red dashed line depicts the path of the microwaves which are generated by the MVNA and transferred over the harmonic generator (HG) to the sample and over the harmonic mixer (HM) back to the MVNA (see main text). A frequency counter stabilizes the microwave frequency. For signal detection a lock-in amplifier is used which is in turn connected to a PC. The sample temperature is controlled and monitored by two temperature controllers connected to a heater and thermometer pair at the needle valve (NV) and in the sample space, respectively. The magnet is controlled by a magnet power supply. All control units are connected to the PC and can be read out and handled over a LabView program.

inside a brass ring which was covered from both sites with microwave transparent capton tape. For the preparation of a so-called loose powder sample, the inner sites of those capton windows was additionally isolated by another layer of capton in order to avoid a sticking of the powder onto the tape and, hence, allow a proper alignment of the sample crystallites within the external magnetic field. The fixed powder samples were prepared by mixing eicosan wax into the powder and heat it up to approx. 40°C in order to melt the wax and glue the sample crystallites together. For both techniques, the sample was ground before the preparation if the crystallite sizes of the powder sample appeared to be too big or too irregular. The grinding had the effect, that in a loose powder experiment, the crystallites could be much easier and more coherently aligned as was monitored by a single nicely sharp orientation jump at relatively low external magnetic fields (< 2 T) in the EPR transmission spectra. For the fixed powder sample the grinding assured a uniform distribution of different crystal orientations and therefore a good powder-like EPR spectra without spikes and

jumps arising from bigger crystallites which are oriented in a particular direction.

3.2. X-Band Electron Paramagnetic Resonance

The X-band electron paramagnetic resonance (X-band EPR) setup used within this work can provide a frequency of f = 9.6 GHz in a magnetic field range between 0 and $\approx$ 1.2 T. The main difference to the HF EPR system described above is the usage of a resonator cavity to increase the coupling between microwaves and sample. Furthermore, in addition to the external applied static magnetic field, a small oscillating field is superimposed, i.e., the transmitted microwave signal is not measured directly, but its derivative. With this, a significantly higher resolution compared to the HF EPR setup can be gained which allows precise investigations of the obtained spectra. However, the frequency in this experiment is fixed to a certain value which depends on the cavity construction. Within this work a commercial *Bruker Elexsys E500* spectrometer was used with an ER 4122SHQE CW cavity. The quality factor Q of this cavity, which is defined by the ration between the line width of the cavity resonance signal and the irradiated frequency, is $\approx$ 4000. The external magnetic field is generated by a water cooled electro magnet. To provide low temperatures down to 4 K a *Cryo Edge* cryostat was used with a compressor system. The temperature control was handled manually by means of an *Mercury iTC* by *Oxford Instruments*.

For the sample preparation an EPR quartz glass tube provided by *Sigma-Aldrich* was used. The powder sample was fixed by eicosan in order to avoid a rearrangement of the crystallites during the measurements.

3.3. Magnetometry

3.3.1. Measurement Devices

The dc susceptibility data shown in this work was mainly acquired by the usage of two different magnetic property measurement systems (MPMS) as well as a physical property measurement system (PPMS), all provided by *Quantum Design*.

Both of the MPMS devices use a superconducting quantum interference device (SQUID) to measure the magnetic moment. The functional principle of such a device can be found in several literature reports.[41, 42] The MPMS-XL system is equipped with a 5 T magnet and can measure the dc susceptibility in a temperature range between 2 and 300 K. The more advanced MPMS3 system can provide magnetic fields up to 7 T in a temperature range between 1.8 and 400 K. With a specific ^{3}He insert, also provided by *Quantum Design*, this temperature range can be extended down to 400 mK. In contrast to the MPMS-XL model, the MPMS3 allows to acquire the dc susceptibility signal not only by the usual dc mode, in which the sample is gradually moved through the pick up coils, but also in a so-called vibrating sample

magnetometer (VSM) mode. Thereby, the sample is vibrating in the pick-up coils and not the direct signal, but the derivative of the induced signal is evaluated. This technique is faster than the common dc acquisition mode and delivers data with higher resolution due to the increased sensitivity. Besides the acquisition of dc susceptibility data, the MPMS3 measurement device also allows to measure the ac susceptibility in a frequency range between 1 and 1000 Hz with a modulation amplitude up to 10 Oe. To reduce the background of the measured signal, the ac option can be driven not only in a so-called one-point-measurement mode, but also offers the option of a three-point- or five-point-measurement. Applying this, the sample's ac response can be measured in different positions or "points" with respect to the gradiometer. As an optimum between time consumption and data quality, the three-point-measurement mode was used for all the ac measurements presented in this work. For a closer description see the respective manual of the device. [43, 44]

The PPMS device can provide external magnetic fields up to 14 T in a temperature range between 1.8 and 300 K. The signal acquisition in this device is comparable to the VSM mode of the MPMS3, but the induced signal is not coupled into a SQUID but directly evaluated.

To acquire dc susceptibility data at even higher external magnetic fields beyond the 14 T provided by the PPMS, pulsed field experiments up to a magnetic field of approx. 60 T were conducted. Thereby, the pulsed magnetic field is generated by the discharge of several capacitors. The measurements shown in this work (see chap. 4.3) were carried out at the High Magnetic Field Laboratory in Dresden (HLD) by S. Spachmann (KIP).[45, 46]

3.3.2. Sample Preparation and Background Correction

Depending on the measurement device and mode, different sample preparation techniques were used. For the dc susceptibility measurements carried out on the MPMS XL device, the powder sample was filled inside a gelatine capsule and fixed with eicosane. Subsequently, the capsule was mounted into a straw sample holder and fixed on the end of a sample rod. For dc susceptibility measurements obtained on the MPMS3 device in the VSM mode, the powder sample was pressed inside a polypropylene capsule which consists of two parts: a cylinder in which the sample is filled and a stamp to properly press the sample into the capsule. Due to this stamp, a further fixing by eicosan wax was not necessary for samples which figure a low anisotropy and thus, the diamagnetic background induced by the eicosan was prevented. However, highly anisotropic samples like $4f$ metal or Co(II) containing compounds strongly tend to align within the external magnetic field and, hence, needed additionally fixing by eicosan. The polypropylene capsules were mounted onto a brass holder which was fixed on the end of a sample rod.

Since the brass holder leads to a frequency dependent background during ac susceptibility data acquisition a straw type preparation method as described for the MPMS XL model was used for this measurements. The same preparation method was also

applied for the measurements within the ^{3}He insert since the brass holder would lead to a heat-bridge between the ^{3}He bath and the sample space.

To correct the background signal arising from the sample holder an empty sample holder with an empty capsule was measured for each acquisition technique separately and the contribution was subtracted from the obtained data. However, due to the proximity of the thermometer to the sample during the ^{3}He measurements, such a correction was not possible in that case which is why the ^{3}He data was scaled in an overlapping temperature range to the results obtained at higher temperatures in the VSM mode of the MPMS3. The same background correction method was used for the data derived by pulsed field experiments, but not with overlapping temperature, but overlapping field ranges between the pulsed field data and the dc susceptibility data acquired with the PPMS in a magnetic field range up to 14 T. The diamagnetic contribution of the sample itself was quantified using PASCAL's constants as described in ref. [47].

4. Co(II) Monomers

Studies of cobalt containing molecules are expanded over a broad range of different scientific disciplines. In medicine, for example, cobalt containing metal-organic materials are explored for decades as "magnetic particle-carriers" to ensure a precise and targeted delivery of a drug to tumor cells.[48] Furthermore, the cobalt ion by itself plays a crucial role in many biological functions e.g. it is the core metal ion of the vitamin B12 complex and other enzymes which are involved in essential biological processes.[49–51] In physics and chemistry, the interest is mainly focused on the magnetic properties of cobalt complexes and how they can be engineered and tuned. Especially the discovery of the first Co(II) complex showing single-molecule magnet behaviour in 2002 by Yang et al. laid the foundation of a whole new field of research.[52, 53]

Co(II) ions naturally provide several advantages which makes them attractive for the construction of molecular systems with high energy barriers like single-molecule or single-ion magnets. Among $3d$ elements, the relatively strong SOC of Co(II) ions offers the possibility to efficiently tune the electronic properties by the variation of the crystal field. Another advantage is the non-integer spin ground state of Co(II) ions which suppresses quantum tunnelling mechanisms [54] and allows the observation of slow relaxation of magnetisation with and without applied external magnetic field as it was shown for many Co(II) containing molecules.[55–60] Finally the broad spatial distribution of d-orbitals can induce strong exchange-interactions between neighbouring ions which leads to high spin ground states for metal clusters and by this to high anisotropy barriers.

Within this chapter, the investigation of several mononuclear Co(II) complexes in different coordination surroundings and spin ground states are discussed. The presented complexes were deeply characterized for their magnetic properties by means of X-Band and HF EPR as well as static and dynamic magnetisation measurements. Furthermore, different theoretical models and calculations are applied to rationalize the experimental findings.

Parts of the following sections have already been published in the same form in ref. [19, 20, 61] which is explicitly indicated and referenced to prior to the respective sections. Figure and table numberings are changed in order to ensure a continuous labelling throughout this thesis. Any contributions originating not from the author L. Spillecke are mentioned in the text or as footnotes.

4.1. Influence of a Counteranion on the Zero-Field Splitting of Tetrahedral Cobalt(II) Thiourea Complexes

Most of the attempts to tune the magnetic single-ion properties of a molecular system focus on the variation and chemical engineering of the first coordination sphere, i.e. the ligating ions which are directly coordinated to the central metal ion. It is a trivial assumption that indeed these ions should have the main impact on the crystal field which is influencing the metal ion due to their vicinity. However, there are examples reported in the literature which show, that not only the first, but also the secondary coordination sphere or the cat- and anions in the crystal lattice can potentially have a significant impact on the crystal field which is faced by the metal ions.[62–64]

To closer investigate the correlation between chemical construction of the second coordination sphere and the single-ion properties, Tripathi et al. synthesizes a sample set of four different Co(II) monomers which all figure a pseudo-tetrahedral geometry of the first coordination sphere, but have different counter-anions in the second coordination sphere.[19] These isolated complexes have the general molecular formula $[Co(L_1)_4]X_2$, where L_1 are thiourea ligands and X = NO_3 (**1**), Br (**2**), I (**3**) and $[Co(L_1)_4](SiF_6)$ (**4**), respectively. As reported in ref. [19] the dc susceptibility measurements reveal, that the compounds **2** to **4** figure indeed a change in magnetic anisotropy parameters. However, fits to the dc susceptibility data can often only give rough or qualitative results regarding the real magnetic anisotropy due to various parameter dependencies. Therefore, sample **3** was picked to perform HF EPR measurements which result in the quantitative definition of the zero field splitting (ZFS) as well as the crystal field parameters and g-value of this exemplary system.

4.1.1. Molecular and Crystal Structure

Fig. 4.1 (a) depicts the molecular structure of the investigated sample.[3] The central Co(II) ion is surrounded by a pseudo-tetrahedral coordination environment formed by thiourea ligans. In fig. 4.1 (b) the molecular packing diagram is shown which vizualises not only the position of the iod counter-anions (purple in fig. 4.1(b)), but also that there are two inequivalent molecular sites which can be distinguished by eye within one unit cell. These two molecular positions are connected by a mirror symmetry. However, theoretical calculations predict, that the anisotropy axis of all molecules in the unit cell are tilted against each other by maximal 14.8° which is to small to have a significant impact on the measured HF EPR resonance branches, as it is discussed in more detail in the subsequent chap. 4.2.[20] The minimal distance between two Co(II) centres can be defined as 6.98 Å. The resulting dipolar magnetic interactions ($J_{DD} \approx 0.1$ GHz) are by this far beyond the expected energy scale of

---

[3]Single crystal XRD and determination of the structure was performed by S. Tripathi under the supervision of M. Shanumgam, IIT Bombay.[19]

the CF anisotropy which is why they can be neglected in a first approximation to obtain the single-ion anisotropy parameters. However, as will be shown in chap. 4.2, to explain the measured HF EPR spectra in detail, it is indispensable to introduce a finite intermolecular interaction between the nearest neighbouring Co(II) ions.
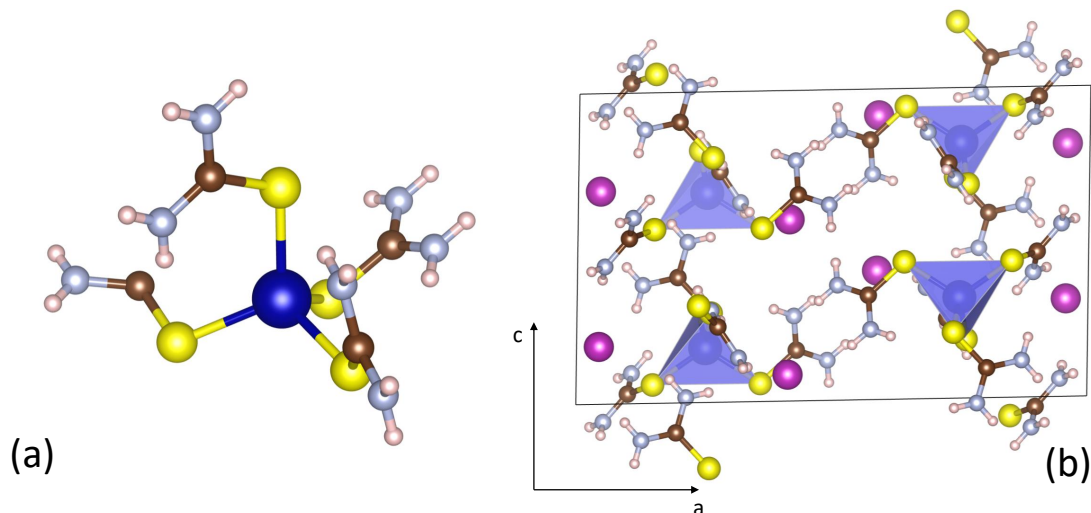

Figure 4.1.: Molecular structure (a) and crystal packing (b) for the investigated pow-
der sample **3**. Blue , Co(II);yellow, S; brown, C; light blue, N; purple,
I; white, H. (*The samples were structurally characterized by S. Tripathi,
IIT Bombay.*)

The following chapters (chap. 4.1.2 and 4.1.3) show data which was acquired and evaluated by L. Spillecke and text which has been mainly written by L. Spillecke under the supervision of C. Koo (KIP Heidelberg). These chapters are published in this form (see Tripathi et al., ref. [19]) as part of a research article in the journal Inorganic Chemistry.

4.1.2. HF-EPR Studies

HF-EPR measurements were carried out on a pure polycrystalline (100 %) sample powder of **3** aligned with the applied magnetic field (see the Experimental Section chap. 4.1.3). Depending on the frequency, four different resonance features are observed at T = 2 K (see Figure A.1 for details[4]). The spectra exhibit strong field-dependent mixing of the phase and amplitude signal, which prevents the appropriate phase correction of the spectra. However, because the experimental setup enables detection of both the phase and amplitude of the signals, the actual resonance fields can be well read-off, thereby enabling precise determination of the resonance frequency-field diagram (Figure 4.2).

---

[4]The supplementary material for the Co(II) monomer chap. 4 is shown in the Appendix chap. A.1.

Figure 4.2 displays the temperature evolution of the HF-EPR spectra measured at 278.6 and 396.6 GHz, respectively. As will be shown below, the chosen frequencies surround the value of the EPR gap at zero field; i.e., $\Delta = 306$ GHz. The gap at zero field, denoted Δ, is the signature of an energy difference between the m_S sublevels and corresponds to $2D$ for an $S = 3/2$ spin state. At 396.6 GHz, three resonance features are present. Resonance features R1 and R3 are most pronounced at 2 K but significantly decrease in intensity upon heating and vanish at 30 and 50 K, respectively. The much weaker resonance R2 observed at the shoulder of R1 becomes invisible at 8 K. Meanwhile, below Δ, at 278.6 GHz, the resonances R1, R3, and R4 are clearly visible in the spectra (Figure 4.2(a)). As the temperature increases, resonance R3 gradually vanishes and completely disappears at 10 K, while the intensity of resonance R4 slightly increases between 2 and 6 K and remains up to 15 K.
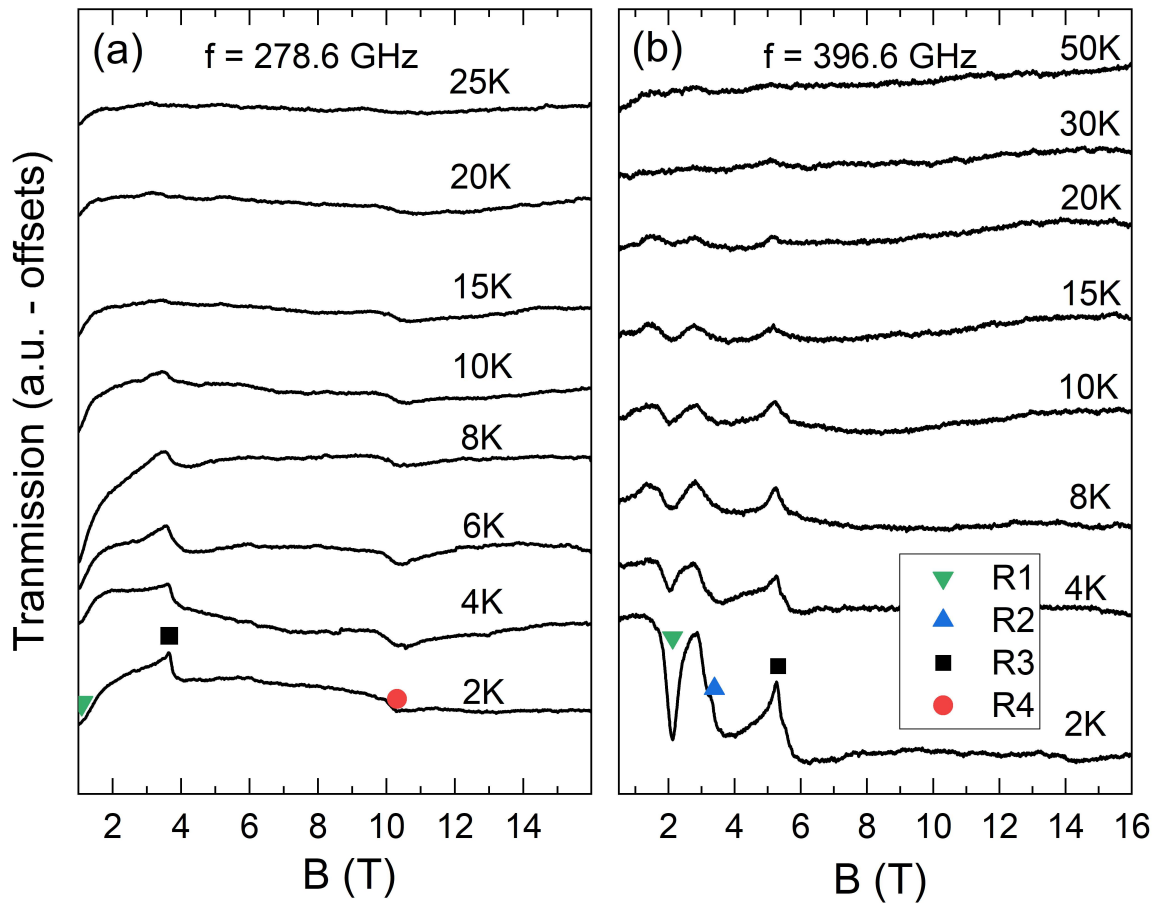
Figure 4.2.: HF-EPR spectra of **3** (100 % polycrystalline sample) measured at (a) f = 278.6 GHz and (b) f = 396.6 GHz at various temperatures. Symbols denote the corresponding resonance branches R1 to R4 (cf. Figure 4.3). (*Figure reprinted from Tripathi et al..[19]*)

A summary of all resonance features observed at different frequencies in the field range $1 \text{ T} \leq B \leq 16 \text{ T}$ shown in Figure 4.3 clearly confirms the presence of four distinct resonance branches R1-R4. In particular, for branches R2-R4, a linear be-

havior is clearly visible. While R1 and R2 exhibit gaps at zero field (Δ) of more than 300 GHz, R3 and R4 show $\Delta \approx 0$, implying that they are associated with transitions within a Kramers' doublet. In addition, the slopes of the branches allow one to attribute R2 and R4 to allowed transitions. Specifically, the slopes imply a g value of $g_{\text{eff}} = 2.00(5)$, suggesting that $\Delta m_S = \pm 1$. In contrast, branches R1 and R3 show much steeper slopes with $g_{\text{eff}} \neq 2$, indicating that they are forbidden resonances. To be specific, $g_{\text{eff}} = 4$ of resonance R1 may be associated with $\Delta m_S = \pm 2$ and $g_{\text{eff}} = 6$ of resonance R3 with $\Delta m_S = \pm 3$.

A quantitative analysis of the frequency-field diagram can be done by simulating the resonance branches by means of the Hamiltonian shown in eq 4.1.

$$H = g_{\text{B}} \vec{B} \cdot \vec{S} + D \left[S_z^2 - \frac{S(S+1)}{3} \right] + E(S_x^2 - S_y^2) \tag{4.1}$$

Simulation with the parameters $g = 2.00(5)$ and $|D| = 5.107$ cm^{-1} (and $E = 0$) yields the four branches shown in Figure 4.3 (see Figure A.2 for more details). The simulated branches are in good agreement with the experimental data. The observed gap at zero field of the transitions between the different doublet states, i.e., between $m_S = \pm 3/2$ and $\pm 1/2$, amounts to $\Delta = 306(4)$ GHz (10.20(14) cm^{-1}). The fact that R3 is more pronounced than R4 indicates the negative sign of the single-ion anisotropy parameter D. The negative sign is further corroborated by the observed temperature dependence of the resonance intensities. Specifically, the spin-state transitions associated with resonances R1-R4 are $|-3/2\rangle \rightarrow |+1/2\rangle$ ($|+3/2\rangle \rightarrow |-1/2\rangle$) for R1, $|-3/2\rangle \rightarrow |-1/2\rangle$ ($|+3/2\rangle \rightarrow |+1/2\rangle$) for R2, $|-3/2\rangle \rightarrow |+3/2\rangle$ for R3, and $|-1/2\rangle \rightarrow |+1/2\rangle$ for R4. Transitions in the parentheses are associated with a measurement frequency below the gap at zero field. For microwave frequencies smaller than Δ, our model hence suggests that R3 is associated with a ground-state transition, while R1 and R4 arise from excited states, as indeed is suggested by the experimental data in Figure 4.2(a). In contrast, for frequencies exceeding Δ, R1 and R2 become visible ground-state transitions, which are confirmed by the fact that maximum intensities are observed at the lowest temperature (Figure 4.2(b)). This assignment agrees with the observed temperature dependence, which tentatively suggests that R1 and R3 are ground-state transitions.

The HF-EPR data do not enable one to precisely quantify the transverse anisotropy parameter E of complex **3**. However, the presence of pronounced forbidden resonances implies vigorous spin-state mixing due to finite transverse anisotropy in the complex.[65] The effect of finite $E = 10$ GHz (0.33 cm^{-1}) on the simulated resonance branches is shown by dashed lines in Figure 4.3. The incorporation of the rhombic term $E(S_x^2 - S_y^2)$ (eq 4.1) yields non-linear behaviour of branch R1 at low energies as well as anti-crossing effects of branches R2/R3 and R2/R4. Larger values of E are not compatible with the experimental data, so that $E = 10$ GHz sets an upper limit of transverse anisotropy. Finite E, however, does not cover a small but finite negative offset Δ of resonance branch R3, which might be associated with finite intermolecular magnetic interaction. Overall, the HF-EPR experiments performed on **3** clearly reveal

the negative anisotropy associated with the ground state and also enable quantitative determination of the zero-field energy gap [$2D$ = -10.20(14) cm^{-1}].

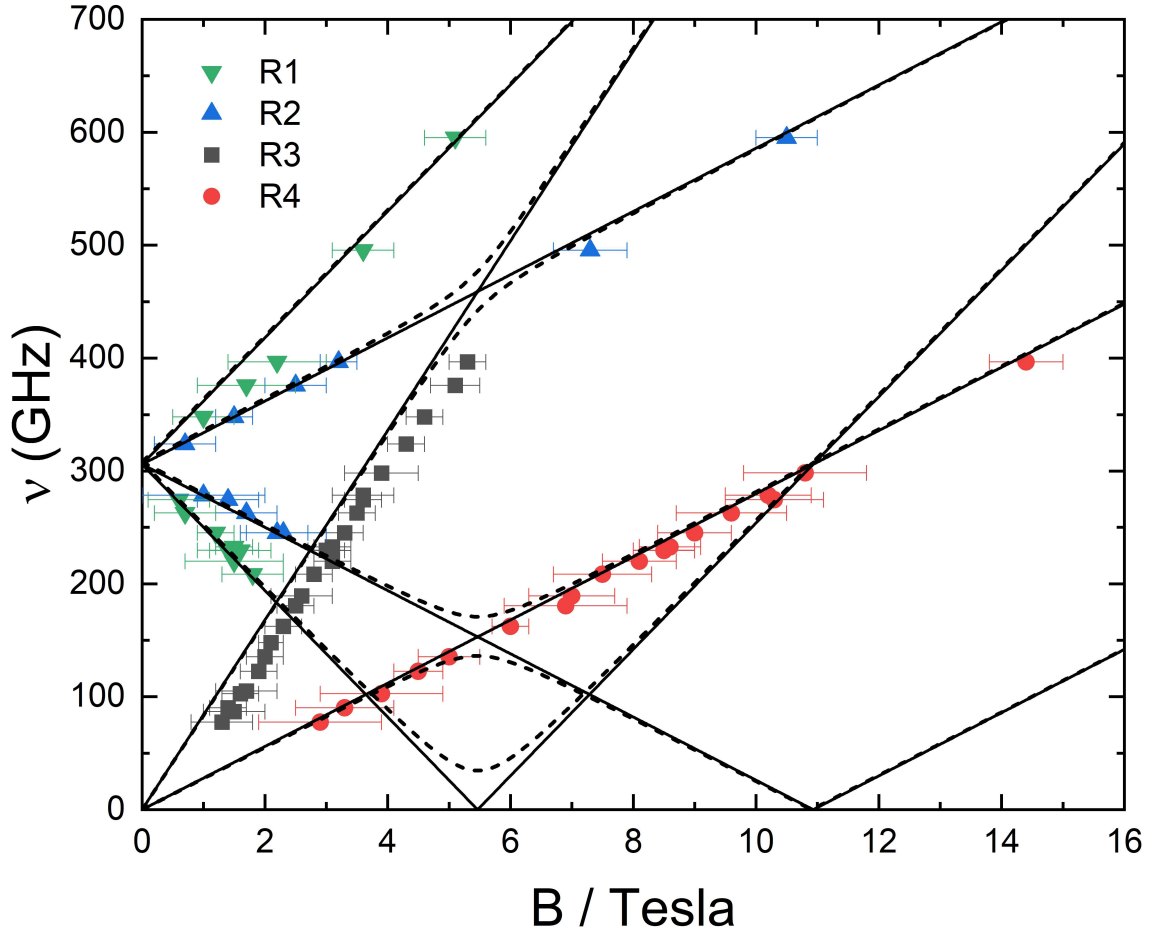Figure 4.3.: HF-EPR absorption frequencies versus magnetic field at T = 2 K. Solid lines show simulation results obtained by solving eq 1 with the EasySpin [66] software package using the parameters S = 3/2, g = 2.00, D = 153 GHz (5.1 cm^{-1}), and E = 0. Dashed lines indicate the effect of finite transversal anisotropy E = 10 GHz (0.33 cm^{-1}). (*Figure reprinted from Tripathi et al..[19]*)

4.1.3. Experimental Details

High-frequency electron paramagnetic resonance (HF-EPR) measurements were carried out by means of a millimeter vector network analyzer by ABmm, which is used as a microwave source and detector.[67] The spectra have been taken at various microwave frequencies between 70 and 600 GHz, which were achieved by means of assembling several band diodes, such as V, W, and D bands, etc. A superconducting magnet by Oxford Instruments provides high magnetic fields up to 16/18 T. The temperature is controlled by means of a variable-temperature insert with a helium

4 gas flow. Powder samples are placed inside a brass sample holder at the end of a transmission-type tube-based probe. No glue or grease has been used so that the loose powder sample is expected to be aligned in the high magnetic field of the experiment.[68] Evidence of powder alignment is indeed observed because abrupt steps of the initial HF-EPR spectra taken preliminarily to the data presented at hand as well as at low fields. The HF-EPR data are, hence, restricted to $B \geq 1$ T.

4.1.4. Conclusion

By using HF EPR spectroscopy on a Co(II) monomeric complex in a pseudo-tetrahedral coordination environment, the axial CF parameter D = -153 GHz and the g-value $g = 2.00$ along the orientation direction of the crystallites within the external magnetic field were precisely defined. Furthermore, a finite E-value was observed. The quantitative comparison of these derived parameters with the results from dc susceptibility measurements and DFT calculations (see ref. [19]) enables to form conclusions about the reliability of these experimental and theoretical approaches as discussed in ref. [19]. The experimental and analytical approach which was followed, will be extended in the following chapter (chap. 4.2) to other compounds from the sample series described above.

4.2. A High-frequency EPR Study of Magnetic Anisotropy and Intermolecular Interactions of Co(II) Ions

Lena Spillecke[a*], Shalini Tripathi[c], Changhyun Koo[a], Mursaleem Ansari[c], Shefali Vaidya[c], Amaleswari Rasamsetty[c], Talal Mallah[d], Gopalan Rajaraman[c], Maheswaran Shanmugam[c*], Rüdiger Klingeler [a,b*]

[a]Kirchhoff Institute for Physics, Heidelberg University, 69120 Heidelberg, Germany
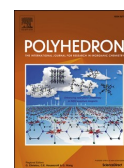[b]Centre for Advanced Materials, Heidelberg University, 69120 Heidelberg, Germany
[c]Department of Chemistry, Indian Institute of Technology Bombay, Powai, Mumbai 400076, Maharashtra, India
[d]Institut de Chimie Moléculaire et des Matériaux d'Orsay, CNRS, Université Paris Sud, Université Paris Saclay, 15, rue Georges Clemenceau, 91405 Orsay Cedex, France
* Communicating authors

This manuscript has been published in 2021 as a research article in the Journal *Polyhedron*.[20] The following list expounds in detail the respective contributions of each co-author, particularly highlighting the specific contributions of L. Spillecke who is the first and communicating author of this publication.

- High-frequency / high-field electron paramagnetic resonance (HF EPR) measurements and evaluation of the acquired data as well as construction of the plotted Figures was done by L. Spillecke (Fig. 3, 4, 5, 6, 7, 8 and 9 and suppl. Fig. S1, S2, S3 and S4). Except the part about the structural description of the compound under study (Fig. 1 and 2) and the chapters *Hirshfeld surface analysis of complexes 1–3* and *Numerical calculation for estimating the exchange interactions*, the manuscript draft was written by L. Spillecke.

- S. Tripathi, S. Vaidya, T. Mallah and M. Shanmugam synthesized the sample, solved the structure and contributed to the manuscript writing.

- M. Ansari, A. Rasamsetty and G. Rajamaran performed numerical calculations, the Hirshfeld analysis and contributed to the manuscript writing.

- C. Koo supervised the HF EPR measurements and supported the data analysis and manuscript writing.

- R. Klingeler supervised the measurements and supported the data analysis and manuscript writing.

- All the authors have proofread the manuscript.

A high-frequency EPR study of magnetic anisotropy and intermolecular interactions of Co(II) ions

Lena Spillecke [a],[*], Shalini Tripathi [c], Changhyun Koo [a], Mursaleem Ansari [c], Shefali Vaidya [c], Amaleswari Rasamsetty [c], Talal Mallah [d], Gopalan Rajaraman [c], Maheswaran Shanmugam [c],[*], Rüdiger Klingeler [a],[b],[*]

[a] Kirchhoff Institute for Physics, Heidelberg University, 69120 Heidelberg, Germany
[b] Centre for Advanced Materials, Heidelberg University, 69120 Heidelberg, Germany
[c] Department of Chemistry, Indian Institute of Technology Bombay, Powai, Mumbai 400076, Maharashtra, India
[d] Institut de Chimie Moléculaire et des Matériaux d'Orsay, CNRS, Université Paris Sud, Université Paris Saclay, 15, rue Georges Clemenceau, 91405 Orsay Cedex, France

ARTICLE INFO

ABSTRACT

Changing the anion in a crystal lattice induces distinct structural distortions in the $[CoS_4]^{2+}$ core for a family of complexes with the general molecular formula $[Co(L_1)_4]X_2$, where L_1 = thiourea (NH_2CSNH_2) and X = I (**1**), Br (**2**), and $[Co(L_1)_4](SiF_6)$ (**3**). The magnetic anisotropy (D) for **1–3** was quantitatively determined with a magnitude of −153(2), −168(5) and < -400 GHz, respectively, by HF-EPR investigation. Also, intermolecular exchange interactions were determined experimentally, whereby an antiferromagnetic exchange for **1** (-5.5 GHz) and **2** (-4.1 GHz) and a ferromagnetic interaction for **3** (+3.5 GHz) are witnessed (based on $H = -JS_1S_2$). The exchange interactions, computed using DFT methods on a model complex of **1**, disclose the presence of an antiferromagnetic exchange interaction, consistent with the experimental observation. Overall, the present study provides convincing experimental evidence for the sizable influence not only of the first but also of the second coordination sphere on the magnetic anisotropy and exchange interactions of Co(II) ions.

1. Introduction

Tuning magnetic anisotropy and ligand fields of metal–organic complexes, and thereby controlling the slow-relaxation behaviour in single-molecule magnets (SMMs), is a key prerequisite to exploit these materials as a future alternative to conventional data storages [1–3]. As an alternative to multi-centre SMMs, which offer the potential of very large spin quantum numbers with however often reduced magnetic anisotropy, restricting to systems with only a single paramagnetic centre, i.e. so-called single-ion magnets (SIM), offers a route to more simple model systems with significant anisotropy [4–11]. Due to large unquenched magnetic moments and large intrinsic magnetic anisotropy, many lanthanide-based SIMs have been investigated which offer record values for magnetic anisotropy barriers [12–15]. Transition metal ions with (partly) unquenched orbital moments provide another promising route towards novel SIMs [16–18].

Distorted tetrahedrally-coordinated high-spin Co(II) monomers exhibit relatively strong spin–orbit coupling and their electronic properties can be tuned by variation of the crystal field [19–24]. The half-integer magnetic ground state of high-spin Co(II) ions prevents quantum tunnelling mechanisms [25], thus allowing the observation of slow relaxation of the magnetisation in the absence of external magnetic fields [6,9,26–29]. Tuning of the spin Hamiltonian parameters is typically achieved by variation of the first coordination sphere around the central ion [29–33]. However, as reported recently, the second or peripheral coordination spheres can also have a significant impact, not only on the magnitude but also on the nature (e.g. the sign of the axial anisotropy parameter D) of the magnetic anisotropy [28,34–40]. In order to quantitatively investigate these effects and to understand the electronic structure of Co(II)-complexes and the magnetic relaxation mechanisms, precise determination of the spin Hamiltonian (SH) parameters (g-value, axial and transversal anisotropy parameters D and E)

are mandatory. The zero-field splitting (ZFS) induced by the axial single-ion magnetic anisotropy (associated with the parameter D) for Co(II)-containing systems is, however, often too large to be measured by conventional electron paramagnetic resonance (EPR) techniques since both the X- and Q-bands cannot be employed as $D \gg h\nu$ implies the absence of allowed EPR signals at the frequencies ν. To investigate such systems, high-frequency/high field electron paramagnetic resonance (HF-EPR) measurements are usually used [41,42]. In this article we present detailed tuneable HF-EPR studies on three high-spin Co(II)-monomers, namely $[Co(L_1)_4]I_2$ (**1**), $[Co(L_1)_4]Br_2$ (**2**) and $[Co(L_1)_4]SiF_6$ (**3**), where L_1 = thiourea (NH_2CSNH_2).

The influence of the secondary coordination on the modulation of the magnetic anisotropy of Co(II) ions is known theoretically [27,28,35,37,38], but experimental evidence, measured on the significant influence which was found for other complexes, is currently relatively scarce in the literature [29,37,38,43,44]. The present work furnishes a further experimental proof for the impact of the variation of the secondary coordination sphere on the magnetic anisotropy of Co(II) ions. The theoretical calculations are in excellent agreement with the experimental observations (*vide infra*) [37].

Besides a detailed investigation on the single ion behaviour of the Co(II) centres, we also observed small intermolecular super-exchange interactions in the range of a few GHz (~3–6 GHz) for all three complexes, which are beyond the resolvable energy scale of a standard SQUID magnetometer. Quantification of these interactions reveals that not only the strength but also the sign changes based on the anions in the crystal lattice, which have an influence on the secondary coordination sphere. Finite intermolecular interactions can play a crucial role in the suppression of slow magnetic relaxation behaviour in such complexes [45–48], therefore, this investigation can help to tune single ion properties via controlling supramolecular interactions by changing the cations/anions in the crystal lattice. This mechanism is discussed in detail in the present study.

2. Experimental section

The complexes investigated in this article were synthesised as reported by us earlier [37]. High-frequency/high-field electron paramagnetic resonance (HF-EPR) measurements were performed using a millimeter vector network analyser (MVNA) from ABmm as a phase sensitive microwave source and detector [49]. The spectra were obtained in the frequency range 70–600 GHz and in external magnetic fields of up to 16 T. Temperature control between 2 and 80 K was ensured by a variable temperature insert (VTI) with a He gas flow. The powder samples were placed inside a brass ring in the form of a loose powder, i.e. no extra glue or grease was used. This setup enables alignment of the crystallites in the external magnetic fields, which was performed by means of applying the maximum field of 16 T prior to the measurements. During this initial field sweep, alignment was ensured by monitoring the corresponding alignment jumps in the transmitted microwave signal. In addition, rearrangement of the crystallites was avoided by restricting the magnetic field to the range 0.2 to 16 T. Analysis of the data was done using the EasySpin software package [50].

Broken Symmetry Density Functional Theory (BS-DFT) calculations were performed on the full coordinates of the crystallographic structure of **1** using unrestricted hybrid B3LYP functionals [51], with the all electron Alhrich's triple-ζ valence (TZV) [52,53] basis set for all the elements, as implemented in the Gaussian 09 suite of programs [54]. The magnetic exchange coupling interaction was calculated on binuclear models that were generated from the crystal structure of **1** and the exchange coupling between the two high spin monomeric Co(II) ions was described by the Heisenberg-Dirac-van Vleck (HDVV) Hamiltonian as follows:

$$H_{HDVV} = -JS_1S_2 \tag{1}$$

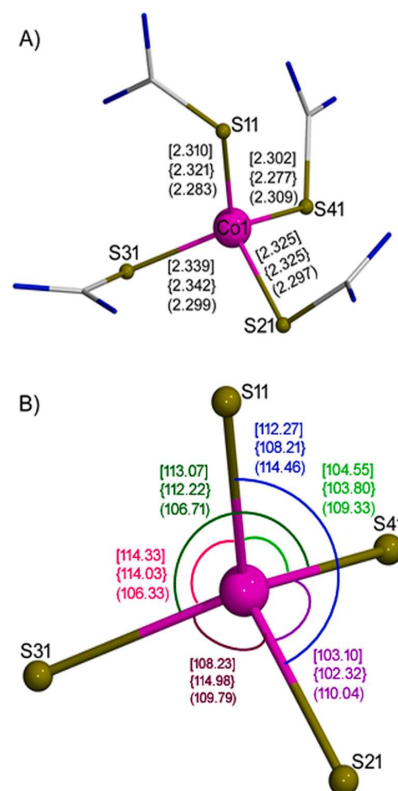This Hamiltonian was used to describe the intermolecular

Fig. 1. Representative molecular structure of complex **1**. Hydrogen atoms are removed for clarity. Colour code: grey = C and blue = N. The parameters in the square, curly and round brackets correspond to the bond lengths (Å, panel A) and bond angles (°, panel B) for **1**, **2** and **3**, respectively. ((Colour online.))

interactions throughout the manuscript in all sections.

For the estimation of the magnetic coupling, Hartree–Fock or DFT methods, together with the broken symmetry (BS) model developed by Noodleman and co-workers, have been employed, coupled with the equation proposed by Ruiz and co-workers.[55–57]

$$J = \frac{(E_{BS} - E_{HS})}{2S_1S_2 + S_2} \tag{2}$$

3. Results and discussion

By employing the thiourea ligand with the corresponding cobalt precursors, we have isolated three different cobalt monomeric complexes (**1–3**). The detailed synthesis, as well as the structural description, along with the crystallographic parameters of all the complexes, were recently reported by us [37].

Complexes **1–3** are structurally analogous to each other. The four coordination sites of the Co(II) ions in the complexes are occupied by sulfur ligands. Thus, the Co(II) ions exhibit a distorted tetrahedral geometry. The overall cationic charge in the coordination sphere of **1–3** is satisfied by two iodides, two bromides and one SiF_6 anion in the crystal lattice, respectively. A representative molecular structure of **1** is shown in Fig. 1. Selected bond lengths and bond angles for the structurally analogous complexes of **1–3** are provided in Fig. 1(A) and (B), respectively.

To understand the geometry around the Co(II) ion, we have performed continuous shape measurement (CShM) analysis, which
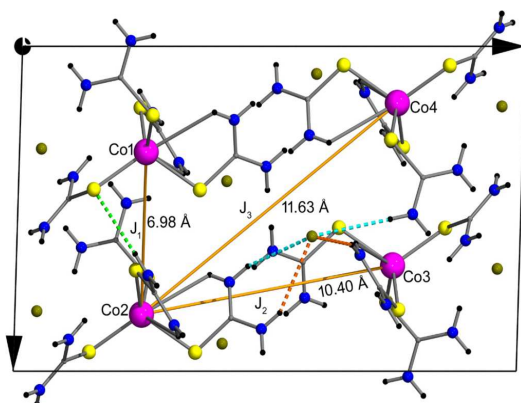
Fig. 2. The packing diagram of **1** (view along the b-axis) shows the interatomic distance between the molecules in the crystal lattice. The dotted bonds represent the intermolecular H-bonding between the molecules in the crystal lattice.

indicates that all three complexes display a distorted tetrahedral geometry (Table S1). For the molecules **1**–**3** the CShM values are estimated to be 0.28, 0.22 and 0.09, respectively, with respect to the ideal T_d geometry. The obtained values suggest, that complex **1** has a higher distortion with respect to the ideal tetrahedral geometry around the Co(II) ion compared to the complexes **2** and **3**. This can be attributed to the change of the anion in the crystal lattice for complexes **1**–**3**. Further, we would like to emphasize that depending on the identity and orientation of the anions in the crystal lattice of these complexes, a distinct supramolecular interaction, namely H-bonding, is observed. Furthermore, the strength of H-bonding differs for all the observed complexes, e.g. the H-bonding strength in **1** is stronger than that in **2**. Consequently, the variation of the secondary coordination sphere, which leads to distinct distortion around the Co(II) ion, does not only modulate the single ion anisotropy of the complexes **1**–**3** but also the strength of intermolecular exchange interactions. This result is in line with the intermolecular exchange interactions determined by HF-EPR i.e. the observed interaction for **1** is stronger compared to that of **2**, as further described below.

Figure 2 shows the packing diagram of the representative complex **1**. It is found that there are four crystallographically equivalent molecules (symmetry code: -X, 0.5 + Y, 0.5-Z; labelled as Co(II)1-Co(II)4 in Fig. 2) within one unit cell. A pair of molecules labelled Co(II)1 and Co(II)2 in Fig. 2 generates another pair labelled Co(II)3 and Co(II)4, respectively, by inversion symmetry. Although, the molecules Co(II)1 and Co(II)2 (and their symmetrically equivalent molecules) are crystallographically equivalent (Fig. 2), they do not overlay on top of each other, i.e. the molecule Co(II)2 is slightly tilted away from the molecule Co(II)1. This leads to a small angle of 14.8° between the anisotropy axes of the respective molecules. Fig. 2 also shows the Co(II)…Co(II) distances between the molecules within the unit cell (6.98, 10.40 and 11.63 Å). A more detailed description of the crystal structure of **1**, as well as those of **2** and **3**, is given in Ref. [37]. The strongly different distances between the Co(II) ions already implies a hierarchy of the possible intermolecular exchange interactions. In particular, magnetic coupling between the further separated molecules, with intermolecular distances of 10.40 and 11.63 Å, is expected to be extremely weak or negligible. A more detailed discussion regarding the possible coupling pathways between the Co(II) ions is given below.

3.1. Magnetic anisotropy and crystal field

To determine the SH parameters of **1**–**3** quantitatively, tuneable HF-EPR studies were performed. The measured spectra of the investigated materials display clear resonance features in the frequency and magnetic
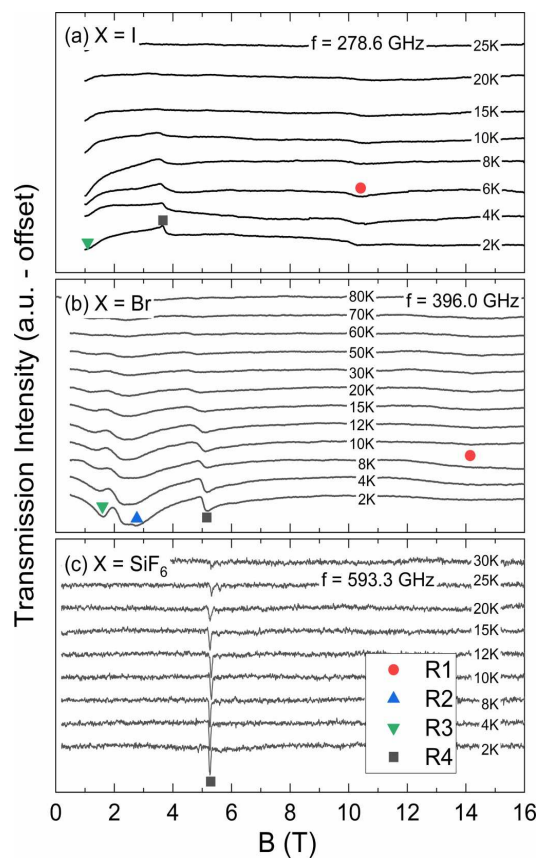

Fig. 3. HF-EPR spectra at different temperatures for (a) complex **1** at $\nu = 278.6$ GHz (9.3 cm^{-1}) (data from Ref. [37]), (b) **2** at $\nu = 396.0$ GHz (13.2 cm^{-1}) and (c) **3** at $\nu = 596.3$ GHz (19.9 cm^{-1}). The symbols denote different resonance features associated with the respective branches R1 to R4 in Fig. 5.

field range under study. Depending on the measurement frequency, up to four different resonances are observed at $T = 2$ K, as shown in Fig. 3. The spectra obtained for **1** and **2** exhibit strong field-dependent mixing of the phase and amplitude signals, which prevents appropriate phase correction of the spectra. However, as the experimental setup enables the detection of both the phase and amplitude of the transmitted microwave radiation, the actual resonance fields can be well read from the data, which enables the precise determination of the resonance field at a given frequency.

Figure 3(c) shows one sharp resonance for **3** at the frequency $\nu = 593.3$ GHz in the field range under study (0 – 16 T). Upon heating, this feature is visible up to 30 K, but becomes weaker, indicating Curie-like behaviour, i.e., the feature is associated with a ground state resonance. Notably, a small side feature appears (see, e.g., the spectrum at $T = 25$ K), which is discussed below. Complex **2** features four resonances at $\nu = 396.0$ GHz, labelled R1 to R4. Again, R2 to R4 are ground state resonances while R1 shows an activated behaviour, as indicated by the observed temperature dependence. The positions of the obtained resonance features for all three investigated complexes are shown in the frequency vs magnetic field diagrams (see Fig. 4). Data for **1** have been reported previously [37] and are presented for comparison purposes with the other structurally analogous complexes. Note, that the resonance branch R1 of **1** displays an activated behaviour similar to R1 of **2** as demonstrated by the temperature dependence of the associated
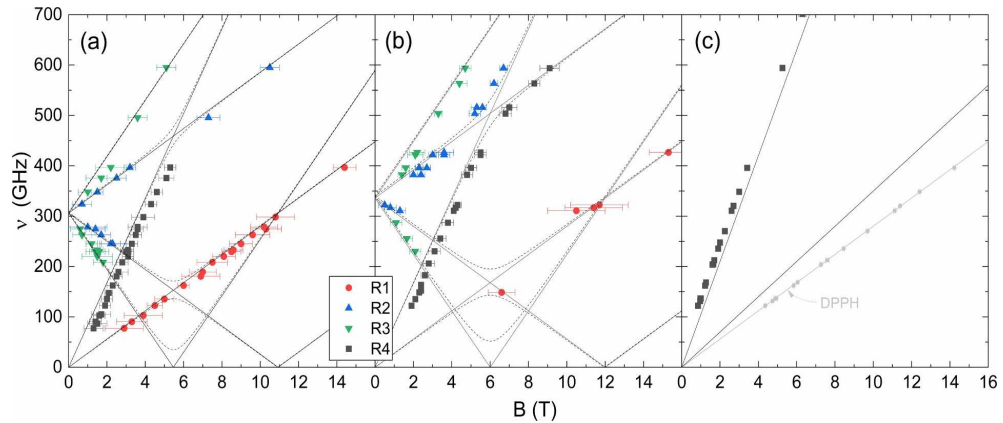
Fig. 4. Frequency vs. magnetic resonance field diagram of complex **1** (a, experimental data from Ref.[37]), **2** (b) and **3** (c) measured at $T = 2$ K. The solid black lines correspond to a simulation using the SH shown in Eqn. (3) with the parameters listed in Table 1 and without transversal anisotropy (i.e., $E = 0$). Dashed lines visualize the influence of a finite value for E ($E = 10$ GHz (0.33 cm^{-1}) for **1** and $E = 15$ GHz (0.50 cm^{-1}) for **2**).

Table 1

Simulation parameters using the SH shown in Eqn. (3) extended by an exchange coupling term as shown in Eqn. (1). The third column provides an upper limit of finite E for **1** and **2**.

Complex	D (GHz)	$|E|$ (GHz)	g_z	J (GHz)
1	−153(2)	≤10	2.00(5)	−5.5(5)
2	−168(5)	≤15	2.00(10)	−4.1(5)
3	< −400	≠ 0	2.65(1)	+3.5(2)

resonance features [37].

The measured resonance positions can be summarised in distinct branches. For **1** and **2**, four branches R1 to R4 are found, while only one branch is observed for **3** (see Fig. 4). Branches R1 and R4 in **1** and **2** as well as the single resonance branch in **3** display linear behaviour and exhibit no excitation gap (Δ) at $B = 0$ T. We conclude that the associated transitions appear within the Kramers doublets $m_S = \pm 1/2$ and $\pm 3/2$. In contrast, R2 and R3 in both **1** and **2** show gaps at zero field of >300 GHz (10 cm^{-1}) indicating splitting of the associated spin states, i.e. the so-called zero-field splitting (ZFS) [58]. Finite ZFS can be attributed to magnetic anisotropy due to the crystal field induced by the surrounding ligands.

Effective g-values can be extracted from the slope of the branches. Since the powder crystallites are aligned with respect to the external field, only one component of the in general anisotropic g-factor is measured, which is denoted here as g_z. Note, that g_z is explicitly not meant as the g_{zz} component of the g-tensor, since g_{zz} and D_{zz} are not in parallel but tilted based on NEVPT2 calculations on the representative complex **1** (see Figure S6 and Ref. [37]). The slopes of the branches R1 and R2 in **1** and **2** imply $g_z = 2.00(5)$ and $g_z = 2.0(1)$, respectively. The features are hence associated with transitions $\Delta m_S = \pm 1$. In contrast, R3 and R4 show much steeper slopes with $g_z = 4.0(1)$ and $g_z = 6.0(1)$, respectively, indicating forbidden transitions, i.e., $\Delta m_S = \pm 2$ and ± 3. The slope of the single branch observed in **3** indicates $g_z = 7.5(1)$. A quantitative analysis of the data applies the effective SH in Eqn. (3), which describes the Co(II) centres as well isolated spins $S = 3/2$ featuring axial and transversal anisotropy, D and E. In addition to axial and transversal anisotropy terms, the SH includes the Zeeman term with the Bohr magneton μ_B and the external magnetic field B [42].

$$H = g\mu_B \vec{B} \cdot \vec{S} + D\left[S_z^2 - \frac{S(S+1)}{3}\right] + E\left(S_x^2 - S_y^2\right) \qquad (3)$$

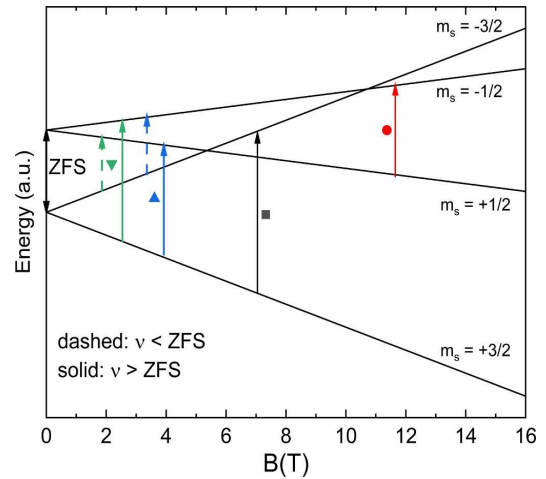A simulation of the resonance branches using Eqn. (3) with the

Fig. 5. Energy-level diagram using Eqn. (3) with $S = 3/2$, $D < 0$, and $E = 0$. The external field is oriented along the direction of the anisotropy axis. Coloured arrows mark transitions between the spin states of the correspondingly marked resonance branches (cf. Figs. 3 and 4). Solid arrows show transitions at measurement frequencies $\nu > \Delta/h$, i.e. larger than the zero-field gap, dashed arrows are associated with $\nu < \Delta/h$.

parameters given in Table 1 and $E = 0$ yields good agreement to the experimental data, as shown in Fig. 4 as solid black lines. As mentioned above, there are two different orientations of the anisotropy axis within the crystal structure. Consequently, the anisotropy axis of the oriented powder is 7.4° tilted away from the magnetic field direction. However, as can be seen in Figure S1, this leads only to marginal effects on the branches in the low field region (below 8 T), where most of the HF-EPR data have been acquired.

Note, there is a slight discrepancy of the modes R4 (black squares), which is discussed below. For complex **3**, only one (forbidden) Kramers resonance is observable, which excludes quantitative determination of the axial anisotropy but implies $|D| > 400$ GHz (13.3 cm^{-1}). However, considering the high measured g_z value of this complex, the real D-anisotropy can be much higher than this lower boundary which is given by the accessible frequency range of the spectrometer. The obtained D-
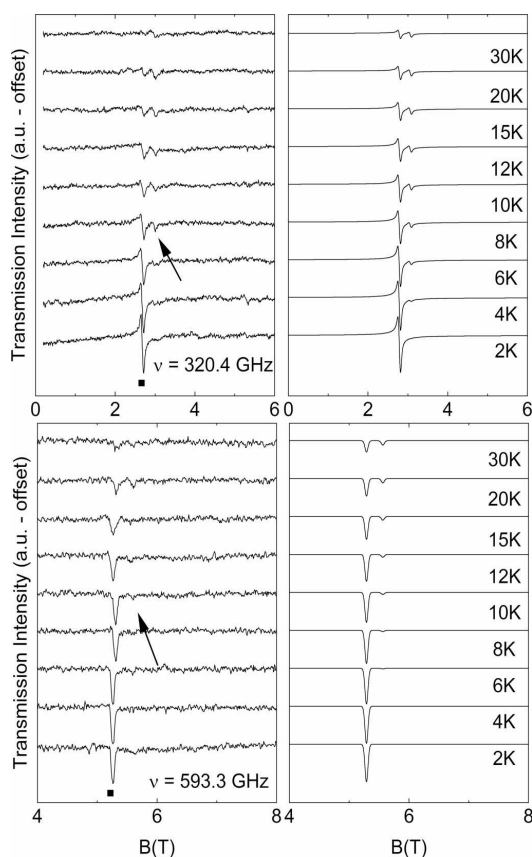
Fig. 6. HF-EPR spectra of complex **3** at different temperatures measured at (a) $\nu = 320.4$ GHz and (c) 593.3 GHz. Arrows indicate the appearance of an extra feature with rising temperatures. (b) and (d) show simulations at each frequency and temperature, respectively, employing $g_z = 2.65$, $J = 3.5$ GHz (0.11 cm^{-1}) and $|E| > 0$ GHz (see the text).

Fig. 7. Frequency vs. magnetic field diagram of complex **3**. Closed symbols mark the main branch which is observable at $T = 2$ K, open symbols show the additional high temperature feature at $T = 10$ K. Solid lines correspond to a simulation using a monomeric approach for the Co(II) ions, dotted lines simulate the dimeric model explained in the main text. The light grey branch shows the DPPH standard to ensure the magnetic field and frequency calibration, and by this the resonance positions.

values for all three investigated samples are in good agreement with the ones obtained from the fit of the dc magnetisation data and they show the same tendency as the respective heights predicted by DFT calculations reported earlier [37].

While $|D|$ is deduced from the simulation of the resonance branches, for experimental determination of the sign of D the temperature dependence of the resonance intensities and/or the relative intensities of the different features at low temperatures must be considered. Except for R1 and R3 in **1** as well as R1 in **2**, all the observed features in Fig. 3 show a Curie-like behaviour, indicating ground state transitions [59]. The other branches show activated behaviour, implying that the initial state of the transition is not a ground state but energetically gapped at $B = 0$ T. These observations evidence a negative sign of D, as seen in the corresponding energy-level diagram visualising the results of our simulations in the case $D < 0$ (Fig. 5). The experimentally observed transitions obtained at frequencies above (below) the ZFS gap Δ/h are visualised in Fig. 5 by solid (dashed) coloured arrows. The red and black branches in Fig. 5 can be assigned to transitions within the $m_S = \pm 1/2$ and $\pm 3/2$ Kramers doublets, respectively, whereas the green and blue branches correspond to gapped transitions between the mentioned doublets. Due to the negative sign of D, the $S = 3/2$ Kramers doublet is shifted to lower energies relative to the $S = 1/2$ doublet. The fact that R4 in **1** is more pronounced than R1 further corroborates the negative sign of the single-
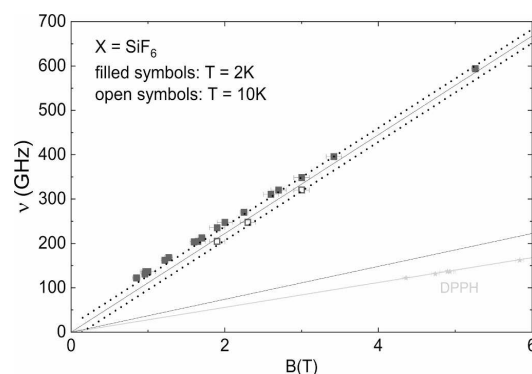
ion anisotropy parameter. We also recall the observed almost linear behaviour of the resonance branches shown in Fig. 4, which indicates a preferential orientation of the anisotropy axis along the direction of the external magnetic field and by this, a negative sign of the anisotropy [60,61].

Our data clearly show forbidden transitions, i.e. transitions with $\Delta m_S > 1$, which are not supposed to be detected in the strict case of $E = 0$ and aligned crystallites. Since our data evidence aligned crystallites, we conclude a mixing of states induced by finite transversal anisotropy. In order to assess the effect of a finite E value, simulation results employing $E > 0$ are shown in Fig. 4 by dashed lines. Expectedly, the associated resonance branches feature anti-crossing and gap formation. Comparing the simulations in the regions of anti-level crossing with the experimental data enables the establishment of upper limits for E in the case of complexes **1** and **2**, which are given in Table 1. For **3**, only the forbidden resonance branch within the lower $S = 3/2$ Kramers doublet is observed in our measurement range below 750 GHz (25 cm^{-1}), which obviates estimating E. However, the fact that the forbidden transition is clearly observed implies finite transversal anisotropy.

3.2. Exchange coupling

In addition to the features discussed above, the rather sharp resonance observed in **3** (as compared to **1** and **2**) enables the detection of an extra resonance at elevated temperatures which is not captured by the SH in Eqn. (3). Upon heating, the spectra measured at $\nu = 320.4$ and 593.3 GHz show the evolution of a distinct second feature in the vicinity of resonance R4 (Fig. 6). The resonance positions of the extra features at $T = 10$ K are shown by open symbols in Fig. 7, while the low-temperature resonances are displayed by filled markers. Identical slopes of the two branches imply equal effective g-values. As demonstrated in Fig. 7 by solid black lines, the elevated temperature features are not captured by the monomer model discussed above. We hence attribute it to the presence of weak intermolecular coupling between neighbouring spins. We note that dipolar interactions should lead to a broadening of the resonance line since they are assumed to prevail between all the Co(II) ions, but not to the appearance of two well separated resonance features, as observed in Fig. 6. Additionally, the calculated dipolar coupling strength between the nearest neighbouring Co(II) centres is in the range of 0.1 GHz, which is almost two orders too small to account for the observed zero field splitting.

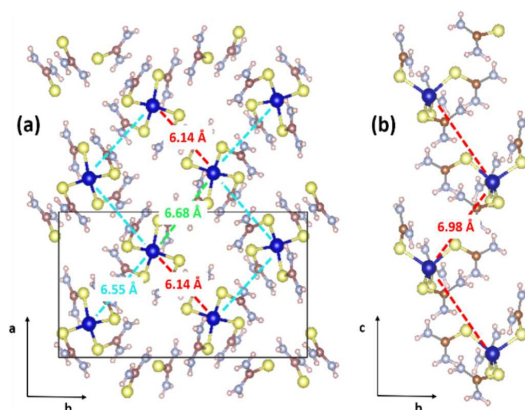Expanding the single molecule simulation by intermolecular

Fig. 8. Structural arrangement of the molecules in the *ab*-plane of complex **3** (a) as well as the chain-like arrangement along the c-direction for complexes **1** and **2** (b). Blue = Co(II), yellow = S, light blue = N, brown = C and white = H. Different intermolecular Co(II)···Co(II) distances are marked by differently coloured dashed lines. Only the molecules with the shortest Co(II)···Co(II) distances are shown. We refer to Ref. [37] for a complete structural description.
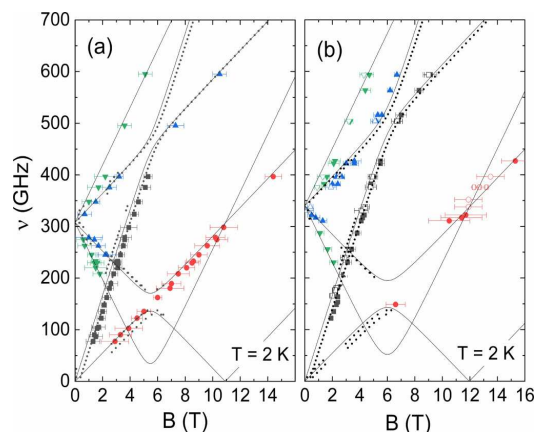

Fig. 9. Frequency vs. magnetic field diagram of complexes **1** (a) and **2** (b). The dotted lines show simulations using the SH in Eqn. (1) extended by finite exchange coupling (see the text) between two neighbouring spins. *D* and *E* anisotropy parameters as well as g_z-values equal those of the single-ion model represented by the solid lines (cf. Table 1). The open symbols in panel (b) represent the resonance branches observed in a magnetically diluted sample of **2**.

exchange interactions mediated via the ligands straightforwardly captures the existence of the additional resonance feature, as visualised in the energy-level diagram shown in Figure S2. Specifically, the presence of one extra feature can be phenomenologically explained by an isotropic dimer-like exchange coupling *J* between two neighbouring sites [62]. The dimer model serves as a minimal model to describe the experimental observations. Indeed, the structure of **3** shows rather short Co(II)–Co(II) distances in the range 6 to 6.5 Å in the *ab*-plane (see Fig. 8 (a)), while the inter-plane distances are considerably larger. Furthermore, as can be seen in Fig. 8(a), the in-plane distances between the Co (II) ions are not equivalent. The shortest distance between the Co(II) ions in the *ab*-plane amounts to 6.14 Å, while the other nearest neighbors distances are at least 6.55 Å which, from a phenomenological point of view, tentatively motivates a dimer-like scenario, which is found to describe our HF-EPR results. Our numerical studies presented below confirm this scenario.

The exchange Hamiltonian corresponding to a dimer interaction is shown in Eqn. (1). Simulating the spectra at ν = 320.4 and 593.3 GHz at various temperatures using the extended (i.e., Eqn. (3) + Eqn. (1)) model yields a good description of both the resonance positions and the spectral intensities, as shown in Fig. 6 (b) and (d). Employing g_z = 2.65 and *E* > 0 GHz, our analysis yields ferromagnetic intermolecular coupling *J* = 3.5(2) GHz (0.110(6) cm^{-1}). This value is in line with the intermolecular couplings found in other high-spin Co(II) compounds [63]. Note, due to the fact that only one resonance branch is detected, no relative intensities between the resonance features, and by this no proper *E*-value, can be quantised. For the simulation, an arbitrary *E*-value with |*E*| > 0 was used.

The broad resonance lines prevent the identification of the corresponding extra features in **1** and **2**, however the similar Co(II)···Co(II) distances in all the samples under investigation suggest that intermolecular coupling is to be expected, too. Indirect evidence is obtained from the temperature dependence of R4 (depicted by the black square in Fig. 3) in complexes **1** and **2**, which clearly shifts to lower fields upon heating (see Figure S3). We attribute this shift to a merging of the main feature with an additional one showing up at the low field side. Notably, this shift is opposite to the additional high-temperature peak observed in **3**, which suggests a different sign of *J*, i.e., an antiferromagnetic intermolecular interaction.

In contrast to **3**, the structures of **1** and **2** imply the shortest Co(II)··· Co(II) distance of 6.98 Å in the bc-plane(see Fig. 2), while the other

distances are much larger. As shown in Fig. 8(b), this yields a zig-zag chain structure with a tilted nature, which may again contribute to the dimer-like magnetic scenario. While our numerical calculations, due to very small interactions, do not discriminate between a uniform or alternating chain scenario, our experimental data are well described by the latter one, e.g. a dimer-like or weakly interacting dimer model as the distinct thermally activated resonance line is not expected in a 1D model [64,65].

The presence of a finite antiferromagnetic interaction indeed explains the discrepancy of the experimental data and the model in Fig. 4, where the resonance branches R4 are not perfectly described by the simulation. As seen in Fig. 4, the experimental data are overall shifted with respect to the simulated branch yielding a seemingly negative Δ in **1** and **2**. This shift is accounted for by the intermolecular exchange interaction. Quantitatively, the experimental data are described by the extended model with *J* = -5.5(5) GHz (-0.18 cm^{-1}) for **1** and −4.1(5) GHz (-0.13 cm^{-1}) for **2**, as seen in Fig. 9. The difference, i.e. positive sign of *J* in **3** implying a ferromagnetic intermolecular interaction, is clearly evidenced by the fact that the corresponding low-temperature branch in **3** exhibits a positive Δ value. Note, that the resonance positions have been confirmed by a DPPH marker.

In order to prove the relevance of the intermolecular effects, additional studies on a diluted sample of **2** have been performed, using a non-magnetic matrix solvent [37]. The resonance features obtained on the diluted sample, shown as open symbols in Fig. 9(b), confirm a much smaller intermolecular coupling by an almost vanishing shift of R4. A direct comparison of an exemplary spectrum obtained at same frequencies for 100 % and diluted 25 % samples of **2**, shown in Figure S4, clearly demonstrates a dilution dependent shift of around 0.5 T. Measurements on diluted samples of **1** and **3** were not successful. However, as stated earlier, **1** is structurally analogous to **2** and hence the same phenomenon observed for **2** can be extended to **1**.

3.3. Hirshfeld surface analysis of complexes 1–3

One of the important aspects of this report is the quantitative determination of the strength of the intermolecular interactions in **1**–**3** using HF-EPR (*vide infra*). To understand the inter- and intramolecular interactions observed in the solid-state of these complexes, a Hirshfeld
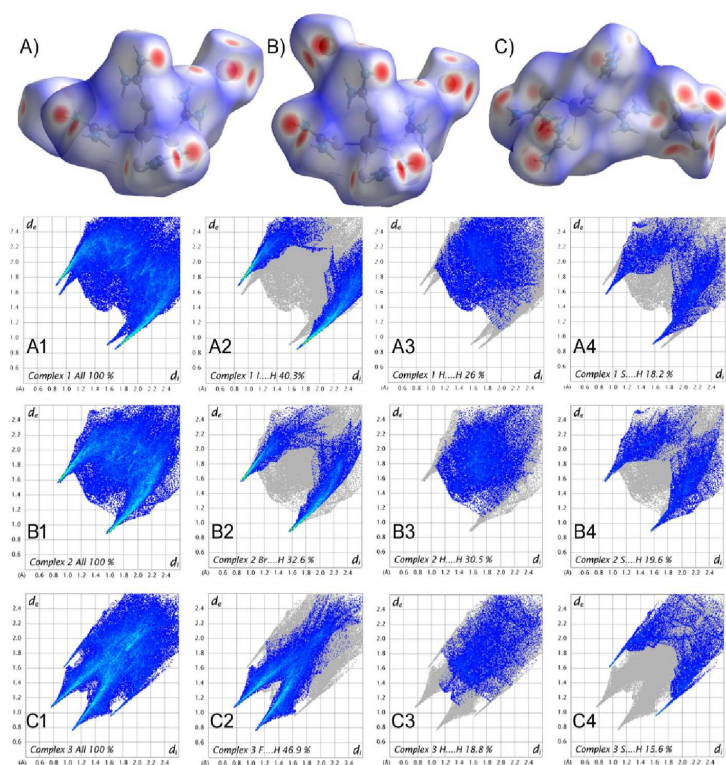
34

Fig. 10. Hirshfeld surface analysis mapped with d_{norm} for complexes **1** (panel A), **2** (Panel B) and **3** (panel C). The red colours indicate contacts with distances shorter than the van der Waals radii, i.e. very weak inter- or intramolecular interactions. Two-dimensional (2D) fingerprint plots are shown for the cation of complex **1**, where d_i is the distance from the Hirshfeld surface to the nearest atom inside the surface and d_e is the distance from the nearest atom outside the surface. Total intermolecular contacts including reciprocal contacts in **1**: (A1) 100% contacts, (A2) the relative percentage of I⋯H contacts (40.3%), (A3) H⋯H contacts (26 %), (A4) S⋯H contacts (18.2 %), **2**: (B1) 100% contacts, (B2) the relative percentage of Br⋯H contacts (32.6%), (B3) H⋯H contacts (22.4%,), (B4) S⋯H contacts (19.6 %), **3**: (C1) 100% contacts, (C2) the relative percentage of F⋯H contacts (46.9 %), (B3) H⋯H contacts (18.8 %,), (B4) S⋯H contacts (15.6 %). The intermolecular contacts including reciprocal contacts with < 5 % in all the complexes are not shown.

analysis was carried out (see Fig. 10). The Hirshfeld surface of all the three complexes shows that the intermolecular interactions between the molecules are mediated predominantly through the halide (anions in the crystal lattice) and hydrogen atoms of the thiourea ligand bound to the Co(II) ion. The various regions of color on these surfaces describe the inter- and intramolecular contacts present in their crystal structures. Two-dimensional (2D) fingerprint plots (Fig. 10, panels A1-C4) were also generated for all the complexes and used to visualize supramolecular features, such as weak inter- and intramolecular interactions and close contacts, as seen in their crystal structures. Both the Hirshfeld surface and fingerprint plots were extracted from the d_i and d_e values using *CrystalExplorer* [66,67], where d_i represents the distance from the Hirshfeld surface to the nearest atom inside the surface and with d_e being the distance from the nearest atom outside the surface [68]. The results of these plots indicate that the percentage of intermolecular X⋯H (where X = I (**1**), Br (**2**) and F (**3**)) contacts are 40.3 % in **1**, 32.6 % in **2**, and 46.9 % in **3** of the total share. The other significant contributions, including reciprocal contacts, are H⋯H and S⋯H, having relative contributions of 26 %, and 18.2 % in **1**; 30.5 % and 19.6 % in **2**, and 18.8 % and 15.6 % in **3**, respectively. As **1** and **2** are structurally analogous to each other, the relative percentage interaction of I⋯H is larger in **1** compared to the Br⋯H interaction in **2**. Hence, the overall exchange strength is expected to be stronger in **1** compared to **2**, which is in excellent agreement with the experimental observation (*vide infra*).

3.4. Numerical calculation for estimating the exchange interactions

Experimentally, there is an antiferromagnetic intermolecular exchange interaction between the molecules in the crystal lattice of **1** or **2**, while a ferromagnetic intermolecular exchange interaction was shown within **3**. To shed light on the mechanism of the intermolecular

exchange interactions, beyond the phenomenological comparison of intermolecular distances, DFT calculations were performed on the representative complex **1**. As stated earlier, **1** possesses both intra- and intermolecular hydrogen-bonding (H-bonding) [37]. Existence of super-exchange interactions between monomeric Cu(II), Fe(II), Fe(III) and Co (III)-Cr(III), V(IV)-Cu(II) ions etc. mediated via H-bonding is well established in literature by Alvarez and co-workers, and experimentally proven for certain Co(II) systems [55,56,69,70]. Besides the thematization of H-bondings, they have also proposed a methodology to mitigate the intermolecular exchange interaction (ferro- or antiferromagnetic) by crystal engineering [5,7,8].

As shown in Fig. 2, the intermolecular distance between the molecules is different in different directions for **1**. Three different J_s values based on the internuclear distances (J_1: Co(II)⋯Co(II) = 6.98 Å, J_2: 10.40 Å and J_3: 11.63 Å, see Fig. 2) are defined within the crystal lattice of **1** as coupling directions in a dimeric model for computing the exchange interaction. Our calculations predict that the exchange interaction between all the pairs of the binuclear system is antiferromagnetic in complex **1**. DFT calculations yield $J_1 = -0.08$ cm^{-1}, $J_2 = -0.001$ cm^{-1} and $J_3 = 0$ cm^{-1}.

It is found, that the J_1 interaction is strongest, while the other two are negligible. Thus, not only the distance dependent dipolar interactions, but also the intermolecular exchange interactions show a clear hierarchy in favour of J_1. The latter can be explained by a strong intermolecular I or S⋯H—N interaction (2.65 Å). Furthermore, a relatively strong anti-ferromagnetic coupling is evidenced from the SOMOs (see Figure S5 in ESI) [55,56,69,70].

Although the nature of the exchange interaction is predicted correctly, the magnitude of the computed J values are different from the experimentally extracted ones, and this may be attributed to relatively smaller intermolecular interactions, which are extremely challenging to
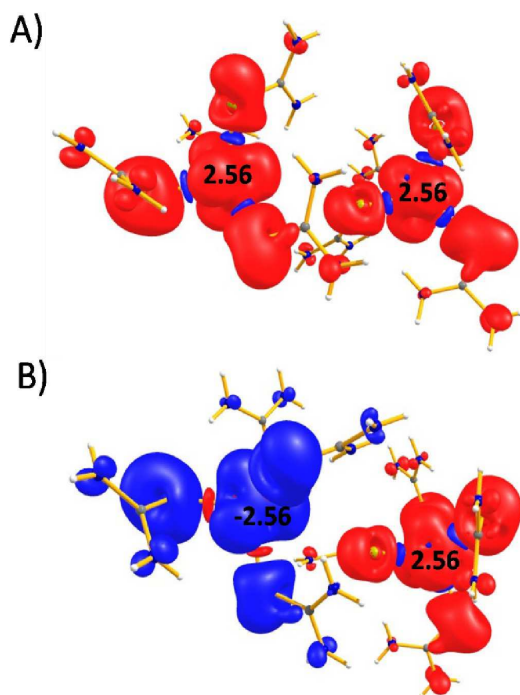
Fig. 11. DFT computed spin density plots of A) the high-spin state and B) the broken symmetry model of complex **1**. Spin densities are plotted using an iso-surface value of 0.001 e/bohr^3.

capture accurately by DFT methods. The spin density plot for the high-spin (HS) and broken symmetry (BS) models corresponding to J_1 reveal strong delocalisation of spin density on the ligands, propagating relatively stronger intermolecular exchange interactions as shown in Fig. 11. A closer inspection reveals a small but non-negligible spin density on the H-atom involved in the H-bonding interactions, supporting our aforementioned claim [70].

4. Conclusions

A sophisticated HF-EPR methodology was employed to quantitatively determine the Spin Hamiltonian parameters on a family of high spin Co(II) complexes $[Co(L_1)_4]X_2$ where X = I (**1**), Br (**2**) and $[Co(L_1)_4]$ SiF_6 (**3**), which also establishes the presence of non-zero E values in all the complexes. The study presented here furnishes the experimental proof for a sizable influence of the secondary coordination sphere on the magnitude of the axial anisotropy parameter D, which was measured directly by HF-EPR for complexes **1–3**. Further, intermolecular antiferromagnetic exchange interactions for **1** ($J = -5.5(5)$ GHz (-0.18 cm^{-1}) and **2** ($J = -4.1(5)$ GHz (-0.13 cm^{-1})) were found, while a ferromagnetic exchange interaction was noticed for **3** ($J = 3.5(2)$ GHz (0.11 cm^{-1})). The presence of a very weak exchange interaction between the molecules of **1** was also confirmed by theoretical calculations. Overall, this study discloses SH parameters accurately using HF-EPR and that through crystal engineering (by changing the anions the supramolecular interactions can be controlled) one can modulate not only the axial anisotropy but also intermolecular interaction pathways. This is an unconventional, yet a versatile approach that will pave the way to reveal a new generation of Co(II) complexes with fascinating magnetic properties.

CRediT authorship contribution statement

Lena Spillecke: Writing - original draft, Investigation, Formal analysis. **Shalini Tripathi:** Investigation, Resources, Formal analysis. **Changhyun Koo:** Supervision, Writing - original draft, Writing - review & editing. **Mursaleem Ansari:** Resources, Formal analysis. **Shefali Vaidya:** Resources, Formal analysis. **Amaleswari Rasamsetty:** Formal analysis. **Talal Mallah:** Writing - review & editing. **Gopalan Rajaraman:** Writing - review & editing, Formal analysis. **Maheswaran Shanmugam:** Conceptualization, Supervision, Writing - review & editing. **Rüdiger Klingeler:** Conceptualization, Supervision, Writing - original draft, Writing - review & editing.

Declaration of Competing Interest

The authors declare that they have no known competing financial interests or personal relationships that could have appeared to influence the work reported in this paper.

Appendix A. Supplementary data

Supplementary data to this article can be found online at https://doi.org/10.1016/j.poly.2021.115389.

References

[1] K.M. Mertes, Y. Suzuki, M.P. Sarachik, Y. Myasoedov, H. Shtrikman, E. Zeldov, E. M. Rumberger, D.N. Henrickson, G. Christou, Mn12-acetate: a prototypical single molecule magnet, Solid State Commun. 127 (2003) 131–139.

[2] H. Oshio, M. Nakano, High-spin molecules with magnetic anisotropy toward single-molecule magnets, Chem. Eur. J. 11 (18) (2005) 5178–5185.

[3] R. Sessoli, D. Gatteschi, A. Caneschi, M.A. Novak, Magnetic bistability in a metal-ion cluster, Nature 365 (6442) (1993) 141–143.

[4] A.K. Bar, C. Pichon, J.-P. Sutter, Magnetic anisotropy in two- to eight-coordinated transition–metal complexes: Recent developments in molecular magnetism, Coord. Chem. Rev. 308 (2016) 346–380.

[5] G.A. Craig, M. Murrie. 3d single-ion magnets, Chem. Soc. Rev., 10.1039/C4CS00439F, 44 (2015) 2135-2147.

[6] M.S. Fataftah, J.M. Zadrozny, D.M. Rogers, D.E. Freedman, A mononuclear transition metal single-molecule magnet in a nuclear spin-free ligand environment, Inorg. Chem. 53 (19) (2014) 10716–10721.

[7] D.E. Freedman, W.H. Harman, T.D. Harris, G.J. Long, C.J. Chang, J.R. Long, Slow Magnetic Relaxation in a High-Spin Iron(II) Complex, J. Am. Chem. Soc. 132 (4) (2010) 1224–1225.

[8] N. Ishikawa, M. Sugita, T. Ishikawa, S.-y. Koshihara, Y. Kaizu, Lanthanide double-decker complexes functioning as magnets at the single-molecular level, J. Am. Chem. Soc. 125 (29) (2003) 8694–8695.

[9] Y. Rechkemmer, F.D. Breitgoff, M. van der Meer, M. Atanasov, M. Hakl, M. Orlita, P. Neugebauer, F. Neese, B. Sarkar, J. van Slageren, A four-coordinate cobalt(II) single-ion magnet with coercivity and a very high energy barrier, Nat. Commun. 7 (2016) 10467.

[10] D. Tu, D. Shao, H. Yan, C. Lu. A carborane-incorporated mononuclear Co(ii) complex showing zero-field slow magnetic relaxation, Chem. Commun. 52 2016 14326-14329. 10.1039/C6CC07728E.

[11] J.M. Zadrozny, J.R. Long, Slow magnetic relaxation at zero field in the tetrahedral complex [Co(SPh)4]2–, J. Am. Chem. Soc. 133 (51) (2011) 20732–20734.

[12] D.S. Krylov, F. Liu, S.M. Avdoshenko, L. Spree, B. Weise, A. Waske, A.U.B. Wolter, B. Büchner, A.A. Popov, Record-high thermal barrier of the relaxation of magnetization in the nitride clusterfullerene Dy2ScN@C80-Ih, Chem. Commun. 53 (56) (2017) 7901–7904.

[13] D. Tanaka, T. Inose, H. Tanaka, S. Lee, N. Ishikawa, T. Ogawa, Proton-induced switching of the single molecule magnetic properties of a porphyrin based TbIII

double-decker complex, Chem. Commu. 48 (63) (2012) 7796, https://doi.org/10.1039/c2cc00086e.

[14] C. Das, A. Upadhyay, S. Vaidya, S.K. Singh, G. Rajaraman, M. Shanmugam, Origin of SMM behaviour in an asymmetric Er(iii) Schiff base complex: a combined experimental and theoretical study, Chem. Commu. 51 (2015) 6137–6140.

[15] P. Cieslik, P. Comba, W. Hergett, R. Klingeler, G.F.P. Plny, L. Spillecke, G. Velmurugan, Molecular magnetic properties of a dysprosium(III) complex coordinated to a nonadentate bispidine ligand, Z. Anorg. Allg. Chem. 647 (8) (2021) 843–849.

[16] M. Atanasov, D. Aravena, E. Suturina, E. Bill, D. Maganas, F. Neese, First principles approach to the electronic structure, magnetic anisotropy and spin relaxation in mononuclear 3d-transition metal single molecule magnets, Coord. Chem. Rev. 289-290 (2015) 177–214.

[17] S. Gomez-Coca, E. Cremades, N. Aliaga-Alcalde, E. Ruiz, Mononuclear Single-Molecule Magnets: Tailoring the Magnetic Anisotropy of First-Row Transition-Metal Complexes, J. Am. Chem. Soc. 135 (2013) 7010–7018.

[18] Y.-Y. Zhu, C. Cui, Y.-Q. Zhang, J.-H. Jia, X. Guo, C. Gao, K. Qian, S.-D. Jiang, B.-W. Wang, Z.-M. Wang, S. Gao, Zero-field slow magnetic relaxation from single Co (ii) ion: a transition metal single-molecule magnet with high anisotropy barrier, Chem. Sci. 4 (2013) 1802–1806.

[19] Z.-Y. Ding, Y.-S. Meng, Y. Xiao, Y.-Q. Zhang, Y.-Y. Zhu, S. Gao, "Probing the influence of molecular symmetry on the magnetic anisotropy of octahedral cobalt (ii) complexes," Inorg. Chem. Front., 10.1039/C7QI00547D, 4, (2017), 1909-1916.

[20] D. Schweinfurth, J. Krzystek, M. Atanasov, J. Klein, S. Hohloch, J. Telser, S. Demeshko, F. Meyer, F. Neese, B. Sarkar, Tuning magnetic anisotropy through ligand substitution in five-coordinate Co(II) complexes, Inorg. Chem. 56 (9) (2017) 5253–5265.

[21] S. Tripathi, A. Dey, M. Shanmugam, R.S. Narayanan, V. Chandrasekhar, Cobalt(II) Complexes as Single-Ion Magnets, in: V. Chandrasekhar, F. Pointillart (Eds.), Organometallic Magnets, Springer International Publishing, Cham, 2019, pp. 35–75.

[22] G. Peng, Y. Chen, B. Li, Y.-Q. Zhang, X.-M. Ren, Bulky Schiff-base ligand supported Co(ii) single-ion magnets with zero-field slow magnetic relaxation, Dalton Trans. 49 (2020) 5798–5802.

[23] A. Świtlicka, B. Machura, A. Bienko, D.C. Bienko, J. Titis, C. Rajnak, R. Boca, A. Ozarowski, Slow magnetic relaxation in hexacoordinated cobalt(ii) field-induced single-ion magnets, Inorg. Chem. Front. 7 (2020) 2637–2650.

[24] S. Tripathi, S. Vaidya, N. Ahmed, E. Andreasen Klahn, H. Cao, L. Spillecke, C. Koo, S. Spachmann, R. Klingeler, G. Rajaraman, J. Overgaard, M. Shanmugam, Structure-property correlation in stabilizing axial magnetic anisotropy in octahedral Co(II) complexes, Cell Rep. Phys. Sci. 2 (4) (2021) 100404, https://doi.org/10.1016/j.xcrp.2021.100404.

[25] W. Wernsdorfer, S. Bhaduri, C. Boskovic, G. Christou, D.N. Hendrickson, Spin-parity dependent tunneling of magnetization in single-molecule magnets, Phys. Rev. B 65 (18) (2002), https://doi.org/10.1103/PhysRevB.65.180403.

[26] M.R. Saber, K.R. Dunbar. Ligands effects on the magnetic anisotropy of tetrahedral cobalt complexes, Chem. Commun. 50 (2014) 12266-12269. 10.1039/C4CC05724D.

[27] E.A. Suturina, D. Maganas, E. Bill, M. Atanasov, F. Neese, Magneto-structural correlations in a series of pseudotetrahedral [CoII(XR)₄]²⁻ single molecule magnets: an ab initio ligand field study, Inorg. Chem. 54 (2015) 9948–9961.

[28] S. Vaidya, S. Tewary, S.K. Singh, S.K. Langley, K.S. Murray, Y. Lan, W. Wernsdorfer, G. Rajaraman, M. Shanmugam. What controls the sign and magnitude of magnetic anisotropy in tetrahedral Cobalt(II) single-ion magnets?, inorg. chem. 55 (20216) 9564-9578.

[29] J.M. Zadrozny, J. Telser, J.R. Long, Slow magnetic relaxation in the tetrahedral cobalt(II) complexes [Co(EPh)₄]²⁻ (EO, S, Se), Polyhedron 64 (2013) 209–217.

[30] M. Idešicová, J. Titiš, J. Krzystek, R. Boča, Zero-field splitting in pseudotetrahedral Co(II) complexes: a magnetic, high-frequency and -field EPR, and computational study, Inorg. Chem. 52 (2013) 9409–9417.

[31] T. Jurca, A. Farghal, P.-H. Lin, I. Korobkov, M. Murugesu, D.S. Richeson, Single-molecule magnet behavior with a single metal center enhanced through peripheral ligand modifications, J. Am. Chem. Soc. 133 (40) (2011) 15814–15817.

[32] X.-L. Mei, Y. Ma, L.-C. Li, D.-Z. Liao. Ligand field-tuned single molecule magnet behaviour of 2p–4f complexes, Dalton Trans. 41 (2012) 505-511. 10.1039/C1DT11795E.

[33] S. Vaidya, A. Upadhyay, S.K. Singh. T. Gupta, S. Tewary, S.K. Langley, J.P.S. Walsh, K.S. Murray, G. Rajaraman, M. Shanmugam. A synthetic strategy for switching the single ion anisotropy in tetrahedral Co(ii) complexes, Chem. Commun. 51 (2015), 3739-3742. 10.1039/C4CC08305A.

[34] Y. Gil, L. Llanos, P. Cancino, P. Fuentealba, A. Vega, E. Spodine, D. Aravena, Effect of second-sphere interactions on the magnetic anisotropy of lanthanide single-molecule magnets: electrostatic interactions and supramolecular contacts, J. Phy. Chem. C 124 (9) (2020) 5308–5320.

[35] D. Maganas, S. Sottini, P. Kyritsis, E.J.J. Groenen, F. Neese, Theoretical analysis of the spin hamiltonian parameters in Co(II)S4 complexes, using density functional theory and correlated ab initio methods, Inorg. Chem. 50 (18) (2011) 8741–8754.

[36] K.S. Pedersen, L. Ungur, M. Sifrist, A. Sundt, M. Schau-Magnussen, V. Vieru, H. Mutka, S. Rols, H. Weihe, O. Waldmann, L.F. Chibotaru, J. Bendix, J. Dreiser. Modifying the properties of 4f single-ion magnets by peripheral ligand functionalisation, Chem. Sci. 5 2014 1650-1660. 10.1039/C3SC53044B.

[37] S. Tripathi, S. Vaidya, K.U. Ansari, N. Ahmed, E. Rivière, L. Spillecke, C. Koo, R. Klingeler, T. Mallah, G. Rajaraman, M. Shanmugam, Influence of a counteranion on the zero-field splitting of tetrahedral Cobalt(II) thiourea complexes, Inorg. Chem. 58 (14) (2019) 9085–9100.

[38] S. Vaidya, P. Shukla, S. Tripathi, E. Riviere, T. Mallah, G. Rajaraman, M. Shanmugam, Substituted versus naked thiourea ligand containing pseudotetrahedral cobalt(II) complexes: a comparative study on its magnetization relaxation dynamics phenomenon, Inorg. Chem. 57 (2018) 3371–3386.

[39] J. Wu, J. Jung, P. Zhang, H. Zhang, J. Tang, B. Le Guennic, Cis–trans isomerism modulates the magnetic relaxation of dysprosium single-molecule magnets, Chem. Sci. (2016) 3632-3639, https://doi.org/10.1039/C5SC04510J,7.

[40] Y.-Y. Zhu, Y.-Q. Zhang, T.-T. Yin, C. Gao, B.-W. Wang, S. Gao, A family of CoᴵᴵCoᴵᴵᴵ₃ single-ion magnets with zero-field slow magnetic relaxation: fine tuning of energy barrier by remote substituent and counter cation, Inorg. Chem. 54 (2015) 5475–5486.

[41] J. Telser, J. Krzystek, A. Ozarowski, High-frequency and high-field electron paramagnetic resonance (HFEPR): a new spectroscopic tool for bioinorganic chemistry, J. Biol. Inorg. Chem. 19 (2014) 297–318.

[42] D. Gatteschi, A.L. Barra, A. Caneschi, A. Cornia, R. Sessoli, L. Sorace, EPR of molecular nanomagnets, Coord. Chem. Rev. 250 (11-12) (2006) 1514–1529.

[43] I. Oyarzabal, J. Ruiz, E. Ruiz, D. Aravena, J.M. Seco, E. Colacio, Increasing the effective energy barrier promoted by the change of a counteranion in a Zn–Dy–Zn SMM: slow relaxation via the second excited state, Chem. Commun. 51 (2015) 12353–12356.

[44] E.A. Suturina, J. Nehrkorn, J.M. Zadrozny, J. Liu, M. Atanasov, T. Weyhermüller, D. Maganas, S. Hill, A. Schnegg, E. Bill, J.R. Long, F. Neese, Magneto-structural correlations in pseudotetrahedral forms of the [Co(SPh)₄]²⁻ complex probed by magnetometry, MCD spectroscopy, advanced EPR techniques, and ab initio electronic structure calculations, Inorg. Chem. 56 (5) (2017) 3102–3118.

[45] S. Titos-Padilla, J. Ruiz, J.M. Herrera, E.K. Brechin, W. Wersndorfer, F. Lloret, E. Colacio, Dilution-triggered SMM behavior under zero field in a luminescent Zn₂Dy₂ tetranuclear complex incorporating carbonato-bridging ligands derived from atmospheric CO₂ fixation, Inorg. Chem. 52 (16) (2013) 9620–9626.

[46] C. Boskovic, R. Bircher, P.L.W. Tregenna-Piggott, H.U. Güdel, C. Paulsen, W. Wernsdorfer, A.-L. Barra, E. Khatsko, A. Neels, H. Stoeckli-Evans, Ferromagnetic and antiferromagnetic intermolecular interactions in a new family of Mn₄ Complexes With An Energy Barrier To Magnetization Reversal, J. Am. Chem. Soc. 125 (46) (2003) 14046–14058.

[47] Z.-B. Hu, Z.-Y. Jing, M.-M. Li, L. Yin, Y.-D. Gao, F. Yu, T.-P. Hu, Z. Wang, Y. Song, Important role of intermolecular interaction in Cobalt(II) single-ion magnet from single slow relaxation to double slow relaxation, Inorg. Chem. 57 (17) (2018) 10761–10767.

[48] F. Habíb, I. Korobkov, M. Murugesu, Exposing the intermolecular nature of the second relaxation pathway in a mononuclear cobalt(ii) single-molecule magnet with positive anisotropy, Dalton Trans. 44 (2015) 6368–6373.

[49] P. Comba, M. Großhauser, R. Klingeler, C. Koo, Y. Lan, D. Müller, J. Park, A. Powell, M.J. Riley, H. Wadepohl, Magnetic interactions in a series of homodinuclear lanthanide complexes, Inorg. Chem. 54 (23) (2015) 11247–11258.

[50] S. Stoll, A. Schweiger, EasySpin, a comprehensive software package for spectral simulation and analysis in EPR, J. Magn. Reson. 178 (1) (2006) 42–55.

[51] R.M. Dickson, A.D. Becke, Basis-set-free local density-functional calculations of geometries of polyatomic molecules, J. Chem. Phys. 99 (5) (1993) 3898–3905.

[52] A. Schäfer, C. Huber, R. Ahlrichs, Fully optimized contracted Gaussian basis sets of triple zeta valence quality for atoms Li to Kr, J. Chem. Phys. 100 (8) (1994) 5829–5835.

[53] R. Calvo, EPR measurements of weak exchange interactions coupling unpaired spins in model compounds, Appl. Magn. Reson. 31 (1-2) (2007) 271–299.

[54] M.J. Frisch, G.W. Trucks, H.B. Schlegel, G.E. Scuseria, M.A. Robb, J.R. Cheeseman, G. Scalmani, V. Barone, G.A. Petersson, H. Nakatsuji, X. Li, M. Caricato, A.V. Marenich, J. Bloino, B.G. Janesko, R. Gomperts, B. Mennucci, HP. Hratchian, J.V. Ortiz, A.F. Izmaylov, JL. Sonnenberg, D. Williams-Young, F. Ding, F. Lipparini, F. Egidi, J. Goings, B. Peng, A. Petrone, T. Henderson, D. Ranasinghe, V.G. Zakrzewski, J. Gao, N. Rega, G. Zheng, W. Liang, M. Hada, M. Ehara, K. Toyota, R. Fukuda, J. Hasegawa, M. Ishida, T. Nakajima, Y. Honda, O. Kitao, H. Nakai, T. Vreven, K. Throssell, J. A. Montgomery, Jr., J.E. Peralta, F. Ogliaro, M.J. Bearpark, J.J. Heyd, E.N. Brothers, K.N. Kudin, V.N. Staroverov, T.A. Keith, R. Kobayashi, J. Normand, K. Raghavachari, A.P. Rendell, J.C. Burant, S.S. Iyengar, J. Tomasi, M. Cossi, J.M. Millam, M. Klene, C. Adamo, R. Cammi, J.W. Ochterski, R.L. Martin, K. Morokuma, O. Farkas, J.B. Foresman, D.J. Fox, "Gaussian 16 Rev. B.01," ed. Wallingford, CT, 2016.

[55] E. Ruiz, J. Cano, S. Alvarez, P. Alemany, Broken symmetry approach to calculation of exchange coupling constants for homobinuclear and heterobinuclear transition metal complexes, J. Comput. Chem. 20 (13) (1999) 1391–1400.

[56] E. Ruiz, A. Rodríguez-Fortea, P. Alemany, S. Alvarez, Density functional study of the exchange coupling in distorted cubane complexes containing the Cu₄O₄ core, Polyhedron 20 (11-14) (2001) 1323–1327.

[57] L. Noodleman, E.R. Davidson, Ligand spin polarization and antiferromagnetic coupling in transition metal dimers, Chem. Phys. 109 (1) (1986) 131–143.

[58] R. Boča, Zero-field splitting in metal complexes, Coord. Chem. Rev. 248 (9-10) (2004) 757–815.

[59] G. Christou, D. Gatteschi, D.N. Hendrickson, R. Sessoli, Single-molecule magnets, MRS Bull. 25 (11) (2000) 66–71.

[60] A.-L. Barra, L.-C. Brunel, D. Gatteschi, L. Pardi, R. Sessoli, High-frequency EPR spectroscopy of large metal ion clusters: from zero field splitting to quantum tunneling of the magnetization, Acc. Chem. Res. 31 (1998) 460–466.

[61] J. Krzystek, S.A. Zvyagin, A. Ozarowski, A.T. Fiedler, T.C. Brunold, J. Telser, Definitive spectroscopic determination of zero-field splitting in high-spin cobalt (II), J. Am. Chem. Soc. 126 (7) (2004) 2148–2155.

[62] T.A. Bazhenova, L.V. Zorina, S.V. Simonov, V.S. Mironov, O.V. Maximova, L. Spillecke, C. Koo, R. Klingeler, Y.V. Manakin, A.N. Vasiliev, E.B. Yagubskii, The

first pentagonal-bipyramidal vanadium (III) complexes with a Schiff-base N_3O_2 pentadentate ligand: synthesis, structure and magnetic properties, Dalton Trans. 49 (2020) 15287–15298.

[63] N.I. Neuman, E. Winkler, O. Peña, M.C.G. Passeggi, A.C. Rizzi, C.D. Brondino, Magnetic properties of weakly exchange-coupled high spin Co(II) ions in pseudooctahedral coordination evaluated by single crystal X-Band EPR spectroscopy and magnetic measurements, Inorg. Chem. 53 (5) (2014) 2535–2544.

[64] Y. Oshima, H. Nojiri, K. Asakura, T. Sakai, M. Yamashita, H. Miyasaka, Collective magnetic excitation in a single-chain magnet by electron spin resonance measurements, Phys. Rev. B 73 (21) (2006), https://doi.org/10.1103/PhysRevB.73.214435.

[65] M. Rams, M. Böhme, V. Kataev, Y. Krupskaya, B. Büchner, W. Plass, T. Neumann, Z. Tomkowicz, C. Näther, Static and dynamic magnetic properties of the ferromagnetic coordination polymer $[Co(NCS)_2(py)_2]_n$, Phys. Chem. Chem. Phys. 19 (36) (2017) 24534–24544.

[66] Crystal Explorer 17, University of Western Australia. http://crystalexplorer.scb.uwa.edu.au/.

[67] P.R. Spackman, M.J. Turner, J.J. McKinnon, S.K. Wolff, D.J. Grimwood, D. Jayatilaka, M.A. Spackman, CrystalExplorer: a program for Hirshfeld surface analysis, visualization and quantitative analysis of molecular crystals, J. Appl. Crystallogr. 54 (2021) 1006–1011.

[68] K.S. Wolff, J.D. Grimwood, J.J. McKinnon, J.M. Turner, D. Jayatilaka, M.A. Spackman. CrystalExplorer (Version 3.1), University of Australia, 2012.

[69] J. Cano, E. Ruiz, S. Alvarez, M. Verdaguer, Spin density distribution in transition metal complexes: some thoughts and hints, Comment. Inorg. Chem. 20 (1998) 27–56.

[70] C. Desplanches, E. Ruiz, A. Rodríguez-Fortea, S. Alvarez, Exchange coupling of transition-metal ions through hydrogen bonding: a theoretical investigation, J. Am. Chem. Soc. 124 (2002) 5197–5205.

38

4.3. Investigation of an Octahedrally Coordinated Co(II) Complex with a Highly Axial Anisotropy

Nowadays it is a well known fact, that one of the key prerequisites to observe long relaxation times in molecular systems is a highly axial crystal field anisotropy.[32, 69–72] Various synthetic approaches were developed to chemically engineer such molecules based on theoretical predictions. However, the high energy scales of the anisotropy parameters which are often beyond the range of usual measurement techniques like X-band EPR or SQUID magnetometry, challenge experimentalists to confirm the predicted CF splittings of the synthesized samples. Usual attempts to experimentally determine the magnetic properties of highly anisotropic molecular compounds are the application of THz spectroscopy or neutron diffraction experiments.[73, 74]

Within the following chapter it is described, how the magnetic properties can be deciphered by detailed investigations of magnetic field dependent susceptibility measurement in an static dc magnetisation experiment up to 14 T, as well as in pulsed fields up to 55.5 T.[5] By the comparison to simulations (e.g. by Quantum Monte Carlo (QMC) methods), not only information about the single-ion anisotropy of the investigated complex is gained, but also the intermolecular interactions are quantified. The latter can have, even on small energy scales, a significant impact on the slow relaxation of magnetisation behaviour of a molecular complex.[20, 75–79]

4.3.1. Molecular and Crystal Structure

Fig. 4.4 (a) depicts the molecular structure of the investigated Co(II) compound described by the formula $[Co(L_1)_4(Cl)_2]$ (**1**), with L_1 = thiourea ($H_2N\text{-}CS\text{-}NH_2$).[6] The crystal structure of **1** was initially described by O'Connor et al. (Cambridge structural database (CSD) code CTHUCO10), however, no magnetic properties are reported within that work.[80] The Co(II) ion figures a high spin S = 3/2 state and is surrounded by a six-coordinated pseudo-octahedral ligation environment build up by four sulphur ions in the plane and two chloride ions in the axial positions. The magenta arrow in fig. 4.4 (a) denotes the direction of the magnetic easy axis which is tilted away from the Co(II)-Cl$^-$ bond by 31(6)°. This tilting is confirmed by both, polarized neutron diffraction measurements as well as calculated *ab initio* results.[61]

The complex crystallizes in a tetragonal space group ($P4_2/n$) as described in detail in ref. [61]. Fig. 4.4 (b) shows the crystal packing for **1** to visualize the position and orientation of the nearest Co(II) ions. As can be seen, all molecules within the unit cell are roughly oriented along the c-direction with the Cl-Co(II)-Cl axis. The minimal distance between two Co(II) ions is given by 8.091 Å.[61] The predicted hydrogen coupling pathways between those neighbouring ions are visualized in fig. A.4.

---

[5]Pulsed field measurements were performed by S. Spachmann (KIP Heidelberg).

[6]The synthesis and crystal structure determination of the sample was performed by S. Tripathi (IIT Bombay).[61]
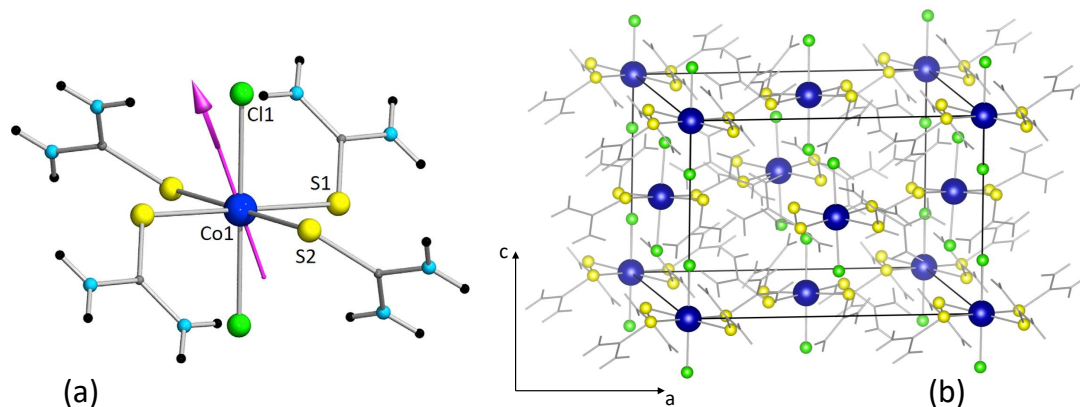
Figure 4.4.: (a) Molecular structure of complex **1**. Blue, Co; yellow, S; green, Cl; sky blue, N; gray, C; black, H. The magneta arrow shows the computed D_{zz} direction from *ab initio* calculations (see ref. [61]). (*Figure reprinted from Tripathi et al. [61].*) (b) Crystal packing diagram for complex **1**. The minimal distance between neighbouring Co(II) ions is found to be 8.091 Å.

The following chapters (chap. 4.3.2 and 4.3.3) were written by L. Spillecke and have been published in this form (see Tripathi et al. [61]) as part of a research article in the journal Cell Reports Physical Science.

4.3.2. Direct Current Magnetization

Variable temperature direct current (DC) magnetic measurements were performed on a polycrystalline fixed powder sample of **1** in the temperature range of 1.8-300 K in the presence of an external magnetic field of 10 kOe. As shown in Figure 4.5 A, the observed room temperature $\chi_M T(T)$ value for **1** (2.98 cm^3 K mol^{-1}) is significantly larger than the theoretical value for an S = 3/2 case (i.e., 1.875 cm^3 K mol^{-1}; with g = 2), as expected for Co(II) complexes. Furthermore, the observed value is in agreement with other results reported in the literature.[81–83] Upon cooling, $\chi_M T(T)$ decreased almost linearly to about 75 K. Below this temperature, $\chi_M T(T)$ decreases more rapidly and reaches a low-temperature value of 0.83 cm^3 K mol^{-1} at 1.8 K (Figure 4.5 A). The magnetic field dependence of the magnetization studied in external static magnetic fields up to 140 kOe at a temperature of T = 2 K (open black circles in Figure 4.5 B) as well as in a pulsed field up to 555 kOe (blue solid line) is presented in the inset in Figure 4.5 A. Additional measurements were performed in magnetic fields up to 70 kOe at several temperatures (Figure A.3)[7]. Upon application of the external magnetic field, the magnetization rises steeply to B = 50 kOe, followed by

---

[7]The magnetisation measurements at several temperatures shown in fig. A.3 were performed by S. Tripathi, IIT Bombay.[61]
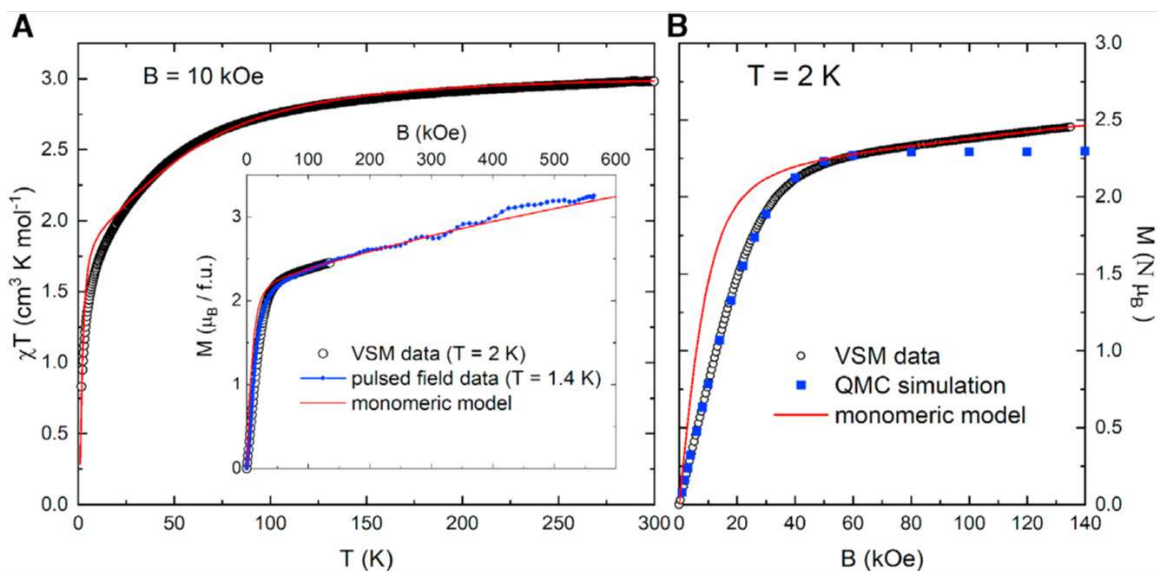
Figure 4.5.: Magnetic characterization of complex **1**. (A) Temperature dependence of the DC magnetic susceptibility measured on a polycrystalline sample of **1** in an external magnetic field of 10 kOe (open black symbols). Inset: pulsed-field magnetization on **1** at T = 1.4 K. The pulsed-field data are scaled to static-field data obtained at T = 2 K (open black symbols). (B) Magnetic field dependence of DC magnetization at T = 2 K (open black symbols). Filled blue squares show QMC simulation results as described in the text. Solid red lines in all plots represent simulations using a monomeric model for $\chi_M T(T)$ and M(B), respectively, with the parameters described in the main text. (*Figure reprinted from Tripathi et al. .[61]*)

a much flatter linear increase without indication of saturation even up to 555 kOe. Furthermore, the maximal measured moment of 3.2 μ_B is significantly lower than the saturation magnetization $M_{sat} = g_{iso}S = 3.66$ μ_B, which is expected from g_{iso} obtained from the calculated g tensor below.

The rapid decrease of the $\chi_M T(T)$ value at low temperatures as well as the linear increase of the magnetization with rising magnetic fields without reaching M_{sat} strongly implies the presence of a high axial anisotropy of the crystal field that acts on the Co(II) moments. This is corroborated by the non-superimposable nature of the reduced magnetization data of **1** (Figure A.3). To quantify the crystal field parameters, we performed simulations on the field (M(B)) and the temperature dependence ($\chi_M T(T)$) of the magnetization, considering the following spin Hamiltonian (SH; Equation 4.2), where g denotes the isotropic g value, μ_B the Bohr magneton, B the external magnetic field, and D and E the axial and transversal anisotropy parameter, respectively.[84, 85] The following SH is a good model to simulate the experimental magnetic data because the symmetry around Co(II) is not strictly octahedral in **1**.[86–90] For the ideal octahedral (homoleptic ligand) complexes, the spin-orbit coupling is expected to be strong; therefore, L and S formalism should be

included when modeling the magnetic data of the complexes.

$$H = g\mu_B \vec{B}\vec{S} + D\left[S_z^2 - \frac{S(S+1)}{3}\right] + E\left(S_x^2 - S_y^2\right) \qquad (4.2)$$

The simulation results are shown as red solid lines in Figure 4.5. To avoid overparameterization, the $|E/D| = 0.22$ ratio was fixed to the calculated result (see ref. [61]), and only D and g were varied. The best simulation parameters are D = -63(10) cm^{-1}, $g_{\chi T} = 2.53(5)$, and $g_{MB} = 2.7(1)$. The different g values obtained for the $\chi_M T(T)$ and M(B) data reflect the fact that $g_{\chi T}$ is mainly determined by the room-temperature value of $\chi_M T$ (i.e., it refers to the isotropic g value of the system), whereas g_{MB} is dominated by the component of g, which points along the anisotropy axis of the, in general, anisotropic g tensor and is less dependent on the other components. However, a simulation using an anisotropic g value leads to overparameterization because the M_{sat} has not been reached in the accessible field of 555 kOe.

Although the high temperature and high magnetic field ranges are well described by the respective optimized parameter sets, the data clearly diverge on lower-energy scales. Especially the diminished slope of low-field magnetization (Figure 4.5 B) compared with the simulation implies an influence of antiferromagnetic intermolecular interactions. Closer investigation of the molecular packing scheme shown in Figure 4.5 as well as Figure A.4 supports a scenario of three-dimensional magnetic coupling between the nearest neighboring Co(II) moments mediated via hydrogen bonds. To estimate the strength of the intermolecular antiferromagnetic interactions, we performed Quantum Monte Carlo (QMC) simulations on a cubic lattice with an edge length of L = 10 Å. To reduce the dimensionality of the system, we approximated the localized Co(II) moments as Ising spins of the length $S_z = 3/2$, which is well justified at low magnetic fields and temperatures where only the $m_S = \pm 3/2$ Kramers doublet is populated significantly because of the high zero field splitting induced by axial anisotropy.[91] Thus, the exchange coupling Hamiltonian can be written as [92]

$$H = -J\sum_{<i,j>} \vec{S}_i^z \vec{S}_j^z. \qquad (4.3)$$

The simulation results are shown as blue filled squares in Figure 4.5 B. The experimental data (open black circles in Figure 4.5 B) are well described by the simulation, with a coupling constant J = -0.45(5) K in the magnetic field range below 50 kOe. The effective g value is fixed to $g_z = 3.06$, which is the maximum component of the calculated g tensor described below. As expected, because of the Ising spin approximation used, the QMC simulation result diverges from the experimental data with increasing fields, where the influence of finite anisotropy becomes non-negligible.

4.3.3. Experimental Details

DC magnetization measurements were performed using a physical property measurement system (PPMS) VSM magnetometer as well as an magnetic property measurement system (MPMS) magnetometer from Quantum Design equipped with a 14 T and 7 T magnet, respectively. Pulsed magnetic field magnetization was measured up to 555 kOe at the High Magnetic Field Laboratory Dresden by an induction method using a coaxial pick-up coil system.[93] The total pulse duration time was 25 ms. Because of the short rise time of only 7 ms, the up-sweep data showed a significant influence of hysteretic effects, which is why only the data obtained during the much slower down sweep were used for evaluation. The pulsed magnetic field magnetization data were calibrated to the static magnetic field measurement (Figure 4.5, inset). Simulation of the data was done using the EasySpin software package [66] as well a QMC method with the stochastic series expansion algorithm as implemented in the Algorithms and Libraries for Physics Simulations (ALPS) software package.[94, 95]

4.3.4. Conclusion

Within this section, a Co(II) mononuclear complex with a large axial anisotropy was studied. By extrapolating pulsed field magnetisation data, the anisotropy parameter $D = $ -63(10) cm^{-1} was defined as well as an averaged g-value of 2.53(5). A comparison of magentic field dependent magnetisation data to the results of a QMC simulation further revealed an intermolecular interaction strength in the range of 0.5 K.

In conclusion it was shown, that by a considerate combination of different spin models which are adjusted to their respective energy scale, i.e. a single-ion model for the high temperature range where the axial anisotropy is the predominant parameter and a correlated model in the low temperature range to account for intermolecular interactions, a conclusive picture of the magnetic properties of a molecular Co(II) system can be build.

4.4. The Role of Coordination Geometry on the Magnetic Relaxation Dynamics of Isomeric Five Coordinated Co(II) Low Spin Complexes

Almost 30 years after the first description of a magnetic moment arising purely from an isolated metal-organic molecule,[5] the research community is still focusing mainly on the tuning and enhancement of magnetic anisotropy in such molecular magnetic materials to find applicable solutions for high-density data storages on the molecular scale.[96–103] Even though the longitudinal relaxation time T_1, which measures the lifetime of a classical bit, can indeed be tremendously enhanced by high anisotropy barriers, for quantum computing and processing it is actually the transversal relaxation time T_2 which is the limiting parameter since it measures the memory time of a superpositioned state.[104, 105]

Within this chapter, the magnetic relaxation properties of low spin Co(II) ions are investigated which figure an S = 1/2 state. S = 1/2 systems have no anisotropy barrier and show consequently no remanent magnetisation at zero applied magnetic fields. However, they can provide long transversal relaxation times up to high temperatures, if a small external magnetic field is applied due to the absence of excited energy levels which could promote the relaxation process.[104, 106] The observation and measurements of these long relaxation times is, although, compared to S > 1/2 systems only rarely reported in literature due to the influence of spin-spin and hyperfine interactions.[75, 104, 107–111] Especially in magnetically non-diluted systems, even weak intermolecular interactions can suppress the observation of a slow relaxation of magnetisation behaviour. Down to the present day and to my knowledge, in the special case of a non-diluted Co(II) low spin monomeric complex, only three examples can be found in literature which figure a magnetic field induced slow relaxation of magnetisation behaviour.[75, 112, 113]

4.4.1. Molecular Structure

Slightly different synthetic procedures, i.e. a change in the order of the added precursors allows to isolate two different geometric isomers with the same general molecular formula: $[Co(DPPE)_2Cl](SnCl_3)$.[8] The obtained samples can be distinguished not only by their characteristic colour (orange-red and dark-green), but more importantly figure a different coordination geometry around the central Co(II) ion, namely a square-pyramidal (hereafter named Co-SP, **1**) and a trigonal-bipyramidal (hereafter named Co-TBP, **2**) coordination environment, respectively. Hence, the fact that the two isolated samples are real geometrical isomers as well as structural polymorphs provides the rare opportunity to directly investigate the influence of the geometrical arrangement of the coordination environment on the magnetic properties for a Co(II)

---

[8]The samples were synthesised and structurally characterized by S. Tripathi (IIT Bombay). Both of the synthesized complexes were initially reported by Stalick et al., see ref. [114–116].

low spin system.

Fig. 4.6 shows the molecular structure of **1** (fig. 4.6 (a)) and **2** (fig. 4.6 (b)). The central Co(II) ion is surrounded by four phosphor ligands as well as one chloride ion in the apical position. Continuous shape measurements, which were performed by S. Tripathi, revealed, that both complexes figure a slight distortion from their ideal square-pyramidal or tetragonal-bipyramidal geometry. Both complexes are in a low spin S = 1/2 ground state, as it was previously found by Stalick et al. employing ^{119}Sn MÖSSBAUER measurements [115] and further confirmed by the dc susceptibility and EPR investigations as described in the following chapters.

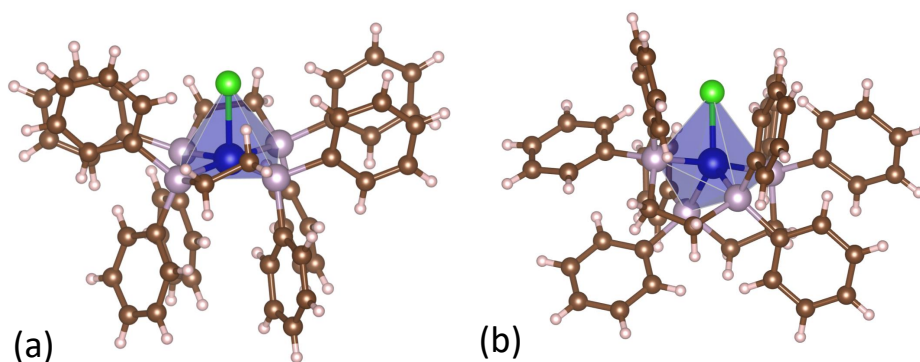(a)   (b)

Figure 4.6.: Molecular structure for complexes **1** (a) and **2** (b). Blue, Co; light grey, P; green, Cl; brown, C; white, H. [114–116]

The following chapters (chap. 4.4.2, 4.4.3, 4.4.4 and 4.4.5) were written by L. Spillecke and are part of a research article (L. Spillecke et al.) which has been submitted to the journal Inorganic Chemistry.

4.4.2. Static Magnetic Properties

Temperature-dependent direct current (dc) magnetic susceptibility measurements performed in a range between 1.8 K and 300 K on polycrystalline fixed powder samples of **1** and **2** in the presence of an external magnetic field of $B = 1$ T are shown in Figures 4.7 (a) and (b), respectively. For both samples, the $\chi_M T$ value figures a constant behavior in a temperature range between 25 K and 300 K. This constant $\chi_M T$ value of 0.44 cm^3 K mol^{-1} and 0.5 cm^3 K mol^{-1} corresponds to an isolated Co(II) low-spin doublet ground state (S = 1/2) with the average g-value of $g_{av} = 2.19(5)$ and 2.33(5), for **1** and **2**, respectively. The field-dependent magnetization measurements on **1** and **2** are shown as an inset in Figure 4.7 (a) and (b), respectively, for an external magnetic field range between 0 T and 7 T at various isothermal conditions ($T = $ 2, 3, and 5 K). Consistent with the low-spin ground state associated with the Co(II)

ions in both complexes (**1** and **2**), the magnetic moment tends to saturate around 1.0 μ_B/f.u. and 1.1 μ_B/f.u. at 2.0 K, respectively. Solid red lines in Figure 2 show a simulation using the following Spin Hamiltonian (SH)

$$H = g\mu_B \vec{B} \cdot \vec{S} \tag{4.4}$$

with the Bohr magneton μ_B, spin $\vec{S}$, external magnetic field $\vec{B}$ and the g-values obtained from the X-EPR measurements which are shown in the following section. To account for small deviations between the simulation and the magnetization data induced by the error-bars of mass determination, a scaling factor of 0.96 and 1.06 had to be introduced for **1** and **2**, respectively, to find the optimal consistency between the measured data and the simulation. Both, the temperature and magnetic field dependence of the magnetic susceptibility is well explained by this model over the whole measurement range. The inverse magnetic susceptibility (χ_M^{-1}) shown in Figure A.5 (a) and (b) for **1** and **2**, respectively, can be fitted by a Curie law (see red dashed lines in Figure A.5 (a) and (b)), i.e., the Weiss temperature in a Curie-Weiss approximation is zero within error bars and thus, no intermolecular interactions are detected on the observed energy scale.
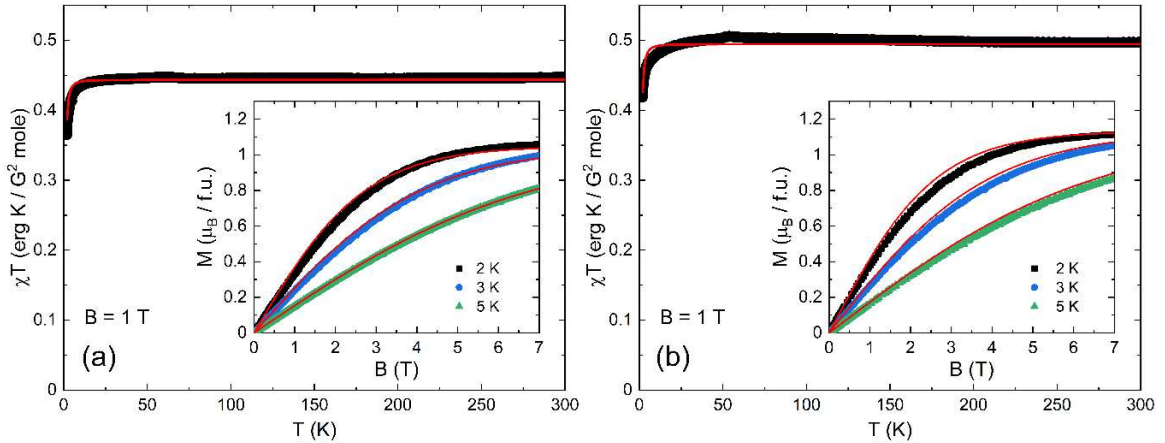

Figure 4.7.: Temperature dependence of the dc susceptibility for **1** (a) and **2** (b) measured in an external magnetic field of $B = 1$ T. Inset: Dc-magnetization for **1** and **2** vs. external magnetic field at various temperatures. Red solid lines in all plots show a simulation using the g-value obtained from the X-EPR measurements considering a scaling factor of 0.96 and 1.06 for **1** and **2**, respectively, to account for the error in the sample weight.

The obtained g-values for **1** and **2** are consistent with the ones reported for other low-spin Co(II) complexes with planar or square-pyramidal coordination geometry. [117–119] Furthermore we find that the averaged g-value for each complex is larger than the spin-only value of 2.0023 which implies a non-zero contribution of spin-orbit coupling and is by this in line with the anisotropic g-value of the ground spin doublet state as it is observed in the EPR investigations described in the following section.

4.4.3. X-band and HF-EPR Measurements

X-band EPR spectra[9] shown in Figure 4.8 on solid samples confirm the $S = 1/2$ ground state and display well-resolved resonance lines providing information not only on the anisotropy of the g-factors but also give evidence for the presence of finite hyperfine interactions between the electronic and the nuclear spin I = 7/2 of the Co(II) ions. In Figure 4.8 (a) it is shown, that for **1** three well-resolved resonance features are distinguished which correspond to the three main axes of the g-factor. Due to the broader line width in **2**, the resonance features are not as well resolved as for **1**. However, at least two different signal positions can be read off by eye from the measured data shown in Figure 4.8 (b). The spectra for both samples figure an anisotropic line broadening, which we attribute to unresolved hyperfine interactions with the nuclear moment I = 7/2 of the Co(II)-ions.[120] To account for this, we introduced the so-called H-strain parameter which describes an anisotropic residual line width.[66] However we would like to mention, that anisotropic line broadening can also arise from the g-strain, i.e., from a distribution of the g-principal values induced by intermolecular interactions. To investigate this point in more detail, we recorded X-band EPR spectra for both **1** and **2** in dichloromethane (DCM) solution at 5.0 K (see Figure A.6)[10]. Upon dissolution of the orange-red crystals of **1** in DCM, the solution turns green and the frozen solution EPR spectra are distinctly different from the ones obtained for the solid powder, but almost perfectly resembles the EPR spectra which were recorded for complex **2** (compare Figure A.6 and A.8). Hence, we conclude that complex **1** converts into **2** upon dissolution in DCM and can thereby not be investigated in its dissolved form. This conclusion is further corroborated by the UV-Vis spectrum recorded for **1** in DCM which shows an absorption profile similar to that observed for **2** in DCM (see Figure A.7). In contrast to **1**, the EPR spectra obtained for a frozen solution of **2** resembles the ones measured on the polycrystalline compound at 5.0 K (Figure A.8). Particularly, we do not observe the reduction of the line-width in the spectra obtained on the dissolved sample **2**. From this observation, we can conclude, that not g-strain, but unresolved hyperfine interactions give indeed the main contribution to the observed anisotropic line-broadening. Furthermore, the neglectable influence of intermolecular interactions is in line with our results from the Hirshfeld-analysis (see Figure A.11 and A.12) and the evaluation of the χ^{-1} vs. T plot (see Figure A.5).

The solid-state EPR spectra of both the complexes **1** and **2** were simulated using the EasySpin-software [66] and the simulation parameters are summarized in Table 4.1. In order to illustrate the influence of a finite H-strain parameter, an additional simulation with just isotropic broadening is given as grey lines in Figure 4.8 which clearly fails to reproduce the measured data shown as black lines.

The application of high magnetic fields enables further resolution of the broad resonance lines. The magnetic field dependence of fixed powder spectra at $T = 2$ K

---

[9]X-Band EPR spectra were recorded by S. Tripathi (IIT Bombay) and analysed and plotted by L. Spillecke.

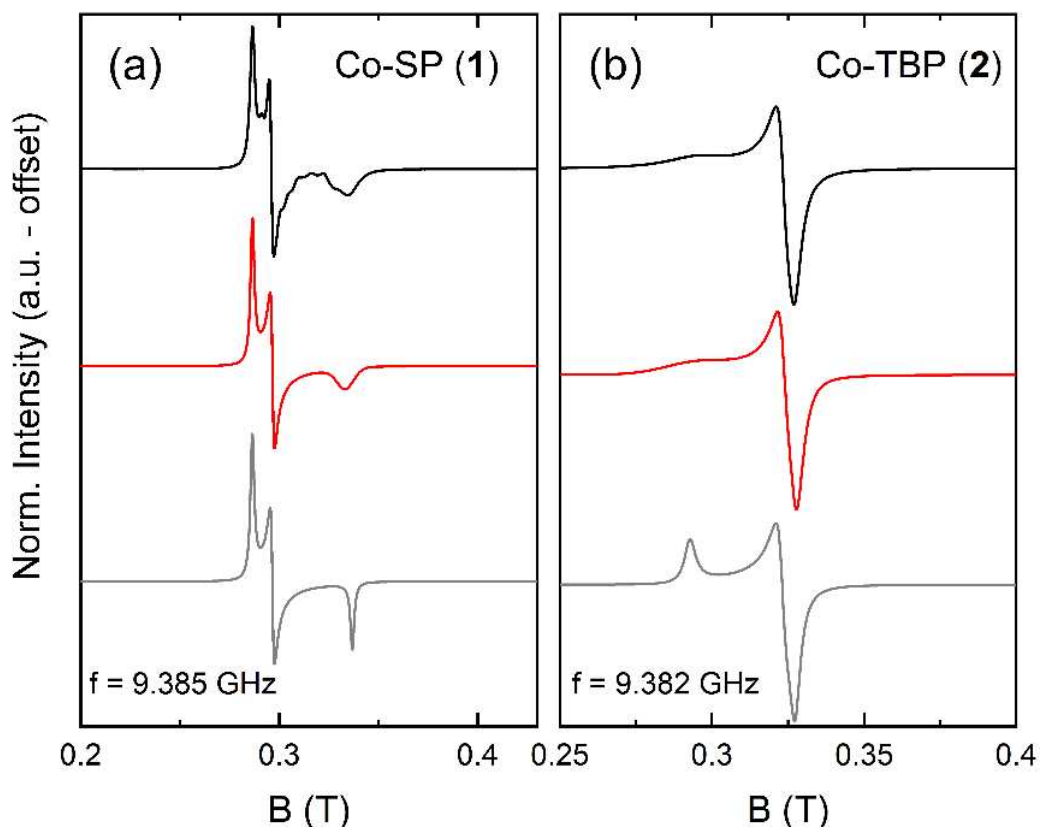[10]UV-Vis and frozen solution spectra were recorded by S. Tripathi (IIT Bombay).

Figure 4.8.: X-band EPR spectra measured at T = 5 K for a fixed powder sample of
1 (a) at f = 9.385 GHz and **2** (b) at f = 9.382 GHz shown as black solid
lines. Red solid lines correspond to a simulation including an anisotropic
g-factor as well as the line width ω, hyperfine splitting (HFS) and H-strain
shown in Table 4.1 for **1** and **2**, respectively. In order to illustrate the
influence of a finite H-strain parameter, an additional simulation without
anisotropic line broadening is given as grey lines.

is studied in the frequency regime between 50 and 300 GHz (black solid lines in
Figure 4.9). For both **1** and **2**, the spectra exhibit two distinguishable resonance
features which enable reading off the respective resonance fields and can be used
to construct the frequency vs. magnetic resonance field diagram (blue symbols in
Figure 4.9). Expectedly, for low-spin Co(II) complexes, the resonance frequency
obeys linear field dependence without a zero field splitting (ZFS) gap (blue solid lines
in Figure 4.9). The data obtained at the respective highest frequencies, where the
resolution of the anisotropic spectra is best, were fitted by using the SH Eqn. 4.4 with
an anisotropic g-factor. The resulting parameters were used to simulate the spectra
measured at lower frequencies in order to demonstrate the consistency of the used
model. The fit-results yield $g(\mathbf{1}) = [1.99(1), 2.26(1), 2.34(1)]$ and $g(\mathbf{2}) = [2.04(1),
2.06(1), 2.27(1)]$ which fully agrees to the analyses of the X-band EPR data as shown
in Table 4.1.[11]

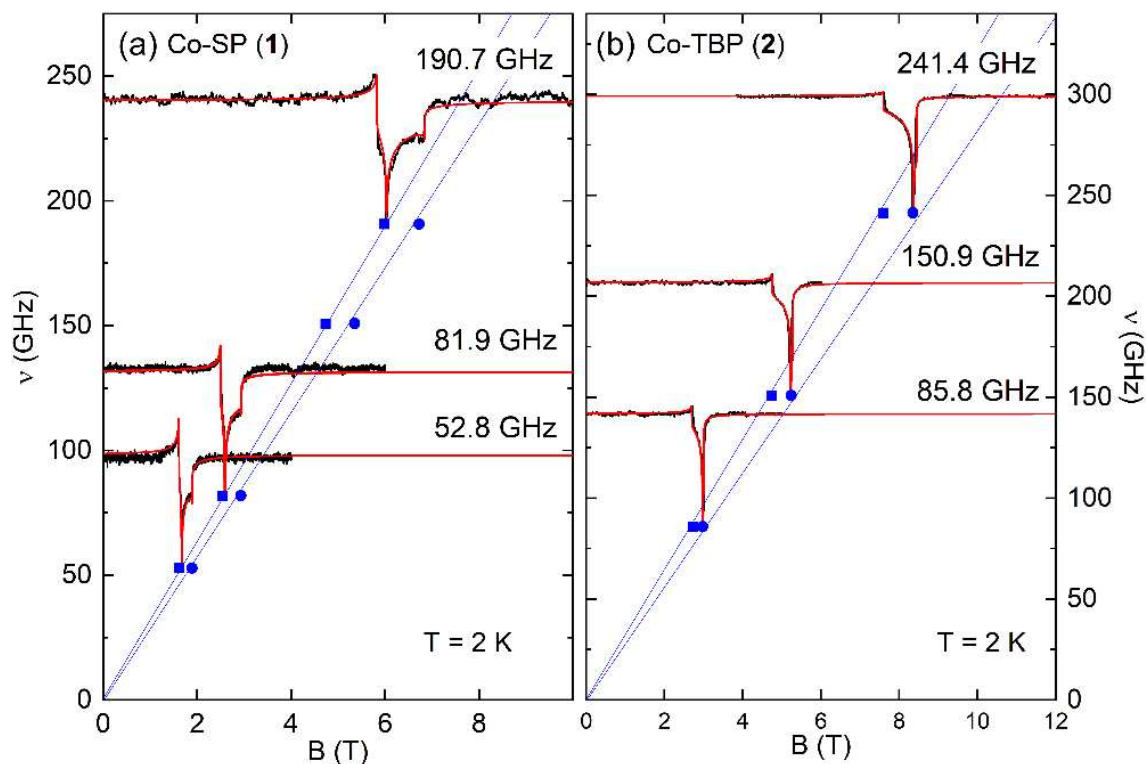[11]DFT-calculations were preformed by S. Tripathi et al.

48

Figure 4.9.: HF-EPR spectra measured at T = 2 K on fixed powder samples of **1** (a) and **2** (b) (black lines). The spectra are normalized and shifted by an offset of the respective measurement frequency which is indicated in the plot. Blue symbols show the resonance field positions of the respective resonance features which can be fitted by a linear fit without ZFS gap (blue solid lines). Red solid lines correspond to a fit or simulation including an anisotropic g-factor as described in the main text.

4.4.4. Magnetization Relaxation Dynamic Studies

Measurements of the ac-susceptibility on **1** and **2** show the absence of an out-of-phase contribution to the dynamic susceptibility at zero magnetic dc-field as expected for a spin $S = 1/2$ system. Field-induced slow magnetic relaxation behavior can however be observed for **1** when small external magnetic fields are applied as demonstrated by a peak in χ" shown in Figure A.9 (c). Fitting the frequency-dependent χ" data by a generalized Debye-model (see Eqn. A.1) yields relaxation times τ up to 35 ms while small eccentricities ($\alpha < 0.120(2)$ at 0.2 T and $< 0.185(3)$ at 1 T) indicate a single relaxation process with narrow distribution. To find a proper model to evaluate the temperature-dependent relaxation times, the high and low-temperature regions can be approximated separately by a linear fit shown as blue dashed lines in Figure 4.10. From the slope of these fits, the exponents of the participating relaxation processes in the respective temperature region can be estimated.[121] For our data we find the temperature exponents of 1.9 and 1.6 in the low as well as 3.6 and 4.4 in the high temperature region for the data measured at 0.2 T and 1 T, respectively. These values are close to the theoretical values of 1 and 5 for the direct process and a Raman process

Table 4.1.: Simulation parameters using the SH Eqn. 4.4 applied to the dc-magnetization, HF-EPR and X-Band data, respectively and calculation results.

	1	**2**
g_{HF-EPR}	1.99(2), 2.26(2), 2.34(2)	2.04(2), 2.06(2), 2.27(2)
g_{x-Band}	2.01(3), 2.26(2), 2.34(2)	2.07(2), 2.05(2), 2.29(3)
ω_{x-Band} (mT)	1.3(2)	2.5(3)
H-strain (MHz)*	250(30), 0, 0	0, 0, 750(50)
SOC constant (NEVPT2)	490.7 cm^{-1}	494.4 cm^{-1}
DFT (g-values)	2.01, 2.16, 2.20	2.06, 2.07, 2.19
NEVPT2 (g-values)	2.0, 2.28, 2.37	2,05, 2.06, 2.41

* The H-strain parameter describes the anisotropic line broadening due to unresolved hyperfine interactions.[66]

Table 4.2.: Parameters obtained by the fit of the temperature dependence of the relaxation times over the whole temperature range shown in Figure 4.10 using Eqn. 4.5 for an external magnetic field of 0.2 T / 1 T.

	A (s^{-1}K^{-1})	B (s^{-1}K^{-n})	n
1	11.6(8) / 10.1(6)	0.5(3) / 0.6(1)	4.7(10) / 4.2(10)
2	96(30) / 72(30)	6(4) / 3(3)	5* / 5*

* These values are fixed to avoid over-parametrization of the fit.

considering the involvement of multiplets with small but finite splitting induced, e.g., by hyperfine-interactions.[18] Furthermore, there is no zero-field energy barrier for an $S = 1/2$ system, which is why we fit our data over the whole temperature range considering a direct and a Raman processes, only (Eqn. 4.5).[18]

$$\tau^{-1} = AT + BT^n \qquad (4.5)$$

While for a Raman relaxation process of a perfect Kramers doublet an exponent of n = 9 is expected, a much smaller value than 9 signifies the involvement of both, acoustic and optical phonons in the Raman relaxation mechanism.[122]

For **2** we also find a peak in χ" signifying a slow relaxation of magnetization behavior. However, the observed relaxation times are much shorter ($\tau_{max} = 5$ ms at 1 T) and the out-of-phase signal is two orders smaller compared to **1** and only observable in the low temperature range (see Figure A.10). Therefore, a detailed investigation of the involved relaxation processes is not possible. However, from a qualitative comparison, we can conclude, that the magnetic relaxation time in complex **2** is significantly reduced compared to **1**. Furthermore, we fitted the data using Eqn. 4.5 but with a fixed temperature exponent of 5 for the Raman relaxation term to avoid over-parametrization. From this, we get an estimate for the pre-factors of the direct
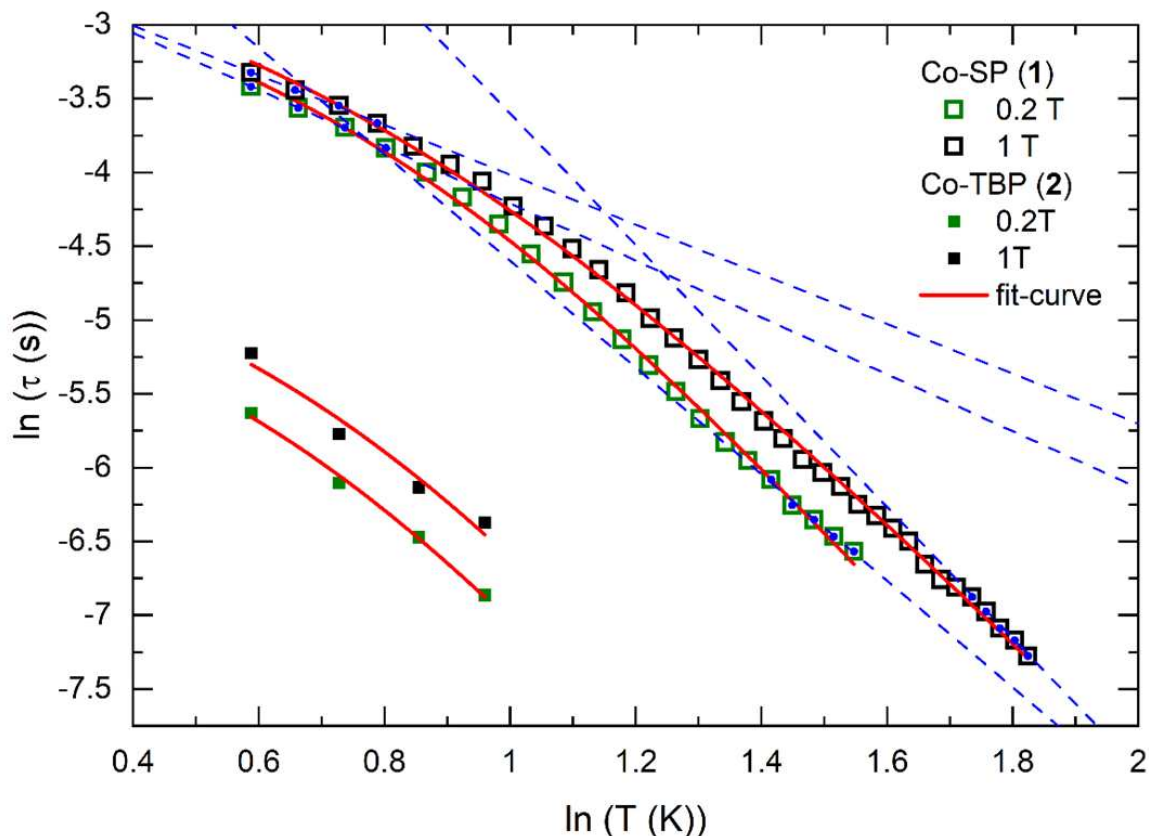
Figure 4.10.: Temperature dependence of the relaxation time for **1** (open symbols) and **2** (filled symbols) in two different external magnetic fields. The data were collected by fitting the respective frequency dependence of χ'' by a generalized Debye model (see Eqn. A.1 and Figure A.9 and A.10). Dashed blue lines correspond to linear fits of the high and low temperature regions as described in the text while solid red lines show a fit over the whole temperature range using Eqn. 4.5. Blue dots mark the fit-range in correspondence to the linear fits.

and the Raman-relaxation term. The evaluation of the corresponding fit-parameters shown in Table 4.2 reveals, that this reduction in relaxation time is induced by an increase of both, the direct and the Raman relaxation term. A fit using a direct term only failed to reproduce the data.

Observation of slow relaxation of magnetization in metal complexes possessing $S > 1/2$ is very common in the molecular magnetism research field. However, as already mentioned in the earlier section, the observation of slow relaxation of the magnetization in an $S = 1/2$ system is relatively scarce in the literature compared to the same phenomenon observed for $S > 1/2$ systems.[123–127] Reported examples for such complexes which show a finite out-of-phase susceptibility signal in the presence of an external magnetic field are, e.g., V(IV), Ni(I), Ni(III), Mn(IV), Cu(II), Fe(III) and Co(II) complexes.[75, 107, 108, 111, 128, 129] In Ref. [129] it is shown, that the unquenched orbital contribution to the magnetic moment of the two-coordinate Ni(I)

is the origin of field-induced slow relaxation of magnetization in these complexes. In the Co(II) complexes studied at hand, strong spin-orbit coupling is clearly evident from our X-band and HF-EPR investigations performed on **1** and **2** which show large g-factors (compared to $g = 2.0023$) and an anisotropic g-value. It is also confirmed by our numerical studies (see Table 4.1). The calculated spin-orbit coupling (SOC) constant is large but only marginally differs between **1** and **2** (see Table 4.1). Hence, while in general the appearance of slow relaxation of the magnetization behavior can be explained by the strong SOC in both complexes, the observed clear differences in the relaxation times must have another origin, i.e., the driving mechanism suppressing the relaxation time in **2** compared to **1** is to be identified.[128]

One candidate to cause the different relaxation times in both complexes is hyperfine interactions. Our simulations of the X-band EPR data strongly imply finite hyperfine interactions in both complexes as evidenced by the anisotropic line broadening which is reflected by the H-strain parameter. Even though due to lack of resolution, no quantitative number for the strength of the hyperfine interaction can be given, the H-strain parameter for **2** appears to be significantly larger than for **1**. We conclude that also the hyperfine interaction is larger in **2** than in **1**, and thereby could drive faster relaxation. However, on an absolute scale, the difference in the observed H-strain parameter is only 500 MHz (0.017 cm^{-1}) and the overall HF interaction strength seems to be too weak to resolve any HF features in the X-Band EPR spectra. Hence we conclude, that the HF interaction may not be the driving mechanism to explain the significant differences in relaxation behavior of the investigated compounds. Instead, we assume, that the dissimilar g-anisotropies induced by the geometrical arrangement of the surrounding ligand might be the most reasonable explanation for the observed magnetic relaxation behavior. We also would like to mention here the scenario considering intermolecular dipolar interactions.[128] Indeed, the distance between nearest neighbouring Co(II) ions in **2** amounts to 9.81 Å which is slightly smaller than the minimal distance in **1** (10.68 Å). This results in different dipolar interaction strengths of 2.7 MHz and 2.1 MHz in **2** and **1**, respectively. However, comparisons to literature results imply, that these small deviations in minimal Co(II)$\cdots$Co(II) distances cannot account for the strong difference in relaxation behavior.[75] This is in line with our experimental findings on a frozen solution sample described in the previous section. However, since intermolecular coupling pathways are a sensitive issue in order to evaluate magnetic relaxation processes, a Hirshfeld surface analysis was applied to investigate the nature and strength of possible intermolecular interactions.[12]

4.4.5. Experimental Details

X-band electron paramagnetic resonance (EPR) spectra were recorded using a Bruker EMXPLUS spectrometer. Direct current (dc) as well as dynamic (ac) magnetization measurements were performed using an MPMS3 SQUID magnetometer (Quantum Design) equipped with a 7 T magnet. Depending on the device and measurement

---

[12]The Hirshfeld surface analysis was performed by S. Tripathi and M. Ansari under the supervision of G. Rajaraman and M. Shanmugam and is shifted to the appendix (see chap. A.1.1).

technique, the samples were fixed in gelatin capsules and placed inside a non-magnetic straw sample holder or pressed in a plastic capsule and mounted on a brass sample holder. Temperature-dependent dc measurements were performed in between 1.8 K and 300 K with an applied magnetic field of 1 T. For the field-dependent measurements, the external magnetic field was swept up to 7 T at several fixed temperatures. The ac measurements were conducted under an applied dc-field of 0 T, 0.2 T and 1 T, respectively, at temperatures ranging from 1.8 - 7 K with an oscillating magnetic field of 3 Oe at frequencies ranging from 1 to 1000 Hz. High-field electron paramagnetic resonance (HF EPR) measurements were carried out using a phase-sensitive millimeter-wave vector network analyzer (MVNA) from AB Millimetre as a microwave source and detector.[67] Measurements have been performed at frequencies between 50 and 300 GHz and in magnetic fields up to 16 T. Various measurement frequencies were realized by assembling of Shottky diodes for different bands, e.g. V, W, and D band. The temperature was controlled by the regulation of ^{4}He gas flow in a variable temperature insert (VTI). The powder samples were fixed by mixing with eicosane inside a brass ring which was placed on the end of a transmission-type tube-shaped probe. Analysis of magnetization and EPR data was done by means of the EasySpin software package.[66]

4.4.6. Conclusion

By the application of different EPR techniques, i.e. X-band EPR for a detailed spectral resolution as well as HF EPR for higher energy scales, it was shown, that the spatial arrangement of the ligand environment around a Co(II) low spin metal centre has indeed an influence on the magnetic anisotropy of the g-value. Furthermore, the non-vanishing impact of this change in anisotropy on the magnetic relaxation behaviour was experimentally proven by measurements of the dynamic susceptibility. While complex **1**, which figures a square-pyramidal coordination environment, shows relaxation times up to 35 ms at T = 1.8 K in an external magnetic field of 1 T, for complex **2** a maximal relaxation time of only 5 ms was measured under the same conditions. A detailed analysis of possible intermolecular coupling pathways showed, that these contributions to the over all relaxation behaviour can be neglected. This finding, combined with the fact, that the investigated sample are real isomers leads to the conclusion, that the tremendous change in relaxation times is controlled by the geometrical arrangement of the surrounding ligands.

5. Vanadium(III) Monomer

5.1. Magnetic Properties of the First Pentagonal-bipyramidal Vanadium(III) Complexes with a Schiff-base N_3O_2 Pentadentate Ligand

Pentagonal-bipyramidal (PBP) coordinated complexes often figure an almost perfectly planar pentadentate ligation in the plane while the apical positions are usually occupied by solvent ions or molecules like Cl^-, NO_3^-, N_3^- or SCN^- anions.[130–134] Especially those apical ligands can easily be substituted which makes PBP coordinated compounds to attractive building blocks for fundamental investigations on the crystal field changes but also for the synthesis of polynuclear magnetic structures in which the apical ions are substituted by bridging units.[85] Thereby, this PBP coordination geometry is not limited to vanadium or $3d$ containing compounds, but can also be found as ligation surrounding in lanthanide mononuclear complexes, where the PBP coordination potentially can provide strong uniaxial anisotropies.[135–137] An example of an Er(III) mononuclear complex figuring PBP coordination geometry is given in chap. 6.2.

The influence of the crystal field induced by the PBP surrounding onto the magnetic V(III) centres can most directly be quantised by the means of EPR spectroscopy. However, EPR investigations on V(III) complexes are not so common in literature compared to other compounds, owed to the fact that systems with S = 1 and significant anisotropy are often "silent" for conventional X-Band EPR applications.[138] Therefore, HF EPR has to be applied to overcome the ZFS gap induced by the crystal field anisotropy and acquire data in a higher frequency and magnetic field range, which is, however, not a standard characterisation technique.

Within the original work published in 2020 by Bazhenova et al. [85], three different novel V(III) complexes with ligands in different charge stages, i.e. 0, -1 and -2, were investigated. Among them, the latter complex (see the next chapter for a structural description) was chosen for a detailed experimental investigation of the magnetic properties by HF EPR and low temperature SQUID magnetometry as described in the main part of this chapter.

5.1.1. Molecular Structure

In fig. 5.1 (a) the molecular structure of the investiagted sample is depicted which can be described by the general formula: $[V(DAPBH)(CH_3OH)_2]$ $Cl \cdot CH_3OH$ (**3**). The sample was synthesized by T. A. Bazhenova at the Institute of Problems of Chemical Physics (IPCP), Chernogolovka.[85] The central V(III) ion has a S = 1 spin ground state and is surrounded by three nitrogen and two oxygen atoms in the equatorial plane. The axial positions are occupied by two additional oxygen atoms which are almost perfectly aligned with the central V(III) ion as can be seen in the frontal view in fig. 5.1 (a) ($\angle$O-V(III)-O $\approx$ 178°). In the perpendicular view onto the molecule in fig. 5.1 (a) it is visible, that the atoms in the plane form a planar pentagonal structure which is slightly distorted due to the inequivalent coordination sites. Thus, the V(III) ion faces a pentagonal-bipyramidal (PBP) coordination geometry.

Fig. 5.1 (b) shows the arrangement of the molecules within the crystalline structure. The complex crystallizes in the monoclinic space group $P2_1/c$.[13] As can be seen, the molecules are found to be in two different crystallographic positions, which can be transformed into each other by a rotation of approximately 28°. The influence of this angle on the outcome and evaluation of the experimentally derived data is discussed in detail in the following sections. The minimal distance between two neighbouring V(III) ions amounts to 7.5 Å.
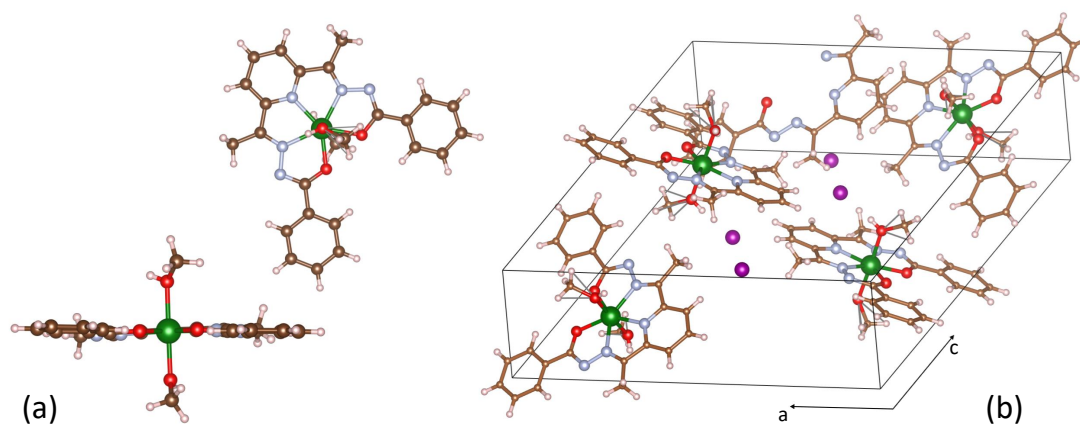

(a)   (b)

Figure 5.1.: (a) Molecular structure of **3** shown from a frontal (lower picture) and a perpendicular (upper picture) view angle. (b) Packing of the two in-equivalent molecular positions in the crystal structure. Green, V; red, O; purple, Cl; sky blue, N; brown, C; white, H. (*Samples were structurally characterized by T.A. Bazhenova, IPCP, Chernogolovka.*)

---

[13]The sample was synthesized and structurally characterized by T. A. Bazhenova et al., IPCP, Chernogolovka.[85]

5.1.2. DC Susceptibility Measurements

To preliminarily analyse the magnetic properties of the investigated sample, the magnetic susceptibility χT(T) was measured in a temperature range between 2 K - 300 K in an external magnetic field of 0.1 T for a fixed powder sample as shown in fig. 5.2. The measurements and the evaluation was performed by O. V. Maximova at the Lomonosov Moscow State University, Russia. As can be seen in fig. 5.2, the χT-value reaches almost 1 cm^3 K mol^{-1} at room-temperature, which is consistent with the expected S = 1 spin state of the V(III) ions and a g-value of $\approx$ 2. Upon cooling the χT-value linearly decreases until a rapid drop below $\approx$ 30 K indicating the presence of an anisotropy. To gain quantitative information from the measured data, a fit assuming the following single-ion spin Hamiltonian was performed:

$$H = g\mu_{\mathrm{B}}\mathbf{BS} + D\left(S_z^2 - S(S+1)/3\right) + E(S_x^2 - S_y^2) + H_{\mathrm{TIP}} \qquad (5.1)$$

where D and E denote the axial and rhombic ZFS parameters, respectively, μ_{B} is the Bohr magneton, $\mathbf{B}$ is the external magnetic field and H_{TIP} is the paramagnetic temperature-independent term. The resulting fit-parameters are $D = +10.1$ cm^{-1}, $E = 0.4$ cm^{-1}, g = 1.940 and $\chi_{\mathrm{TIP}} = 1.12 \times 10^{-4}$ cm^3 mol^{-1}. As can be seen in fig. 5.2 as red solid line, the used single-ion model reproduces the measured data well, however, a small discrepancy can be observed around 30 K. An explanation for this deviation will be given in the following section.
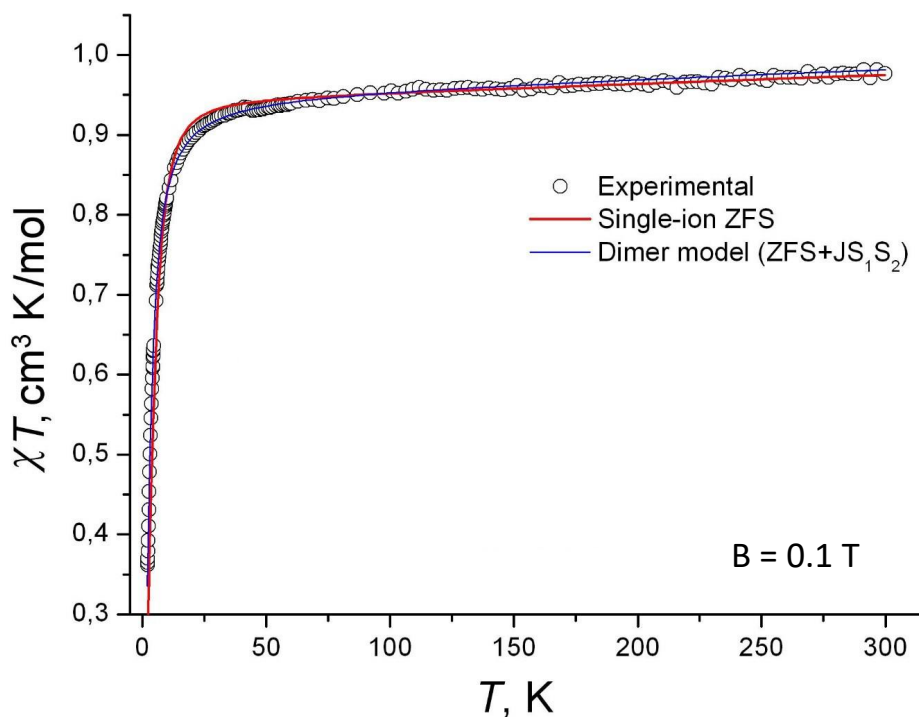
Figure 5.2.: Temperature dependence of dc susceptibility measured in an external magnetic field of 0.1 T for **3** is shown as open black circles. The red and blue solid lines depict the results of a fit using a single-ion model (eqn. 5.1) and a dimer model (eqn. 5.2), respectively. (*Figure adapted from Bazhenova et al. 2020.[85] Measurements, fitting and plot construction was performed by O. V. Maximova, LMSU, Russia.*)

The following chapter (chap. 5.1.3) was written by L. Spillecke and has been published in this form (see Bazhenova et al., ref. [85]) as part of a research article in the journal Dalton Transactions.

5.1.3. HF-EPR Spectroscopy

In order to obtain straightforward information on the ZFS parameters and to elucidate the basic magnetic interactions underlying the magnetic behavior of the V(III) PBP complex **3**, we have undertaken a high-frequency/high-field electron paramagnetic resonance (HF-EPR) study for compound **3**. The HF-EPR measurements were performed on loose and fixed powder samples of complex **3**. For both preparation techniques, the measured resonance spectra exhibit clearly resolvable features as can be seen in Fig. 5.3. The obvious differences between the shown spectra measured at approximately the same frequencies on the loose and fixed powder sample prove proper alignment of the loose powder in the external magnetic field. Both spectra exhibit some mixing of phase and amplitude information, which is due to the applied measurement technique and was included as a parameter in the corresponding simulations displayed as red lines, respectively.

The temperature dependence of the loose powder spectra of **3** at a constant frequency of 396.2 GHz (Fig. 5.4, left) implies that the pronounced low-temperature feature is associated with a ground state transition. In addition, while at $T = 2$ K only one main feature is visible, an excited feature appears on the high field site of the main one with increasing temperatures.

Tuning the microwave frequency allows determining the magnetic field dependence of the resonance features. The corresponding resonance frequency vs. the magnetic field diagram for the loose powder of complex **3** is shown in Fig. 5.5.
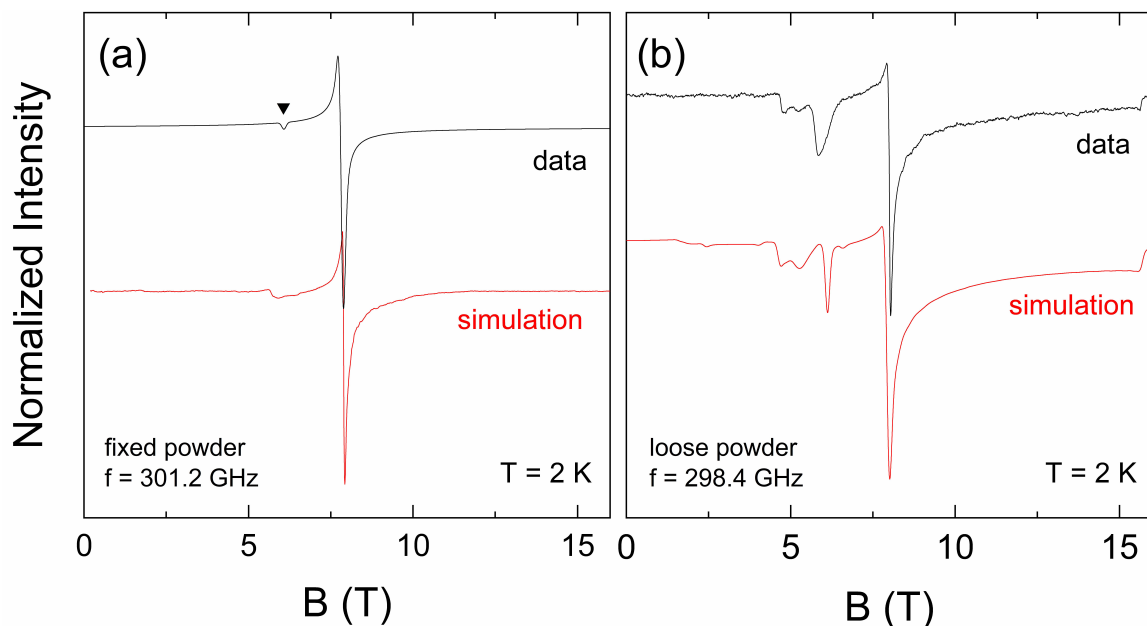

Figure 5.3.: HF-EPR spectra (black lines) of aligned loose powder (a) and fixed powder (b) of complex **3** measured at $T = 2$ K and a fixed frequency of 301.2 GHz and 298.4 GHz, respectively. The black triangle indicates an extra feature as discussed in the text. The red lines correspond to a simulation using the SH (eqn 5.1) with the parameters listed in Table 5.1. (*Figure reprinted from Bazhenova et al. 2020.[85]*)

At $T = 2$ K, there is one main branch shown by black squares in Fig. 5.5 and in Fig. A.13.[14] The branch features a ZFS of around 180 GHz and pronounced bending in the low-field regime, while linear behavior corresponding to a g-factor of ≈ 2 is found at high magnetic fields. Measurements at higher temperatures (10 K – 15 K) show the appearance of additional resonance branches, which are associated with several excited features. The main feature of the spectra displayed in Fig. 5.3 (a) and the presence of a single resonance branch at $T = 2$ K are explained in terms of the single-ion ZFS model for an anisotropic S = 1 system. The observed pronounced bending of the low-temperature branch in the low-field regime confirms the proper alignment of the crystallites perpendicular to the external field direction and a positive sign for the axial crystal field anisotropy parameter D can be read-off.[139, 140] How-

---

[14]The supplementary material for the V(III) monomer chap. 5.1 is shown in the Appendix chap. A.2.
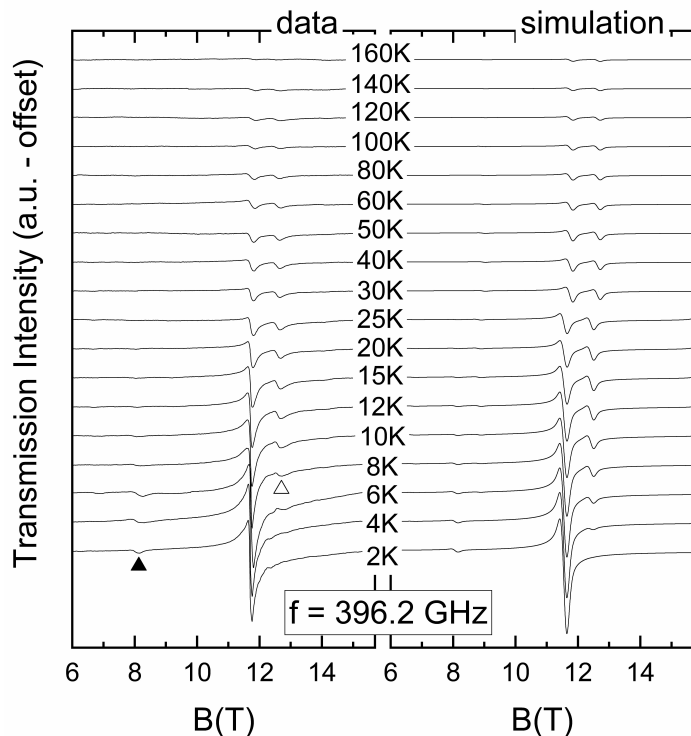
Figure 5.4.: (Left) HF-EPR spectra for an aligned loose powder sample of **3** at $f = 396.2$ GHz at various temperatures between 2 K and 160 K. The data are vertically shifted for clarity. A weak feature arising from a forbidden transition (see the text) at $T = 2$ K and an excited one are indicated by filled and open triangles, respectively. (Right) Corresponding simulation using the SH in eqn 5.1 and the parameters listed in Table 5.1. (*Figure reprinted from Bazhenova et al. 2020.[85]*)

ever, the appearance of thermally excited branches as shown in Fig. 5.4 and 5.5 (the black open triangle in Fig. 5.4) is not predicted by simple models of non-interacting V(III)-centers. Instead, the data suggest the presence of finite intermolecular spin coupling between neighboring metal centers.[19] The corresponding spin Hamiltonian transforms to

$$H = \mu_{\mathrm{B}}\mathbf{B}g\mathbf{S} + D\left(S_z^2 - S(S+1)/3\right) + E(S_x^2 - S_y^2) - J\mathbf{S_1}\mathbf{S_2} \qquad (5.2)$$

where the first term describes anisotropic Zeeman interaction of the spin S with the external magnetic field **B**, D and E are ZFS parameters, and the last term covers the magnetic interaction between two neighboring spins $\mathbf{S}_1$ and $\mathbf{S}_2$ with the exchange parameter J. In general, the g-tensor exhibits three components g_x, g_y and g_z. From the axial structure of the molecule, we assume axial symmetry for the g-tensor so that it can be simplified to axial $(g_\parallel)$ and transversal $(g_\perp)$ components. This is supported by our ligand-field (LF) calculations for **3** combined with the angular overlap model [141, 142], evidencing the uniaxial character of the ZFS tensor, for example, $D \approx +4$,
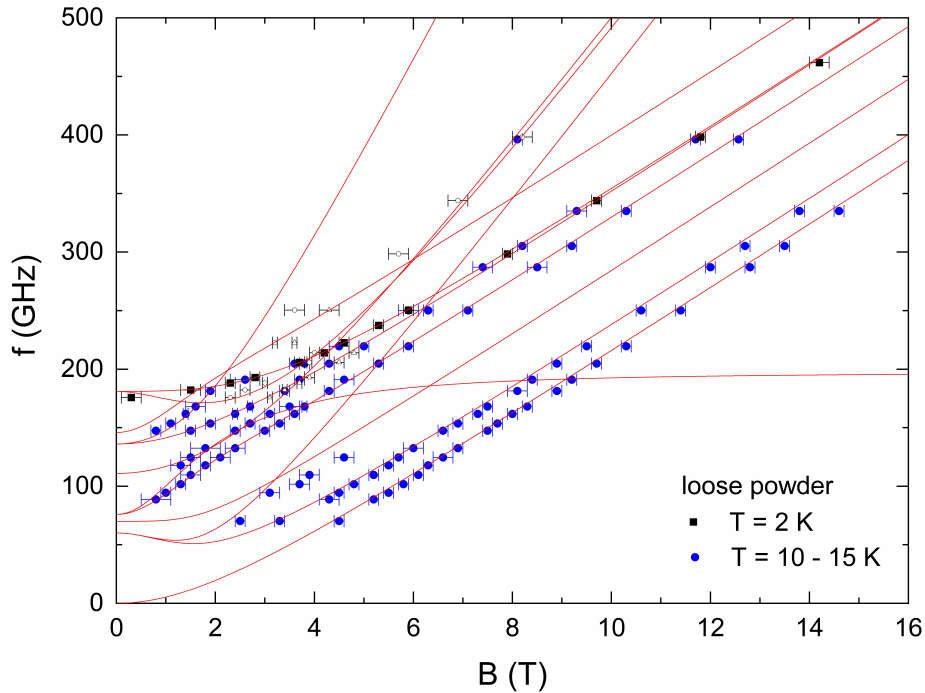
Figure 5.5.: Magnetic field dependence of the resonance frequencies for a loose powder sample of **3**. Black squares correspond to measurements at $T = 2$ K and blue dots correspond to thermally activated features at $T = 10$ K. The red lines show a simulation of the resonance branches using the SH in eqn 5.2 with the parameters listed in Table 5.1. For the sake of simplicity, only the simulated branches that correspond to the observed transitions are shown. Open small symbols display weak features showing up in the spectra obtained at $T = 2$ K that are arising from forbidden or excited transitions. (*Figure reprinted from Bazhenova et al. 2020.[85]*)

$E = 0.035$–0.09 cm^{-1}.[15] Employing this model allows one to simulate the resonance branches shown in Fig. 5.5 and Fig. A.14 as well as the spectra shown in Fig. 5.3 and 5.4. The results show that the experimental data on both loose and fixed powder samples are well described by the simulation using the SH in eqn 5.2. The resulting SH parameters are listed in Table 5.1.

Our analysis shows that powder spectra are well described by assuming well aligned molecules with $g_\parallel \perp \mathbf{B}$. Associating the loose powder spectra with the response of aligned molecules is further confirmed when all resonance branches observed in the fixed, i.e., randomly aligned powder are considered (see Fig. A.14). While all resonance branches in Fig. A.14 are explained by the model, a comparison with the simulation shows that the branches that are also observed in the loose powder indeed correspond to the ones with $g_\parallel \perp \mathbf{B}$.

Our finding of D being much larger than J allows sketching the anisotropy effects

---

[15]The LF calculations where performed by V. S. Mironov, IPCP, Russia and are omitted within this work. The results can be found in the original publication (see ref. [85]).

Table 5.1.: SH parameters obtained from simulations of the resonance frequency vs. field dependence of the loose and fixed powder sample shown in Fig. 5.5 and A.14. These parameters were used to simulate the spectra shown in Fig. 5.3 and 5.4. The third column shows calculated g-values

SH parameter	Simulation results	Calculated parameters[a]
$g_\parallel$	1.97(2)	1.9715834, 1.9722007
$g_\perp$	1.99(2)	1.9984610
D	$+136(3)$ GHz (4.5(1) cm^{-1})	-
E	0(1) GHz	-
J	-34(3) GHz (-1.1(1) cm^{-1})	-

[a] DFT calculations.

by means of a monomer picture: the positive sign of D implies zero field splitting of the triplet states with $m_S = 0$ being the ground state, i.e., planar anisotropy without significant in-plane anisotropy. These results are well consistent with our LF calculations[15] ($D \approx +4$ cm^{-1}, $E \ll D$). While loose powders are hence aligned so that $g_\parallel \perp \mathbf{B}$, rotational symmetry ($g_x = g_y$ and $E \approx 0$) implies that there is no preferential direction within the xy-plane so that the observed single feature can be straightforwardly attributed to the transversal direction. These conclusions are well corroborated by our calculations of the angular dependence of magnetization for the isolated [V(DAPBH)(CH3OH)$_2$]$^+$ molecule, which show a distinct easy-plane nature of magnetization (Fig. A.17) and the absence of magnetic anisotropy in the equatorial xy plane (at $\mathbf{B} \parallel xy$, Fig. A.18). The presence of two molecules within one unit cell in general allows for different directions of the respective easy anisotropy plane, which may be misaligned by the angle 2ϕ between both molecules. In a loose powder measurement, this implies the alignment of the crystallites perpendicular to the effective anisotropy axis so that the external magnetic field is misaligned by ϕ to the xy-plane of the molecular anisotropy. However, as demonstrated in Fig. A.15 where the field dependence of the ground state transition is simulated for different angles ϕ, such misalignment would lead to a splitting of the branch observed at low temperatures. A comparison of the simulation with the experimental data implies that the angle between the crystal field axes of the two molecules in the unit cell is smaller than 10°, while the best simulation of the branch is obtained for $\phi = 0°$. Hence, the crystal field axes for all molecules are almost perfectly aligned. This result is corroborated by the simulation of the fixed powder studies.

Our analysis implies that the thermally excited resonance feature is attributed to the effect of dimer-like antiferromagnetic coupling between two neighboring vanadium centers, thus, its origin is analyzed below in terms of superexchange calculations between the [V(DAPBH)(CH$_3$OH)$_2$]$^+$ units (see chap. 5.1.5). Estimating dipolar interactions[26] between S = 1 centers separated by about 7.5 Å yields magnetic coupling in the range of J$_{\text{dipolar}} \approx 0.2$ GHz, which is much too small to account for the observed separation of the extra feature from the main one and its temperature dependence.[143] The small feature showing up in the loose powder spectra marked by

a black filled triangle in Fig. 5.3 (a) is a forbidden transition, i.e., it is associated with a change of spin state $\Delta m_S = \pm 2$. In general, forbidden transitions are not supposed to be detected for $E = 0$ and aligned crystallites but for higher order transverse terms, the presence of mixed modes of microwave radiation or various molecular orientations in the unit cell may account for forbidden features. Specifically, mode mixing in the transmission-type probe setup implies that not only the conventional perpendicular mode is detected but also the parallel one, which may cause forbidden transitions even in the absence of a transversal anisotropy term.[143, 144] A mixture of the microwave modes was hence included as a parameter in all simulations of the spectra. In addition, slight misalignment of molecules at different unit cell positions implies that even in the case of perfect alignment with respect to the crystals' effective anisotropies, misalignment of the individual molecules is present.
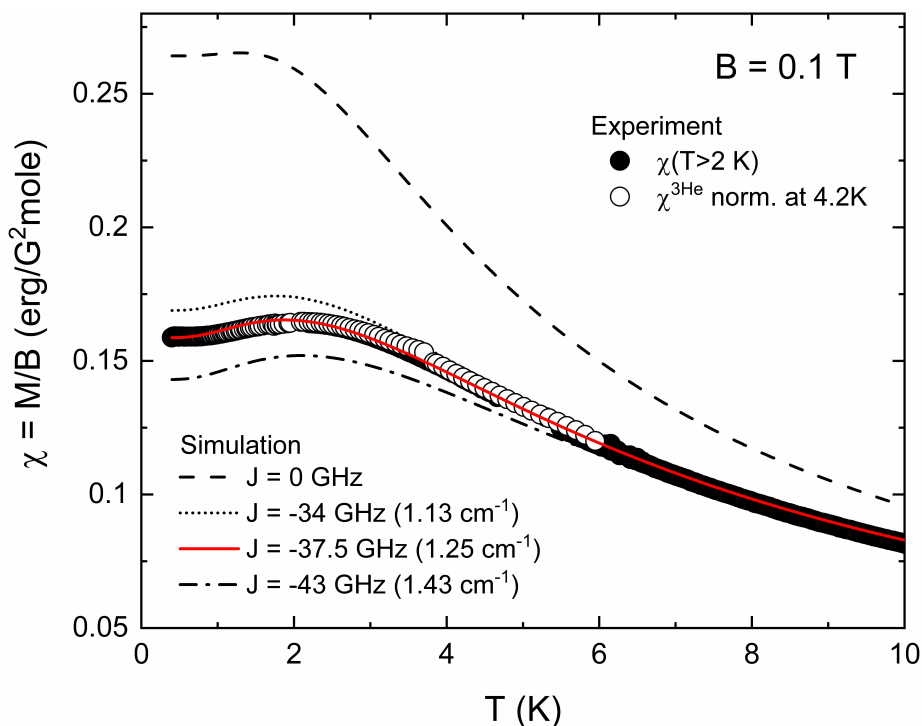

Figure 5.6.: Temperature dependence of the static magnetic susceptibility of **3** between 0.4 K and 10 K. The data obtained in the ^{3}He-setup on a fixed powder of complex **3** were normalized at 4.2 K to the higher temperature data also shown in this figure. The solid line shows a simulation using SH eqn 5.2 and the parameters described in the text. For comparison, a simulation using the same SH parameters but with $J = 0$ is given as the dashed line. (*Figure reprinted from Bazhenova et al. 2020.[85]*)

The presence of small dimer-like spin coupling is supposed to yield a maximum in the magnetic susceptibility at $T \approx 2$ K and downturn below.[145] This behavior is clearly confirmed by Fig. 5.6 where low-temperature dc-susceptibility data are presented. The data are well described by a simulation using the SH eqn 5.2 and employing g-values and anisotropy parameters as shown in Table 5.1 but an antiferromagnetic dimer coupling of -37.5 GHz. This coupling value is within the error range

of the value obtained by HF-EPR. In contrast, ignoring intermolecular magnetic interaction but employing the same anisotropy and g-values obtained from EPR fails to describe the experimental data. Simulation with J = -34 GHz as obtained from the best fit to the EPR data still shows a good qualitative agreement, while the position of the maximum in χ is reproduced best by using J = -43 GHz (see Fig. 5.6). The latter value is however too large to account for the position of the excited features in Fig. 5.4 and 5.5.

It is also important to note that the ZFS model with the isotropic g-tensor and with dimer-like antiferromagnetic spin coupling reproduces the experimental χT curve for **3** over the entire temperature range of 2 − 300 K at g = 1.950, D = +4.6 cm^{-1}, E = 0, J = -1.1 cm^{-1} and χ_{TIP} = 1.12 × 10^{-4} cm^3 mol^{-1}, Fig. 5.2.

5.1.4. Experimental Details

High-frequency/high-field electron paramagnetic resonance (HF-EPR) measurements were performed by means of a commercial millimeterwave vector network analyzer (MVNA) from ABmm as a phase sensitive microwave source and detector.[67] The spectra were obtained in the frequency range between 50 GHz and 500 GHz in external magnetic fields up to 16 T. The temperature control between 2 K and 160 K was ensured by using a variable temperature insert (VTI) with a ^{4}He gas flow cryostat from Oxford Instruments. The loose powder samples were placed inside a brass ring in a home-made transmission type EPR probe with no extra glue or grease to align the crystallites with respect to the external magnetic field direction. In order to ensure alignment of the loose powder, the maximum magnetic field of 16 T was applied prior to the measurements and the alignment was monitored by using corresponding orientation jumps in the transmitted microwave signal. Rearrangement of the crystallites to a non-aligned situation was avoided by restricting the magnetic field to a range between 0.2 T and 16 T. For fixed powder measurements, the material was thoroughly ground and then fixed with eicosane. Analysis and simulation of the HF-EPR data as well as that of the low-temperature magnetization data was done by means of the EasySpin software package.[66]

Ab initio density functional theory (DFT) calculations of the g-tensor anisotropy were performed using a spin unrestricted self-consistent field method (SCF)[146] with B3LYP hybrid functionals and a SVP[147] basis set for all electrons as implemented in the ORCA software package.[148, 149]

5.1.5. Discussion and Conclusion

By HF EPR investigations is was found, that both, the crystal field anisotropy as well as the g-anisotropy of a novel V(III) mononuclear complex (**3**) figure a, within the resolution of the experiment, perfectly planar shape. Beyond the single ion properties of the V(III) ions, a small but well resolved anti-ferromagnetic intermolecular coupling of J = -1.1 cm^{-1} between two neighbouring ions has been found. This dimer like

interaction is a surprising result considering the large spatial separation of about 7.5 Å between the paramagnetic centres within the crystal structure. However, the by HF EPR measured couplings were conclusively confirmed by low temperature SQUID measurements down to 0.4 K. Furthermore, the extension of a single-ion model by a finite dimeric coupling term leads to a significantly improved overlap between the measured and fitted $\chi T(T)$ data as it is demonstrated in fig. 5.2. Yet, it has to be mentioned, that from the evaluation of the $\chi T(T)$ data alone, the different contributions arising from couplings or anisotropy terms can not be distinguished.

To understand the origin of this long-range dimer-like spin coupling, the probable super-exchange interactions between the molecular units were theoretically explored.[16] From this it is found, that actually a π-stacking mechanism between the planar DAPBH ligands provides the most efficient super-exchange coupling pathway (see fig. 5.7). A more detailed description of this coupling mechanism and the corresponding calculations is given in ref. [85].
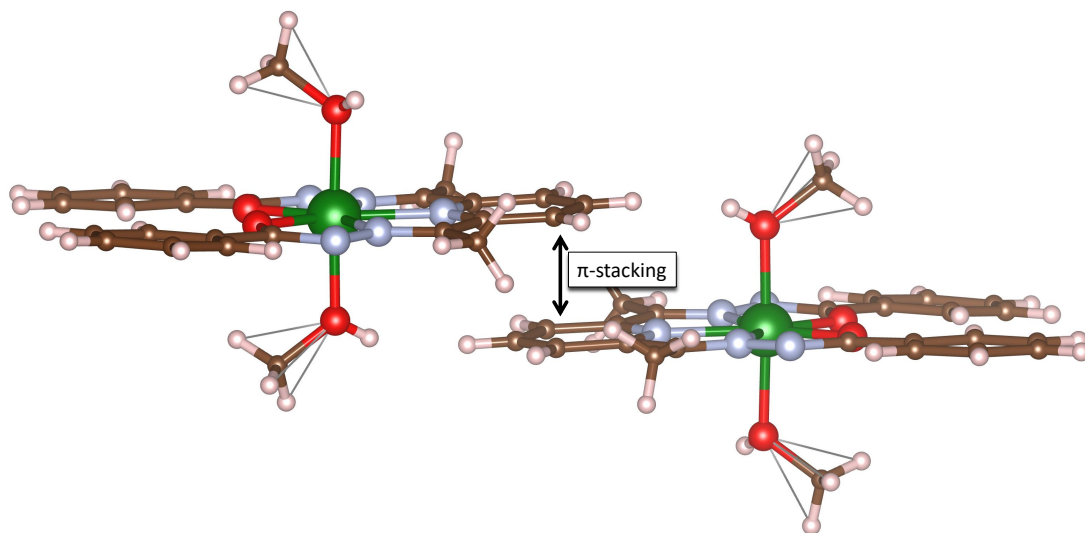

Figure 5.7.: Predicted π-stacking mechanism between the DAPBH ligands of two neighbouring molecules within **3**. The colour code of the atoms is given in the caption of fig. 5.1.(*Figure adapted from ref. [85].*)

Thus, this work delivers, next to the dimeric coupling of Co(II) ions described in chap. 4.2, a further example how detailed HF EPR analysis can not only precisely determine the crystal field induced properties of a given paramagnetic system, but also resolves small intermolecular interactions which are beyond the resolution of a standard SQUID magnetometer.

---

[16]Theoretical calculations were performed by Bazhenova et al., see ref. [85]

6. From $3d$ to $4f$ Magnetism: Rare-earth Metal Containing Compounds

The molecular compounds discussed within the preceding chapters have an obvious similarity as their magnetic properties are arising from a central $3d$ metal ion which is surrounded by organic ligands. The interest in $3d$ transition metal ions mainly arose, among others, due to their representation as crucial ion in many biological molecular compounds in the form of, e.g., the central iron ion in the haemoglobin or myoglobin molecule.[150–153] Furthermore, they were strongly investigated for their catalytic activity and magnetic properties.[154, 155] The great potential of the latter was proven, when the first SMM, the famous Mn_{12},[5] was reported, which consists of twelve strongly coupled $3d$ metal ions, which form a total spin of S = 10. This discovery triggered the investigation of numerous transition metal clusters to gain high spin multiplicity and thereby efficient SMMs.[156–159]

Beginning of the 21th century, Ishikawa et al. firstly reported a SMM which was distinctly different in its structure from the $3d$ compounds reported before. The magnetic centre of this complex was not formed by a strongly coupled cluster of $3d$ metal ions, but by a single $4f$ terbium ion.[160, 161] This founded not only the new approach of employing $4f$ elements into the construction of SMMs, but was also the first example of a so-called single-ion magnet (SIM) with a single metal ion as paramagnetic centre.[162–164] The investigation of further examples within this new class of molecular magnets showed that the involvement of $4f$ elements can potentially lead to high energy-barriers.[25, 165–168] The reason for this observation can be found in the strong spin-orbit coupling of $4f$ electrons which leads to high magnetic single-ion anisotropies.[25] The energy scale of the spin-orbit coupling is thereby the crucial difference to $3d$ ions, where the spin-orbit coupling is usually overcome by the crystal field strength and thereby the orbital moment is partly or completely quenched and does not contribute to the total momentum. Another fundamental difference between $3d$ and $4f$ ions is the spatial electronic distribution. While $3d$ transition metals figure rather extended electronic orbitals which allow the emergence of strong exchange-interactions with neighbouring ions, the electronic distribution of $4f$ elements is concentrated around the nucleus and further shielded by surrounding $5s$ and $5p$ states.[12, 25, 165] Therefore, exchange interactions in $4f$ compounds are usually weak or negligible compared to the energy scale of the single-ion anisotropy. The mentioned differences in the electronic structure has also a severe impact on the overall magnetic relaxation behaviour of those compounds. In $3d$ metal containing

SMMs, the magnetic relaxation is mostly defined by many transitions between the m_S states i.e. it is dominated by direct processes. Therefore the often quoted relations $U_{\text{eff}} = S^2|D|$ or $U_{\text{eff}} = (S^2 - 1/2)|D|$ for integer or non-integer spins hold for most of the $3d$-based SMMs.[11] For $4f$ compounds on the other hand, the magnetic relaxation process is usually promoted over quantum tunnelling mechanisms (QTMs) within the first excited or, in rare cases, the second excited states.[126, 165, 169] Since higher lying states are consequently not involved in the overall relaxation process, the relation between the effective energy-barrier and the anisotropy as used for the $3d$ elements can hardly be applied.

Even though $4f$ elements figure high magnetic single-ion anisotropies, many compounds show no remanent magnetic moment in the absence of an externally applied magnetic field (see e.g. chap. 6.2). The reason for this can be found in the usually high ligation number of Ln centres and the distortion of crystal field leading to transversal anisotropy components which promote QTMs through the energy-barrier.[170, 171] By the application of a small magnetic field, those QTMs can be quenched as it is shown in chap. 6.1 on the example of a Dy(III) monomeric complex. A synthetic approach to quench those relaxation pathways is the coupling of the highly anisotropic $4f$ element to a $3d$ ion.[172, 173] By this coupling, the degeneracy of the $4f$-Kramers doublets can be, comparable to the application of an external field, intrinsically lifted and thereby the QTMs get quenched. How this coupling strength can be quantitatively determined by HF EPR investigations is shown in chap. 6.3 on a sample set of Cu_2Ln compounds.

6.1. Molecular Magnetic Properties of a Dysprosium(III) Complex Coordinated to a Nonadentate Bispidine Ligand

Due to the influence of the strong spin-orbit coupling and according to Hund's rule, the free Dy(III) ion figures a ground state which can be described by the term symbol $^6H_{15/2}$.[174] The total momentum $J = 15/2$ which arises from the coupling of the spins $S = 5/2$ to the angular momentum of $L = 5$, is thereby one of the highest which can be found amongst free Lanthanide ions. Furthermore, Dy(III) ions have an odd number of electrons, i.e., it is a Kramers ion with a doubly degenerated ground state. This electronic properties raised great attention towards Dy(III) ions as building blocks for the construction of SMMs.[175–177]

Even though Dy(III) seems to be a perfect candidate to figure SMM behaviour up to high temperatures it has been observed that most of the reported complexes show no remanent magnetisation in the absence of an external magnetic field.[175, 178–182] The reason for this are various quantum tunnelling processes which are short-cutting the energy barrier. By the application of a small external magnetic field, these processes can be suppressed which enables to investigate the magnetic relaxation behaviour for those compounds.

Within this chapter, a novel Dy(III) monomeric complex is discussed which shows a field induced slow relaxation of magnetisation behaviour as witnessed by AC magnetic susceptibility measurements. The results are rationalised by the comparison to quantum chemical calculations.[19]

6.1.1. Structural Description

The central Dy(III) ion of the investigated complex with the formula $[Dy^{III}L^1]OTf$, where L denotes a novel nonadentate bispidine ligand, figures a nine-coordinated ligand surrounding. Due to the novelty of the complex, no precise structural data for this Dy(III) monomeric compound is available, yet. However, from the analysis of the structurally similar complexes $[Ln^{III}L^1]NO_3$ (Ln=Tb, Gd and Yb) and $[Eu^{III}L^1]CF_3CO_2$ it is expected, that the coordination geometry around the Dy(III) ions can be described as capped square anti-prismatic (CSAPR).[126] Fig. 6.1 (a) shows the predicted coordination cage of the Dy(III) complex based on calculations on the Yb(III) containing analogue. In the first coordination sphere this cage consists of seven nitrogen ions (light blue) and two oxygen ions (red). For a better visualization fig. 6.1 (b) shows a sketch of the corresponding coordination polyhedron.
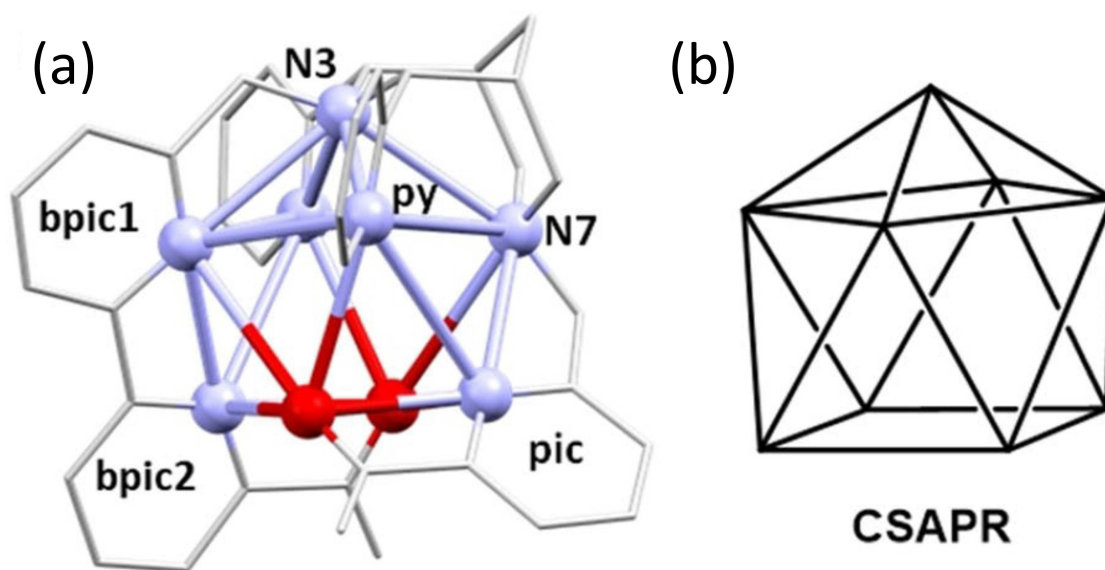

Figure 6.1.: (a) Plot of the predicted coordination polyhedron around the Dy(III) ions. N, light blue; O, red; Dy, not shown. (b) Sketch of the CSAPR geometry (*Figure reprinted from Cieslik et al. 2021.[126] Plot was constructed by Cieslik et. al. .*)

The following chapters (chap. 6.1.2, 6.1.3 and 6.1.4) were written by L. Spillecke and have been published in this form (see Cieslik et al., [126]) as part of a research article in the journal Zeitschrift für anorganische und allgemeine Chemie.

6.1.2. DC Magnetic Susceptibility and Magnetization

The temperature dependence of the direct current (DC) magnetic susceptibility χ (shown as χT vs. T in Figure 6.2) was measured on a fixed powder sample of [Dy^{III}L^1]OTf in the temperature range between 1.8 K and 300 K in an external static magnetic field of 0.1 T.[17] Upon further increase of the temperatures up to 400 K, the susceptibility data show a small hump around 320 K (see Figure A.19[18]). TGA investigations[19] imply, that this hump is due to the loss of one molecule water per formula unit (f.u.) so that the further analysis is restricted to T < 300 K.

The room temperature χT value of 13.28 erg K/(mol G^2) is close to the theoretically predicted free-ion value for the ^{6}H$_{15/2}$ configuration, with g$_J$ = 4/3, i. e., 14.17 erg K/(mol G^2),[165] and it agrees well with other results for mononuclear Dy^{III} complexes reported in the literature.[67, 160, 183] With lowering the temperature, χT smoothly decreases until it drops more significantly below about 100 K, reaching a value of 9.91 erg K/(mol G^2) at T = 1.8 K. The decrease in χT can be assigned to the depopulation of energetically higher multiplets with decreasing temperatures as well as the Zeeman splitting induced by the external magnetic field. The drop at lower temperatures is likely due to magnetic anisotropy.

The inset to Figure 6.2 shows the magnetization measured in external magnetic fields up to 7 T at various isothermal conditions. With increasing magnetic field, the magnetization measured at 1.8 K sharply rises to approximately 1 T while it saturates to a linear increase at the highest measured magnetic fields. Extrapolation of the high-field magnetization to zero field yields about 4.5 μ_B/f.u. which is much smaller than the theoretical predicted saturation value for an m_J = 15/2 ground state (10 μ_B/f.u.). This observation indicates the presence of low-lying excited states and/or significant influence of magnetic anisotropy, and this is supported by the quantum-chemical analysis. Both is further witnessed by the linear increase of the M vs. B curve at higher magnetic field without indication of saturation in the accessible field range.[184, 185]

6.1.3. AC Magnetic Susceptibility

To investigate the dynamic magnetic response, alternating current (AC) magnetic susceptibility measurements were performed in a frequency range between 5 Hz – 1000 Hz with an AC magnetic field amplitude of 3 Oe. In the absence of static magnetic fields, no out-of-phase signal was observed within the studied temperature range of 1.8 K – 20 K (data not shown). We attribute this to a quantum tunneling mechanism (QTM) due to the weak axial ligand field and low overall symmetry of the coordination polyhedron, resulting in transverse anisotropy and therefore mixing

---

[17]DC magnetic susceptibility measurements were performed by G. F. P. Plny under the supervision of L. Spillecke.

[18]The supplementary material for the Dy(III) monomer chap. 6.1 is shown in the Appendix chap. A.3.

[19]Thermogravimetrical analysis (TGA) and quantum chemical calculations were performed by Cieslik et al. and are more detailed shown in the original publication in ref. [126].
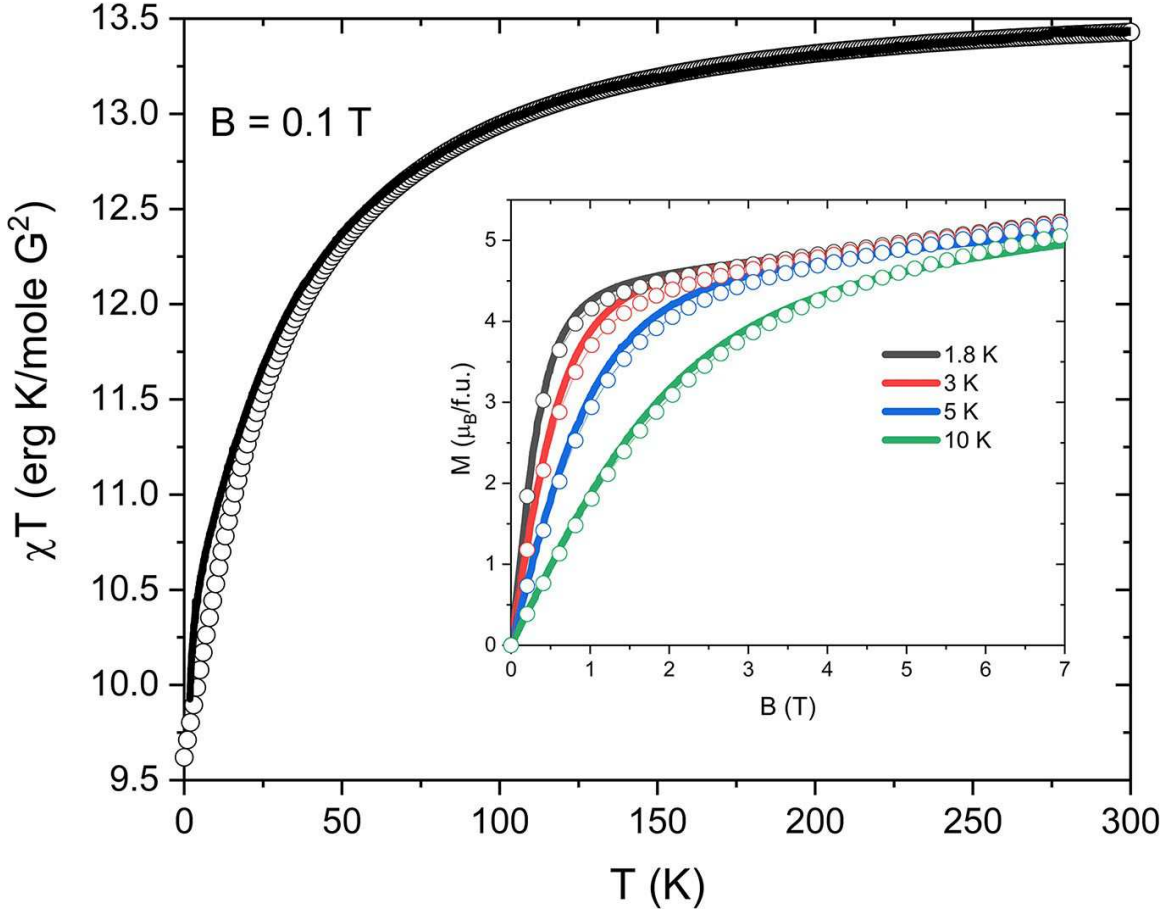
Figure 6.2.: Temperature dependence of the DC susceptibility measured in an external magnetic field of 0.1 T. Inset: Magnetic field dependence of the dc magnetization measured at various constant temperatures. The solid lines are experimental data, the open circles are simulated data from the quantum chemical calculations.[19] (*Figure reprinted from Cieslik et al. 2021.[126]*)

of the m_J states.[175] By applying a small external magnetic field of 0.1 T, the QTM is suppressed and field-induced slow relaxation of the magnetization is observed as indicated by the peak in the logarithmically scaled frequency dependence of the out-of-phase (χ") signal as shown in Figure 6.3 (b). For further analysis, the χ" data were fitted using a generalized Debye model [11] as described in Eqn. A.2. The obtained relaxation times τ are shown as an Arrhenius plot in Figure 6.4 (a).

In the Arrhenius plot of the obtained relaxation times (Figure 6.4 (a)), two different linear regimes separated by a kink at around T = 4 K are visible, which indicate the presence of two different effective energy barriers U_{eff}.[186, 187] Fitting the obtained relaxation times by means of the Arrhenius law:

$$\tau = \tau_0 exp\left(\frac{-U_{\mathrm{eff}}}{k_{\mathrm{B}}T}\right) \tag{6.1}$$

where τ_0 is a constant prefactor and k_{B} the Boltzmann constant, yields the effective energy barriers $U_{\mathrm{eff},1} = 31.4(5)$ K ($21.8(3)$ cm^{-1}; $\tau_{0,1}$=2.9e-5 s) and $U_{\mathrm{eff},2} = 66.2(5)$ K ($46.0(3)$ cm^{-1}; $\tau_{0,2} = 2.5$e-8 s) in the two regimes. Note, that in the literature often a combination of Orbach, Raman and direct processes is used,[188] which however fails qualitatively and quantitatively to describe the data at hand.

The presence of two energy barriers is not only signaled by the different regimes in the temperature dependence of the relaxation times but also by the temperature dependence of the eccentricity parameter α (see chap. A.3 for further information). The parameter α is a measure of the distribution of relaxations times τ so that α close to zero implies the presence of only one dominating relaxation process. While α, shown in Figure 6.4 (b), is rather small and constant at higher temperatures, indicating a single dominant relaxation process characterized by one energy barrier or time scale, it strongly increases upon cooling below 4 K (please note the inverse scaling of the x-axis). This increase of α signifies the evolution of (at least) a second relaxation process associated with a smaller timescale, i. e., a second relaxation barrier as also directly visible in the Arrhenius plot of the relaxation times in Figure 6.4 (a).

Note, that in general also intermolecular interactions can give rise to magnetic barriers. However, the DC susceptibility and magnetization measurements exclude the presence of significant intermolecular interaction on energy scales larger than 2 K. We hence conclude that the observed relaxation barriers are of purely molecular origin. The presence of two unequivalent molecules in the unit cell could also explain the two different pathways.[189]
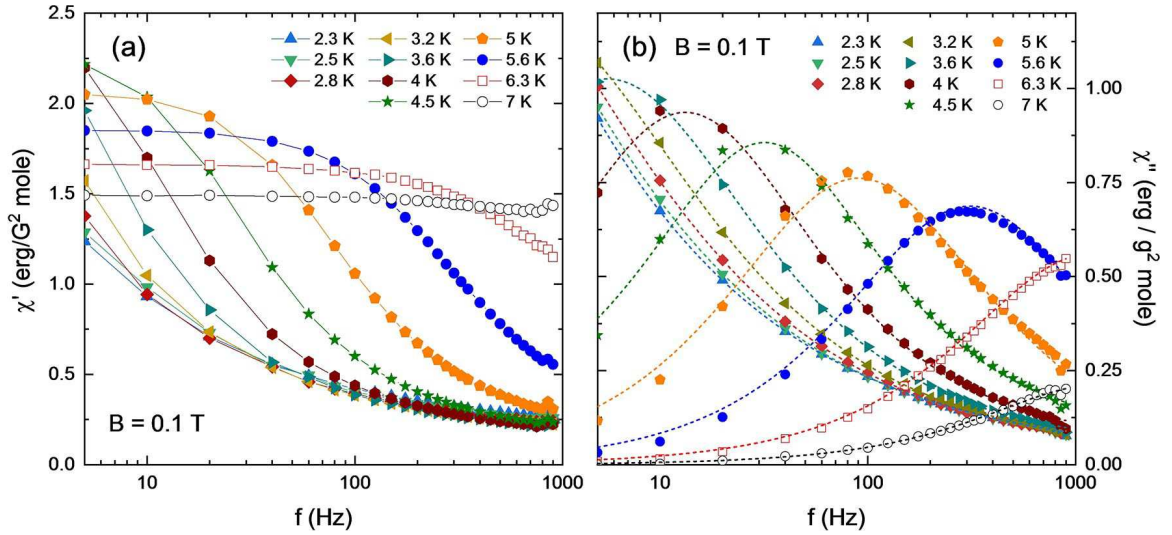

Figure 6.3.: In-phase (a) and out-of-phase (b) AC magnetic susceptibility of [Dy$^{\mathrm{III}}$L^1]OTf measured in an external static magnetic field of 0.1 T at several constant temperatures. Dashed lines in (b) correspond to fits using the generalized Debye model (see the main text and chap. A.3). (*Figure reprinted from Cieslik et al. 2021.[126]*)
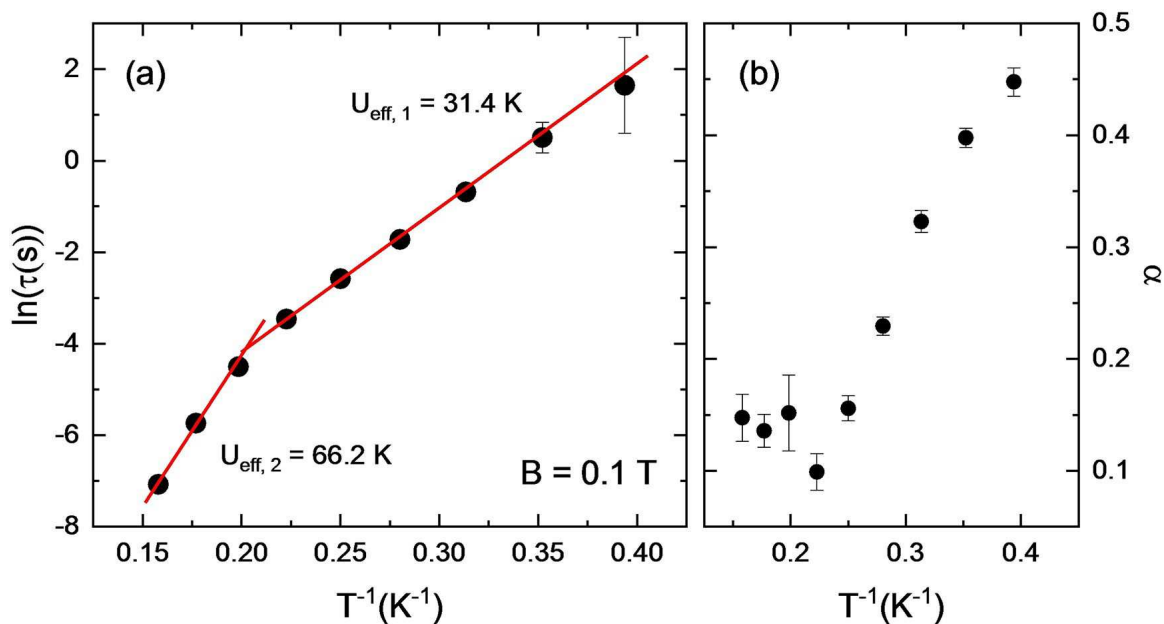
Figure 6.4.: (a) Arrhenius plot of the relaxation times obtained from fitting of the AC susceptibilities (see Figure 6.3 (b)) of $[\mathrm{Dy^{III}L^1}]$OTf in an external magnetic field of 0.1 T. (b) Temperature dependence of the fit parameter α (see chap. A.3 for more information).(*Figure reprinted from Cieslik et al. 2021.[126]*)

6.1.4. Experimental Section

DC and AC magnetic data were measured using a MPMS3 SQUID magnetometer from Quantum Design equipped with a 7 T magnet. The powder samples were fixed with eicosane in order to avoid orientation or motion of the crystallites in the external magnetic field. The data were corrected by the background of the used sample holder and the diamagnetic contribution of the sample using Pascal's constants.[47]

6.1.5. Discussion and Conclusion

The central result from the investigation of the magnetic properties of the novel $[\mathrm{Dy^{III}L^1}]$OTf is the observation of two different effective energy barriers $U_{\mathrm{eff,1}} = 31.4(5)$ K ($21.8(3)$ cm^{-1}) and $U_{\mathrm{eff,2}} = 66.2(5)$ K ($46.0(3)$ cm^{-1}). The two relaxation processes appear in different temperature ranges but do not overlap, i.e. the $\chi''(T)$ curves in fig. 6.3 (b) can be fitted by assuming just one τ, but the temperature dependence of τ figures a change in slope. This implies that, as expected for a monomeric compound, only one magnetic species contributes to the overall magnetic relaxation, but the energy-barrier which has to be overcome is changing depending on the temperature regime. To decipher the origin of the two relaxation regimes the energy separation between the KRAMERs doublets of the $^6\mathrm{H}_{15/2}$ ground state multiplet, as well as the predicted relaxation dynamics between those states was theoretically

obtained by quantum chemical calculations.[19]

Fig. 6.5 shows the calculated results for the lowest three KRAMERs doublets. A description of the used model and a complete summary of all resulting parameters is given in ref. [126]. The energy of the respective KRAMERs doublet is marked by thick black bars in fig. 6.5. The first excited states can be found around 43 cm^{-1} while the second excited KRAMERs doublet is predicted to be at ≈ 92 cm^{-1}. Solid blue, dashed black and dotted red arrows in fig. 6.5 show the possible ORBACH-, temperature assisted (TA) QTM and QTM relaxation pathways, respectively. The numbers on the arrows state the absolute value of the transition matrix element, i.e. they are correlated to the transition probabilities. The increased TA-QTM and QTM probabilities between or within the first and second excited KRAMERs doublets imply, that these are the relaxation pathways which can be connected to the experimentally observed ones, i.e. $U_{\mathrm{eff},1}$ corresponds to the gap between the ground and first excited and $U_{\mathrm{eff},2}$ to the gap between the ground and second excited KRAMERs doublet. While the measured magnitudes of those gaps are smaller than the calculated ones, the experimentally and theoretical obtained ratio ($U_{\mathrm{eff},1}/U_{\mathrm{eff},2}$) perfectly coincides.

As a conclusion it is worth to mention, that the observation of a relaxation process not only via the first, but also via the second excited state is rather scarcely reported in literature.[190–192] The reason for this can be found firstly in the usually distorted structure of Ln containing complexes which leads to transversal anisotropy contributions and therefore to effective relaxation pathways via QTMs and secondly in the often non-coinciding anisotropy axis between the ground and first excited states.[165]
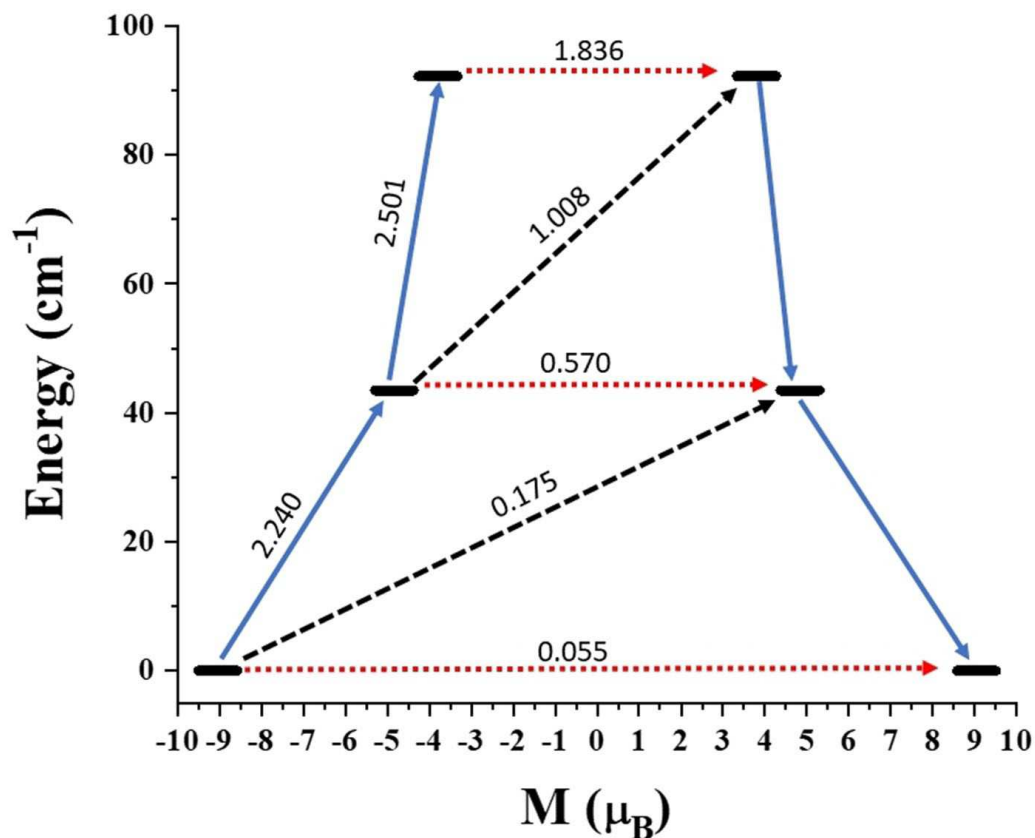
Figure 6.5.: Ab initio calculated relaxation dynamics for the Dy$^{\text{III}}$ complex. The thick black lines are the Kramers doublets as a function of the magnetic moment. The dashed black lines show possible Orbach pathways. The blue lines are the most probable relaxation pathways for magnetization reversal, and the dotted red lines represent the presence of QTM/TA-QTM between the connecting pairs. The numbers at each arrow are the mean absolute values for the corresponding matrix element of the transition magnetic moment.(*Figure reprinted from Cieslik et al. 2021.[126] Plot was constructed by Cieslik et al. .*)

6.2. Magnetic Behaviour of two Novel Pentagonal-bipyramidal Erbium(III) Complexes: a High-frequency EPR Study

This chapter reports the magnetic properties of two novel pentagonal-bipyramidal (PBP) Er(III) mononucelar complexes with the general formula [Er(DAPMBH)Cl (H_2O)] $2C_2H_5OH$ (hereafter named Er(III), Cl/H_2O or **1**) and $(Et_3NH)[Er(H_2DAPS)Cl_2]$ (hereafter named Er(III), Cl/Cl or **2**). Due to the strong spin-orbit coupling (SOC) the Er(III) ion figures a well isolated $J = 15/2$ ground state which can be described by the term symbol $^6H_{15/2}$.[165] As already mentioned in chap. 5.1, the PBP coordination surrounding allows to easily substitute the ions located in the apical positions, which offers a simple route to tune the crystal field acting on the central metal ion and by this leading to a change of the magnetic properties.[85] While complex **1** is coordinated by a chloride ion and a water molecule in the apical positions, the water molecule is substituted by an additional chloride ion in complex **2**. Preliminary recorded ac susceptibility measurements (data not shown) revealed, that while complex **1** shows a field induced slow relaxation of magnetization behaviour with an energy-barrier of approx. 16 K, complex **2** figures no indication of a remanent magnetisation within an applied magnetic field. This tremendous change in magnetic relaxation behaviour gives a first indication for the significant influence of the apical ligated ions onto the crystal field which is acting on the central Er(III) ions and by this on the magnetic properties in molecular magnetic compounds figuring a PBP coordination.

To decipher the origin of the different relaxation behaviour on a quantitative level, HF EPR measurements were performed on both complexes to directly evaluate the zero field splitting gaps and g-values and thereby the magnetic anisotropy induced by the CF. In this respect it is noteworthy, that the measurement technique of HF EPR is still only rarely applied to Er(III) complexes or lanthanide compounds (excluding Gd) in general.[193–195] The reasons for this are the usually large zero field splitting gaps exceeding the capable energy range of an HF EPR setup as well as highly forbidden ground state transitions with $|\Delta m_S| > 1$.

6.2.1. Molecular Structure

In fig. 6.6 the molecular structure of the investigated Er(III) mononuclear compounds is shown. Both samples were synthesized and characterized by T.A. Bazhenova at the Institute of Problems of Chemical Physics, Chernogolovka. The Er(III) ions are surrounded by a pentagonal ligand plane consisting of two oxygen and three nitrogen ions in the first coordination sphere. For complex **1** (Er(III), Cl/H_2O) shown in fig. 6.6 (a), the apical coordination sites around the central Er(III) ion are occupied by a chloride and a water molecule while in complex **2** (Er(III), Cl/Cl) the water molecule is substituted by an additional chloride ion.
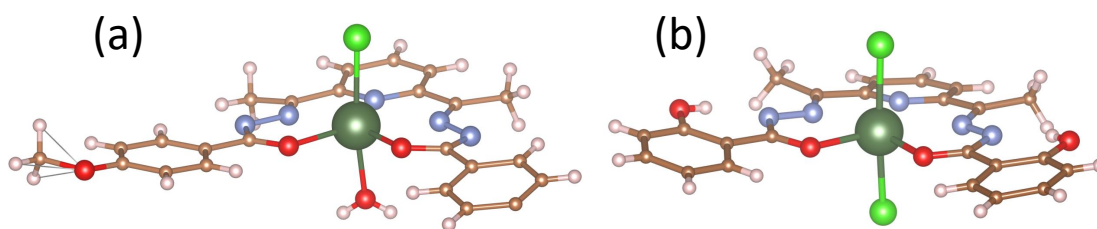
Figure 6.6.: Molecular structure of sample **1** or Er(III), Cl/H_2O (a) and **2** or Er(III), Cl/Cl (b). Dark green, Er; Red, O; light green, Cl; light blue, N; brown, C; white, H. (*The samples were structurally characterized by T.A. Bazhenova, IPCP, Chernogolovka.*)

Fig. A.20[20] shows the respective packing diagram for both compounds under investigation. In this it can be witnessed that even though there are two orientations of crystallographically equivalent Er(III)-molecules within complex **1** (see fig. A.20 (a)), the symmetry axis of the PBP ligation surrounding, which is roughly pointing along the Cl-Er(III)-O connection and perpendicular to the pentagonal plane, is almost perfectly in parallel for all the molecules. Therefore it can be assumed, that the effective crystal field (CF) anisotropy axes of each individual molecule also coincide. Opposing to this, the packing diagram for complex **2** shown in fig. A.20 (b) implies, that the Cl-Er(III)-Cl symmetry axis for the equivalent but differently oriented molecules are not in parallel but tilted against each other by an angle of $\approx 45°$. The influence of this tilting on the derived loose and fixed powder HF EPR data is discussed for sample **2** in chap. 6.2.4.

6.2.2. Er(III), Cl/H_2O: HF EPR Studies

To investigate the magnetic properties and decipher the origin of the different relaxation behaviour between complex **1** and **2**, HF EPR investigations were performed. The obtained spectra on an oriented loose powder sample of **1** are shown as solid black lines in fig. 6.7 (a) and can be followed over the whole observed frequency range between 100 and 850 GHz at $T = 2$ K (see black filled squares in fig. 6.7 (a) and 6.8 (a)). Black filled squares in fig. 6.7 (a) mark the observed resonance field positions of the sharp feature for different microwave frequencies. From a linear fit as shown as red solid line in fig. 6.7 (a), an effective g-value, $g_{\text{eff}} = 12.0(3)$, can be quantified for the corresponding transition which is responsible for the obtained spectral feature.

Fig. 6.7 (b) shows the evolution of the spectral shape with rising temperatures for a fixed microwave frequency of $f = 593.9$ GHz. As already found from the

---

[20]The supplementary material for the Er(III) monomer chap. 6.2 is shown in the Appendix chap. A.4.

frequency dependent investigations shown in fig. 6.7 (a), there is only one sharp feature distinguishable at lowest temperatures of 2 K, which is marked by the back square. A small shoulder next to this sharp feature is attributed to a minor part of the powder sample which is not perfectly aligned within the external magnetic field. With rising temperatures, the intensity of the sharp feature gradually decreases in a CURIE-like manner indicating that this transition arises from a ground state. Around $T = 8$ K, a second, much weaker feature shows up on the low field site of the main one, which is marked by a blue circle in fig. 6.7 (b). This second feature becomes more intense with further increasing temperatures, until it also decreases and completely vanishes at $T = 60$ K. From the appearance of this feature at elevated temperatures it can be concluded that the corresponding transition does not arise from the ground state but from an excited state.
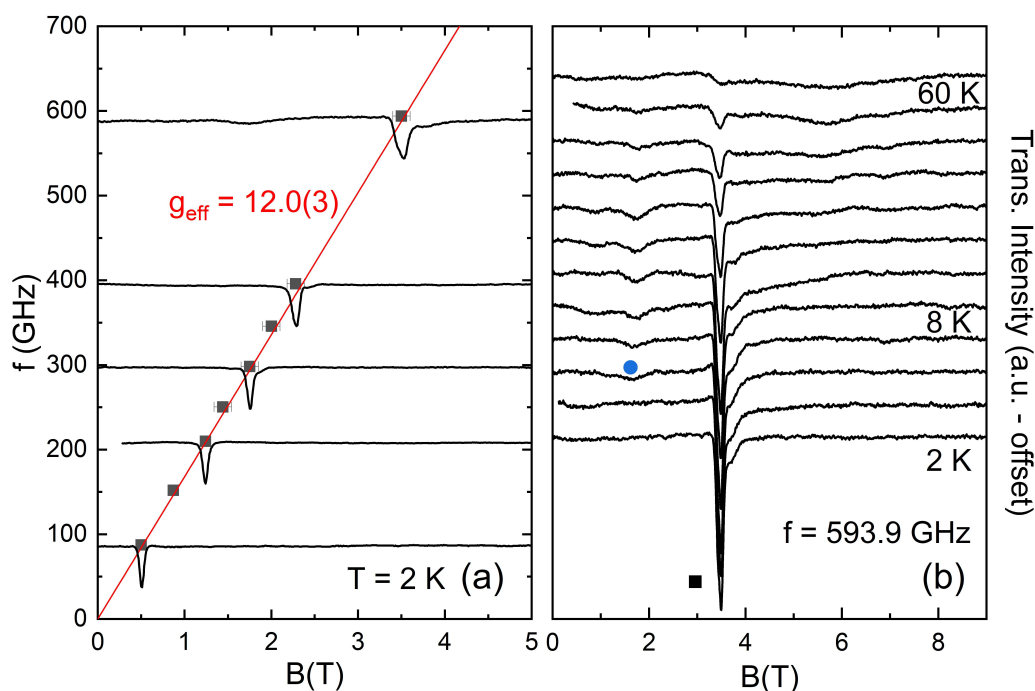

Figure 6.7.: (a) Exemplary HF EPR spectra measured at $T = 2$ K and different frequencies on an oriented loose powder of **1** are shown as black solid lines (spectra are normalized and vertically shifted by the respective measurement frequency). Black filled squares in (a) mark the resonance field positions of the respective spectral feature. The result of a linear fit is shown by the red solid line. (b) HF EPR spectra measured at a fixed frequency of $f = 593.9$ GHz at different temperatures between 2 and 60 K. The black filled square and the blue circle mark the appearing resonance features in correspondence with the resonance branches shown in fig. 6.8 (a).

Fig. 6.8 (a) shows a summary of the frequency dependent resonance field positions of the low temperature and the high temperature features as black squares and blue circles, respectively. To obtain the latter, additional frequency dependent HF EPR

spectra were measured at elevated temperatures above 4 K. From this it can be seen that the high temperature resonance branch figures a gap at zero applied field of $\Delta \approx 800$ GHz indicating that this branch arises from a transition in between the two lowest lying KRAMERs doublets (KDs). Furthermore, it figures a negative slope as it can be found for so-called inverse transitions between two KDs. The effective g-value, $g_{\text{eff}} = 9.4(5)$, of this transition can again be quantified from a linear fit to the data as shown by the solid blue line in fig. 6.8 (a).
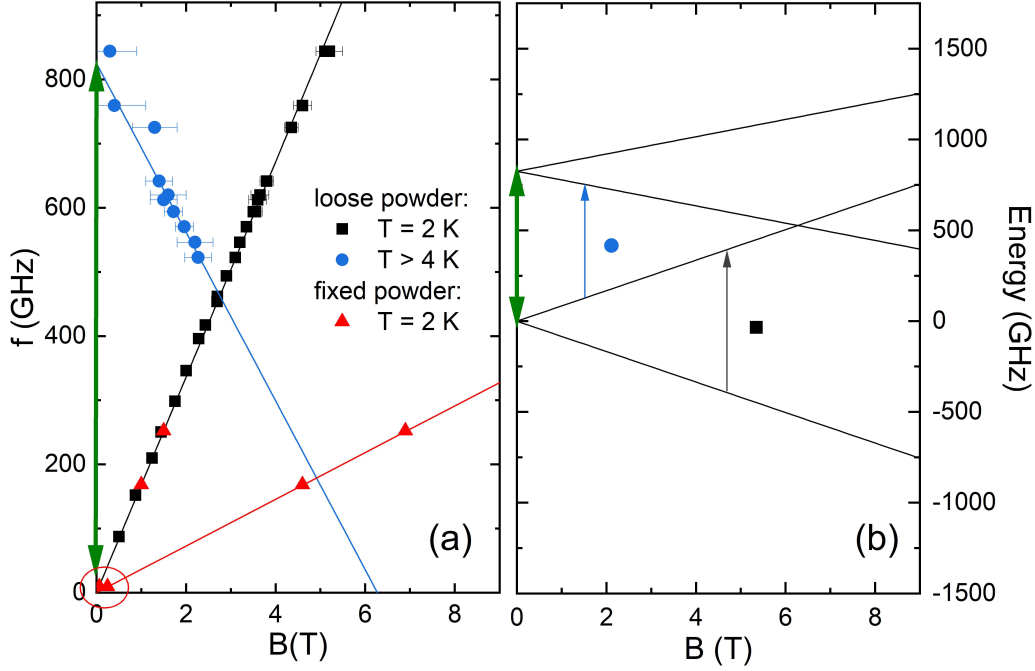

Figure 6.8.: (a) Frequency vs. magnetic resonance field diagram obtained for an oriented loose powder sample of **1** at $T = 2$ K (black filled squares) as well as elevated temperatures above 4 K (blue filled circles). Red triangles show the results from a measurement on a fixed powder sample as shown in fig. A.21. The red circle marks data points which were acquired by an X-band EPR measurement (see fig. A.21 (c)). Solid lines show linear fits to the respective resonance branches. (b) Energy-level diagram modelled for the energetically lowest two KDs based on the parameters obtained from the fit of the energy branches shown in (a). The arrows mark transitions between the energy-levels in correspondence with the observed resonance branches shown in (a). Green arrows in both plots visualize the zero field splitting gap.

The findings from the spectroscopical HF EPR investigations can be rationalised assuming a S = 1/2 pseudospin approximation for each individual KD of the ^{6}H$_{15/2}$ ground state multiplet.[18, 193] The black solid lines in fig. 6.8 (b) show the corresponding energy-level diagram. Since within the energy scale of the experiment only the lowest two KDs can be covered, the higher lying KDs are omitted in fig. 6.8 (b) for clarity. As deduced from the temperature dependent measurements shown in fig. 6.7 (b) the black branch is assumed to be a ground state transition. Besides,

the absence of a zero field splitting gap implies that the black resonance branch in fig. 6.8 (a) corresponds to a transition within the lowest KD as indicated by the black arrow in fig. 6.8 (b). The blue branch on the other hand can be assigned to a transition between the ground state and the first excited KD as shown by the blue arrow in fig. 6.8 (b). The zero field gap Δ between those two KDs can thereby be directly read off from the intersect of the blue resonance branch in fig. 6.8 (b) as it is indicated by the green arrows.

Due to the alignment of the crystallites with respect to the external magnetic field during a loose powder measurement, the obtained resonance spectra arise from just one molecular direction and thus, only the g-value component pointing along this direction can be quantified. However, to obtain the contributions from all the molecular directions and thereby measure the g-anisotropy, a fixed powder sample was prepared. The corresponding spectra obtained at $f = 525.3$ GHz and 168.4 GHz as well as in the X-Band EPR range of $f = 9.639$ GHz are shown in fig. A.21.[21] Red triangles in fig. 6.8 (a) show the corresponding resonance feature positions obtained for a fixed powder sample. As can be seen by comparing the spectra shown in fig. A.21 with the resonance positions depicted in fig. 6.8 (a), the left resonance feature can be attributed to the loose powder orientation direction and is therefore denoted as g_z-direction, while the g-value component in the other directions (g_x and g_y) seem to be much smaller. In particular, the almost equal intensity of the two features in the fixed powder spectra implies, that only two directions (g_z and g_y) contribute to the spectra while the g-value of the third direction (g_x) is so small that the corresponding resonance feature appears beyond the reachable magnetic field range of the measurement set-up, i.e., $g_z > g_y \gg g_x$. A fit assuming a S = 1/2 pseudospin approximation with a strongly anisotropic g-value as shown as red lines in fig. A.21 results in the g-value components 0.5(5), 2.6(5) and 12.0(1) for g_x, g_y and g_z, respectively. Thereby, the g_x component is fixed to the highest value which still gives a good reproduction of the measured data, while the other two components are varied.

The following chapters (chap. 6.2.3, 6.2.4 and 6.2.5) were written by L. Spillecke and are part of a research article (L. Spillecke et al.) which has been submitted to the journal Dalton Transactions.

6.2.3. Er(III), Cl/Cl: Magnetic Susceptibility

The temperature dependence of the magnetic susceptibility for complex **2** was measured under an applied dc magnetic field of 0.1 T in the temperature range of 1.8 - 300 K as shown in Fig. 6.9. The χT product at 300 K (11.67(60) cm^3 K mol^{-1}) is close to the expected value of 11.48 cm^3 K mol^{-1} for a free Er(III) ion ($^4I_{15/2}$).[165] Upon cooling down to 100 K, it gradually decreases and then rapidly drops below 100 K as it is characteristic for many lanthanide complexes. The inset in Fig. 6.9 shows the magnetisation measured at various isothermal conditions in external magnetic fields up to 7 T. In the low field region between 0 and 1 T the magnetisation

---

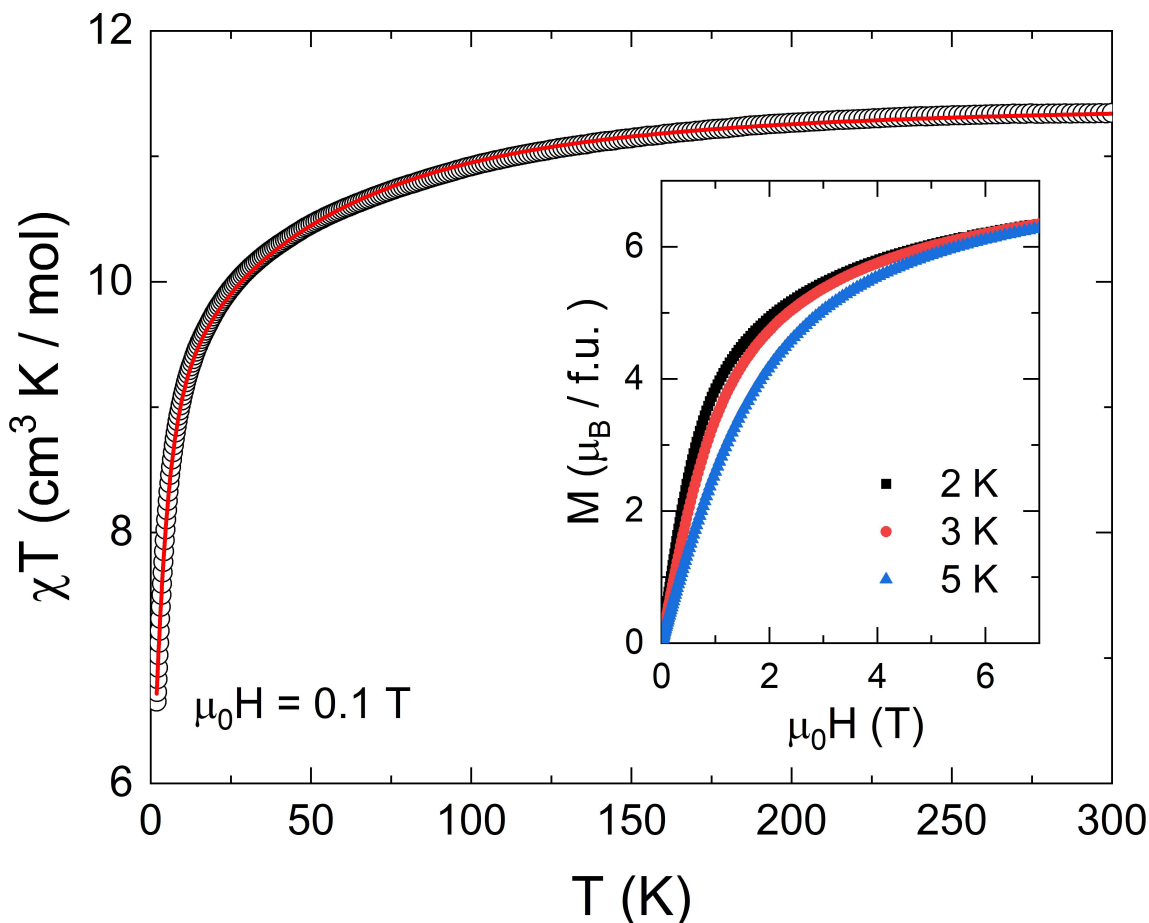[21]Details regarding the X-Band spectrometer are given in chap. 3.2.

Figure 6.9.: Experimental (black symbols) and calculated (solid red line) temperature dependence of the χT product for complex **2** measured at $\mu_0 H = 0.1$ T. Inset: Magnetic field dependence of the dc magnetisation measured at various temperatures as indicated in the plot.

figures a steep slope. With further increasing external magnetic fields the slope flattens to a nearly linear behaviour until the magnetisation reaches its maximum value of 6.36(30) μ_B/f.u. at $H\mu_0 = 7$ T and 2 K. Within the accessible field range, no saturation of magnetisation is observed.

6.2.4. Er(III), Cl/Cl: HF-EPR Studies

HF-EPR spectra of an oriented loose powder sample **2**, obtained at $T = 2$ K, display well resolved resonance signals in the whole accessible frequency regime up to 900 GHz (Fig. 6.10). The resonance features form clear branches (labelled $R1$ to $R3$) as indicated by the filled squares and solid lines in the frequency vs. magnetic field diagram. In addition to the main resonances, shoulder-like anomalies appearing at the high-field side of the features summarized by $R3$ are attributed to a small non-perfect alignment of the loose powder as proven by comparative measurements on a
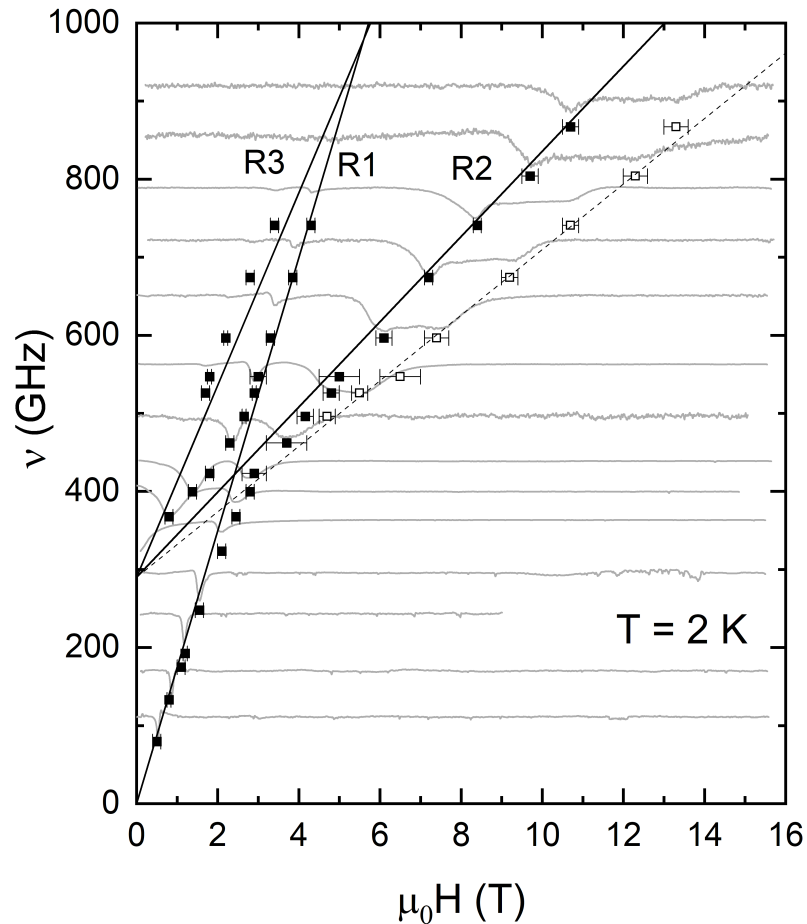
Figure 6.10.: Frequency vs. magnetic field diagram obtained at $T = 2$ K for an oriented loose powder sample of **2**. Filled squares correspond to the resonance positions of the observed features which form the branches $R1$ - $R3$ as indicated by the solid lines. Open squares mark a resonance shoulder originating from not perfectly aligned powder. The measured HF-EPR spectra are plotted as grey lines in the background and are vertically shifted in correspondence of the respective resonance positions.

fixed powder sample (see Fig. A.22). The main branches feature linear behaviour except for the crossing regime of $R1$ and $R2$ which implies an avoided crossing behavior, i.e., it indicates mixing of states.[196] While branch $R1$ appears to be gapless, the branches $R2$ and $R3$ figure a zero-field splitting (ZFS) gap Δ_1 of around 300 GHz.

The temperature dependence of the resonance spectra obtained at measurement frequencies both below and above the ZFS gap (Fig. 6.11) demonstrates that the resonance features $R1$ to $R3$ are associated with ground state transitions. At both frequencies, the features which are observable at $T = 2$ K (black squares) become weaker in intensity as the temperature rises. In addition, the spectra imply the presence of excited states (ES) which get thermally populated. This is evidenced by the appearance of several additional features indicated by blue and red symbols in Fig. 6.11. The excited features again obey a linear dependence of the resonance
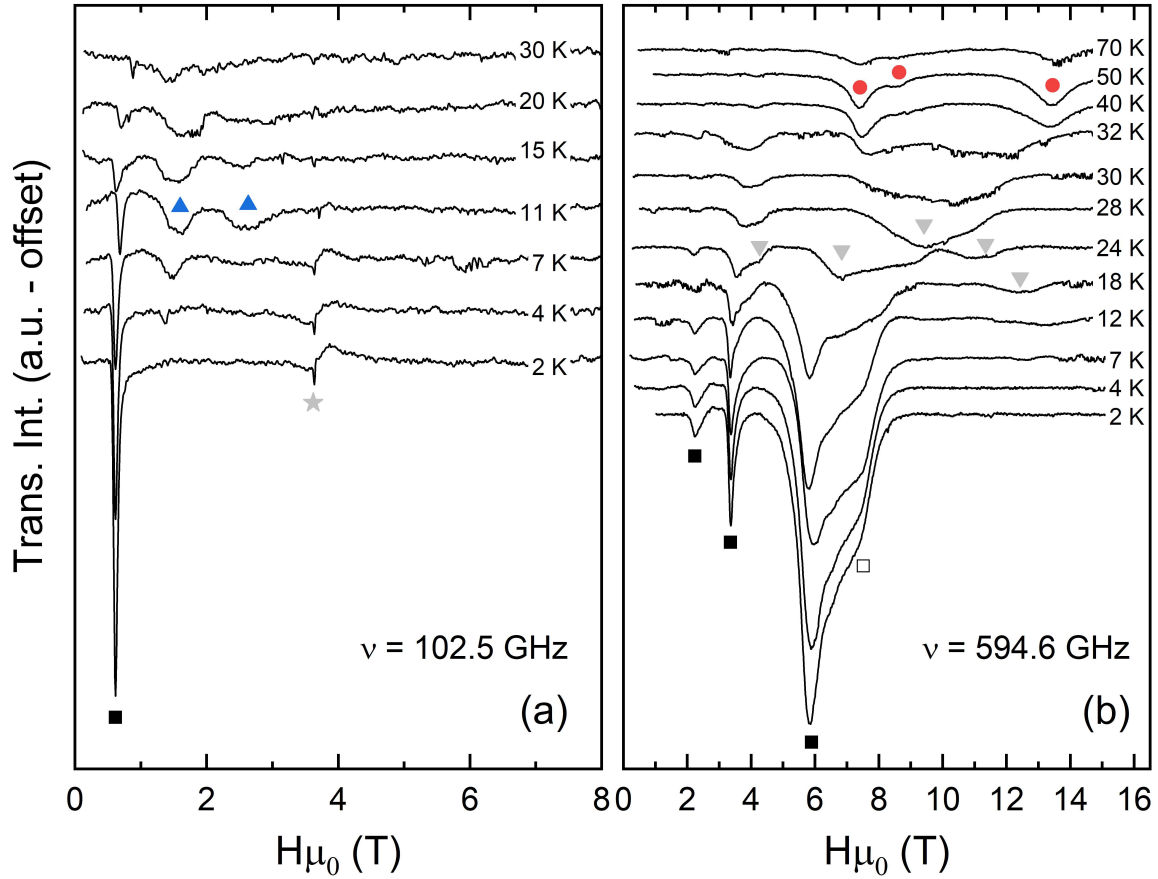
Figure 6.11.: HF-EPR spectra measured at different fixed temperatures at (a) $\nu = 102.5$ GHz and (b) 594.6 GHz for an oriented loose powder sample of **2**. The symbols mark different resonance features which appear at $T = 2$ K (black squares), $T = 10$ K (blue triangles) and $T = 50$ K (red circles) in correspondence to the branches shown in Fig. 6.12. Grey triangles in (b) mark features which could not be followed in a frequency-dependent measurement. The grey asterisk in (a) indicates the DPPH marker.

frequencies on the magnetic fields as shown in Fig. 6.12 (a) (for the measured HF-EPR spectra at $T = 10$ K and 50 K see Fig. A.23). In contrast, the spectra did not allow to study the frequency dependence of the broad resonances marked by grey triangles in Fig. 6.11 (b). These features are rather weak and only visible in a narrow temperature range so that they can be hardly discriminated. We attribute their origin to thermal population of excited doublets due to mixing of states which is not covered by the model presented below.

All obtained resonance branches measured at different temperatures on an oriented loose powder sample are summarized in Fig. 6.12 (a). The branches $R1$, $R5$ and $R4$ show no ZFS gap which allows us to assign them to transitions within the lowest (KD1), first (KD2) and second (KD3) excited KD, respectively, according to their appearance upon heating as shown in Fig. 6.11 (a). From the slope of these branches effective g-values, g_{eff}, of 12.50(40), 4.85(20) and 3.20(20) can be assigned for KD1,

KD2 and KD3, respectively. [22] The branches $R2$, $R3$ and $R6$ figure finite ZFS gaps of $\Delta_1 = 290$ GHz for $R2$ and $R3$ and $\Delta_2 = 170$ GHz for $R6$ as well as $g_{\mathrm{eff}} = 3.9(3)$, $8.8(3)$ and $4.5(2)$, respectively.

These results, i.e., the effective g-values of the ground state and excited KDs as well as the observed ZFS gaps, enable to construct a phenomenological energy-level diagram using a $S = 1/2$ pseudo-spin approximation for each KD as shown in Fig. 6.12 (b). [18, 193] The arrows in Fig. 6.12 (b) assign the observed branches to the transitions from the ground state (black) or excited states (red), respectively. While the construction of this energy-level diagram is exclusively based on the effective g-values observed for the branches $R1$, $R5$ and $R4$ as well as the ZFS gaps Δ_1 and Δ_2, the consistency of the used model is conclusively demonstrated by the observed effective g-values of the branches $R2$, $R3$ and $R6$ which perfectly agree to a transition between the observed KDs as can be seen from the comparison of the measured data with the respective simulated branches shown as solid lines in Fig. 6.12 (a).
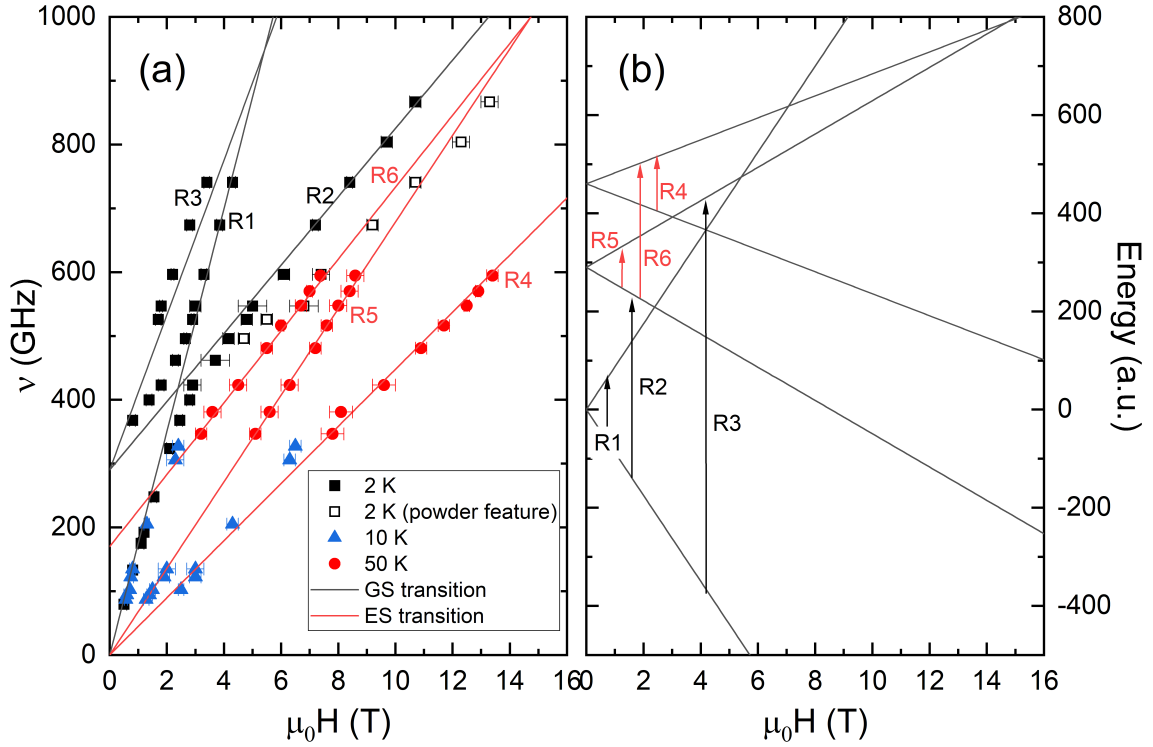

Figure 6.12.: (a) Frequency vs. magnetic field diagram with resonances obtained at different temperatures for an oriented loose powder sample of **2**. Solid black and red lines show simulated ground state (GS) and excited state (ES) transitions corresponding to the arrows in (b) which follow the same color scheme. (b) Modeled energy-level diagram of the energetically lowest three KDs. The arrows mark transitions between the energy-levels for all the observed branches, respectively.

---

[22]Note, that due to the alignment of the crystallites, only the g-value component which is oriented parallel to the external magnetic field direction can be assigned here.

To further investigate the anisotropy of the lowest lying KD we obtained HF-EPR spectra on a fixed powder sample at $T = 2$ K. The spectra shown as black solid lines in Fig. 6.13 figure a typical shape for an axial g-anisotropy. [197] Thus, two distinct resonance positions can be read off, which are marked by filled and open black squares in Fig. 6.10, respectively. From this, the components of the anisotropic effective g-value of the lowest KD are determined as $g_{eff,z} = 12.5(1)$ and $g_{eff,x/y} = 2.9(2)$.
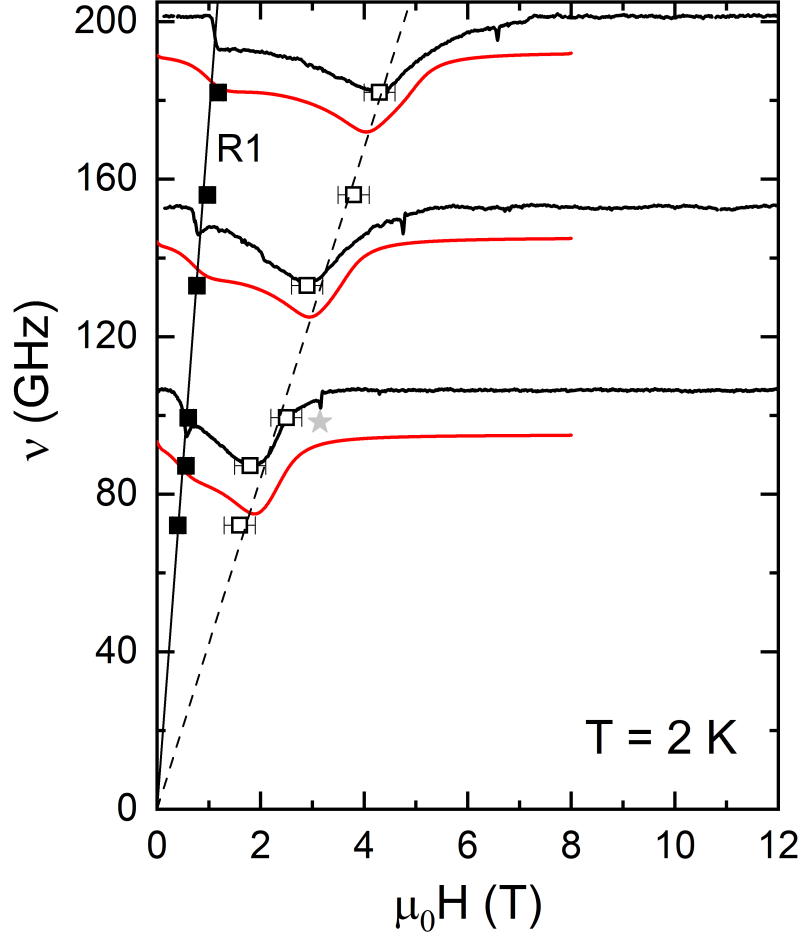

Figure 6.13.: Frequency vs. magnetic field diagram obtained at $T = 2$ K for a fixed powder sample of **2**. Filled and open squares mark positions of the obtained resonance features. Solid and dashed straight lines show a linear fit of the resonance positions. Measured and simulated HF-EPR spectra are plotted as black and red lines, respectively, and are vertically shifted for comparison with the corresponding resonance position. The grey asterisk marks the DPPH signal.

The red solid lines in Fig. 6.13 show a spectral simulation using a $S = 1/2$ pseudo-spin approximation. By comparing the measured data with this simulations we observe a small rhomboicity of the g-anisotropy which is not visible by the eye in the individual spectra due to the spectral line broadening. The best simulation parameters are determined to be $g_{eff,z} = 12.5(1)$, $g_{eff,x} = 2.6(3)$ and $g_{eff,y} = 3.2(3)$. All

experimentally obtained parameters from the investigation of the aligned loose and fixed powder are summarized in Tab. 6.1.

The obtained x,y and z component of the anisotropic g-value can be related to the effective g-value obtained on an oriented loose powder via the following projection relation:

$$g_{\text{eff}}^2 = g_{\text{eff,z}}^2 cos^2(\theta) + g_{\text{eff,xy}}^2 sin^2(\theta) \tag{6.2}$$

with θ being the angle between the $g_{\text{eff,z}}$ axis and the external magnetic field. Due to the finite angle between the two non-equivalently oriented Er(III) molecules within the unit cell it is supposed that the local anisotropy axis, which is in the simplest approximation assumed to point perpendicular to the equatorial planes along the Cl-Er(III)-Cl axis, is off the magnetic field direction by about 22°. Consequently, the g_{eff} calculated from the components of the anisotropic g-value derived from fixed powder measurements using eqn. 6.2 should be $\approx 11.6(1)$.[23] However, even under consideration of the error-bar on the measured value for g_{eff} shown in tab. 6.1, the calculated value is significantly lower implying, that the angle θ is much smaller or close to zero and thus the assumption of a perfectly perpendicular oriented anisotropy axis with respect to the pentagonal plane is may not true.

A closer investigation of the packing diagram shown in fig. A.20 (b) as well as the extract of this packing diagram shown in fig. 6.14 reveals, that the two in-equivalently oriented molecules are connected not only by a tilting of $\approx 45°$ but also by a mirror symmetry along the c-axis in the crystal frame. Thus, if the assumption of an orientation of the anisotropy axis perpendicular to the pentagonal plane is dropped, a tilting of the very same away from this axis (see β in fig. 6.14) in the molecular frame effects a tilting of the anisotropy axis in opposing directions within the crystal frame due to the mirrored arrangement of the molecules. This consideration is further visualized in fig. 6.14. Consequently, it can be speculated based on structural symmetry assumptions and the results of the HF EPR investigations, that the structural tilting of the molecules with respect to the crystal frame (α in fig. 6.14) is almost completely compensated by a tilting of the anisotropy axis within the molecular frame (β in fig. 6.14). A similarly sized tilting angle ($\approx 20°$) of the anisotropy axis away from the molecular symmetry axis was found for a Dy(III) monomer figuring a PBP surrounding, which supports the presented implications.[87]

6.2.5. Experimental Details

Dc magnetic properties were measured using a MPMS3 Magnetometer (Quantum Design) in the temperature range of $T = 1.8 - 300$ K in magnetic fields up to $B = 7$ T. The sample in the polycrystalline (powder) form was loaded into a gelatine capsule and fixed by eicosane to avoid rearrangements of the crystallites. The experimental data were corrected for the sample holder and the diamagnetic ligand contribution

---

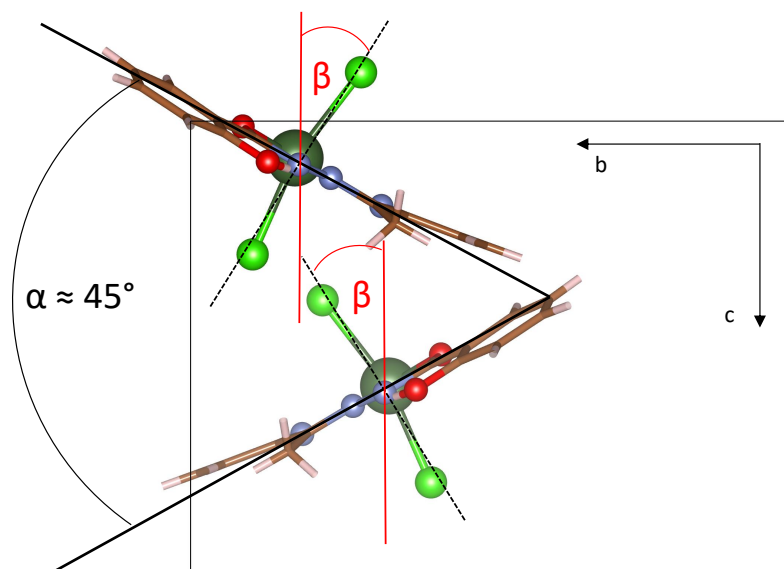[23] $g_{\text{eff,xy}} = \frac{1}{2}(g_{\text{eff,x}} + g_{\text{eff,y}})$

Figure 6.14.: Extract of two in-equivalently oriented molecules from the packing diagram shown in fig. A.20 (b). The black framed box shows the boundaries of the unit cell. Black lines visualize the orientation of the pentagonal plane of each molecule which are tilted by 45° against each other. Dashed black lines show the symmetry axis of the molecule perpendicular to the pentagonal plane. The red line shows a speculative orientation of the anisotropy axis within each molecule which is tilted away from the symmetry axis by the angle β.

as calculated using Pascal's constants. [47]

High-frequency/high-field electron paramagnetic resonance (HF-EPR) measurements were performed by usage of a millimeter vector network analyser (MVNA) by ABmm as phase sensitive microwave source and detector. [67] The measured spectra were obtained in a frequency range between 80 - 900 GHz and in external magnetic fields up to 16 T. Temperature control between 2 K and 70 K was ensured by a variable temperature insert (VTI) with He gas flow. The sample was freshly ground and placed inside a brass ring without glue or grease, i.e., as loose powder sample to allow alignment of the crystallites along the effective anisotropy axis in the external magnetic field. While the g-values of the lowest multiplets are deduced from fixed-powder studies, the obtained ZFS parameters do not dependent on the orientation of the molecules with respect to the external magnetic field. Alignment was ensured by applying the maximum field of 16 T prior to the measurements and monitoring the corresponding alignment jumps in the transmitted microwave signal. To avoid rearrangement of the crystallites, the magnetic field range was restricted to 0.2 - 16 T. To investigate the magnetic anisotropy in various orientations of the crystallites we additionally measured a powder sample which was fixed by eicosan. A commercial DPPH standard was used to approve the external magnetic field strength at the sample po-

Table 6.1.: Effective g-values and ZFS gaps obtained from analysing the HF-EPR data by means of a $S = 1/2$ pseudo-spin approximation for the lowest three KDs for complex **2**. Δ_1 and Δ_2 are the ZFS gaps separating KD1 and KD2 as well as KD2 and KD3, respectively.

	g_{eff}	$g_{\text{eff,x,y,z}}$	ZFS
KD1	12.5(40)	2.6(3), 3.2(3), 12.5(1)	$\Delta_1 = 290(10)$ GHz
KD2	4.85(20)		$\Delta_2 = 170(10)$ GHz
KD3	3.20(20)		

sition. Spectral simulations were done by using the EasySpin software package. [66]

6.2.6. Crystal Field Analysis

To relate the results obtained by HF EPR measurements on complex **2** to its electronic structure, a CF analysis of the Er(III) ion was performed. The calculations were thereby done by V. Mironov from the Institute of Problems of Chemical Physics, Chernogolovka. For these the temperature dependent dc susceptibility data as shown in fig. 6.9 is fitted in terms of the CF theory with the following hamiltonian which consists of a free ion part H_0 as well as a CF part H_{CF}:

$$\mathcal{H} = H_0 + H_{\text{CF}}. \tag{6.3}$$

While H_0 describes the atomic interactions of the $4f$-electron, H_{CF} incorporates metal-ligand interactions which are parametrized in the Wybourne scheme:

$$H_{\text{CF}} = \sum_{k,q} B_{kq} C_q^k \tag{6.4}$$

where B_{kq} are the CF parameters ($k = 2, 4, 6$; $q \leq k$) and C_q^k the spherical tensor operators.[198–200] A direct fit of the dc susceptibility data assuming the hamiltonian in eqn. 6.3 is however strongly over-parametrized due to 27 B_{kq} parameters. Therefore, the superposition CF model is used in which the B_{kq} are expressed via the geometry of the corresponding metal site in terms of intrinsic CF parameters $b_k(R_0)$ which describe the local metal-ligand interaction:

$$B_{kq} = \sum_n b_k(R_0) \left(\frac{R_0}{R_n} \right)^{t_k} C_q^k(\theta_n, \phi_n) \tag{6.5}$$

where n runs over all metal-ligand pairs, (R_n, θ_n, ϕ_n) are polar coordinates, t^k are the power-law exponents which are fixed to $t^2 = 5$, $t^4 = 8$ and $t^6 = 11$, and R_0 is the average metal-ligand distance.[201–203] The red solid line in fig. 6.9 shows the fit of the described model to the experimentally obtained dc susceptibility data. From the resulting $b_k(R_0)$ parameters the crystal field splitting energies can be calculated by the usage of eqn. 6.4 and 6.5. The results are summarized in tab. 6.2.

Table 6.2.: Calculated CF splitting energies of the ground $^4I_{15/2}$ multiplet of the Er(III) ion in **2** and the g-tensors components of the ground and first excited CF states.

CF energies (GHz)	g_x, g_y, g_z
0	2.07, 4.88, 12.37
270	2.70, 6.34, 7.75
660	2.14, 5.36, 10.03
2223	
3909	
6111	
6234	
7365	

A comparison of the g-values obtained from the CF analysis as shown in tab. 6.2 with the results from the HF EPR measurements ($g = [2.6(3), 3.2(3), 12.5(1)]$, see tab. 6.1) reveals, that the values are in fairly good agreement. Also the calculated CF splitting gap between the lowest and first excited KD is, considering the error-bars, in almost perfect consistency with the measured value of 290(10) GHz. However, while the parameters for the lowest KDs can be well predicted by the CF analysis, the splittings between the higher lying KDs start to differ from the measured ones and are thereby not well reflected by the theoretical model which was used.

6.2.7. Discussion and Conclusion

Tab. 6.3 summarizes the CF splitting parameters as well as the g-values which were experiemtnally obtained by HF and X-Band EPR measurements on **1** (Er(III), Cl/$H_2$0) and **2** (Er(III), Cl/Cl). For the evaluation of this data, a S = 1/2 pseudospin approximation for each KD was used. From the comparison of the g-anisotropy within the lowest KD of both investigated samples it can be witnessed, that complex **1** figures a slightly higher axiality, i.e., g_x, g_y(**1**) $<$ g_x, g_y(**2**) whilst g_z(**1**) $>$ g_z(**2**). Furthermore, the gap between the lowest and the first excited KD is almost three times larger in **1** compared to **2**. Both, the reduced axiality of the g-value as well as the presence of low lying excited CF states in **2** compared to **1** increases direct and thermally assisted quantum tunneling mechanisms (QTMs and TA QTMs) and consequently accelerates the magnetic relaxation. The low CF symmetry in complex **2** is further witnessed by the avoided crossing behaviour of the black resonance branches shown in fig. 6.10 which is not visible for complex **1** in fig. 6.8 (a). Thus, the change in CF anisotropy which triggers the change in relaxation behaviour of the respective compound can be directly traced back to the electronic energy-states which were measured out by precise HF EPR investigations.

Table 6.3.: Summarized results from the HF and X-band EPR investigations on loose and fixed powder samples of **1** and **2**. The values in italic show the calculated results obtained by a CF analysis performed for complex **2**.[*]

KD	g_{eff}	g_x, g_y, g_z	g_{eff}	g_x, g_y, g_z
1	12.0(3)	0.5(5), 2.5(3), 12.0(3)	12.5(4)	2.6(3), 3.2(3), 12.5(1)
				(2.07, 4.88, 12.37)
2	9.4(5)		4.85(20)	*(2.70, 6.34, 7.75)*
3			3.20(20)	*(2.14, 5.36, 10.03)*
$\Delta(\text{KD}_{1/2})$		825(10) GHz		290(10) GHz
				(294 GHz)
$\Delta(\text{KD}_{2/3})$				170(10) GHz
				(420 GHz)

[*] CF Analysis was performed by V. Mironov, IPCP, Chernogolovka.

6.3. Probing Exchange Interactions in Different $3d$-$4f$ Cu(II)$_2$Ln(III) Complexes

A synthetic approach towards the quenching of quantum tunnelling mechanisms (QTMs) in lanthanide containing molecular systems is the coupling of the highly anisotropic lanthanide ion to a $3d$ transition metal ion. This coupling can potentially lift the degeneracy of the ground state and thus, comparable to the application of an external magnetic field, quench the QTMs.[172, 173] However, even though the nature of magnetism in lanthanide ions is rather well understood, the rationalization of the exchange mechanism between $4f$ and $3d$ ions is still a challenging task. The reason for this is the complicated electronic structure of the lanthanide ions due to the unquenched orbital momentum. Therefore, semi-empirical spin models to analyse magnetic correlations analogous to the GOODENOUGH-KANAMORI-ANDERSON rules, which have been used to understand the interactions in transition metal complexes, can often not be applied.[204–206] To establish a deeper insight into the coupling mechanism between $4f$ and $3d$ ions and thereby develop strategies to tune the magnetic properties of those compounds in a more targeted way, it is crucial to obtain reliable experimental data which can be subsequently related to theoretical predictions. In this respect, HF EPR has been proven itself as proper tool to quantitatively determine the interaction strength between $4f$ and $3d$ ions.[207–210]

In the following chapter a HF EPR investigation of four novel $3d$-$4f$ coupled systems with the molecular formula [Cu$_2$Ln(HL)$_4$(NO$_3$)](NO$_3$)$_2$, where HL is a mono-deprotonated Schiff base ligand and Ln = Gd(III) ($\mathbf{4}_{\text{Gd}}$), Tb(III) ($\mathbf{5}_{\text{Tb}}$), Dy(III) ($\mathbf{6}_{\text{Dy}}$) or La(III) ($\mathbf{1}_{\text{La}}$) is shown. The samples were synthesized and crystallographically characterized by N. Ahmed at the Indian Institute of Technology (IIT), Bombay.

6.3.1. Molecular Structure

Fig. 6.15 depicts the molecular structure of a representative compound $\mathbf{4}_{\text{Gd}}$. The cationic core for all the four investigated samples $\mathbf{4}_{\text{Gd}}$, $\mathbf{5}_{\text{Tb}}$, $\mathbf{6}_{\text{Dy}}$ and $\mathbf{1}_{\text{La}}$ appears to be equivalent, i.e., the three metal centres of the hetero trinucelar complex are arranged approximately linear ($\angle$Cu(II)-Ln(III)-Cu(II) = 169° - 170°). All the Cu(II) ions are placed in a distorted octahedral coordination surrounding formed by two oxygen and two nitrogen ions in the plane as well as two addition oxygen ions in the apical positions. This octahedral surrounding induces a JAHN-TELLER distortion on the Cu(II) sites. The central Ln(III) ion is coordinated by ten oxygen ions and is thus figuring a sphenocorona coordination geometry. The Cu(II) and Ln(III) ions are coupled via an oxygen ion. Thereby, the averaged Ln(II)-O bound distance is decreasing with raising atomic number from $\mathbf{1}_{\text{La}}$ towards $\mathbf{6}_{\text{Dy}}$, due to the lanthanide contraction.[211] All the investigated complexes crystallize in the same monoclinic space group $C2/c$ and the minimal distance between two paramagnetic Ln(III) centres amounts to 12.01 Å (packing diagram not shown).
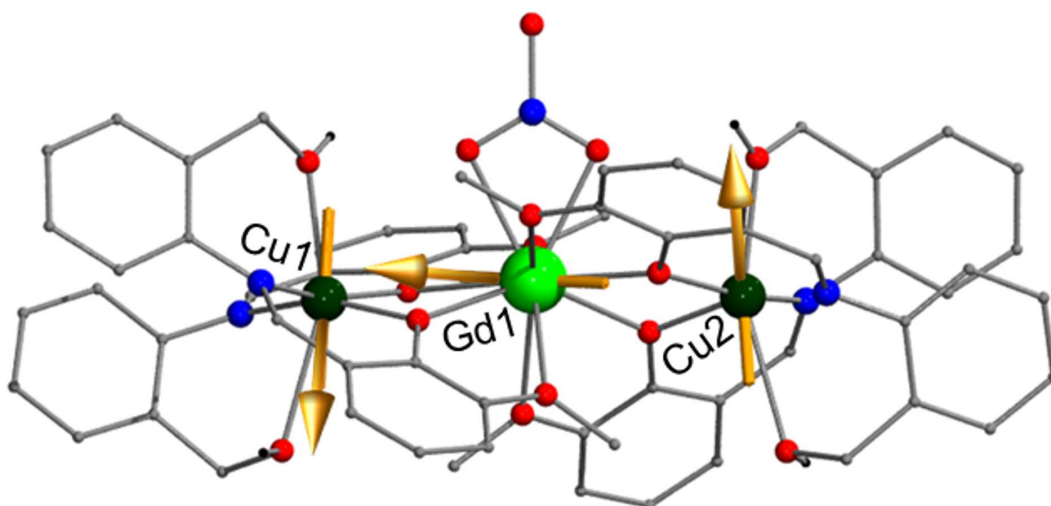
Figure 6.15.: Molecular structure of a representative compound 4_{Gd}. Colour code: red, O; blue, N; grey, C; black, H; dark green, Cu(II); light green Gd(III). Yellow arrows show the calculated spin projection of the paramagnetic Cu(II) and Gd(III) ions, respectively. (*Figure was constructed by N. Ahmed et. al, IIT Bombay.*)

The following chapters (chap. 6.3.2 and 6.3.3) were written by L. Spillecke and are part of a research article (N. Ahmed et al.) which has been submitted to the journal Inorganic Chemistry.

6.3.2. HF-EPR Studies

The high frequency/high field electron paramagnetic resonance (HF-EPR) technique is well suited for the direct determination of spin Hamiltonian (SH) parameters such as coupling constants or anisotropy parameters.[19, 20, 85, 88, 184, 212, 213] On this account we performed frequency (see Figure 6.16) and temperature-dependent (see Figure 6.17 and Figure A.25-A.27[24]) HF-EPR measurements on fixed (4_{Gd} and 1_{La}) and oriented loose (5_{Tb} and 6_{Dy}) powder samples.

For all complexes under investigation, we obtained well-resolved resonance features in the spectra measured at T = 2 K within the accessible field and frequency range as shown as grey lines in the background of Figure 6.16 (a)-(d), respectively. Distinct resonance positions are marked by different symbols corresponding to the resonance branches. Solid lines show a simulation or fit of selected resonance branches using the proper spin Hamiltonian (SH) shown in Eqn. 6.8 (for 4_{Gd}) or Eqn. 6.9 (5_{Tb} and 6_{Dy}) and the parameters discussed below for each investigated compound, separately. The HF-EPR data acquired for 1_{La} is discussed in terms of a simple S = 1/2 approach as will be justified in the following section.

---

[24] The supplementary material for the Cu(II)$_2$Ln(III) chap. 6.3 is shown in the Appendix chap. A.5.

Figure 6.16 (a) depicts the frequency vs. resonance field diagram for a fixed powder sample of $\mathbf{4}_{Gd}$ at T = 2 K. The measured spectra, shown as grey lines in Figure 6.16 (a), clearly display a powder-like spectral shape featuring axial anisotropy as it is obvious from the large spectral weight in the high field region of the spectra while a small spectral weight is observed in the low field region.
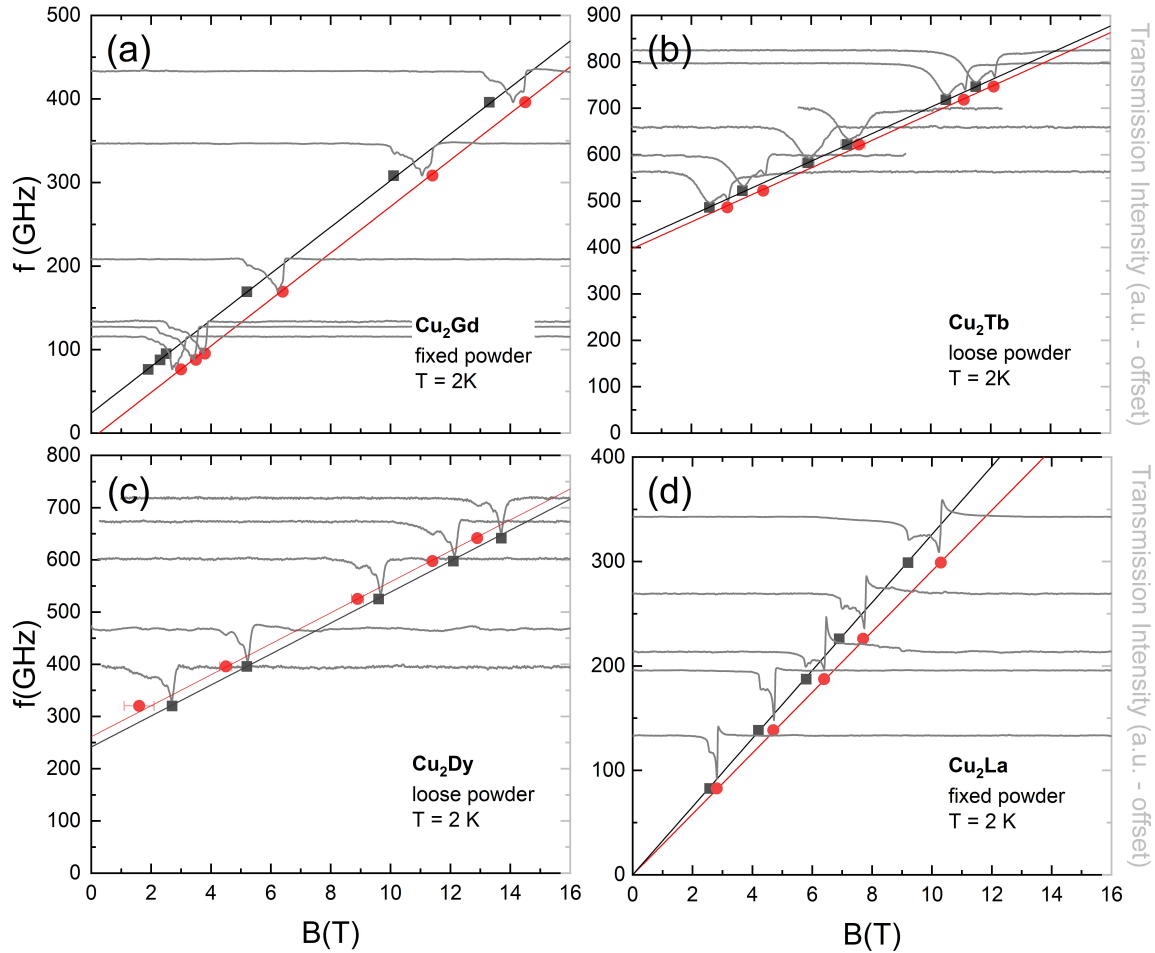

Figure 6.16.: Frequency vs. resonance field diagram for (a) $\mathbf{4}_{Gd}$, (b) $\mathbf{5}_{Tb}$, (c) $\mathbf{6}_{Dy}$ and (d) $\mathbf{1}_{La}$, at T = 2 K. The magnetic resonance field positions for selected features are marked by different symbols. Solid lines show a simulation or a fit of the field dependence of the selected features using the SH shown in Eqn. 6.8 ($\mathbf{4}_{Gd}$), Eqn. 6.9 ($\mathbf{5}_{Tb}$ and $\mathbf{6}_{Dy}$) or an S = 1/2 approach ($\mathbf{1}_{La}$) and the parameters shown in Table 6.4 or the text. Grey lines display the measured HF-EPR spectra which are vertically shifted for better comparison with the corresponding resonance positions.

Black squares and red dots in Figure 6.16 (a) mark the low field and high field edges of the corresponding resonance feature, respectively. The edges of the features were used as a reference since the spectra comprise a variety of overlapping transitions (see Figure A.24) due to the sample configuration as a fixed powder. Straight lines in Figure 6.16 (a) show a linear fit to the marked edges. The slope of these fits corresponds to the effective g-value of the respective transitions which amounts to

$g_{\text{eff}} = 2.15(2)$. Note, that the g-value for both selected features is the same, i.e. no broadening of the spectra is observed upon increasing the frequencies which implies at the first glance a vanishing g-anisotropy on the Cu sites within the resolution of our experiment. However, even though it cannot be resolved by our magnetic field dependent measurements, a g-value significantly higher than 2.00 implies that a g-anisotropy on the Cu sites is likely to be present. Indeed, the measurements on $\mathbf{1}_{\text{La}}$ (see the further text) reveal a significant g-anisotropy on the Cu sites when the central magnetic Ln ions is replaced by a diamagnetic one. Thus, it can be speculated that the exchange interaction between the Gd and the Cu moments is responsible for the non-observable g-anisotropy in the EPR data for $\mathbf{4}_{\text{Gd}}$. Besides the evaluation of the slope of the resonance branches, a zero-field splitting (ZFS) gap of 24 GHz (0.8 cm^{-1}) and -7 GHz (-0.23 cm^{-1}) can be obtained for the intercept of the black and red lines, respectively. Since the S = 1/2 spin state of the Cu ions excludes a ZFS, we attribute these gaps to a small but finite anisotropy acting on the Gd sites.

Due to the absence of orbital contribution to the ground state of the free Gd ion, there is no anisotropy gap or ZFS in the case of strict spherical symmetry. However, as it is shown in several examples in literature,[67, 214] the dipolar interaction to neighbouring ions, e.g. the Cu ions in the present case, can induce an anisotropy on the Gd-site. To rationalize this influence, the predicted ZFS gap Δ_{dip} induced by the dipolar interactions is estimated.

$$\Delta_{\text{dip}} = \mathbf{S}_{\text{Cu1}} \overset{\leftrightarrow}{D}_{\text{dip}} \mathbf{S}_{\text{Gd}} + \mathbf{S}_{\text{Cu2}} \overset{\leftrightarrow}{D}_{\text{dip}} \mathbf{S}_{\text{Gd}} \tag{6.6}$$

The dipolar anisotropy tensor $\overset{\leftrightarrow}{D}_{\text{dip}}$ can be written in the following form: [215]

$$\overset{\leftrightarrow}{D}_{\text{dip}} = \frac{\mu_{\text{B}}^2}{r^3} \begin{pmatrix} g_{Cu}^x g_{Gd}^x (1 - 3\sin^2\eta\sin^2\xi) & -3g_{Gd}^x g_{Cu}^y \sin^2\xi\sin\eta\cos\eta & -3g_{Gd}^x g_{Cu}^y \sin\xi\sin\eta\cos\xi \\ -3g_{Cu}^x g_{Gd}^y \sin^2\xi\sin\eta\cos\eta & g_{Cu}^y g_{Gd}^y (1 - 3\cos^2\eta\sin^2\xi) & -3g_{Gd}^x g_{Cu}^y \sin\xi\cos\eta\cos\xi \\ -3g_{Cu}^x g_{Gd}^y \sin\xi\sin\eta\cos\xi & -3g_{Cu}^x g_{Gd}^y \sin\xi\cos\eta\cos\xi & g_{Cu}^z g_{Gd}^z (1 - 3\cos^2\xi) \end{pmatrix} \tag{6.7}$$

where r denotes the distance between the respective Cu and Gd ion and ξ or η define the angle which is formed by the ionic z- or y-axis and the distant vector $\mathbf{r}$. For the calculations it is assumed, that both Cu ions figure the same g-value g_{Cu} and the anisotropy of g_{Cu} is fixed to the one derived from the HF EPR measurements on the $\mathbf{1}_{\text{La}}$ sample, for which it is assumed, that the Cu-Ln interaction is negligible and the pure single ion properties of the Cu ions are shown. g_{Gd} is fixed to the isotropic value of 2.

Figure 6.15 shows the respective calculated spin projections of the Cu and Gd ion. In a good approximation, it can be assumed that the spin projection of the Gd ion and the Cu ions is perpendicular to each other and thus $\xi = \eta = 0$. Consequently, only the diagonal elements in Eqn. 6.7 remain which can be quantified to $D_{\text{dip}}^{xx} = D_{\text{dip}}^{yy} = 0.051$ cm^{-1} and $D_{\text{dip}}^{zz} = $ -0.113 cm^{-1}. Considering Eqn. 6.6 these values lead to an absolute value for the ZFS gap of $\Delta_{\text{dip}}^{xx} = \Delta_{\text{dip}}^{yy} = 0.18$ cm^{-1} and $\Delta_{\text{dip}}^{zz} = 0.40$ cm^{-1}, which is in the same order as the experimentally observed ZFS gaps. Hence it can be concluded, that the main origin of the observed finite single-ion anisotropy on the Gd site is

induced by dipolar interactions with the Cu ions. However, it has to be mentioned, that due to the error-bars and several approximations, it cannot be excluded, that there are additional but much smaller contributions to the observed anisotropy due to anisotropic exchange interactions between Gd and Cu ions or distortions of the coordination environment.[216–219] With the relations $D = 3/2$ D_{dip}^{zz} = -0.170 cm^{-1} and E $= (D_{\text{dip}}^{xx}$ - $D_{\text{dip}}^{yy})/2 = 0$ the entries in the tensor matrix can be translated to the commonly used phenomenological axial (D) and transversal (E) anisotropy parameters.[18]

Figure 6.17 (a) shows the temperature dependence between T = 2 K and 60 K of the resonance feature in $\mathbf{4}_{\text{Gd}}$ at the frequency of 169.3 GHz. At lowest temperatures, we observe a powder-like spectrum with a sharp peak at B = 6.2 T and a shoulder ending at B = 5 T. Upon increasing the temperature up to 6 K, the sharp peak starts to broaden and shifts to lower fields. At more elevated temperatures, it sharpens again while staying at a constant field position of B = 6 T. The shoulder on the low field side shifts to higher fields upon heating.

$$
\begin{aligned}
\mathbf{H} =& \mu_{\text{B}}\mathbf{B}\overleftrightarrow{g}_{Gd}\mathbf{S}_{Gd} + \sum_{i}^{2} \mu_{\text{B}}\mathbf{B}\overleftrightarrow{g}_{Cu,i}\mathbf{S}_{Cu,i} + D_{Gd}\left[(S_{Gd}^{z})^{2} - \frac{S_{Gd}^{2}}{3}\right] \\
& - 2J_{Cu-Gd}\left(\mathbf{S}_{Cu,1} \cdot \mathbf{S}_{Gd} + \mathbf{S}_{Cu,2} \cdot \mathbf{S}_{Gd}\right) \\
& - 2J_{Cu-Cu}\mathbf{S}_{Cu,1} \cdot \mathbf{S}_{Cu,2}
\end{aligned}
\tag{6.8}
$$

The temperature dependence of the spectra can be simulated using the SH shown in Eqn. 6.8 where the first and second terms describe the Zeeman effect on the Cu and Gd spins induced by the external magnetic field $\mathbf{B}$ and the fourth and fifth term reflects the magnetic interaction between the Cu and Gd spin and the two Cu spins, repsectively. The third term describes a phenomenological anisotropy term acting on the Gd ion defined by the axial anisotropy parameter D_{Gd}.

Figure 6.8 (b) shows the best simulation results of the temperature dependent data displayed in Figure 6.8 (a). The parameters and their error-bars, which were obtained by finding the variation interval in which the simulation gives still a reasonable reproduction, are summarised in Table 6.4. The coupling between the Cu spins described by J_{Cu-Cu} in the last term of Eqn. 6.8 is fixed to the value obtained by DFT calculations[25] since an additional coupling parameter would lead to over parametrization. However it is noteworthy, that the neglection of this coupling, i.e. $J_{Cu-Cu} = 0$, does not affect the resulting parameters within error-bars. The best simulation value for the anisotropy parameter D_{Gd} is, within the error-bars, in perfect agreement with the one obtained from the calculation of the dipolar interaction between the spins.

The resonance features in the powder spectra exhibit a temperature-dependent shift. This shift can be illustrated and explained by the energy level diagram shown in Figure A.24. For $D_{Gd}^{z} \parallel \mathbf{B}$ (see Figure A.24 (a)), where D_{Gd}^{z} denotes the principal axis of the anisotropy tensor in the eigenframe of the Gd ion, the spectral weight is

---

[25]DFT calculations were preformed by N. Ahmed et al. at the IIT Bombay. The calculation details are omitted within this work and only the crucial results are shown in Table 6.4.

expected to shift to higher fields upon heating. This simulation corresponds to the low field edge of the measured spectra which figures the same temperature dependent behaviour. In contrast, the opposite is observed for $D_{Gd}^z \perp \mathbf{B}$(see Figure A.24 (b)). The assignment of the low field and high field edge to a certain orientation direction of the crystallites is thereby deduced from the distribution of the spectral weight, i.e., a higher spectral weight marks the transversal direction while a lower spectral weight marks the axial direction of the overall anisotropy tensor.

For $\mathbf{5}_{\text{Tb}}$ and $\mathbf{6}_{\text{Dy}}$ an oriented loose powder is measured (see the experimental section for details). Since the anisotropy of the Ln ions dominates over the one of the Cu ions, it is assumed that the crystallites are most likely oriented with the main anisotropy direction $\mathbf{d}_{Ln}$ in the local frame of the respective Ln ion along the external magnetic field $\mathbf{B}$. Consequently, the measured spectra consist of contributions arising exclusively from this orientation direction and thereby only an effective g-value g_{eff} can be measured. In the frequency vs. magnetic field diagram for $\mathbf{5}_{\text{Tb}}$ and $\mathbf{6}_{\text{Dy}}$ two distinct features can be followed over the whole frequency range under study (see Figures 6.16 (b) and 6.16 (c), respectively). At T = 2 K, the most pronounced feature, marked with black symbols, is attributed to the ground state transition. This assignment is further confirmed by the temperature-dependent measurements (see Figures A.25 (a) and Figure A.26 (a)) which show that the intensity of the selected features is highest at T = 2 K. Figure A.25 (b) and Figure A.26 (b) show the temperature-dependence of the integrated area over the whole spectra. For both compounds ($\mathbf{5}_{\text{Tb}}$ and $\mathbf{6}_{\text{Dy}}$), activated behavior can be observed with a peak around T = 10 K. This indicates the presence of energetically higher states, which are separated from the ground state by more than 10 K and can hence be neglected for discussing the ground state transitions at T = 2 K.

The frequency dependence of the selected features, assigned as black symbols, for both samples shows a linear behavior figuring an effective g-value of $g_{\text{eff}} = 2.08$ and ZFS of 405 GHz for $\mathbf{5}_{\text{Tb}}$ while $g_{\text{eff}} = 2.11$ and ZFS = 235 GHz for $\mathbf{6}_{\text{Dy}}$ is observed. Due to the unquenched orbital contribution to the anisotropy of the Ln ions, the separation between the ground and first excited state is much larger than the energy scales of our experiment so that the Ln moments can be treated as Ising spins.[92, 207, 220, 221] Thus, the effective SH considering the Ln ions as Ising spins can be written as:

$$
\begin{aligned}
\mathbf{H} = & \mu_{\text{B}} g_{Ln} B^z J_{Ln}^z + \sum_i^2 \mu_{\text{B}} \mathbf{B} \overleftrightarrow{g}_{Cu,i} \mathbf{S}_{Cu,i} \\
& - 2 J_{Cu-Ln} \left(S_{Cu1}^z \cdot J_{Ln}^z + S_{Cu2}^z \cdot J_{Ln}^z \right) - 2 J_{Cu-Cu} \mathbf{S}_{Cu1} \cdot \mathbf{S}_{Cu2}
\end{aligned}
\tag{6.9}
$$

As shown in Figure 6.16, the experimental data are well described by the SH in Eqn. 6.9. g_{Ln} is thereby fixed to the respective Lande g-value of $g_{\text{Lande}} = 3/2$ for Tb(III) or 4/3 for Dy(III).[165] In particular, the experimental data do not imply the presence of forbidden transitions with $\Delta_{m_S} > \pm 1$ which corroborates usage of Eqn. 6.9, i.e., approximating J_{Ln} by an Ising spin and neglecting further anisotropy. Hence, the coupling between Ln and Cu moments (J_{Cu-Ln}) can be directly read-off

from the ZFS gap of the branches corresponding to the most pronounced feature at low temperatures. The simulation results for 5_{Tb} and 6_{Dy} using the SH in Eqn. 6.9 are shown as solid black lines in Figure 6.16 (b) and 6.16 (c), respectively. The J_{Ln-Cu} values amount to 1.16(5) cm^{-1} and 0.58(5) cm^{-1} for 5_{Tb} and 6_{Dy}, respectively. All parameters used for these simulations are listed in Table 6.4.

Besides the main feature, the obtained spectra for 5_{Tb} and 6_{Dy} figure a fine structure in the form of a second feature which can be followed over the whole measured frequency range, as indicated by the red dots in Figure 6.16 (b) and 6.16 (c). The appearance of these additional features with a ZFS gap only marginal different from the main branch can be explained if a finite coupling between the Cu ions is considered which gives rise to a triplet state which is coupled to the Ln ion. Including a $|J_{Cu-Cu}| = 0.33(5)$ cm^{-1} and 0.35(5) cm^{-1} for 5_{Tb} and 6_{Dy}, respectively, leads to a simulation which perfectly fits the measured data as shown by the red solid lines in Figure 6.16 (b) and 6.16 (c). The obtained values are further in the same range as the J_{Cu-Cu}-values obtained for 4_{Gd} and 1_{La} from DFT calculations or PHI fit[26], respectively. However, since the relative intensities of the different features are hard to evaluate due to the fact, that both, the orientation of the molecules within the field as well as other anisotropy effects can have an impact on the very same, a definition of the sign of J_{Cu-Cu} exclusively based on the HF EPR data would be an over-interpretation of our measurement results. Further we would like to mention, that the explanation of the additional fine structure in the measured spectra by a finite coupling between the Cu ions is, even if well justified by the predictions from dc susceptibility data and DFT calculations, a rather speculative assumption, since there are other mechanisms as e.g. a mixed ground state of the Ln ion [210] or minimal differences in coupling strength to the two Cu ions, which in principle could also promote additional features.

Investigating 1_{La} enables to determine the g-anisotropy of the Cu spins in the absence of an Ln moment. The obtained spectra, depicted as grey lines in Figure 6.16 (d), show a typical powder like spectral shape, again figuring an axial anisotropy.[197, 222] Such anisotropic powder spectra can be described by a S = 1/2 approach with an anisotropic g-value. The axial symmetry suggests that only the axial ($g_{\parallel}$) and transversal ($g_{\perp}$) contributions of the anisotropic g-tensor needs to be considered. The features corresponding to $g_{\parallel}$ and $g_{\perp}$ are marked by red dots and black squares in Figure 6.16 (d), respectively. From linear fits to the resonance field positions we obtain $g_{\parallel} = 2.31(2)$ and $g_{\perp} = 2.09(2)$.

Note, that there is no ZFS for either branch as expected for a spin S = 1/2 system. The temperature dependence of dc magnetization of 1_{La} implies the presence of a small but finite antiferromagnetic (afm) coupling between the Cu spins.[27] However, as demonstrated by the simulation (Figure A.27) of the energy-level diagram with the expected transitions shown in Figure A.28, the excitation gap induced by this coupling

---

[26]DC susceptibility measurements were performed and evaluated by N. Ahmed et al., IIT Bombay. The susceptibility data were fitted by the program PHI, however, within this work only the resulting coupling parameter for 1_{La} is given in Table 6.4.
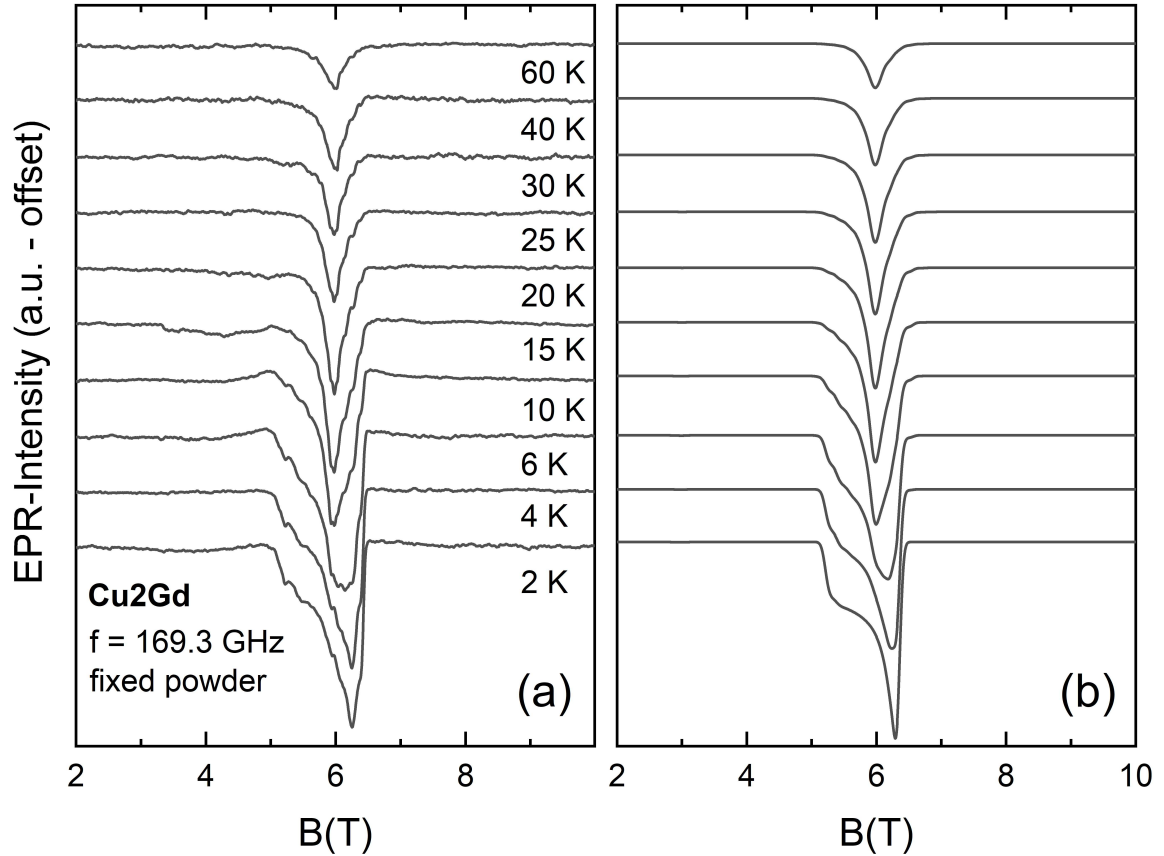
[27]Data not shown within this work.

Figure 6.17.: (a) HF-EPR spectra obtained for a fixed powder sample of 4_{Gd} at the frequency of f = 169.3 GHz for different temperatures as indicated in the plot. (b) Simulation of the measured spectra shown in (a) using the SH in Eqn. 6.8 with the parameters shown in Table 6.4.

cannot be directly observed by HF-EPR measurements since there is no transition probability between the gapped energy levels. Also due to the weak coupling, ≈ 1.3 K, the contribution of a singlet ground state is ignored in our analysis of the HF-EPR data.

6.3.3. Experimental Details

All high-frequency/high-field electron paramagnetic resonance (HF-EPR) measurements were performed using a millimeter-wave vector network analyzer (MVNA) from ABmm as a phase-sensitive microwave source and detector and a superconducting magnet from Oxford instruments.[67] Measurements were performed between 80 GHz and 900 GHz, and in magnetic fields up to 16 T. Temperature control between T = 2 K and 70 K was ensured by a variable temperature insert (VTI) with a ^{4}He gas flow cryostat. To enhance signal intensities, the 5_{Tb} and 6_{Dy} samples were measured as loose powders. They were placed inside a brass ring in a home-made transmission-type EPR probe with no extra glue or grease so that the crystallites

Table 6.4.: SH parameters obtained by simulation of the temperature dependence of the measured HF-EPR spectra (4_{Gd} see Figure 6.17) and of the resonance branches in the frequency vs. magnetic field diagram using the SH shown in Eqn. 6.8 (4_{Gd}) and Eqn. 6.9 (5_{Tb} and 6_{Dy}) as well as a spin S = 1/2 approach for 1_{La}.

	g_{eff}	J_{Ln-Cu}	D (cm^{-1})	J_{Cu-Cu}
4_{Gd} fixed	2.15(2) (2.18***)	1.5(10) (1.70***)	-0.15(10)	-0.25*
5_{Tb} loose	2.08(2)	1.16(5)		±0.33(5)
6_{Dy} loose	2.11(2)	0.58(5)		±0.35(5)
1_{La} loose	$g_{\parallel}$c= 2.31(2); $g_{\perp}$ = 2.09(2)			-0.88**

* Value is taken from DFT calculations on 4_{Gd}.
** Obtained by PHI fit of the dc magnetization data on 1_{La}.
*** Obtained by PHI fit of the dc magnetization data on 4_{Gd}.

were free to align with respect to the external magnetic field direction. To ensure alignment of the loose powder, the maximum magnetic field of B = 16 T was applied prior to the measurements and the alignment was monitored by observation of corresponding orientation jumps in the transmitted microwave signal. Meanwhile, 4_{Gd} and 1_{La} samples were ground and then fixed with eicosane to avoid partial orientation of the powder. Analysis and simulations of the HF-EPR data were done using the EasySpin software package.[66]

6.3.4. Conclusion

Within this chapter, four different representatives of a nearly linear trinucelar series of Cu(II)-Ln(III)-Cu(II) compounds were investigated by the means of HF-EPR. The focus of this investigation was thereby on the measurement of the Cu(II)-Ln(III) interaction strength which was quantified to 1.5(10) cm^{-1}, 1.18(10) cm^{-1} and 0.56(10) cm^{-1} in 4_{Gd}, 5_{Tb} and 6_{Dy}, respectively. The observed decrease in the ferromagnetic coupling strength with increasing atomic number is in coherence with other comparable sample sets reported in literature.[208, 210, 223] To rationalize this observation for Ln$_n$Cu$_m$ complexes, Kahn proposed the following model:[224] As observed by experiments, the exchange coupling strength between the Cu(II) and the Ln(III) ions monotonically decreases with increasing atomic number and decreasing number of electronic spins from 7 to 4 in the order from Gd(III) to Dy(III), respectively. Kahn proposed, that the more unpaired $4f$ electrons are given, the higher the possible energy reduction which can be gained by the exchange coupling according to HUND's rules and thus, the stronger the ferromagnetic exchange coupling. In particular, this proposed model implies, that even though the Ln ion contraction is observed as a reduction of the Ln-O bond distance in the crystallographic analysis from 4_{Gd} to 6_{Dy}, it most likely plays only a minor role for the Cu-Ln interaction strength in general.[210] The latter is further supported by the observed derivations between calculated values for the exchange interaction strength obtained by the variation of the Ln-O bond distance in the respective structure and experimentally derived parameters as reported in the

literature.[223]

Beyond the detailed investigation of the Cu(II)-Ln(III) coupling strength, an axial g-anisotropy of the Cu(II) moments was observed as a result of measurements on the $\mathbf{1}_{La}$ sample in which the paramagnetic Ln species is replaced by a diamagnetic La(III) ion. This anisotropy is in accordance with the structurally witnessed JAHN-TELLER distortion on the Cu sites. The anisotropic g-value obtained for the Cu(II) ions in $\mathbf{1}_{La}$, which is expected to be independent from additional anisotropy contributions induced by coupling mechanisms to the central Ln ion, was used to rationalize the non-vanishing anisotropy on the Gd site in $\mathbf{4}_{Gd}$ by the introduction of a finite dipolar interaction between the Gd(III) ion and the Cu(II) ions.

7. Additional Materials

7.1. HF EPR Investigations on Co_2Lu_2-MeOH

As it was described in the previous chapter, the coupling of $4f$-Lanthanide ions to a transition metal d element proved to be a promising approach to suppress so-called "under-barrier"[225] tunnelling processes. An example of such coupled complexes which was heavily investigated throughout the last years is given by the group of so-called "butterfly"-compounds [186, 226–230]. Even though, the exchange coupling strength between the ions in the metal cluster tremendously controls the dynamic relaxation behaviour in such butterfly compounds, the direct evaluation of a molecular cluster with four coupled ions figures often too much free parameters which depend on each other and are thereby not well defined. [186, 226–228] Therefore it is a common attempt to synthesize analogous samples which have the same molecular and crystalline structure, but a part of the paramagnetic ions are replaced by equally sized diamagnetic ones. By this approach a reduced cluster can be investigated independently from the influence of the replaced ions. The obtained parameters can subsequently be fixed in the investigation of the whole cluster which significantly reduces the amount of free parameters. Within this chapter, an analogue to the Co_2Dy_2-MeOH compound reported in ref. [186] is discussed, where the paramagnetic Dy(III)-ions are replaced by diamagnetic Lu(III)-ions.

7.1.1. DC Magnetisation and HF-EPR Studies

In fig. 7.1 the molecular structure of the investigated sample with the general formula $[Co_2Lu_2(L)_4 (NO_3)_2(MeOH)_2]\cdot 2CH_2Cl_2$ (hereafter called Co_2Lu_4-MeOH) is shown, where L denotes a SCHIFF-base ligand as it is closer described in [228]. The sample was synthesised and structurally characterized by Y. Peng in the group of A. Powell at the Karlsruhe Institute of Technology.

Fig. 7.2 depicts the temperature dependent dc magnetic susceptibility which was measured on a fixed powder Co_2Lu_2-MeOH sample in a temperature range between 1.8 and 300 K under application of an external magnetic field of 0.1 T. The constant χT-product of 6.53 erg K/mole G^2 between 50 and 300 K corresponds to two uncoupled Co(II) S = 3/2 ions with an respective averaged g-value of $g = 2.6$.[26] This value is in line with g-values reported for other Co(II) high-spin compounds.[20, 231–233] With decreasing temperatures below 50 K, the χT-product increases until it reaches a maximum of 8.45 erg K/mole G^2 at T = 5 K. The appearance of this maximum is
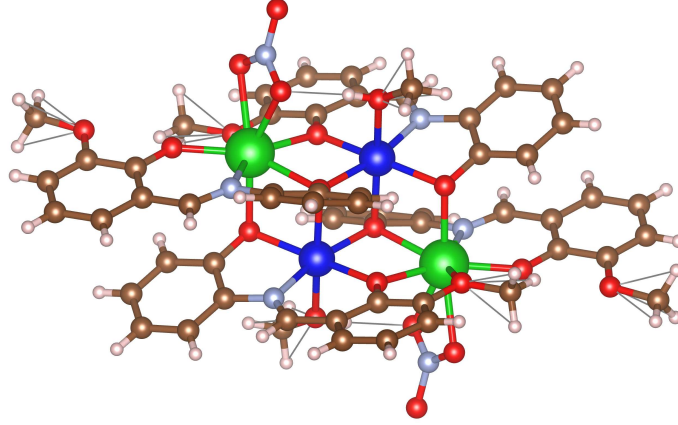
Figure 7.1.: Molecular structure of the investigated Co_2Lu_2-MeOH compound. Co(II), blue; Lu(III), green; O, red; N, light blue; C, brown; H, white. (*Sample was structurally characterized by Y. Peng, KIT.*)

a direct evidence for the presence of a ferromagnetic dimer-like interaction between the two Co(II)-ions.[234, 235]

The external magnetic field dependence of the magnetization measured at different temperatures is shown as inset in fig. 7.2. For the lowest temperature of T = 1.8 K the magnetization tends to increase quickly in the low magnetic field region until the slope decreases at fields around 2 T and follows a linear behavior. At the maximum field of 7 T the magnetic moment figures a value of 5 μ_B/f.u. which is below the expected value of 7.8 μ_B/f.u. assuming two Co(II)-ions and the averaged g-value obtained from the room-temperature χT-product as described above. Furthermore, no saturation of magnetization within the accessible field range can be witnessed. Both, the diminished maximal moment as well as the absence of a saturation behavior indicates that either, a strong single-ion anisotropy on each Co(II)-ion site, or a significant exchange interaction between the two Co(II) ions is present.[61] From the qualitative analysis of the χT(T) data discussed above it is, however, expected, that the exchange interaction between the Co(II) ions is ferromagnetic in nature and should thereby lead to a steep increase of the magnetisation and a saturation behaviour even at relatively small external fields. Thus, it is concluded that the diminished magnetisation originates from a strong axial single-ion anisotropy against which the randomly oriented Co(II) spins are fighting if an external magnetic field is applied.

To determine the relevant parameters which define the coupling strength and magnetic anisotropy of the compound under investigation, the χT-data can be fitted assuming the following SH, where D and E describe the axial and transversal single-ion anisotropy parameters and J the coupling strength between the two Co(II)-ions.[28]

$$\mathcal{H} = \mathbf{g}\mu_B \mathbf{B} \cdot \mathbf{S} + D \left[S_z^2 - \frac{S(S+1)}{3} \right] + E \left[S_x^2 - S_y^2 \right] - J\mathbf{S_1S_2} \qquad (7.1)$$

---

[28]For the description of the SH approach it is referred to chap. 2.5.
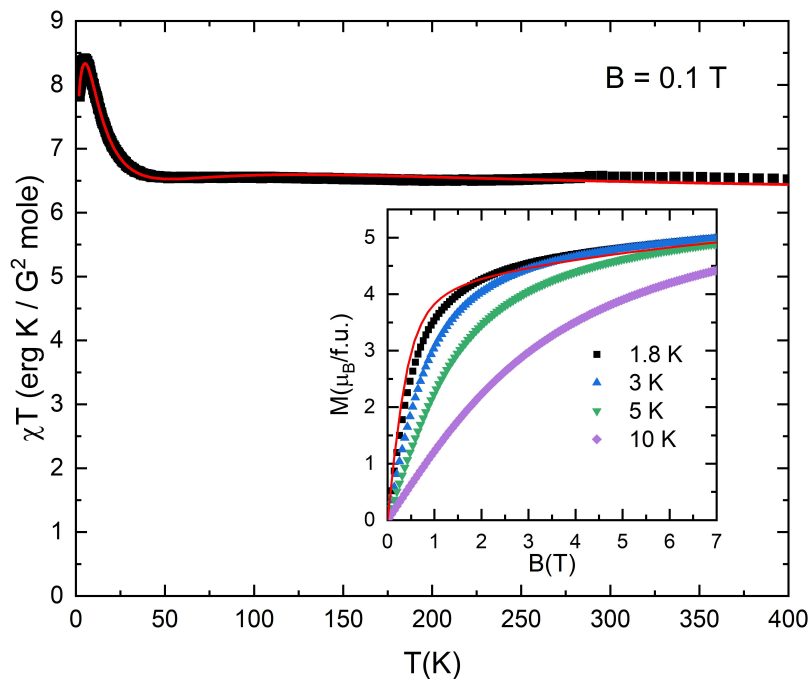
Figure 7.2.: Temperature dependence of the dc magnetic susceptibility measured in an applied field of 0.1 T is shown as black symbols. The red solid line corresponds to a fit using the SH eqn. 7.1 as described in the main text. Inset: Magnetic field dependence of the magnetic moment measured at various isothermal conditions as indicated in the plot. The red solid line corresponds to a simulation at 1.8 K using the resulting parameters from the fit of the temperature dependent data.

Due to structural symmetry of the molecule it is assumed that both Co(II)-ions figure the same single-ion anisotropy, which can both be described by the same D and E parameter. By this the best fit-parameters can be quantized to $g_\perp$ = 2.4(3), $g_{||}$ = 2.9, D = -2070(500) GHz, |E| = 660(100) GHz and J = 128(10) GHz. A fit model using just an averaged g-value and a vanishing transversal anisotropy ($E = 0$) failed to reproduce the measured data.

The obtained parameters are in perfect agreement with the averaged g-value obtained from the room-temperature χT-value. Furthermore the presumption of a high axial single-ion anisotropy and a ferromagnetic interaction between the Co(II)-ions is confirmed by the fit-results.

To directly measure the zero field splittings and magnetic field dependence of the energetically lowest spin multiplets, HF EPR measurements were employed. The high anisotropy of the Co(II)-ions can induce quite broad HF EPR spectra in a non-oriented powder measurement due to the strong angle-dependence of the resonance field positions. Therefore, the sample was aligned along the external magnetic field direction prior to the actual measurements. Fig. 7.3 (a) shows the corresponding frequency vs. resonance field position diagram as back and red symbols. Exemplary HF EPR spectra are plotted as grey lines in the background of fig. 7.3 (a). At lowest

measurement temperatures of T = 2 K one resonance branch is found which figures a zero field splitting gap of $\Delta = 440$ GHz. A second resonance branch appears at slightly elevated temperatures around 15 K with almost the same zero field gap as the low temperature branch, but a negative slope.
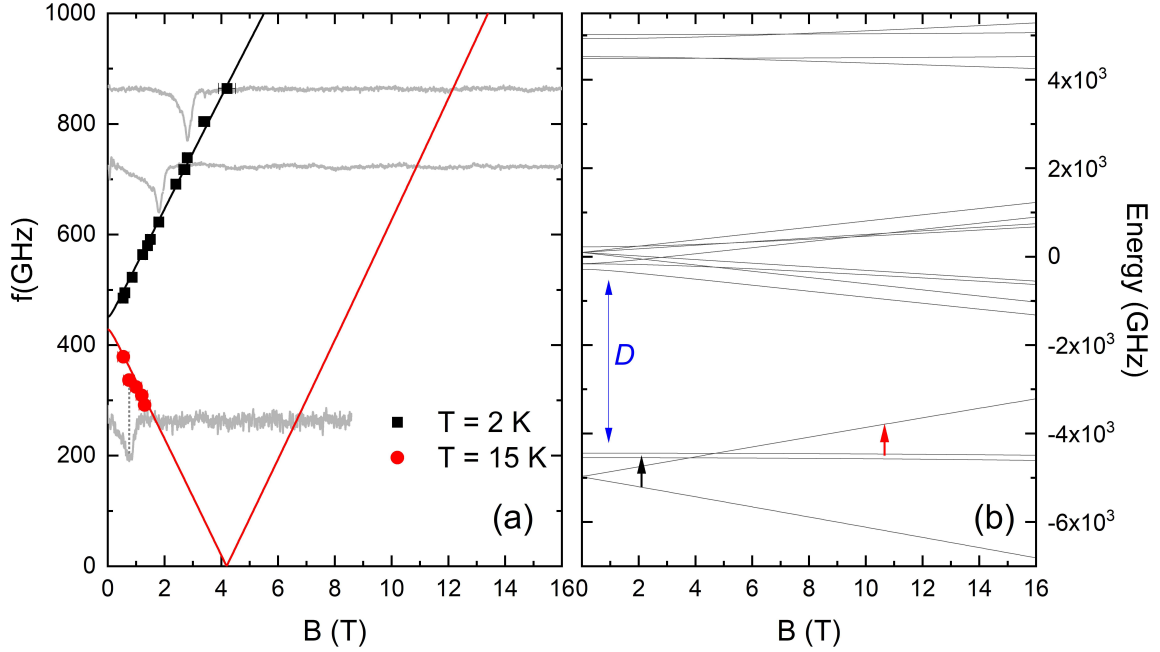

Figure 7.3.: (a) The frequency vs. magnetic resonance field diagram measured at different temperatures is shown by black squares and red circles. Solid black and red lines show the results of a simulation using the SH eqn. 7.1. Gray lines correspond to examples of the measured HF EPR spectra. (b) Simulated energy-level diagram using the SH eqn. 7.1 with the parameters described in the main text. Black and red arrows mark the respective transitions in correspondence to the same colored simulated branches in (a).

From a linear fit to the respective slope of the two observed branches (fit not shown in fig. 7.3) an effective g-value of $g_{\text{eff}} = 8.0(1)$ and $7.8(5)$ for the black and the red branch can be quantizes. The obtained effective g-values are much higher than the expected value of $g \approx 2$ for an allowed transition with $\Delta S = 1$. Therefore, it can be concluded that the observed resonances with $g_{\text{eff}} \approx 8$ arise from a forbidden transitions with $\Delta S = 3$. Furthermore, the almost equivalent g-value for both observed branches implies, that these resonances arise from the same energy-levels, but the red branch is an inverse transition.

The obtained resonance vs. magnetic field diagram shown in fig. 7.3 (a) can be rationalized by simulating the energy-levels using the SH shown in eqn. 7.1 with the anisotropy (D and E) and coupling (J) parameters obtained from the fit of the dc susceptibility measurements discussed above (see fig. 7.3 (b)). Three multiplets of the energy-level diagram are separated by the high D-anisotropy as indicated by the blue arrow in fig. 7.3 (b). However, within the accessible frequency range, only the lowest

multiplet is accessible. Due to the coupling between the two Co(II) spins, this lowest multiplet is further splitted in an S = 3 ground state doublet and two S = 0 singlets. The small splitting between the two singlet-levels is induced by the high transversal E-anisotropy. A black and red arrow in fig. 7.3 (b) mark the transitions between the energy-levels which are predicted from the simulation model. As can be seen by the black an red solid line in fig. 7.3 (a) which show the corresponding resonance branches to these transitions, a perfect agreement with the ZFS gap of the measured data can be witnessed. The g-value of the simulation was thereby tuned to fit the slope of the experimentally derived data points. By this a g-value of 2.9(2) can be extracted which is in accordance to the $g_{||}$-value obtained from the dc susceptibility measurements as expected for an oriented loose powder measurement.

7.1.2. Conclusion

By employing static magnetometry investigations and HF EPR measurements a detailed picture of the magnetic single-ion anisotropy and exchange coupling strength for the Co(II) ions in a Co_2Lu_2-MeOH butterfly compound was derived. The precise investigation of this analogous sample is the first step to decipher the single-ion and exchange coupling properties in the Co_2Dy_2-MeOH mother compound. Especially the latter is critical in terms of single molecular magnet and magnetic relaxation behaviour.

7.2. X-band EPR Investigations of a Cu(II)$_4$Cu(II)-Metallacrown

The basic building block of metallacrowns was firstly reported in 1967 by C. J. Pedersen who described his pioneering work in the synthesise of macrocyclic crown ethers, i.e., organic molecules which form a ring structure.[236] Subsequently, chemists started to discover the broad variety of macrocyclic organic molecules which turned out to be pretty flexible in terms of their application as ion transport agents [237, 238], stabilizers of unstable molecules [239, 240] or hosts for chemical reactions.[241–243] The discovery of the crown ethers played a groundbreaking role for a completely new field in chemistry, which is why Pedersen, together with D. J. Cram and J. M. Lehn was awarded with the Nobel Prize for chemistry in 1987 "for their development and use of molecules with structure-specific interactions of high selectivity".[244]

Shortly after the awarding of this Nobel Prize, V. L. Pecoraro and M. S. Lah described in 1989 the first macrocyclic complex containing metal ions which are nowadays know as metallacrowns.[245] Due to the broad variety of different metallocrowns, numerous possible applications were discussed. Among them, the most prominent example is the potential use of metallacrowns as single-molecule magnet (SMM)[246–249] but they find also application in medicine e.g. as contrast agents in magnetic resonance imaging (MRI).[250–252]

Metallacrowns are characterized by a repeating [M-N-O]$_n$ (MC) unit were M denotes the respective metal ion. Since they can be almost arbitrary in size and composition, a naming scheme was evolved to easily categorize them. The notation A^{ox}[X-MC-Y] names the central ion A with its oxidation state ox as well as the absolute number of atoms (X) and metal ions (Y) of the ring (excluding the central ion). Within this chapter the investigation of a Cu(II) matallacrown is described which has the general formula Cu^{II}[12-MC$_{Cu^{II}}$-4]. A deeper structural description is given in the following chapter.

7.2.1. Molecular Structure

The investigated sample has the chemical formula C$_{115}$Cu$_5$N$_{18}$O$_{19}$Si$_8$ and was synthesized in the group of Prof. Eva Rentschler at Mainz University. Fig. 7.4 (a) shows the molecular structure in the crystalline packing of the complex. The unit cell consists of two in-equivalent molecular sites which are connected to each other by an inversion symmetry. In fig. 7.4 (b) a top view of an individual molecule is shown. For a more comprehensible depiction, the structurally complicated organic ligand surrounding is omitted in this plot. The Cu(II) ions (dark blue in fig. 7.4) are arranged in an almost perfectly planar manner and have a $3d^9$ electron configuration. Thus, all Cu(II) ions figure a S = 1/2 ground state. The Cu(II) ions in the metallacrown ring are bridged via a (N-O) group while the central Cu(II) ion is coupled to the outer ones via pure oxygen bridges. The corresponding coupling parameters are referred to as J_2 and J_1, respectively (see light and dark green arrows in fig. 7.4 (b)). While the ligation surrounding of the Cu(II) ions in the ring is almost perfectly planar, an additional oxygen ion can be found in the apical position of the central Cu(II) ion, i.e., the central Cu(II) ion is located in a square-pyramidal surrounding.

7.2.2. Static Magnetic Properties

Fig. 7.5 shows the temperature dependent susceptibility measured in an external applied magnetic field of B = 0.1 T on a fixed powder sample. The static susceptibility measurements were performed at the Mainz University in the group of Prof. Eva Rentschler. Between 1.8 and 40 K, the χT product figures a constant behaviour with a χT-value of 0.41(2) erg K/mol G^2 in accordance with an isolated S = 1/2 ground state assuming a g-value of g = 2.11. With increasing temperature, the χT-product rises almost linearly with a broad hump centred around 100 to 150 K. Even up to room-temperature, no indication of a constant, i.e. paramagnetic behaviour is observed which implies a strong antiferromagnetic coupling between the Cu(II) ions. The red solid line in fig. 7.5 corresponds to a fit using the software PHI [253] with the following spin Hamiltonian:
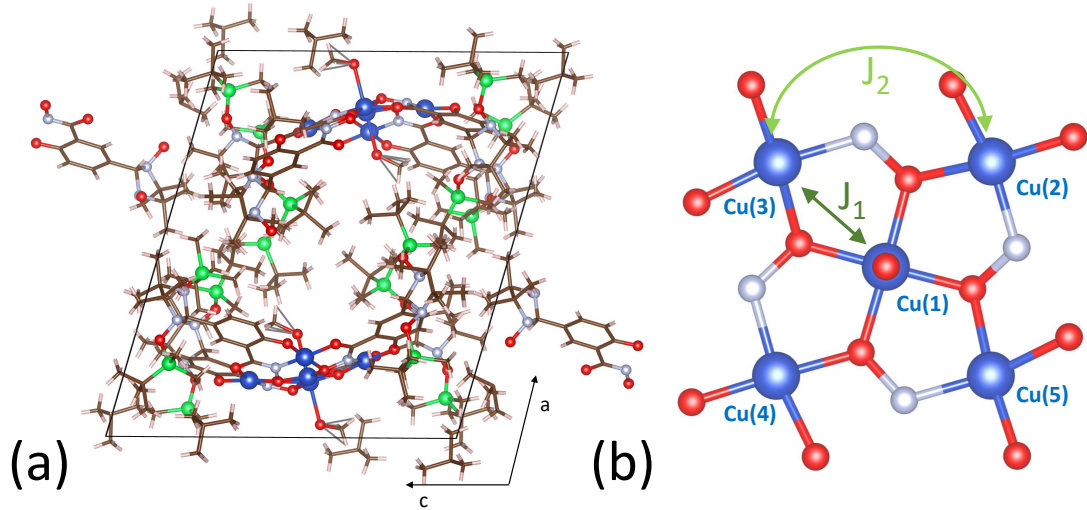
Figure 7.4.: (a) Crystal packing of the investigated Cu-metallacrown sample. Blue, Cu; red, O; light blue, N; green, Si; brown, C; white, H. (b) Top view of a single metallacrown molecule. The organic ligand surrounding is not shown. J_1 and J_2 define the exchange interactions between the central Cu(II) ion and the ones in the ring as well as between the neighbouring Cu(II) ions within the ring, respectively. (*The samples were structurally characterized in the group of Prof. E. Rentschler, Mainz University.*)

$$\mathcal{H} = \sum_{i=1}^{5} g_i \mu_B \mathbf{S_i B} - J_1 \mathbf{S_1} \left(\mathbf{S_2} + \mathbf{S_3} + \mathbf{S_4} + \mathbf{S_5} \right) - J_2 \left(\mathbf{S_2 S_3} + \mathbf{S_3 S_4} + \mathbf{S_4 S_5} + \mathbf{S_5 S_2} \right)$$

(7.2)

where the first term describes the ZEEMAN interaction of the electronic spins with the external magentic field and the second and third term consider the interactions between the central and the outer Cu(II) ions (J_1) and between the neighbouring Cu(II) within the ring (J_2), respectively. To reduce various parameter dependencies, it is assumed that the g-value can be treated in a first approximation as isotropic and equivalent for all the Cu(II) ions. The obtained parameters from the fit of the $\chi T(T)$ data are $g_{\chi T} = 2.11(5)$, $J_1 = $ -4.7(7) THz (-226(30) K) and $J_2 = $ -2.6(6) THz (-124(30) K). These values as well as the ratio $J_1/J_2 = 1.8(4)$ is in a range which was already obtained for other antiferromagnetically coupled, square planar Cu(II) based metallacrown complexes.[254–257]

The inset in fig. 7.5 depicts the magnetic field dependence of the magnetisation for several isothermal conditions as indicated in the figure. At lowest temperatures of T = 2 K the magnetisation curve almost linearly increases in the low magnetic field range, until it figures a saturation behaviour towards $M_{sat} = 1.02(2)$ μ_B/f.u..

107

This value implies the presence of a spin S = 1/2 ground state in accordance to the observation of an isolated S = 1/2 ground state at low temperatures in the χT(T) data. Thus, the observation of an isolated S = 1/2 ground state motivates to fit the M(B) data set at lowest temperatures with a BRILLOUIN-function as shown in eqn. 7.3, which describes the field dependent magnetisation behaviour of a purely paramagnetic system:[26]

$$B_J(y) = M_S \cdot \left(\frac{2J+1}{2J} \cdot coth \left(\frac{2J+1}{2J} y \right) - \frac{1}{2J} \cdot coth \left(\frac{y}{2J} \right) \right) \qquad (7.3)$$

with $J = 1/2$ being the spin state and $y = J\frac{g\mu_B B}{k_B T}$. From this fit a g-value of $g_{M(B)}$ = 2.10(2) can be extracted which is, within the error-bars, in perfect agreement with the one obtained from the fit of the temperature dependent data.
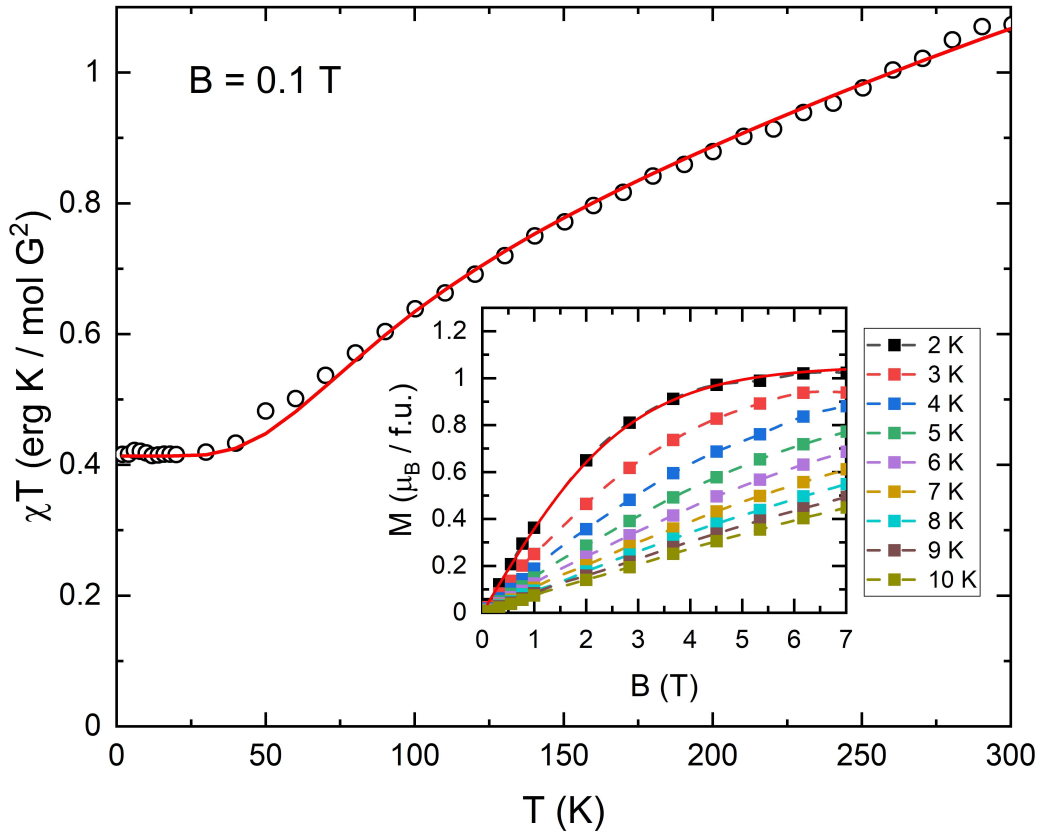

Figure 7.5.: Temperature dependent susceptibility measured in an applied field of B = 0.1 T on a fixed powder sample is shown. The red solid line corresponds to a fit using the spin hamiltonian, eqn. 7.2, with the parameters described in the main text. Inset: Magnetic field dependent magnetisation data measured at several isothermal conditions as indicated in the plot. The red solid line shows the result of a fit using the BRILLOUIN-function shown in eqn. 7.3. (*The experimental data was measured in the group of Prof. E. Rentschler, Mainz University and shared by private correspondence.*)

7.2.3. X-band EPR Investigations

To closely investigate the magnetic properties of the Cu ions within the metallacrown structure, X-band EPR measurements[29] were performed.[258] In fig. 7.6 the obtained spectra at different temperatures are shown. At low temperatures (see fig. 7.6 (a)) one resonance signal can be observed which figures a slight anisotropy as reflected by the enhanced spectral weight on the high magnetic field site compared to the low field site. With increasing temperatures, the signal intensity decreases. Fig. 7.6 (b) shows the enlargement of the spectra measured at higher temperatures (above 33 K) which are marked in fig. 7.6 (a) in grey. Superimposed on the intense main signal which is already visible at low temperatures, a second feature appears between 33 and 40 K as indicated by the black arrow in fig. 7.6 (b). This feature figures a fine structure which is in more detail discussed below.
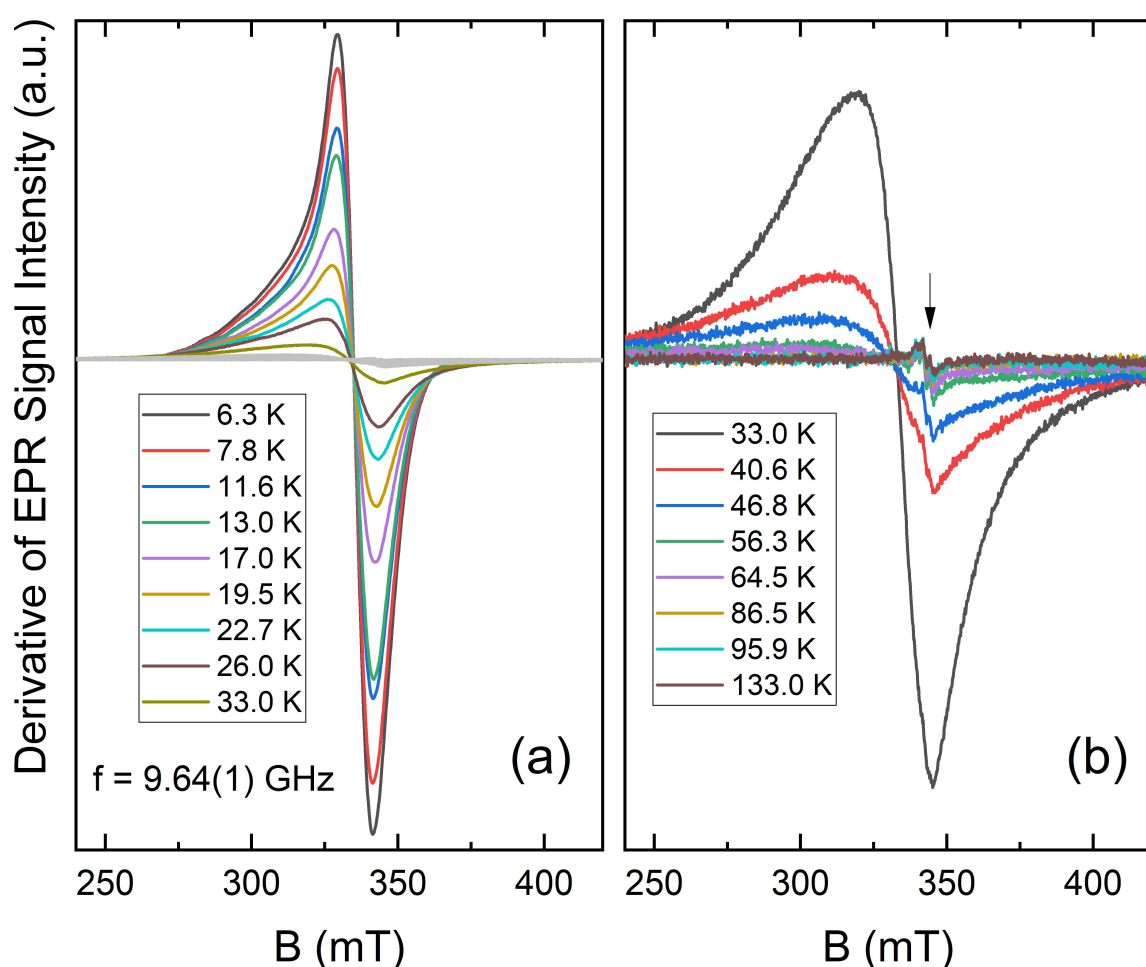

Figure 7.6.: X-band EPR spectra measured on a fixed powder sample at different temperatures as indicated in (a) and (b), respectively, at a frequency of f = 9.64 GHz. Panel (b) shows the enlargement of the spectra which are marked in grey in panel (a).(*Figure adapted from ref. [258].*)

[29]The X-band measurements were performed in the frame of a Bachelor thesis by I. Heckelmann under the supervision of L. Spillecke.

In fig. 7.7 (a) an enlarged plot of the spectra obtained at T = 6.5 K is shown as black symbols. The red solid line corresponds to a fit using the software EasySpin[66]. Since at this temperatures only one feature (signal 1) is resolvable, the model of a single spin S = 1/2 is used with an anisotropic g-value. Furthermore, to gain the best conformity of the measured data and the fit, an anisotropic line broadening has to be considered. The finite nuclear spin of the Cu(II) ions implies a non-vanishing hyperfine interaction. Therefore, the parameter H_{strain} is introduced to describes an anisotropic residual line width due to unresolved hyperfine interactions or other effects which do not depend on the respective transition.[66, 259] The obtained fit-parameters are summarized in tab. 7.1. The g-value figures an almost perfectly axial anisotropy. From the H_{strain} parameter, which has a finite component in z-direction while the x and y components are small or not resolvable, it can be concluded that the hyperfine interaction strength figures the same anisotropy.
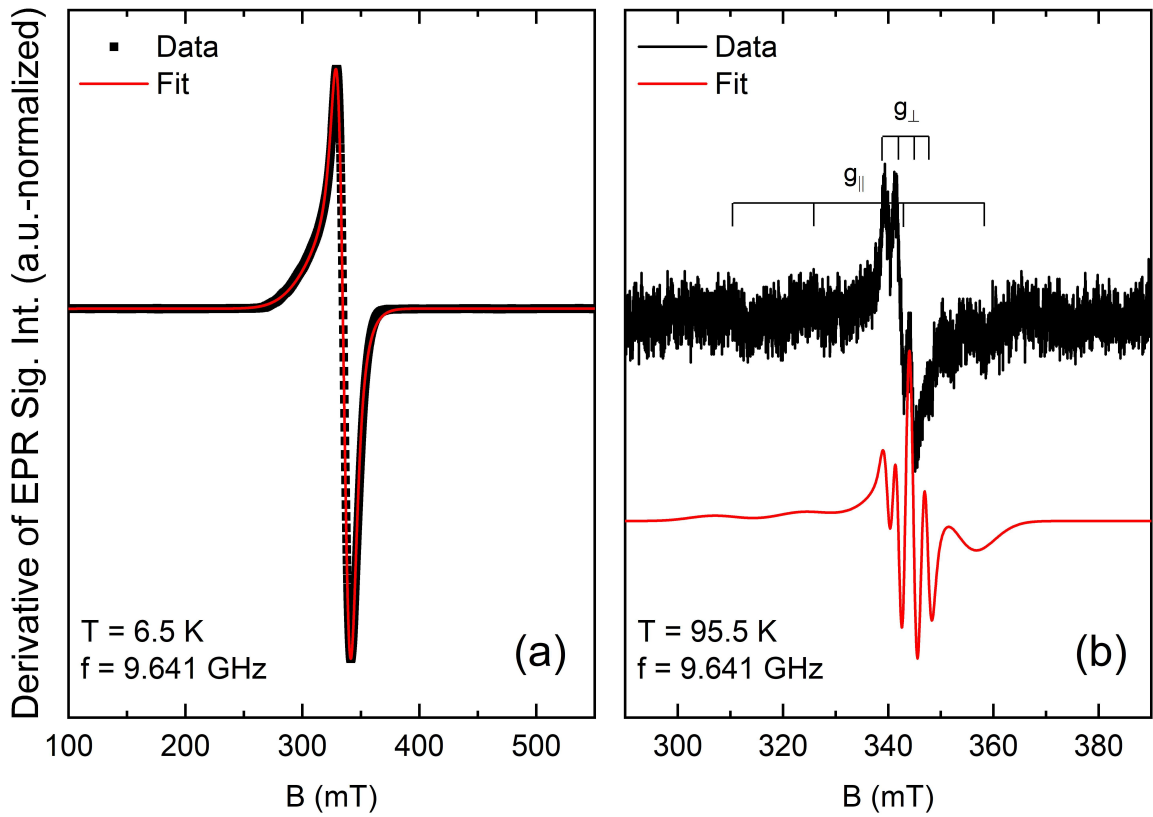

Figure 7.7.: X-band EPR spectra obtained at lowest temperatures of T = 6.5 K (a) and elevated temperatures of T = 95.5 K (b) at a frequency of f = 9.641 GHz. Solid red lines correspond to the result of a fit using an S = 1/2 approach with an anisotropic g-value, line-broadening and hyperfine interaction as more closely described in the main text. $g_\perp$ and $g_\parallel$ visualize the resonance positions obtained from the fit for the planar and axial direction of the g-value, respectively. (*Experimental data adapted from ref. [258].*)

Fig. 7.7 (b) depicts a spectra as black line (signal 2), which was acquired at elevated

Table 7.1.: Fitting parameters for the x, y and z component of the g-value, the hyperfine tensor A as well as for the H_{strain} parameter obtained for signal 1 (low temperature signal) and signal 2 (high temperature signal) using an S = 1/2 approach, respectively.

	signal 1			signal 2		
	x	y	z	x	y	z
g	2.060(3)	2.041(3)	2.189(3)	2.002(1)	2.002(1)	2.080(5)
A (MHz)	-	-	-	65	65	480
H_{strain} (MHz)	0	0	1611(100)	0	0	310(20)
lw (mT)		9.82(20)			1.5(5)	

temperatures (T = 95.5 K), where the influence of signal 1 is almost completely vanished and thus, the fine-structure of signal 2 can be resolved. The main feature which is centred around B = 345 mT in fig. 7.7 (b) shows a splitting into at least three resonances which can be distinguished by eye, however, the rather broad shape of the sub-feature at highest field implies that there are two resonance positions which are merged due to the limited resolution. Consequently, it is assumed that the main signal consists of four equidistant sub-features which can be assigned to the four transitions arising from the splitting of the main energy-levels induced by the hyperfine interaction with the $I = 5/2$ nuclear spin of the Cu(II) ions.

Next to the main feature there are several weak features showing up around 310, 320 or 355 mT in the measured spectra depicted in fig. 7.7 (b). Deduced from the overall spectral weight it can be concluded that the intense main feature can be assigned to the planar component $g_\perp$ of the anisotropic g-tensor (x- and y-direction), while the weak features correspond to the axial direction $g_\parallel$ (z-direction) which figures a much stronger hyperfine splitting than the planar direction. The red solid line in fig. 7.7 (b) shows the result of a fit using an S = 1/2 approach with an anisotropic g-value and a finite hyperfine interaction A. The directional dependence of the line broadening is again included by the H_{strain} parameter. As can be seen in fig. 7.7 (b), while the signal intensities shows a slight discrepancy for the main signal, the resonance positions and line broadening between the measured and simulated data are in perfect agreement to each other. Again, the obtained fit-parameters are summarized in tab. 7.1. The resonance positions of the hyperfine splitted signals are visualized in fig. 7.7 (b) by black bars for $g_\perp$ and $g_\parallel$, respectively, to empathise the differences in hyperfine interaction strength. Notably, the general line width for signal 2 appears to be almost one order smaller compared to signal 1 which straight forwardly explains, why the hyperfine structure can be directly observed for signal 2 while it is not resolved for signal 1.

For the fit of the X-band EPR data as described above, the two observed signals were evaluated separately by an S = 1/2 approach, i.e., the coupling between the Cu(II) spins was neglected. Generally, due to the high energy scale of the exchange interaction between the Cu(II) ions it is in principal also not possible, to directly estimate those exchange interactions exclusively from X-band EPR data. However, the

integrated EPR signal intensity depends on the thermal population of the respective states and thereby also on the energy gap between the ground state and the excited states which is defined by the interaction strength. Filled blue squares in fig. 7.8 show the temperature dependence of the integrated EPR signal intensity. Since the coupling of the microwaves to the sample can technically not be controlled, only the relative change in signal intensity can be evaluated. Therefore, the data is scaled at T = 6.5 K to the results from the SQUID measurements discussed above (see green dot in fig. 7.8). As can be seen, the temperature dependent slope of the data obtained from integration of the EPR signal is in good accordance to the data set from SQUID magnetometry. To verify the quality of this consistency, the EPR data set is further compared to a simulation assuming an uncoupled system with five S = 1/2 spins and a g-value of $g = 2.11$ as found from the PHI fit described in chap. 7.2.2 (see red solid line in fig. 7.8). At temperature below 40 K it can be seen that the data set obtained from SQUID measurements (open black circles in fig. 7.8) as well as the uncoupled simulated model (red solid line in fig. 7.8) have the same quality of congruence with the data from the integrated EPR intensity (open and filled blue squares in fig. 7.8) if this is scaled accordingly (see green dots in fig. 7.8 as reference for the respective scaling). This observation is not further surprising since it was already found from the evaluation of the χT(T) data in chap. 7.2.2 that at temperatures below 40 K the investigated system behaves like an isolated S = 1/2 paramagnet i.e. the measured SQUID data and the simulation of an uncoupled system show a Curie like behaviour, separated only by a scaling factor. At more elevated temperatures, were the system can not be described as S = 1/2 spin but the coupling between the Cu(II) ions has to be considered, it is however obvious, that the data obtained from the integration of the EPR signal is in much closer agreement with the SQUID data compared to the simulated uncoupled model. Thus, it can be concluded, that even if no quantitative analyse of the temperature dependence of the X-band EPR intensity regarding the coupling strength can be given, the relative comparison to quantitative SQUID data and the simulation of an uncoupled model shows that the presence of an antiferromagnetic coupling between the Cu(II) ions is also witnessed in the EPR data set.

7.2.4. Discussion and Conclusion

Fig. 7.9 shows an energy-level diagram (blue solid lines in fig. 7.9) which is calculated assuming the Hamiltonian shown in eqn. 7.2 with the coupling constants derived from the fit of the susceptibility measurements shown in fig. 7.5. In order to visualize the magnetic field dependence of the energy-levels, the slope is exaggerated by a factor of 40 in fig. 7.9. As can be seen in the calculated energy-level diagram, the ground state of the antiferromagnetically coupled spin system is well separated from the first excited doublet by $\Delta \approx 2$ THz which leads to the observed isolated S = 1/2 behaviour shown as plateau at temperatures below 50 K in the χT(T) data. The highest multiplet of the spin system is, according to the simulated energy-level diagram, more than 16 THz (≈ 750 K) separated from the ground state doublet which causes the non-saturating behaviour of the χT-value even up to room-temperature.
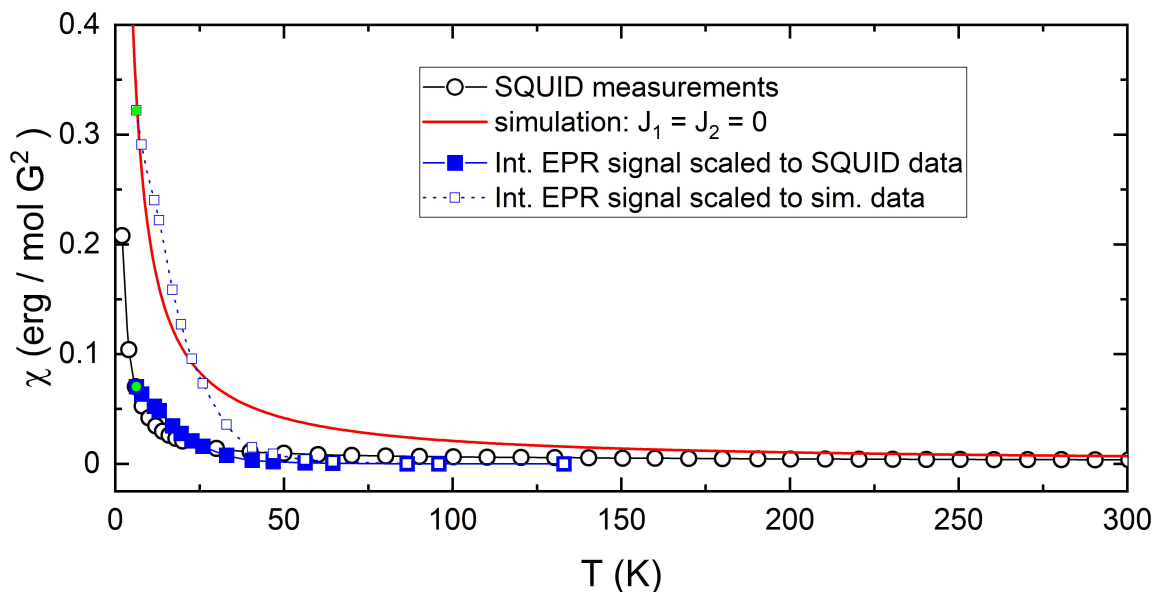
Figure 7.8.: Filled blue squares show the integrated signal intensity of the X-band EPR data scaled at 6.4 K (see green dot) to the $\chi(T)$ data (open black circles). Open blue squares show the integrated signal intensity scaled to the result of a simulation assuming five uncoupled Cu(II) spins (see red solid line).

Red dashes in fig. 7.9 visualize predicted, i.e., allowed transitions between the calculated energy-levels for a microwave frequency of f = 9.641 GHz and an orientation of the molecules with $g_\perp$ along the external magnetic field. This direction was chosen since the measured EPR spectra show the most pronounced spectral weight for this direction. The black ellipse marks the energy scale which was covered by the temperature dependent X-band EPR measurements shown in fig. 7.6. A simulation model in which the g-value of signal 1 is assigned to the central Cu(II) ion (Cu(1) in fig. 7.4) while signal 2 is assigned to the Cu(II) ions in the metallacrown ring (Cu(2) - Cu(5) in fig. 7.4) leads to a good agreement between the positions of the predicted transitions and the observed signals 1 and 2 in the respective temperature range. A further indication that signal 1 mainly arises from the central Cu(II) ion is the relatively broad line width compared to signal 2. The line width of an EPR signal is in general defined by the transversal relaxation time T_2 which measures the phase coherence time of the excited spins.[18, 260] An relaxation enhancement can thereby be induced by, amongst others, dipolar spin-spin interactions to neighbouring paramagnetic species [259] or the proximity to oxygen ions.[261, 262] From the structural description shown above (see chap. 7.2.1) it can be deduced, that, while each Cu(II) ion in the matallacrown ring is surrounded by just one neighbouring Cu(II) ion as well as three oxygen ions, the central Cu(II) ion figures four Cu(II) ions in close proximity and is surrounded by five oxygen ions. This difference in local surrounding of the Cu(II) ions could be an explanation for the observed deviations in line broadening between signal 1 and 2.

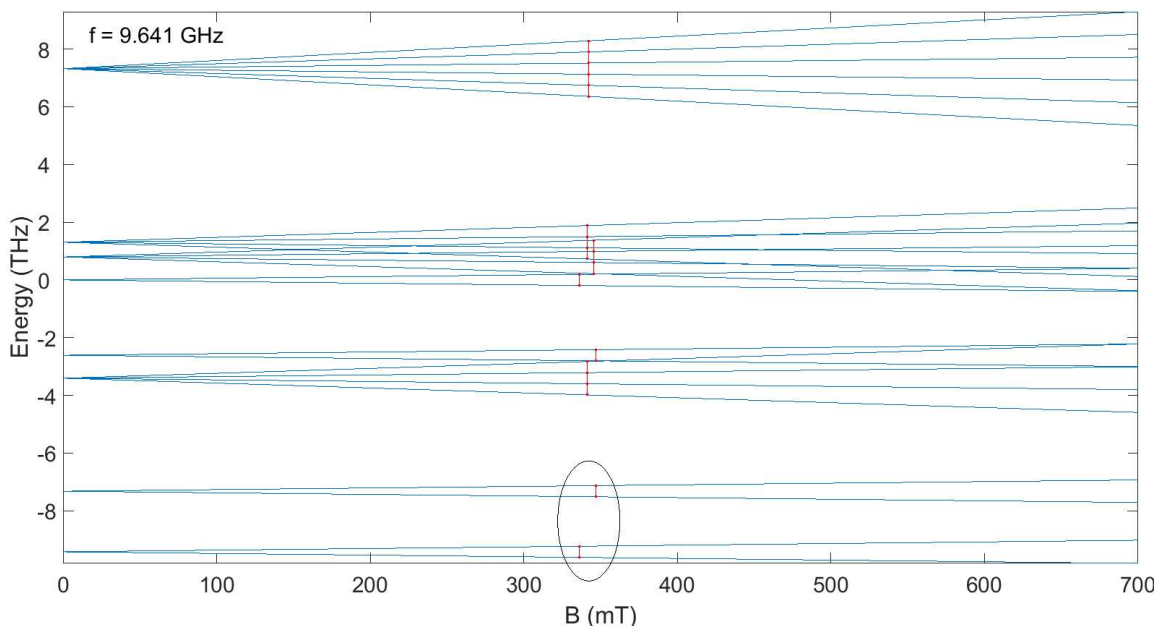In conclusion, the magnetic properties of a Cu(II) containing metallacrown with

Figure 7.9.: The calculated energy-level diagram for a microwave frequency of f = 9.641 GHz using the Hamiltonian shown in eqn. 7.2 and the coupling constants fixed to the parameters derived from the $\chi T(T)$ data is shown as blue solid lines. The slope of the energy-levels is exaggerated by a factor of 40 to visualize the magnetic field dependence. Red dashes mark the allowed resonance transitions for a model in which the g-value measured for signal 1 is assigned to the central Cu(II) ion, while the g-value measured for signal 2 is assigned to the Cu(II) ions in the metallacrown ring.

the general formula $Cu^{II}[12\text{-}MC_{Cu^{II}}\text{-}4]$ was investigated by temperature and magnetic field dependent susceptibility measurements as well as X-band EPR investigations. Thereby, not only the anti-ferromagnetic coupling strength between the Cu(II) ions was deciphered, but also the appearance of two X-band EPR signals figuring different spectral shape and temperature dependence is discussed. Related to the latter it is speculated, that the signal which is most intense at low temperatures (signal 1) is mainly arising from the central Cu(II) ion, while the high temperature signal originates from the Cu(II) ions in the metallacrown ring. In this regard it has to be noted, that the assignment of spectral features to individual Cu(II) ions is rather a phenomenological approach which well describes our measurement results. In a more precise formulation, the two appearing signals should be rather treated at the results of correlated states due to the high coupling strength between the Cu(II) ions.

Beyond the evaluation of specific magnetic property parameters for an Cu(II) metallacrown, it was demonstrated that by the application of X-band EPR spectroscopy it is possible, to not only detect and evaluate the resonance arising from the ground state transition, but also the one within the first excited doublet, even though the intensity is, due to the elevated temperatures, significantly reduced compared to the

low temperature feature.

8. Summary and Conclusion

The aim of this thesis is the investigation of novel molecular magnetic materials by the application of tunable high-frequency / high-field electron paramagnetic resonance (HF EPR) spectroscopy backed-up by detailed dc and ac magnetisation studies. The first part in chap. 4 focusses on the investigation of Co(II) containing mononuclear molecular compounds with different coordination geometries. Thereby, the detailed analysis of the respective HF EPR spectra shown in chap. 4.1 and 4.2 enable to deduce the axial and transversal anisotropy parameters for a sample set of tetrahedrally coordinated Co(II) high-spin ions with the general formula $[Co(L_1)_4]X_2$, where L_1 are thiourea ligands and X = Br, I and $[Co(L_1)_4](SiF_6)$. In particular, this study reveals a direct connection between the observed axiality of the magnetic anisotropy and the ions in the second coordination sphere. The subsequent chap. 4.3 addresses an octahedrally coordinated Co(II) compound $[Co(L_1)_4(Cl)_2]$ (**1**), with L_1 = thiourea (H_2N-CS-NH_2) which figures a strongly axial anisotropy. The energy scale of this anisotropy exceeds the ranges of our HF EPR measurement setup, which is why pulsed field magnetisation measurements were employed in addition. Through the latter an axial anisotropy parameter of D = -1890 GHz was quantified. As a more exotic example for Co(II) containing compounds, two Co(II) low-spin complexes figuring a spin state of S = 1/2 are described in the final part of the Co(II) monomer chapter (see chap. 4.4), both of which having the same formula $[Co(DPPE)_2Cl](SnCl_3)$. The interesting feature of those compounds is, that they are real geometrical isomers as well as structural polymorphs which provides the rare opportunity to directly observe the impact of the geometrical arrangement of the ligands around the central Co(II) ion onto the magnetic properties. HF EPR measurements revealed, that there is indeed a change in anisotropy of the measured g-value which can be associated with the geometrical arrangement of the surrounding ligands. Furthermore, ac susceptibility measurements showed a significant change in magnetic relaxation behaviour coupled to the ligand arrangement. As common theme across all the discussed Co(II) monomeric compounds, intermolecular interactions were studied, which is a crucial parameter for the estimation of single molecular properties. In these investigations, a small dimer-like intermolecular interaction in the range of $\approx$ 0.2 K was witnessed for the tetrahedrally coordinated Co(II) compounds discussed in chap. 4.2, while a rather two dimensional intermolecular coupling scheme was found for the octahedrally coordinated Co(II) monomer as shown in chap. 4.3. For the Co(II) low-spin complexes (see chap. 4.4) it was shown on the other hand, that the influence of intermolecular interactions is negligible in this compounds.

The precise quantification of weak intermolecular interactions is also a main result from the HF EPR study on the mononuclear complex $[V(III)(DAPBH)(CH_3OH)_2]$

Cl·CH$_3$OH described in the subsequent chap. 5.1. The observed dimer-like inter-molecular coupling constant of J = -1.1 cm^{-1}, which was conclusively confirmed by both, HF EPR investigations and low temperature SQUID magnetometry, is a particularly surprising result considering the large spatial separation of about 7.5 Å between the paramagnetic centres within the crystal structure. Furthermore, a single-ion anisotropy gap of D = 4.5(1) cm^{-1} was found for the spin S = 1 V(III) ions.

The second part of this thesis shifts the subject of matter from the so far discussed mononuclear 3d metal containing complexes towards molecules with magnetic centres made from 4f rare earth ions. To observe the magnetic relaxation behaviour of a Dy(III) monomeric complex with the formula [Dy^{III}L^1]OTf ac susceptibility measurements were performed as shown in chap. 6.1. Even though, this complex figures no remanent magnetisation in the absence of an applied magnetic field, an interesting two step relaxation behaviour was observed when a small external field of 0.1 T was applied. The comparison to quantum chemical calculations strongly implies that the magnetic relaxation within this complex does not just incorporate the first but also the second excited KRAMERs doublet. In the subsequent chap. 6.2, two novel Er(III) complexes figuring a pentagonal-bipyramidal coordination surrounding and a general formula of [Er(DAPMBH)Cl(H$_2$O)]2C$_2$H$_5$OH and (Et$_3$NH)[Er(H$_2$DAPS)Cl$_2$] were comparatively investigated. Thereby, the effect of apical ligand substitution on the magnetic relaxation behaviour was directly traced back to the changes in crystal field parameters, which were measured by HF EPR. Besides the analysis of the magnetic relaxation behaviour, the obtained HF EPR spectra themself represent a rare example of high quality HF EPR spectra on purely lanthanide containing compounds (excluding Gd). In the final chap. 6.3 in this second part of the thesis, the interplay between 4f and 3d metal ions is discussed on the example of four Cu(II)-Ln-Cu(II) samples with Ln = Gd, Tb, Dy and La. Therein, the coupling between the Cu ions to the Tb or Dy ions was directly quantified by HF EPR measurements. Furthermore, a detailed analysis of the temperature dependent spectra obtained for the Gd containing compound revealed a finite anisotropy on the Gd site, whose origin is mainly attributed to dipolar interactions with the Cu(II) spins.

The broad variety of molecular magnetic compounds is demonstrated in chap. 7, where two complexes are discussed which do not fit straightforwardly either of the afore-mentioned groups of molecular magnets. For the butterfly-shaped compound Co$_2$Lu$_2$-MeOH shown in chap. 7.1 the single-ion anisotropy on the Co(II) sites as well as the exchange coupling strength between the two Co(II) ions was obtained by a combined study of dc susceptibility and HF EPR investigations. This characterization of the effectively dimeric Co(II) molecule marks a first step towards a comprehensive investigation of the exchange coupling constants within the Co$_2$Dy$_2$-MeOH analogue. Furthermore, a Cu(II) metallacrown compound was investigated in chap. 7.2 by means of dc susceptibility and temperature dependent X-Band EPR spectroscopy, which consists of five Cu(II) ions arranged in a square planar form. As a result the anti-ferromagnetic coupling constants between the five Cu(II) ions were obtained and the hyperfine splitting of the resonance spectra could be evaluated.

In conclusion, this thesis delivers a comprehensive overview on the investigation of

magnetic properties for a total of sixteen metal-organic compounds. Amongst others, the discussion of these complexes is thereby mainly concentrated on the evaluation of magnetic anisotropies induced by the crystal field, the dynamic magnetic relaxation behaviour and the deciphering of intermolecular interaction pathways. Beyond this, the focus is, in particular, directed onto the demonstration of HF EPR spectroscopy as powerful tool to gain direct insights into the magnetic anisotropy parameters for a given metal-organic compound.

A. Appendix

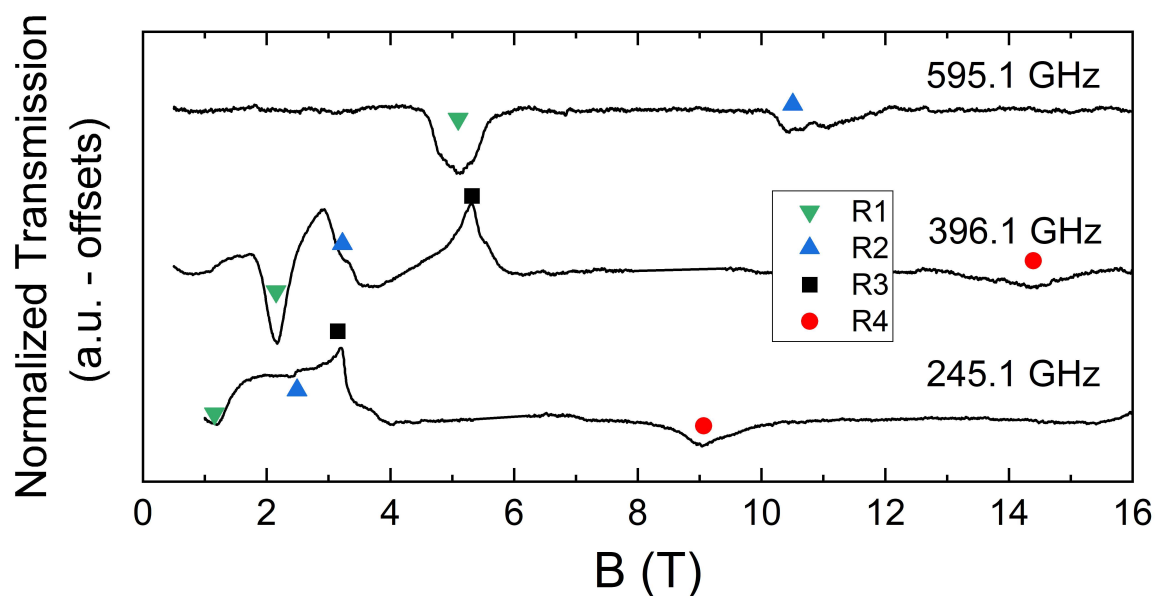## A.1. Supplementary Materials: Co(II) Monomers

Figure A.1.: Exemplary HF-EPR transmission spectra measured on complex **3**. Markers label resonance branches as in Fig. 4.3. The shape of several resonance features (e.g., at f = 245.1 GHz, B = 3 T) is due to phase mixing effects (see the main manuscript text). (*Figure reprinted from Tripathi et al. 2019.[19]*)
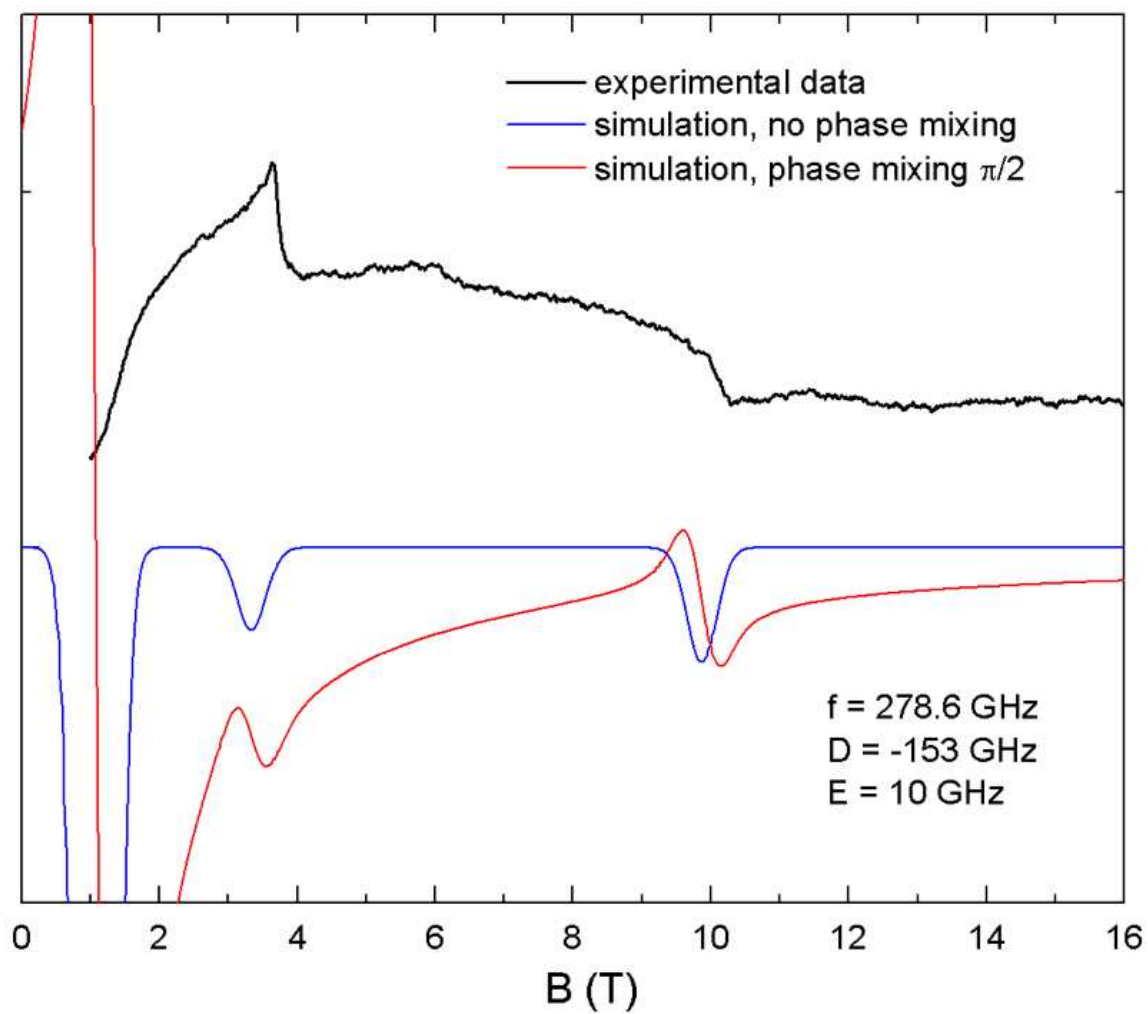
Figure A.2.: Simulation of experimental HF-EPR for complex **3** with indicated parameters. (*Figure reprinted from Tripathi et al. 2019.[19]*)

A high-frequency EPR study of magnetic anisotropy and intermolecular interactions on Co(II) ions

Lena Spillecke,*[a] Shalini Tripathi,[c] Changhyun Koo,[a] Mursaleem Ansari,[c] Shefali Vaidya,[c] Amaleswari Rasamsetty,[c] Talal Mallah,[d] Gopalan Rajaraman,[c] Maheswaran Shanmugam,*[c] and Rüdiger Klingeler *[a,b]

[a]Kirchhoff Institute for Physics, Heidelberg University, 69120 Heidelberg
E-Mail: lena.spillecke@kip.uni-heidelberg.de
[b]Centre for Advanced Materials, Heidelberg University, 69120 Heidelberg
E-Mail: ruediger.klingeler@kip.uni-heidelberg.de
[c]Department of Chemistry, Indian Institute of Technology Bombay, Powai, Mumbai-400076, Maharashtra, India
E-Mail: eswar@chem.iitb.ac.in
[d]Institut de Chimie Moléculaire et des Matériaux d'Orsay, CNRS, Université Paris Sud, Université Paris Saclay, 15, rue Georges Clemenceau, 91405 Orsay Cedex France

*Corresponding authors

Table S1. CShM parameters for the coordination geometries of the complexes **1**-**3**.

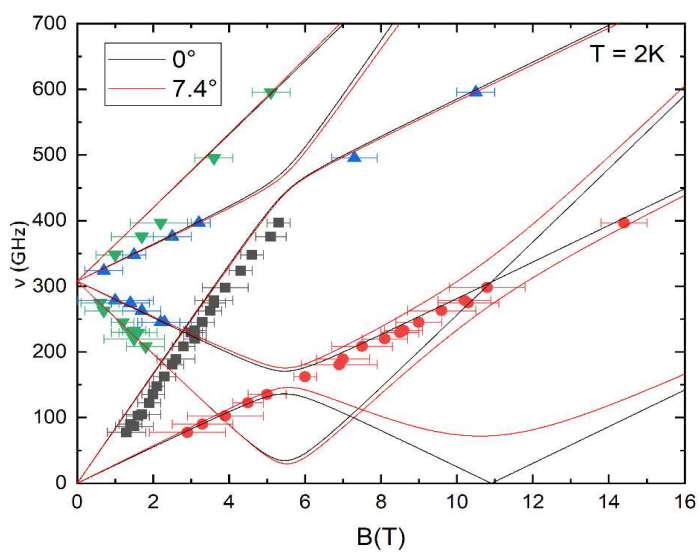|	Symmetry	1	2	3
S (Tetrahedral)	T_d	0.22	0.28	0.09
S (Square planar)	D_{4h}	32.5	31.5	31.2
S (Seesaw)	C_{2v}	8.7	8.3	8.3

Figure S1. Influence of a tilting angel of 7.4° (red lines) between the direction of *D* and the external magnetic field on the simulated branches (solid lines) for **1**.
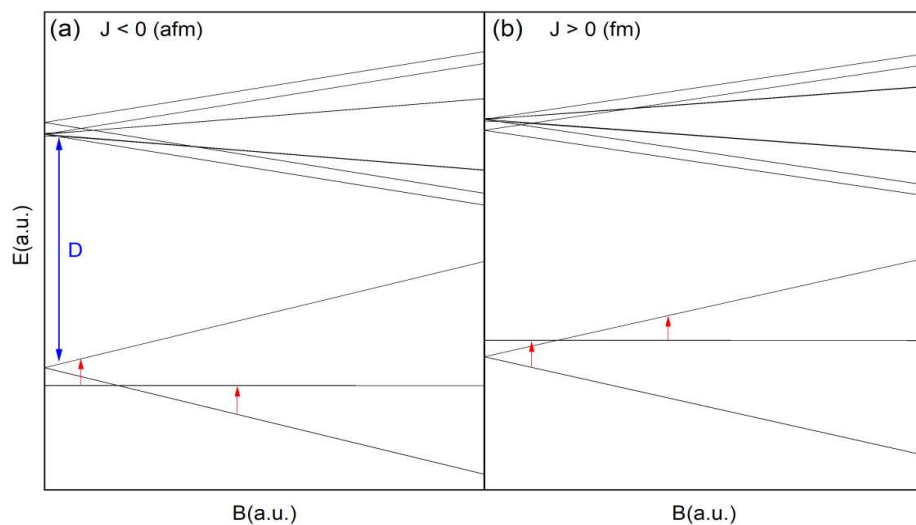
Figure S2. Simulated energy-level diagrams using SH in Eqn. 2 expanded by the coupling term shown in Eqn. 1 with positive (a) or negative (b) sign of the exchange coupling constant *J*. For better clarification, only the lowest multiplets are shown which are split by the axial anisotropy parameter *D* (visualised by blue arrow). The zero-field gap of the lowest multiplet directly depends on the sign and amplitude of the exchange interaction between the spins. Expected transitions between the spin states are marked with red arrows.
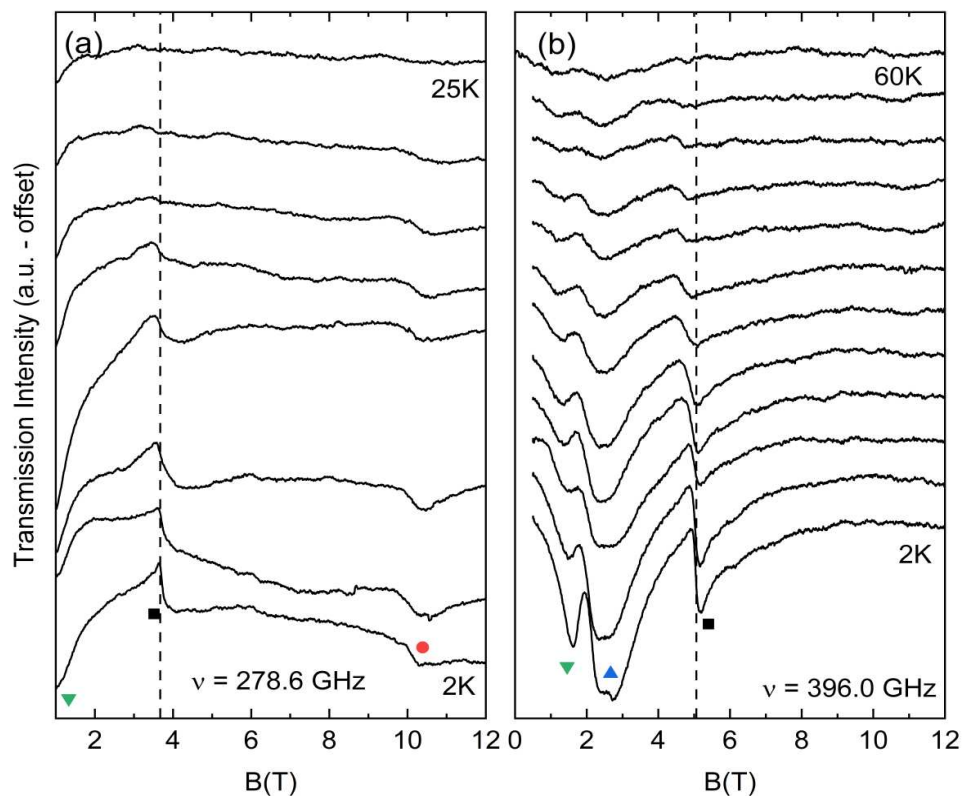
Figure S3. Temperature dependent measurements for sample **1** (reprinted from Ref [1]) and **2**. With rising temperatures, the feature which corresponds to the black resonance branch is shifted to lower fields for both samples like indicated by the horizontal dashed line. This shift is most likely due to a merging with a smaller feature which is up showing on the low field site of the main one with rising temperatures.
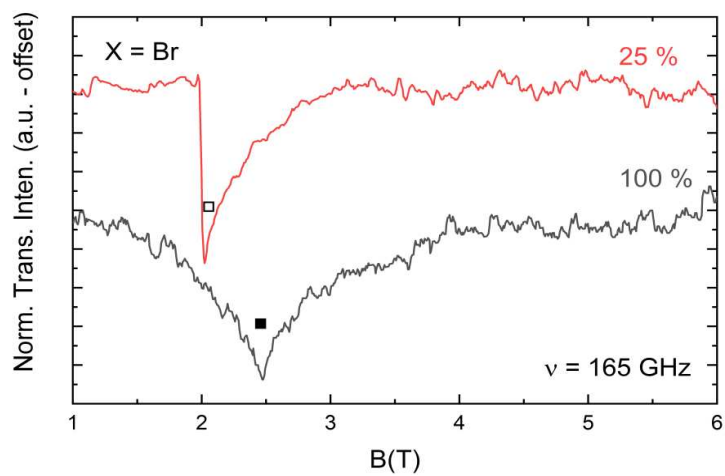
126

Figure S4. HF-EPR spectra measured on a 100 % as well as a diluted 25 % sample of **2** at same resonance frequency of 165 GHz. A clear dilution dependent shift of the observed feature of around 0.5 T is visible which can be attributed to the presence of intermolecular interactions in the undiluted sample. Open and filled black squares refer to the corresponding resonance branch shown in Figure 3 (b) and 7 (b) in the main text.
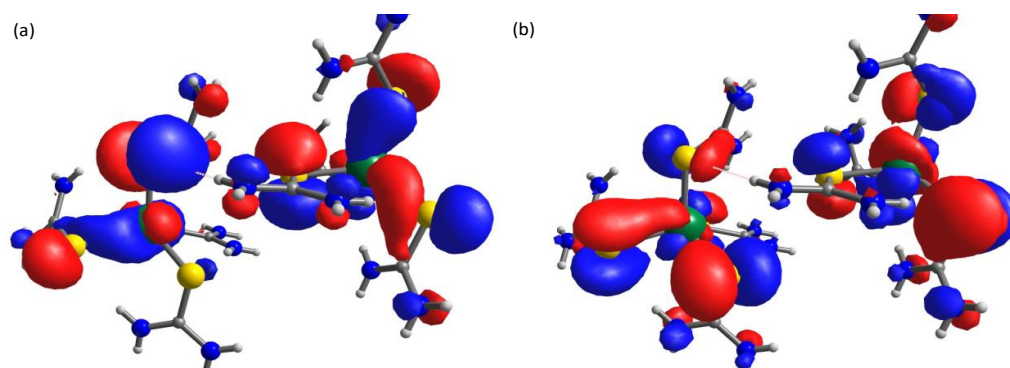

Figure S5. Computed (a) 177α + 178 β SOMOs and (b) 179α + 184 β SOMOs of **1**. The red and blue iso-density surfaces (0.025 e$^-$ bohr^{-3}) indicate positive and negative spin phases, respectively.
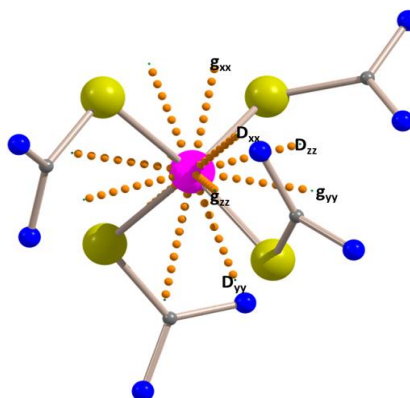
Figure S6. Computed orientations of the easy axis of the *g*-tensor and the *D*-tensor based on NEVPT2 calculations on a representative complex **1**. The D_{zz} and g_{zz} directions form an angle of 72.3°. We refer to Ref. [1] for calculational details.

[1]   S. Tripathi *et al.*, "Influence of a Counteranion on the Zero-Field Splitting of Tetrahedral Cobalt(II) Thiourea Complexes," *Inorganic Chemistry,* vol. 58, no. 14, pp. 9085-9100, 2019/07/15 2019.
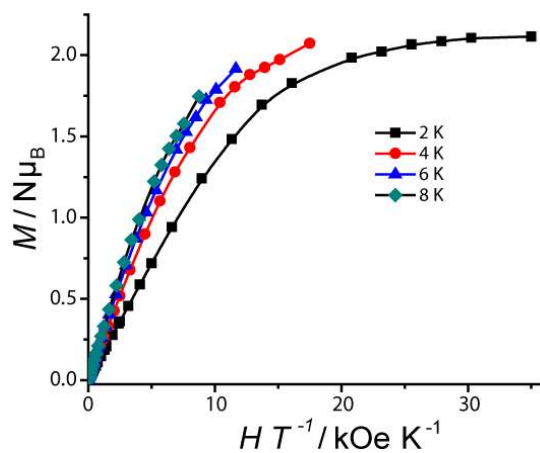
128

Figure A.3.: The reduced magnetization of complex **1** at indicated temperatures.(*Figure reprinted from Tripathi et al. 2021.[61]*)
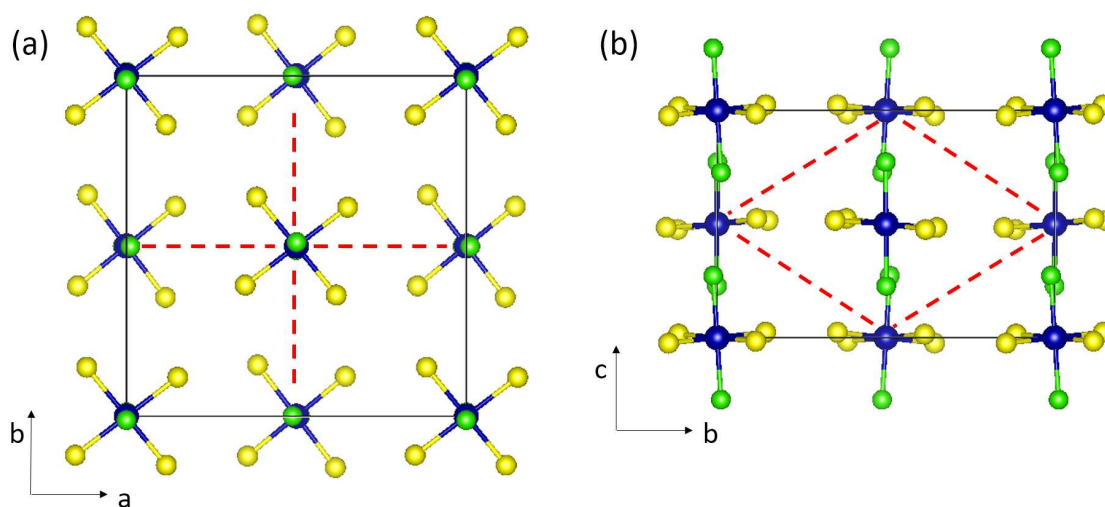

Figure A.4.: Predicted hydrogen coupling pathways within the crystal lattice are shown for two different orientations (red dashed lines) for compound **1**. Colour code: blue, Co; yellow, S; green, Cl. Only the first coordination sphere is shown for clarity. (*Figure reprinted from Tripathi et al. 2021.[61]*)
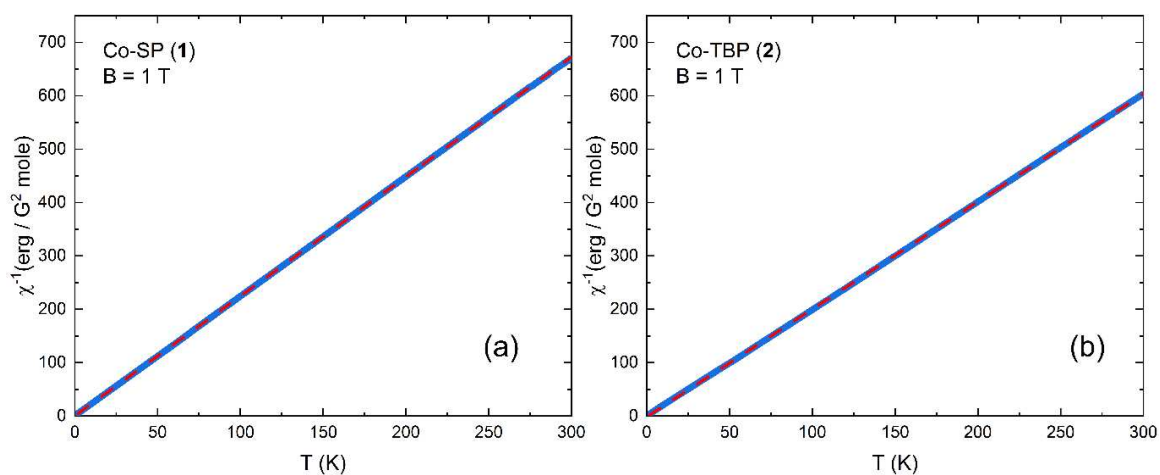
Figure A.5.: Temperature dependence of the inverse magnetic susceptibility measured in an external magnetic field of 1 T is shown as blue symbols for complex **1** (a) and **2** (b), respectively. Dashed red lines correspond to a fit using a Curie-law.

Figure A.6.: X-band EPR spectra of **1** measured as polycrystalline sample (panel A) and frozen DCM solution (Panel B) at 5 K. (*X-band measurements were performed by S. Tripathi, IIT Bombay.*)
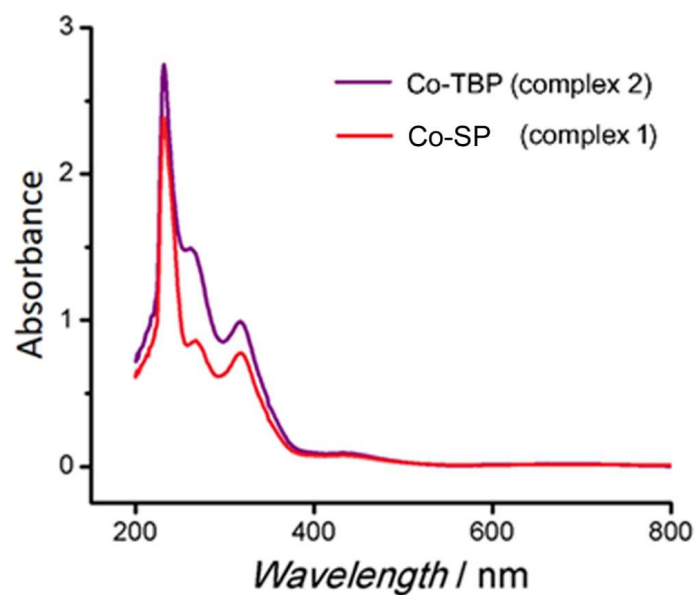
Figure A.7.: The UV-Vis spectra of complexes **1** (red) and **2** (purple) were measured in DCM solution at room temperature. (*UV-Vis measurements were performed by S. Tripathi, IIT Bombay.*)
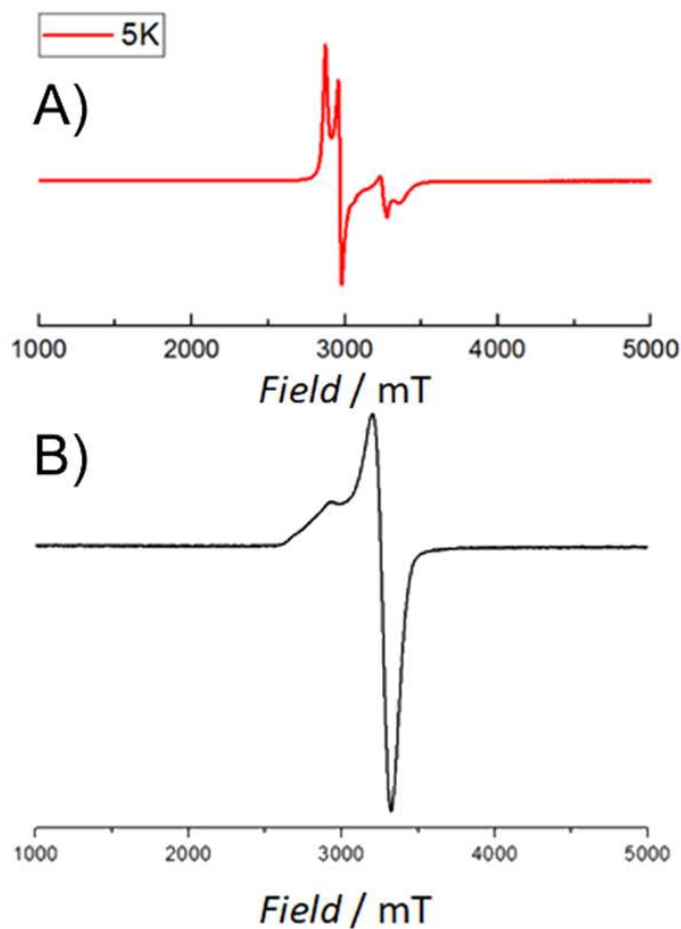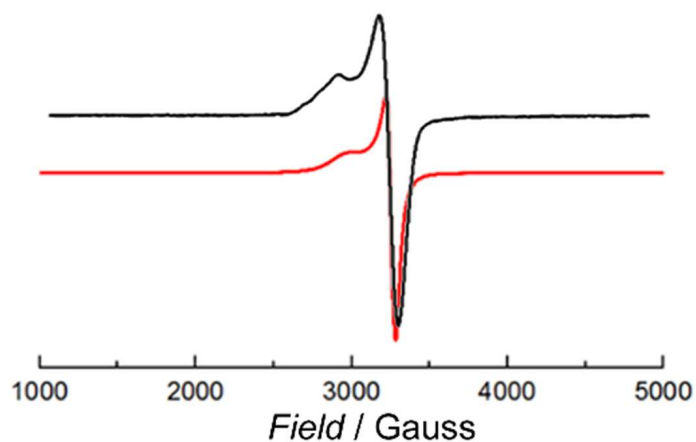

Figure A.8.: X-band EPR spectra of **2** measured as polycrystalline sample (red trace) and frozen DCM solution (black trace) at 5 K. (*X-band measurements were performed by S. Tripathi, IIT Bombay.*)
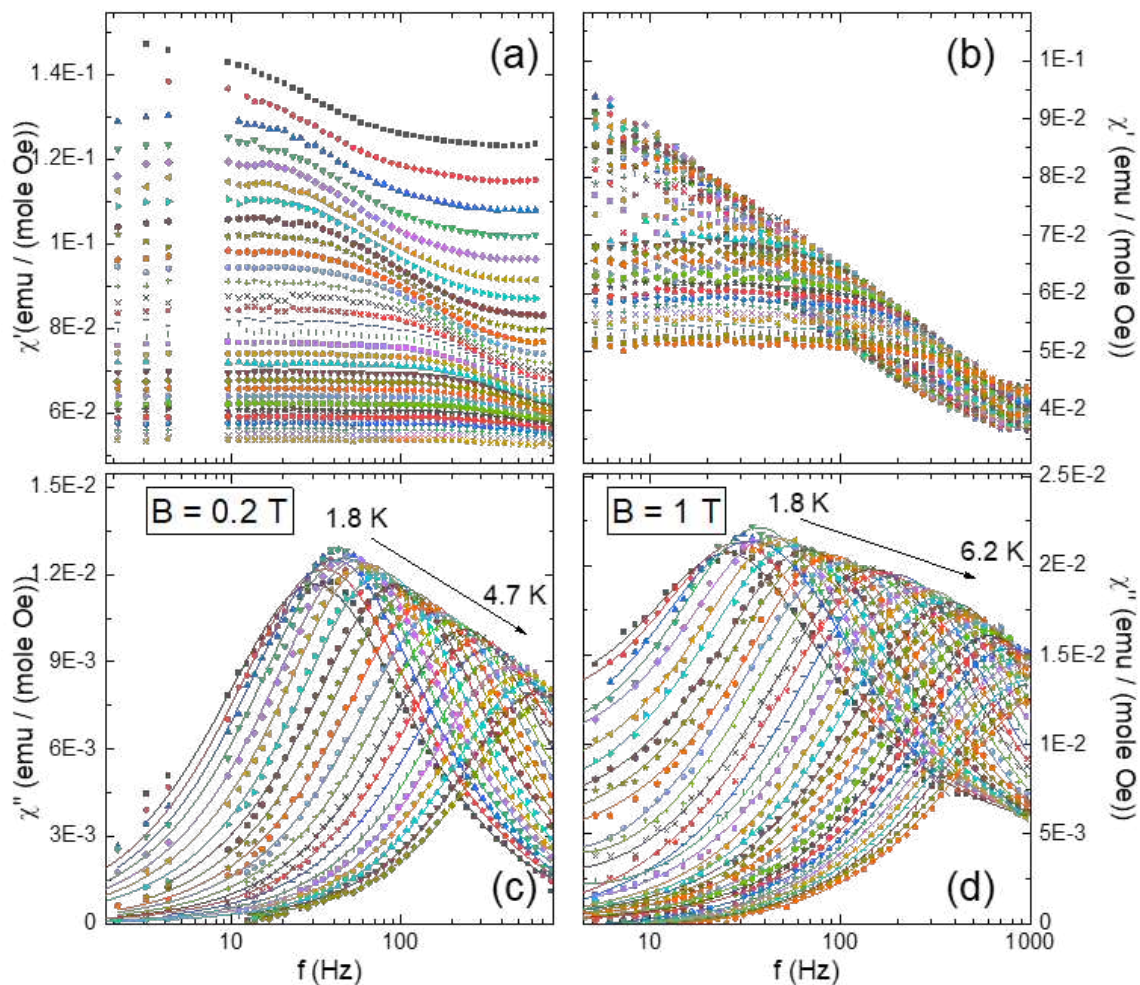
Figure A.9.: In-phase (panel (a) and (b)) and out-of phase (panel (c) and (d)) contribution to the measured ac susceptibility on **1** at external magnetic fields of B = 0.2 T and 1 T, respectively. Solid red lines in (c) and (d) correspond to a fit using the generalized Debye model as shown in Eqn. A.1 at different temperatures between 1.8 K and 4.7 K or 6.2 K. The obtained fit parameters as well as the precise measurement temperatures are summarised in table A.1 and A.2.
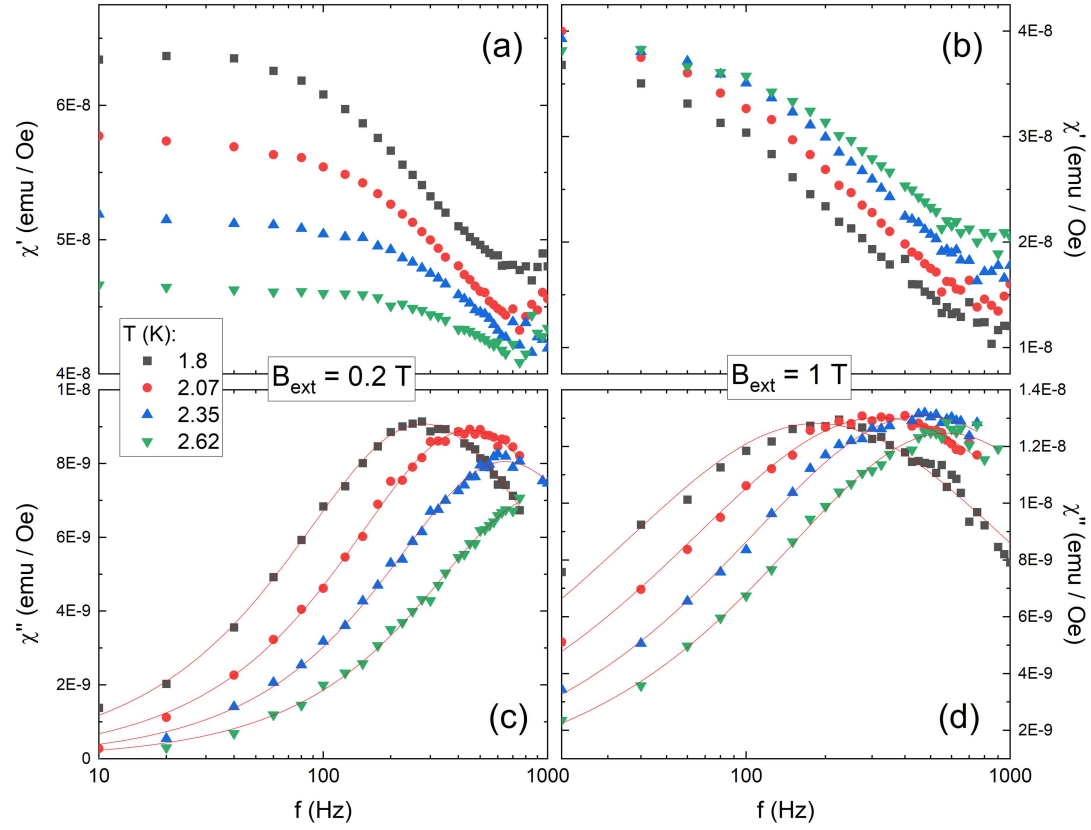
Figure A.10.: In-phase (panel (a) and (b)) and out-of phase (panel (c) and (d)) contribution to the measured AC susceptibility on **2** at external magnetic field of 0.2 T and 1 T, respectively. The solid red lines correspond to a fit using the generalized Debye model in Eqn. A.1 at different temperatures between 1.8 K and 2.62 K. The obtained fit parameters are summarised in table A.3.

Generalised Debye model:

$$\chi''_{\mathrm{AC}}(\omega) = \frac{(\chi_{\mathrm{T}} - \chi_{\mathrm{S}}) \, (\omega\tau)^{(1-\alpha)} \, cos\left(\frac{\pi\alpha}{2}\right)}{1 + 2(\omega\tau)^{(1-\alpha)} sin\left(\frac{\pi\alpha}{2}\right) + (\omega\tau)^{(2-2\alpha)}} \tag{A.1}$$

With the isothermal and the adiabatic susceptibility χ_{T} and χ_{S}, respectively, and α being an eccentricity parameter which takes the distribution of different relaxation times τ into account.[11]

Table A.1.: Parameters obtained by fitting the generalised Debye model (Eqn. A.1) to the frequency dependent out of phase susceptibility shown in Figure A.9 (c) for **1** at B = 0.2 T.

B (T)	T (K)	χ_T - χ_S (emu / Oe)	τ (s)	α
0.2	1.8	1.46159E-6	0.03277	0.12072
	1.94	1.48816E-6	0.02835	0.10482
	2.09	1.50252E-6	0.02484	0.09388
	2.23	1.49295E-6	0.02159	0.08708
	2.38	1.46563E-6	0.01829	0.07943
	2.52	1.43337E-6	0.01549	0.07286
	2.67	1.38521E-6	0.01289	0.06585
	2.81	1.35438E-6	0.01053	0.07319
	2.96	1.30689E-6	0.00869	0.06534
	3.1	1.26196E-6	0.00712	0.06366
	3.25	1.22332E-6	0.00591	0.06301
	3.39	1.16684E-6	0.00496	0.0515
	3.54	1.12079E-6	0.00415	0.0433
	3.68	1.09607E-6	0.00345	0.05067
	3.83	1.0515E-6	0.00294	0.04407
	3.97	9.87074E-7	0.0026	0.02237
	4.12	9.38603E-7	0.00229	0.01834
	4.26	9.30093E-7	0.00192	0.02994
	4.41	8.78126E-7	0.00174	0.019
	4.55	8.39194E-7	0.00155	0.01567
	4.7	7.97528E-7	0.0014	0.00756

Table A.2.: Parameters obtained by fitting the generalised Debye model (Eqn. A.1) to the frequency dependent out of phase susceptibility shown in Figure A.9 (d) for **1** at B = 1 T.

B (T)	T (K)	χ_T - χ_S (emu / Oe)	τ (s)	α
1	1.8	1.246E-6	0.036	0
	1.93	1.3866E-6	0.032	0
	2.07	2.93835E-6	0.02878	0.18533
	2.2	1.6115E-6	0.02556	0.00306
	2.33	1.6846E-6	0.02181	0.02885
	2.47	1.77518E-6	0.01932	0.03114
	2.6	1.89576E-6	0.01725	0.05788
	2.73	1.85038E-6	0.01457	0.04255
	2.87	1.93189E-6	0.01274	0.0533
	3	1.90381E-6	0.01092	0.04213
	3.13	2.62783E-6	0.00948	0.14582
	3.27	2.58664E-6	0.00811	0.14091
	3.4	2.50978E-6	0.00681	0.12851
	3.53	2.52454E-6	0.00595	0.13327
	3.67	2.40193E-6	0.00515	0.10946
	3.8	2.35485E-6	0.00447	0.11026
	3.93	2.32089E-6	0.00388	0.11149
	4.07	2.22906E-6	0.00339	0.09212
	4.2	2.16686E-6	0.00301	0.08781
	4.33	2.13856E-6	0.00262	0.08945
	4.47	2.06604E-6	0.0024	0.08338
	4.6	1.97986E-6	0.00218	0.06792
	4.73	2.04037E-6	0.00193	0.08439
	4.87	1.85828E-6	0.00179	0.05625
	5	1.79471E-6	0.00164	0.04819
	5.13	1.73307E-6	0.00151	0.04193
	5.26	1.89406E-6	0.00129	0.08809
	5.4	2.1527E-6	0.00116	0.10899
	5.53	1.8521E-6	0.0011	0.09834
	5.67	1.84506E-6	0.00103	0.09518
	5.8	1.90008E-6	9.34897E-4	0.10981
	5.93	1.96214E-6	8.34727E-4	0.11763
	6.07	1.80142E-6	7.69252E-4	0.1218
	6.2	1.99296E-6	6.91281E-4	0.12618

Table A.3.: Parameters obtained by fitting the generalised Debye model (Eqn. A.1) to the frequency dependent out of phase susceptibility shown in Figure A.10 (d) and (d) for **2**.

B (T)	T (K)	χT - χS (emu / Oe)	τ (s)	α
0.2	1.8	3.0E-5	0.00360	0.130
	2.07	8E-6	0.00223	0.10
	2.35	4.1E-5	0.00155	0.08
	2.61	7E-6	0.00105	0.07
1	1.8	2.0E-5	0.0053	0.32
	2.07	7.61-4	0.00312	0.304
	2.35	1.9E-5	0.00215	0.258
	2.62	5E-7	0.00175	0.21

The following chapter was written by S. Tripathi and M. Ansari under the supervision of G. Rajamaran and M. Shanmugam as part of a research article (L. Spillecke et al.) which has been submitted to the journal Inorganic Chemistry.

A.1.1. Hirshfeld Surface analysis of Co-SP (1) and Co-TBP (2)

In order to analyse the inter- and intramolecular interactions observed in the solid-state, a Hirshfeld surface analysis was carried out on the cation moieties of both complexes (Figure A.11). The various regions of color on these surfaces describe the inter-and intramolecular contacts present in their crystal structures. Two-dimensional (2D) fingerprint plots (Figure A.12) were also generated for the cations of both complexes and used to visualize supramolecular features such as weak inter- and intramolecular interactions and close contacts as seen in their crystal structures. Both the Hirshfeld surface and fingerprint plots were extracted from the d_i and d_e values using CrystalExplorer.[263] d_i represents the distance from the Hirshfeld surface to the nearest atom inside the surface with d_e being the distance from the nearest atom outside the surface.[263] The results of these plots indicate that the percentage of intermolecular H$\cdots$H contacts is 55.8 % in **1** and 54.3 % in **2** of the total share. The other significant contributions including reciprocal contacts are Cl$\cdots$H, C$\cdots$H, Sn$\cdots$H and C$\cdots$C having relative contributions of 22.4, 14.4, 5.3 and 1.3 % in **1** and 20.2, 17.8, 5.3 and 1.3 % in **2**, respectively. These values and the absence of sharp spikes in the fingerprint plots support the notion that all of the inter- and intramolecular interactions in the cations of both complexes are relativity weak in support of no classical hydrogen bonds being observed in their crystal structures.
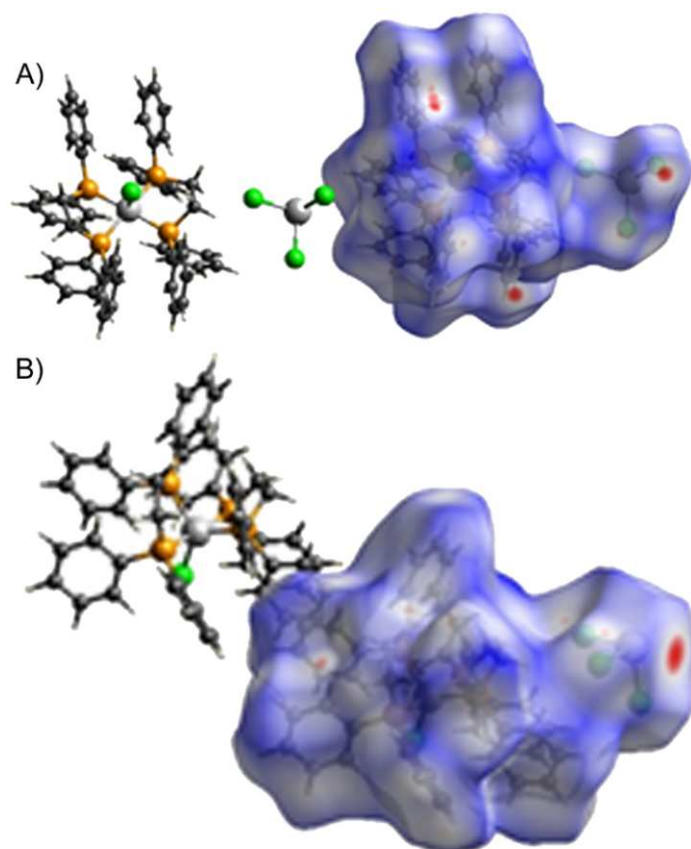
Figure A.11.: Hirshfeld surface analysis mapped with d_{norm} and showing two adjacent molecules outside the surface for the cations in complex **1** (A) and complex **2** (B). The red colors indicate contacts with distances shorter than the van der Waals radii, and indicate very weak inter- or intramolecular interactions. (*This plot was constructed by S. Tripathi et al. .*)
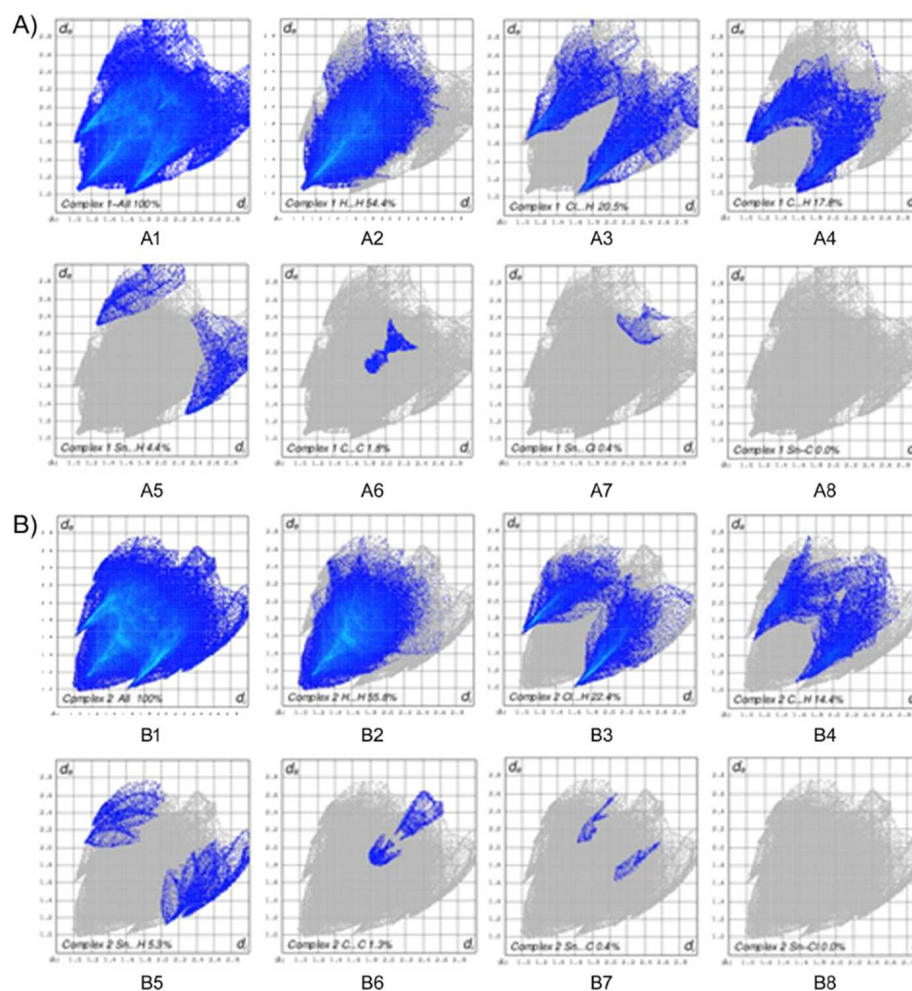
Figure A.12.: Two-dimensional (2D) fingerprint plots of the cation of complex **2**, where d_i is the distance from the Hirshfeld surface to the nearest atom inside the surface and d_e is the distance from the nearest atom outside the surface. Total intermolecular contacts including reciprocal contacts in **2**: (A1) 100 % contacts, (A2) the relative percentage of H$\cdots$H contacts (54.3 %), (A3) Cl$\cdots$H contacts (20.5 %), (A4) Cl$\cdots$H contacts (17.8 %), (A5) Sn$\cdots$H contacts (4.4 %), (A6) C$\cdots$C contacts (1.3 %), (A7) Sn$\cdots$Cl contacts (0.5 %) and (A8) Sn$\cdots$C contacts (0.0 %). Total intermolecular contacts including reciprocal contacts in **1**: (B1) 100 % contacts, (B2) the relative percentage of H$\cdots$H contacts (55.8 %), (B3) Cl$\cdots$H contacts (22.4 %,), (B4) Cl$\cdots$H contacts (14.4 %), (B5) Sn$\cdots$H contacts (5.3 %), (B6) C$\cdots$C contacts (1.3 %), (B7) Sn$\cdots$C contacts (0.4 %) and (B8) Sn$\cdots$Cl contacts (0.0 %). (*This plot was constructed by S. Tripathi et al. .*)
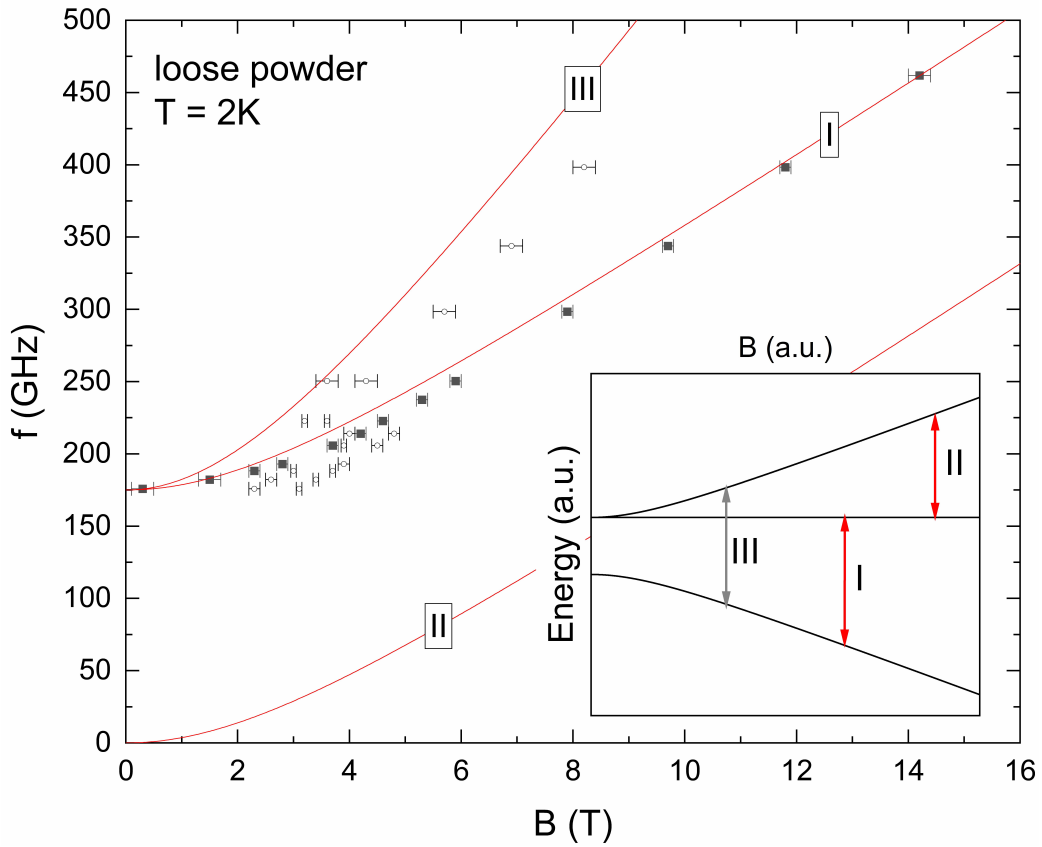
A.2. Supplementary Materials: V(III) Monomer

Figure A.13.: Magnetic field dependence of the resonance frequencies for a loose powder sample of **3**, at T = 2 K (Fig. 5.5 shows data obtained at higher temperatures, too). Filled squares correspond to the main feature while open circles show features which are only slightly visible and arising from forbidden or excited transitions (cf. Fig. 5.3, 5.4). Simulation of resonance branches by means of a monomeric S = 1 model (i.e., without considering intermolecular coupling) fails. A best simulation using a monomeric SH with D = 175 GHz and g = 1.83 is shown by red lines. Inset: Corresponding arbitrary scaled energy level diagram with allowed (red arrows) and forbidden (grey arrow) transitions. (*Figure reprinted from Bazhenova et al. 2020.[85]*)
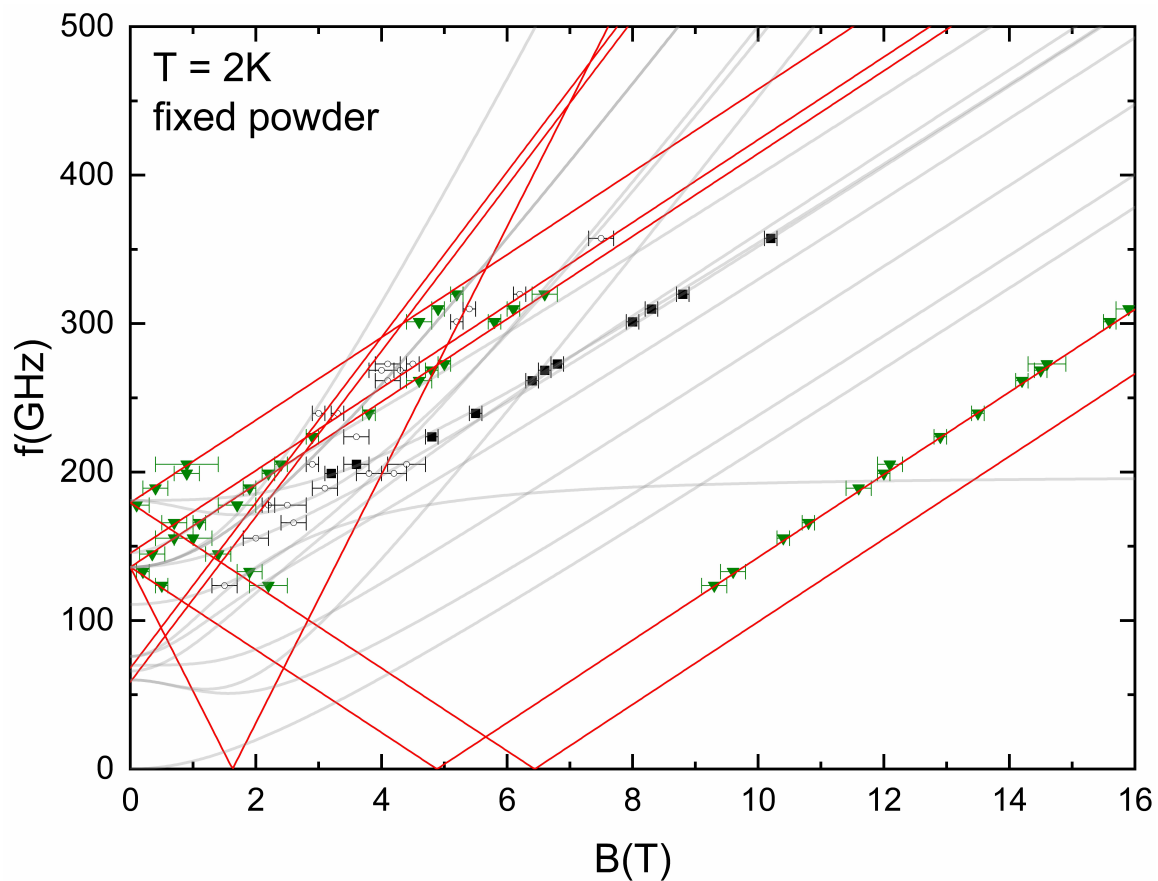
Figure A.14.: Magnetic field dependence of the resonance frequencies for a fixed powder sample of **3**, at T = 2 K. Green triangles show features which were absent in the loose powder measurements and can be attributed to features arising from the axial direction of the molecular frame. The black squares show the resonance branch which was already obtained in the loose powder measurement. Red lines show a simulation of the parallel branches ($\mathbf{B}_{ext}\|g_{\|}$) while the grey lines reproduce a simulation of $\mathbf{B}_{ext}\|g_{\perp}$. Open circles show features with much less intensity as compared to the main branches which can be attributed to excited or forbidden transitions. (*Figure reprinted from Bazhenova et al. 2020.[85]*)
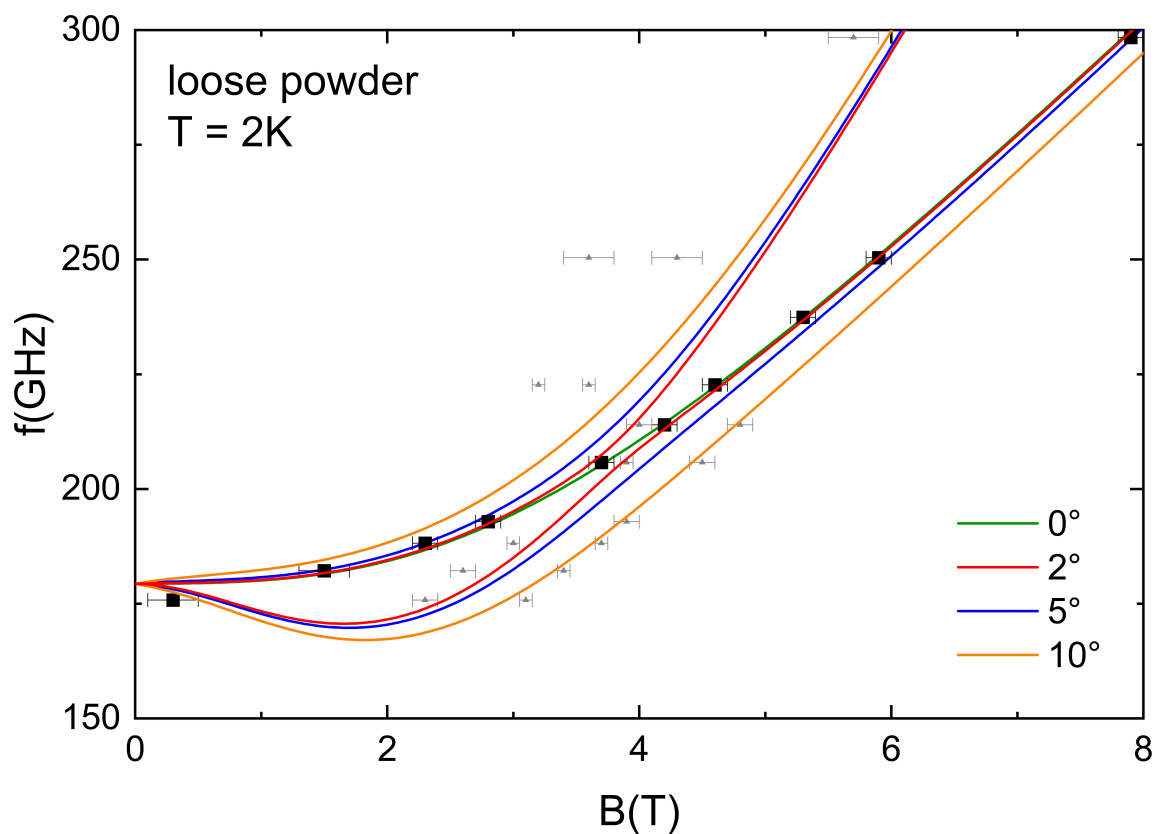
Figure A.15.: Magnetic field dependence of the resonance frequencies for a loose powder sample of **3**, at T = 2 K, and respective simulation results. Filled squares correspond to the main feature while grey symbols show features which are only slightly visible and associated with forbidden or excited transitions (cf. Fig. 5.3, 5.4). The solid lines visualize simulations of the observed main branch which corresponds to the ground state transition using the SH for a coupled dimer system shown in Eqn. 5.2 with the parameters listed in Tab. 5.1 and different angles between the direction of the crystal field xy-plane and the external magnetic field. (*Figure reprinted from Bazhenova et al. 2020.[85]*)
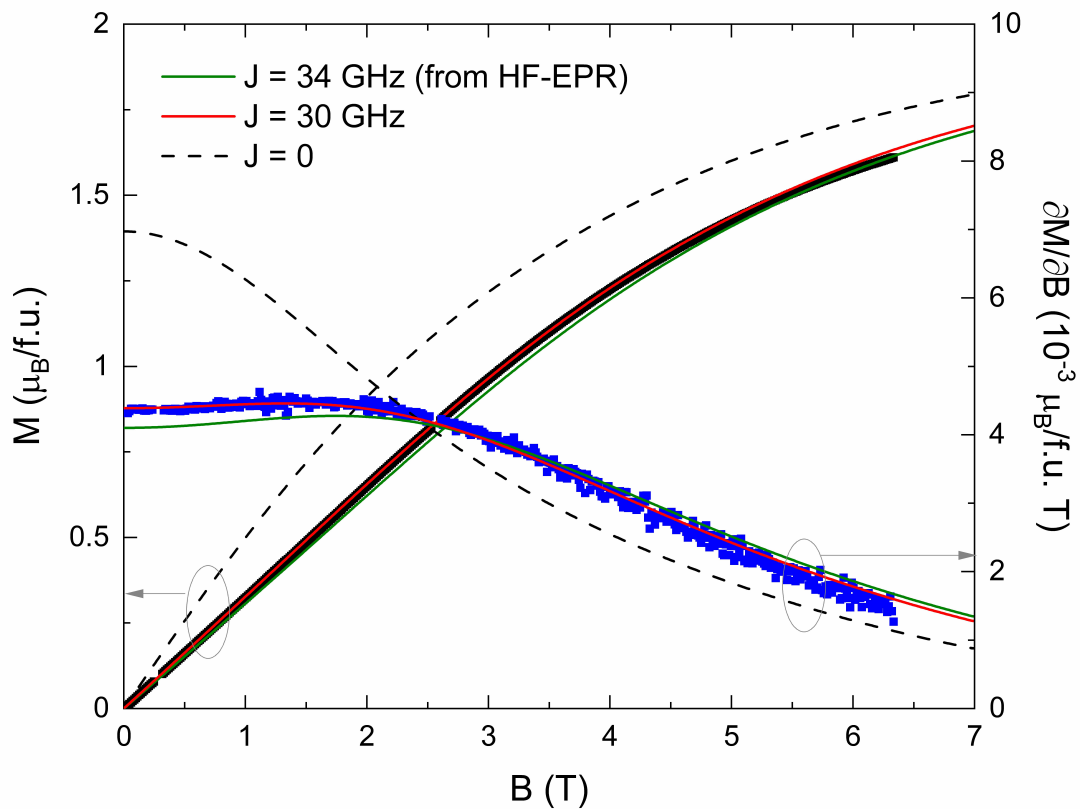
Figure A.16.: DC magnetization of (**3**) vs. magnetic field (black symbols, left ordinate) and its derivative (blue symbols, right ordinate) obtained at T = 2 K. Solid lines show simulations using the dimer model SH in Eqn. 5.2 with a coupling constant of $J = 34$ GHz (green) and $J = 30$ GHz (red), respectively. The dashed lines correspond to a simulation using a monomeric model for the vanadium centers. (*Figure reprinted from Bazhenova et al. 2020.[85]*)
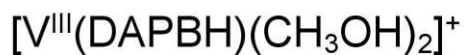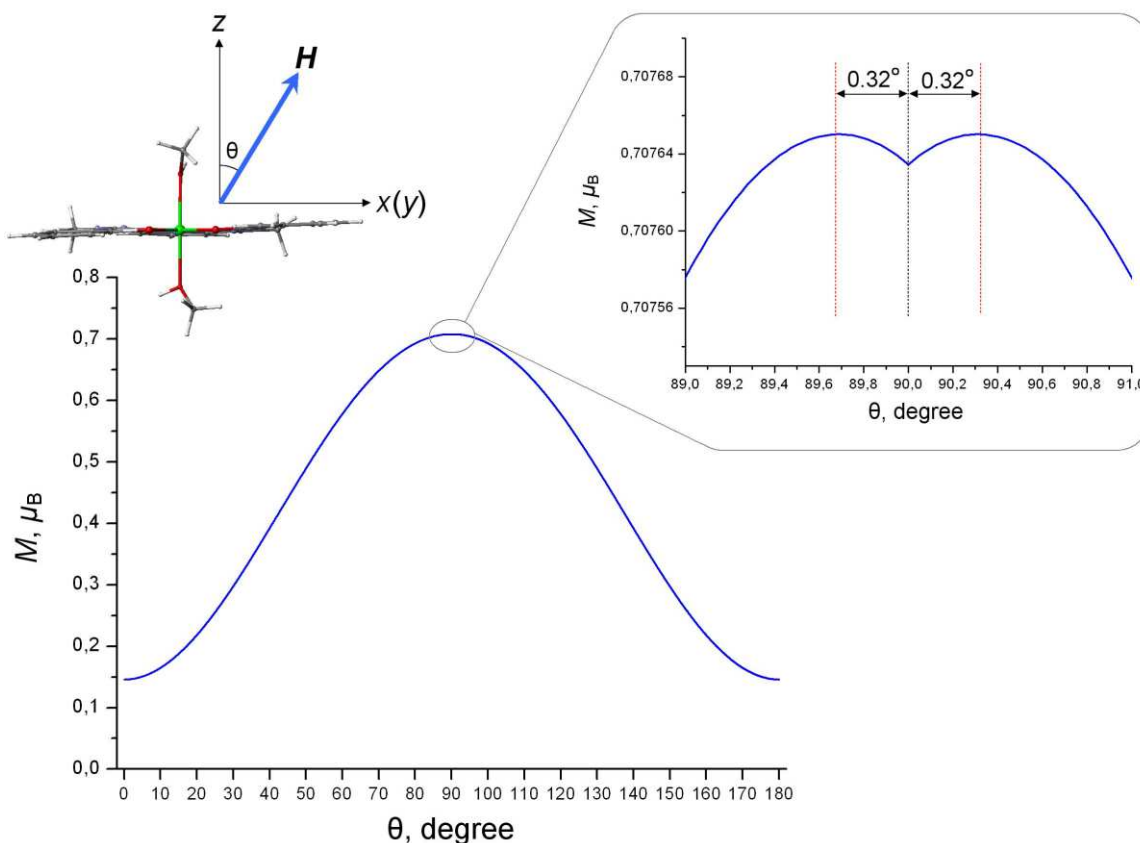
Figure A.17.: Calculated angular variation of the out-of-plane magnetization $M(\phi)$ of complex $[V(III)(DAPBH)(CH_3OH)_2]^+$ in **3** (at $H = 10000$ kOe and T = 2 K). Complex displays strongly positive magnetic anisotropy with a distinct maximum of magnetization in the equatorial VN_3O_2 plane (xy), with a deviation from it within $\approx 0.3°$ (shown in the inset). (*Computational details are given in the original work in ref. [85]. Calculations and construction of the plot was performed by Bazhenova et al.. Figure reprinted from Bazhenova et al. 2020.[85]*)
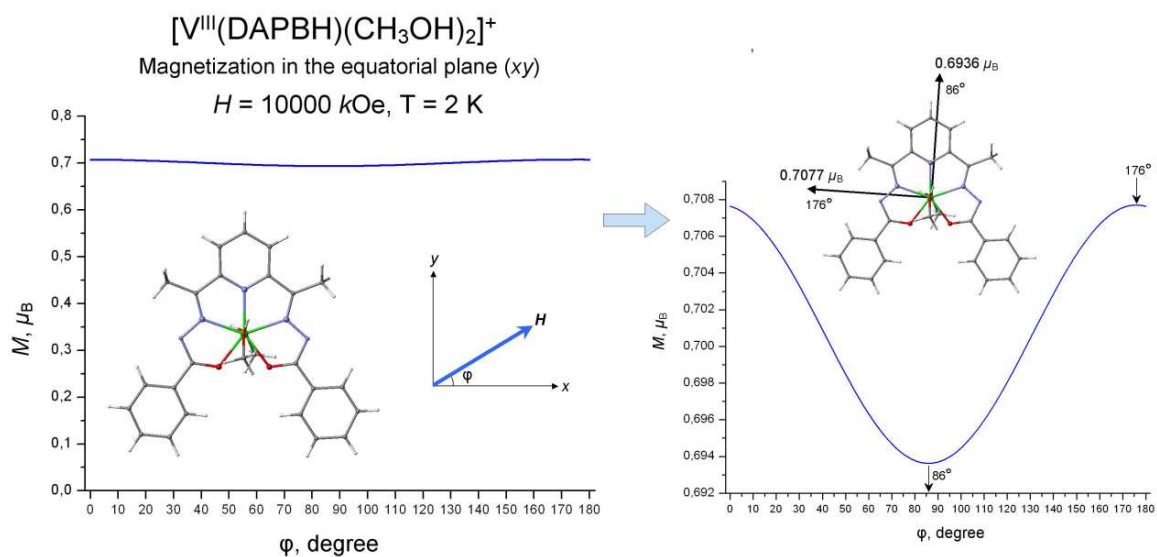
Figure A.18.: Calculated angular variation of the in-plane magnetization M(ϕ) of complex [V(III)(DAPBH)(CH$_3$OH)$_2$]$^+$ in **3** (at H = 10000 kOe and T = 2 K). In the equatorial plane ($H \parallel$ xy), magnetization is nearly isotropic with respect to the azimuthal angle ϕ. On the right: the orientations of the two principal magnetic axes in the equatorial xy plane are indicated. These two in-plane principal axes are almost equivalent in the magnetization. (*Calculations and construction of the plot was performed by Bazhenova et al.. Figure reprinted from Bazhenova et al. 2020.[85]*)

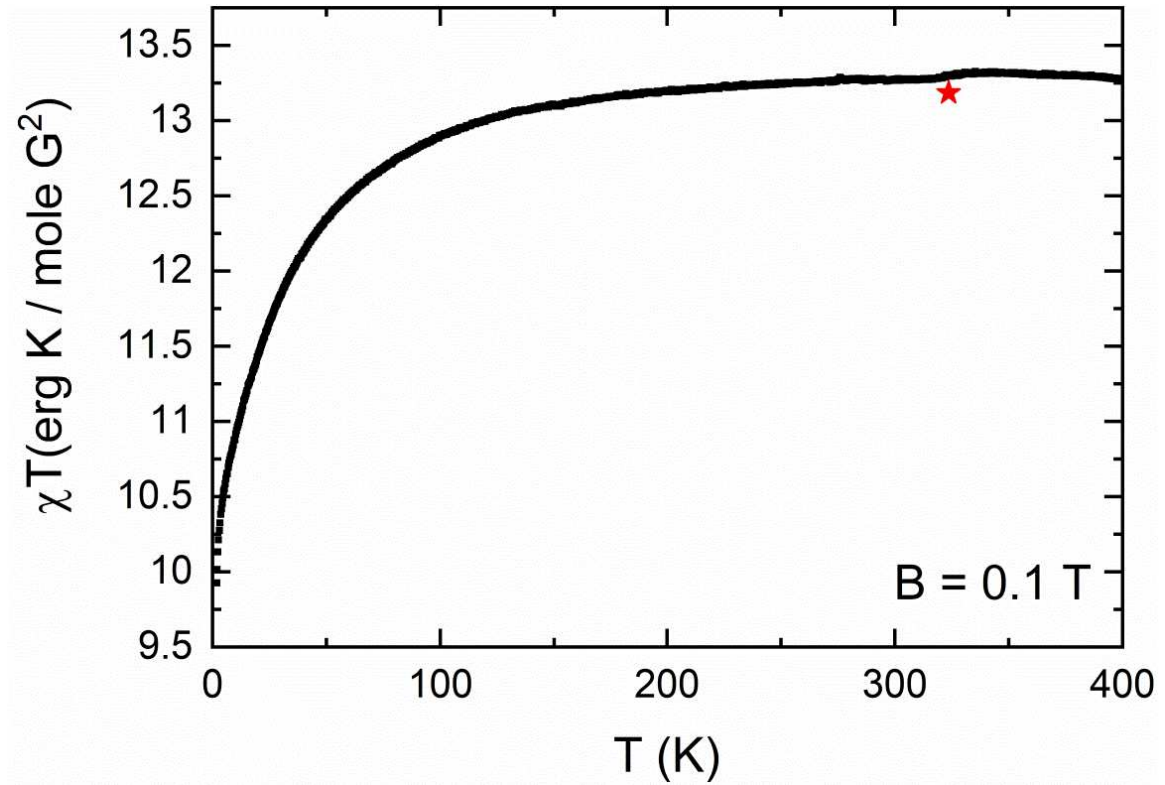# A.3. Supplementary Materials: Dy(III) Monomer

Figure A.19.: Temperature dependence of the DC magnetic susceptibility measured up to 400 K. The red star marks a small hump which is attributed to the loss of one water molecule per formula unit as confirmed by TGA investigations. (*Figure reprinted from Cieslik et al. 2021, ref. [126].*)

Generalized Debye model:

$$\chi''_{\text{AC}}(\omega) = \frac{(\chi_{\text{T}} - \chi_{\text{S}}) (\omega\tau)^{(1-\alpha)} \cos\left(\frac{\pi\alpha}{2}\right)}{1 + 2(\omega\tau)^{(1-\alpha)} \sin\left(\frac{\pi\alpha}{2}\right) + (\omega\tau)^{(2-2\alpha)}} \tag{A.2}$$

With the isothermal and the adiabatic susceptibility χ_{T} and χ_{S}, respectively, and α being an eccentricity parameter between 0 and 1 which takes the distribution of different relaxation times τ into account. An α value close to zero implies the presence of just one main relaxation constant or process.[11]
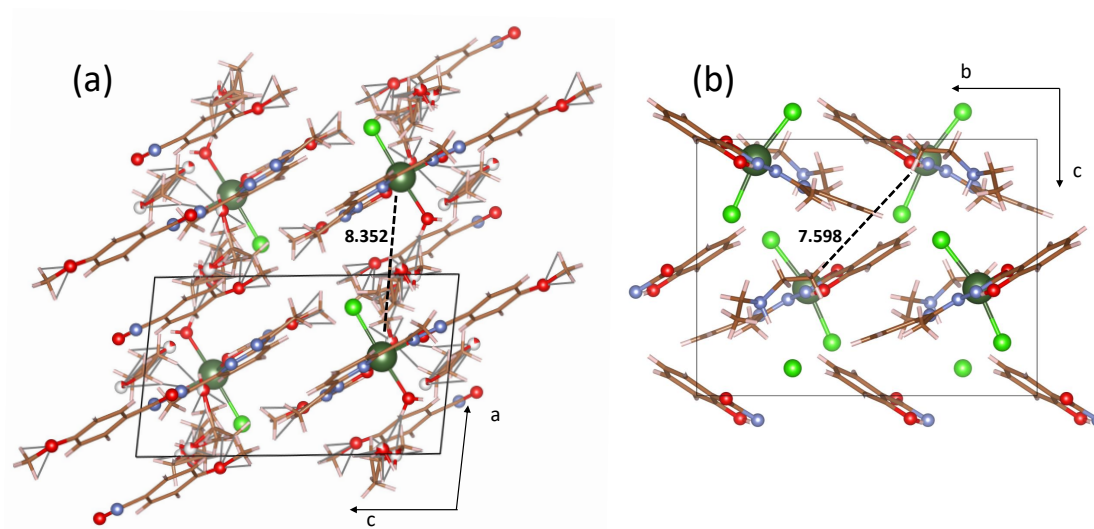
A.4. Supplementary Materials: Er(III) Monomers

Figure A.20.: Crystal Packing diagram for complex **1** (a) and **2** (b) along the crystallographic b and a axis, respectively. Dashed lines show the shortest intermolecular Er(III)-Er(III) distances which are indicated in the plot in Å. Dark green, Er; Red, O; light green, Cl; light blue, N; brown, C; white, H.
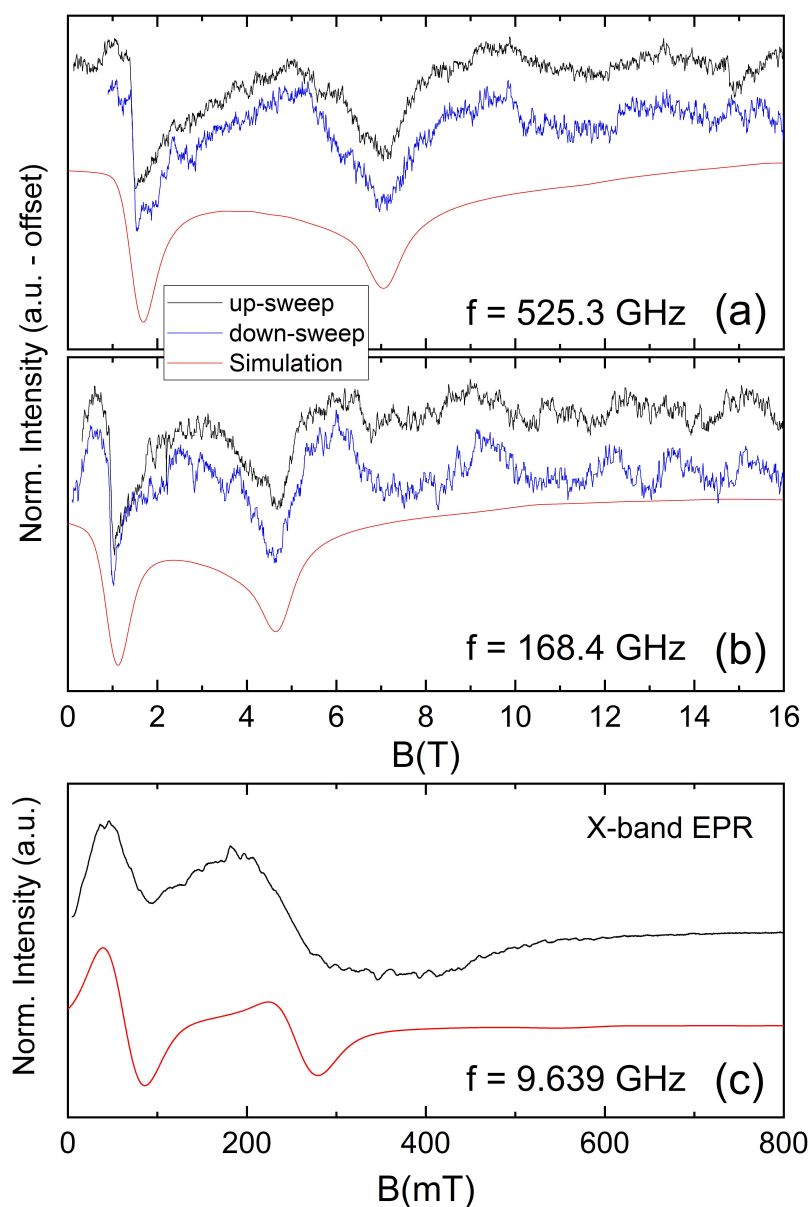
Figure A.21.: HF EPR spectra measured on a fixed powder sample **1** in an at $T = 2$ K at a frequency of f = 525.3 GHz (a), f = 168.4 GHz (b) as well as with the X-band EPR device at a frequency of f = 9.639 GHz (c). Due to the small signal intensity during the HF EPR measurements the signal position was deduced by the comparison of the up (black solid line in (a) and (b)) and the down sweep (blue solid lines). Red solid lines in all panels show a simulation assuming a S = 1/2 pseudospin approximation with a strongly anisotropic g-value as described in the main text.
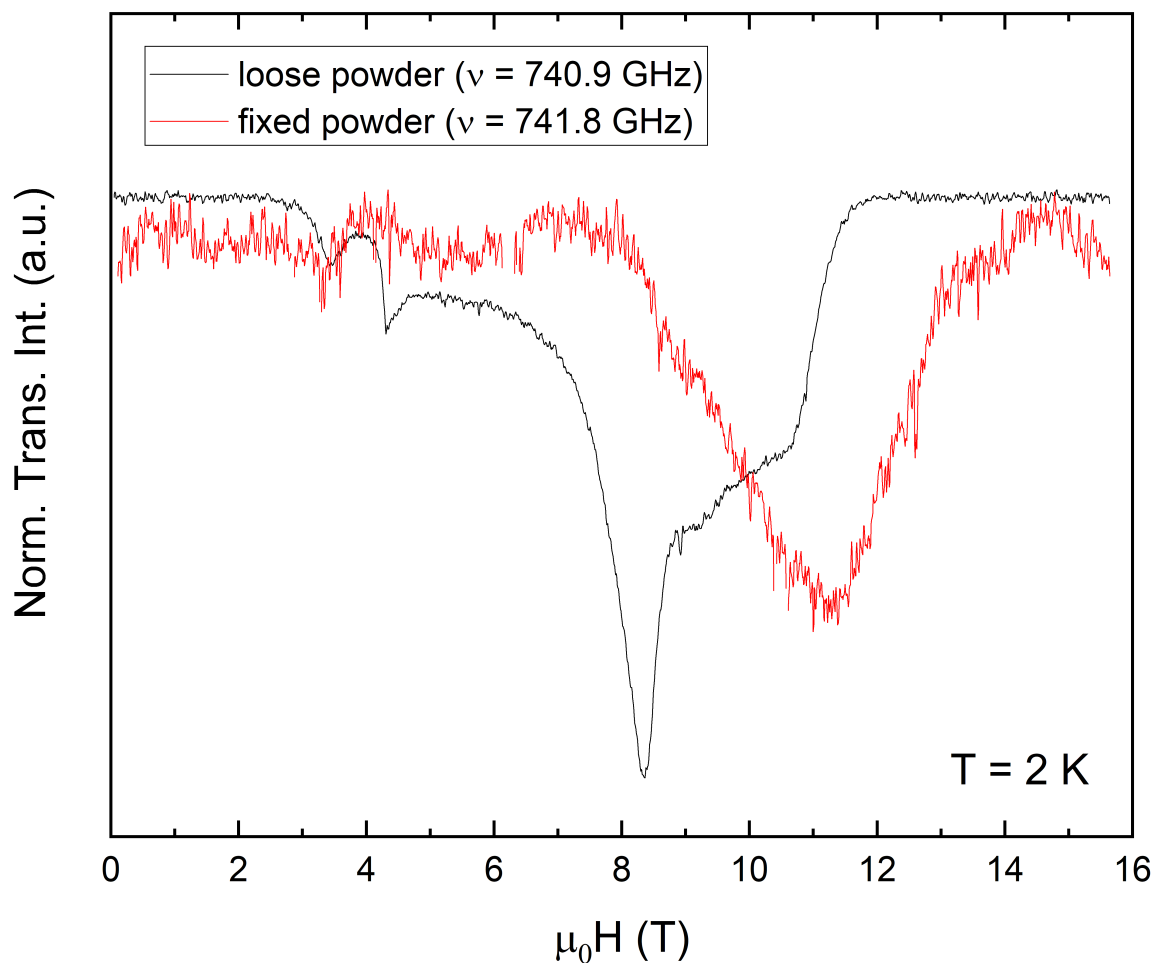
Figure A.22.: HF-EPR spectra measured on a loose and a fixed powder sample **2**, respectively, at almost the same frequency. For the fixed powder sample, spectral weight is shifted to higher fields and the resonance maximum is at the position of the shoulder-like feature of the loose powder spectra. We conclude: (1) The shoulder-like feature in the loose powder sample is arising from a small amount of crystallites which are not perfectly aligned. (2) The obvious differences between the spectral shape obtained for loose and fixed powder samples unambiguously show, that an alignment of the crystallites within the external magnetic field was successful for the majority of the loose powder.
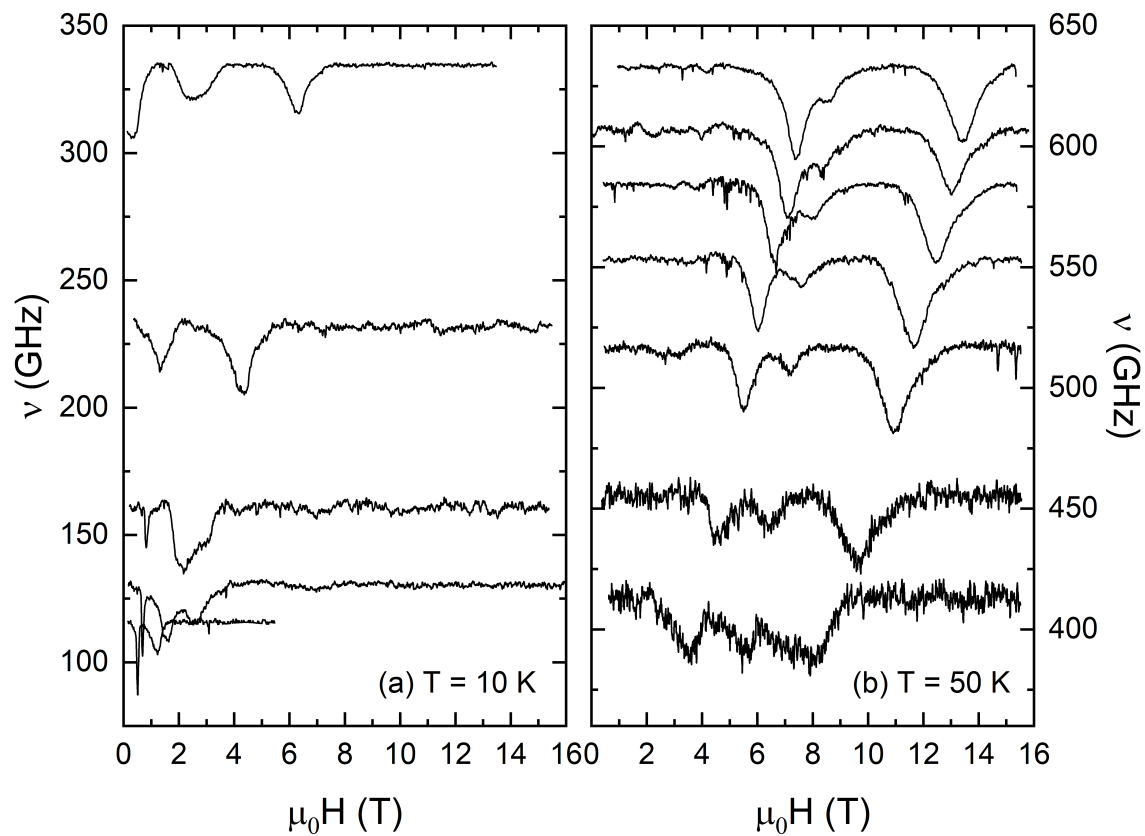
Figure A.23.: HF-EPR spectra obtained at a fixed temperature of (a) $T = 10$ K and (b) $T = 50$ K for **2**. The spectra are vertically shifted so that the minimum of each spectra coincides with the measurement frequency.

A.5. Supplementary Materials: Cu(II)$_2$Ln(III)
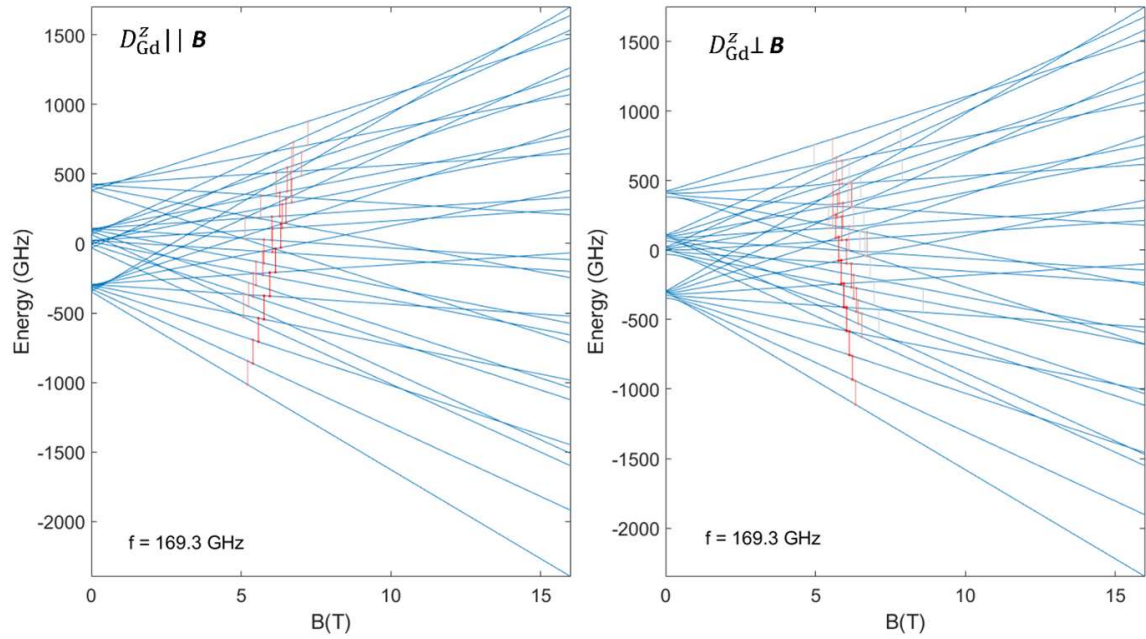
Figure A.24.: Simulation of the energy-level diagram (blue solid lines) for Cu$_2$Gd (complex **4**$_{Gd}$) at f = 169.3 GHz using the SH in Eqn. 6.8 with the parameters listed in Table 6.4 for (a) $D_{Gd}^z \parallel \mathbf{B}$ and (b) $D_{Gd}^z \perp \mathbf{B}$. Red and grey lines mark the allowed and forbidden transitions between the respective energy levels, respectively. The darker the red lines, the higher the transition probability and vice versa.
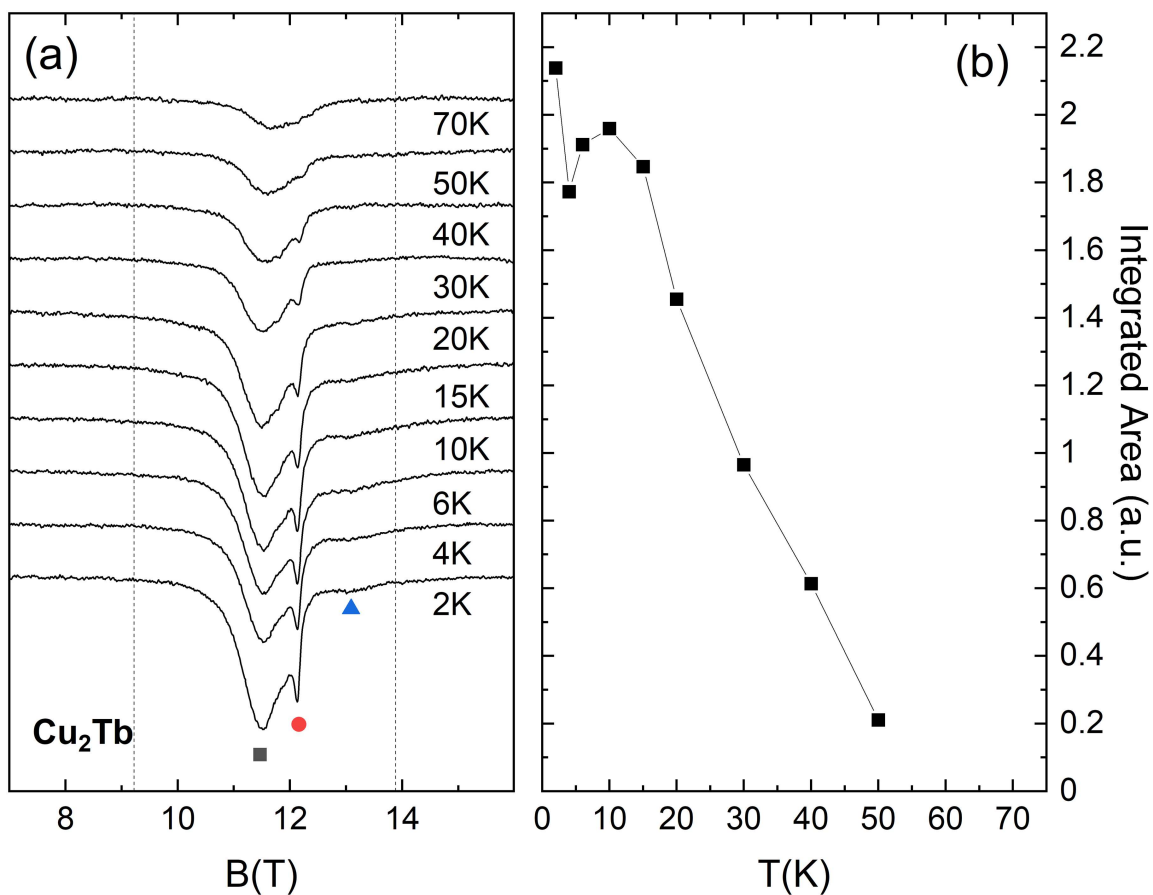
Figure A.25.: (a) HF-EPR spectra obtained on an oriented loose powder sample of Cu_2Tb (complex 5_{Tb}) at a measurement frequency of f = 746.6 GHz for different temperatures. Different symbols mark the corresponding branches shown in Figure 6.16 (b) (Blue branch not shown in Figure 6.16). (b) Integrated area of the signal peak (integrated range of data marked by dashed vertical lines in panel (a)).
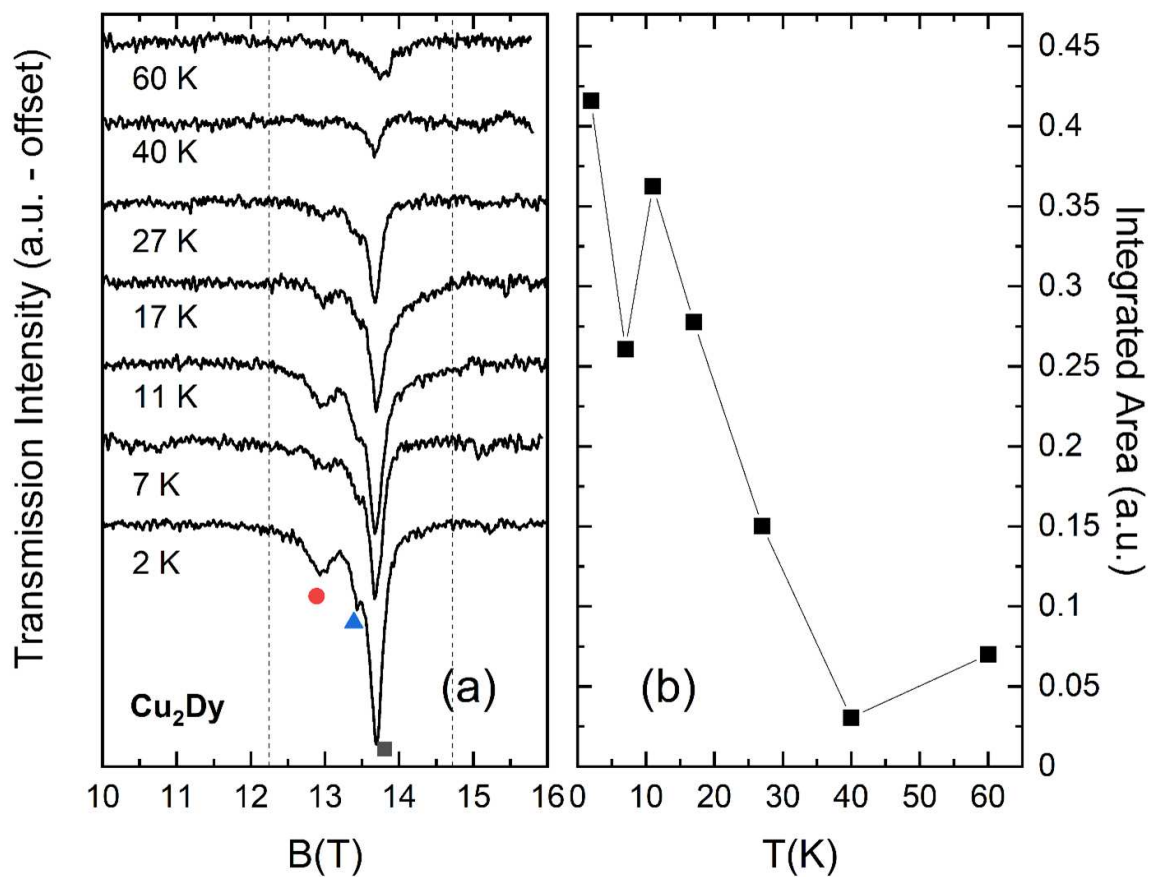
Figure A.26.: (a) HF-EPR spectra obtained on an oriented loose powder sample of Cu$_2$Dy (complex **6**$_{Dy}$) at a measurement frequency of f = 641.7 GHz for different temperatures. Different symbols mark the corresponding branches shown in Figure 6.16 (c) (Blue branch not shown in Figure 6.16) . (b) Integrated area of the signal peak (integrated range of data marked by dashed vertical lines in panel (a)).
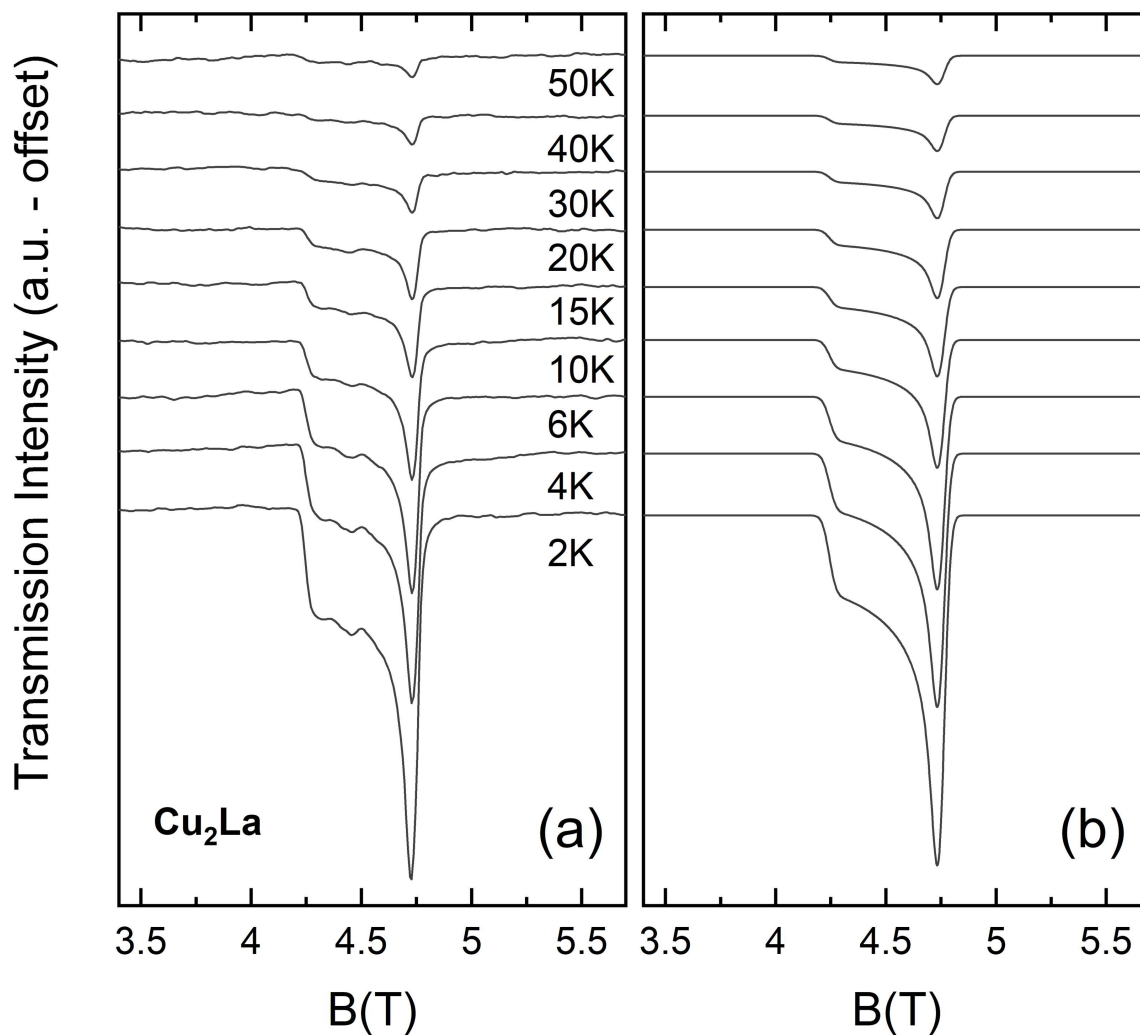
Figure A.27.: (a) HF-EPR spectra obtained on a fixed powder sample of Cu_2La (complex $\mathbf{1}_{La}$) at a measurement frequency of f = 138.4 GHz obtained for different temperatures. (b) Simulation using an anisotropic g-value for the Cu spins. Simulation parameters are shown in Table 6.4 in the main manuscript.
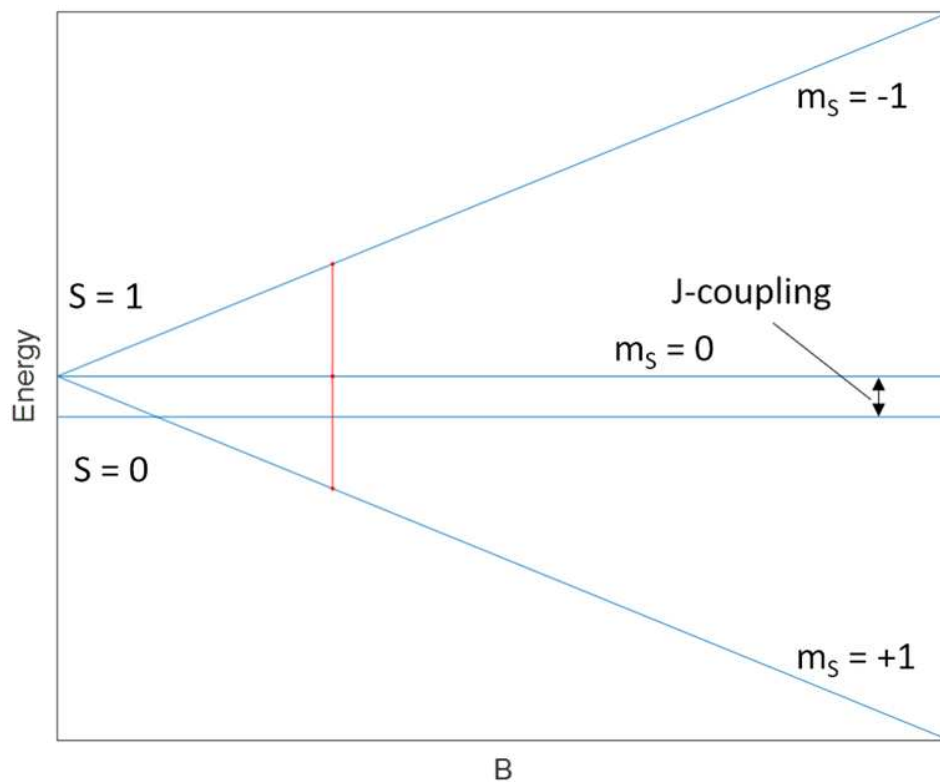
Figure A.28.: Simulation of the energy-level diagram for two antiferromagnetically coupled spins S = 1/2. Red lines show the expected transitions between the corresponding energy levels. Note that the gap due to afm coupling is not expected to show up in HF-EPR spectra.

Bibliography

[1] F. L. Bauer, K. Zuse, and H. Zemanek, *Der computer mein lebenswerk* (Springer Berlin / Heidelberg, Berlin, Heidelberg, 2013).

[2] C. Shi, V. Andino-Pavlovsky, S. A. Lee, T. Costa, J. Elloian, E. E. Konofagou, and K. L. Shepard, "Application of a sub 0.1-mm ^{3} implantable mote for in vivo real-time wireless temperature sensing", Science Advances **7**, 6312 (2021).

[3] I. Ross, "The invention of the transistor", Proceedings of the IEEE **86**, 7 (1998).

[4] A. I. of Physics, "1956 nobel prize in physics", Physics Today **10**, 16 (1957).

[5] R. Sessoli, D. Gatteschi, A. Caneschi, and M. A. Novak, "Magnetic bistability in a metal-ion cluster", Nature **365**, 141 (1993).

[6] M. N. Leuenberger and D. Loss, "Quantum computing in molecular magnets", Nature **410**, 789 (2001).

[7] C. J. Wedge, G. A. Timco, E. T. Spielberg, R. E. George, F. Tuna, S. Rigby, E. J. L. McInnes, R. E. P. Winpenny, S. J. Blundell, and A. Ardavan, "Chemical engineering of molecular qubits", Physical Review Letters **108**, 107204 (2012).

[8] G. A. Timco, S. Carretta, F. Troiani, F. Tuna, R. J. Pritchard, C. A. Muryn, E. J. L. McInnes, A. Ghirri, A. Candini, P. Santini, G. Amoretti, M. Affronte, and R. E. P. Winpenny, "Engineering the coupling between molecular spin qubits by coordination chemistry", Nature Nanotechnology **4**, 173 (2009).

[9] S. Accorsi, A.-L. Barra, A. Caneschi, G. Chastanet, A. Cornia, A. C. Fabretti, D. Gatteschi, C. Mortalò, E. Olivieri, F. Parenti, P. Rosa, R. Sessoli, L. Sorace, W. Wernsdorfer, and L. Zobbi, "Tuning anisotropy barriers in a family of tetrairon(III) single-molecule magnets with an $S = 5$ ground state", Journal of the American Chemical Society **128**, 4742 (2006).

[10] Y.-L. Wang, C.-B. Han, Y.-Q. Zhang, Q.-Y. Liu, C.-M. Liu, and S.-G. Yin, "Fine-tuning ligand to modulate the magnetic anisotropy in a carboxylate-bridged dy$_2$ single-molecule magnet system", Inorganic Chemistry **55**, 5578 (2016).

[11] D. Gatteschi, R. Sessoli, and J. Villain, *Molecular nanomagnets*, Mesoscopic physics and nanotechnology 5 (Oxford University Press, Oxford ; New York, 2006).

[12] C. Benelli and D. Gatteschi, *Introduction to molecular magnetism: from transition metals to lanthanides* (Wiley-VCH, Weinheim, 2015).

[13] J. J. Baldoví, E. Coronado, A. Gaita-Ariño, C. Gamer, M. Giménez-Marqués, and G. Mínguez Espallargas, "A SIM-MOF: three-dimensional organisation of single-ion magnets with anion-exchange capabilities", Chemistry - A European Journal **20**, 10695 (2014).

[14] G. Huang, G. Fernandez-Garcia, I. Badiane, M. Camarra, S. Freslon, O. Guillou, C. Daiguebonne, F. Totti, O. Cador, T. Guizouarn, B. Le Guennic, and K. Bernot, "Magnetic slow relaxation in a metal-organic framework made of chains of ferromagnetically coupled single-molecule magnets", Chemistry - A European Journal **24**, 6983 (2018).

[15] N. Hoshino, A. M. Ako, A. K. Powell, and H. Oshio, "Molecular magnets containing wheel motifs", Inorganic Chemistry **48**, 3396 (2009).

[16] Y. Pavlyukh, E. Rentschler, H. J. Elmers, W. Hübner, and G. Lefkidis, "Magnetism of metallacrown single-molecule magnets: from a simplest model to realistic systems", Physical Review B **97**, 214408 (2018).

[17] D. Luneau, "Molecular magnets", Current Opinion in Solid State and Materials Science **5**, 123 (2001).

[18] A. Abragam and B. Bleaney, *Electron paramagnetic resonance of transition ions*, Oxford classic texts in the physical sciences (Oxford University Press, Oxford, 2012).

[19] S. Tripathi, S. Vaidya, K. U. Ansari, N. Ahmed, E. Rivière, L. Spillecke, C. Koo, R. Klingeler, T. Mallah, G. Rajaraman, and M. Shanmugam, "Influence of a counteranion on the zero-field splitting of tetrahedral cobalt(II) thiourea complexes", Inorganic Chemistry **58**, 9085 (2019).

[20] L. Spillecke, S. Tripathi, C. Koo, M. Ansari, S. Vaidya, A. Rasamsetty, T. Mallah, G. Rajaraman, M. Shanmugam, and R. Klingeler, "A high-frequency EPR study of magnetic anisotropy and intermolecular interactions of co(II) ions", Polyhedron **208**, 115389 (2021).

[21] L. Gregoli, C. Danieli, A.-L. Barra, P. Neugebauer, G. Pellegrino, G. Poneti, R. Sessoli, and A. Cornia, "Magnetostructural correlations in tetrairon(III) single-molecule magnets", Chemistry - A European Journal **15**, 6456 (2009).

[22] Y.-F. Deng, T. Han, Z. Wang, Z. Ouyang, B. Yin, Z. Zheng, J. Krzystek, and Y.-Z. Zheng, "Uniaxial magnetic anisotropy of square-planar chromium(ii) complexes revealed by magnetic and HF-EPR studies", Chemical Communications **51**, 17688 (2015).

[23] E.-C. Yang, W. Wernsdorfer, S. Hill, R. S. Edwards, M. Nakano, S. Maccagnano, L. N. Zakharov, A. L. Rheingold, G. Christou, and D. N. Hendrickson, "Exchange bias in ni4 single-molecule magnets", Polyhedron **22**, 1727 (2003).

[24] E. Moreno Pineda, N. F. Chilton, R. Marx, M. Dörfel, D. O. Sells, P. Neugebauer, S.-D. Jiang, D. Collison, J. van Slageren, E. J. McInnes, and R. E. Winpenny, "Direct measurement of dysprosium(III)···dysprosium(III) interactions in a single-molecule magnet", Nature Communications **5**, 5243 (2014).

[25] S.-D. Jiang, B.-W. Wang, and S. Gao, "Advances in lanthanide single-ion magnets", in *Molecular nanomagnets and related phenomena*, Vol. 164, edited by S. Gao, Series Title: Structure and Bonding (Springer Berlin Heidelberg, Berlin, Heidelberg, 2014), pp. 111–141.

[26] S. Blundell, *Magnetism in condensed matter*, Reprint, Oxford master series in condensed matter physics 4 (Oxford Univ. Press, Oxford, 2014).

[27] P. Fazekas, *Lecture notes on electron correlation and magnetism*, Series in modern condensed matter physics v. 5 (World Scientific, Singapore ; River Edge, N.J, 1999).

[28] W. Nolting, *Grundkurs theoretische physik 5/1*, Springer-Lehrbuch, ISSN: 0937-7433 (Springer Berlin Heidelberg, Berlin, Heidelberg, 2009).

[29] T. Fließbach and H. Walliser, *Arbeitsbuch zur theoretischen physik: repetitorium und übungsbuch*, 3. Aufl (Spektrum Akademischer Verl, Heidelberg, 2012).

[30] M. Born and R. Oppenheimer, "Zur quantentheorie der moleküle", Annalen der Physik **389**, 457 (1927).

[31] L. Mollabashi and S. Jalali-Asadabadi, "Crystal fields of lithium rare-earth tetrafluorides and multiplet splitting of the +3 rare-earth ions", Physical Review B **102**, 045120 (2020).

[32] M. Murrie, "Cobalt(ii) single-molecule magnets", Chemical Society Reviews **39**, 1986 (2010).

[33] L. Llanos and D. Aravena, "Relaxation time enhancement by magnetic dilution in single-molecule magnets: an ab initio study", Journal of Magnetism and Magnetic Materials **489**, 165456 (2019).

[34] R. Boscaino, F. M. Gelardi, and J. P. Korb, "Non-bloch decay of transient nutations in $S = 1/2$ systems: an experimental investigation", Physical Review B **48**, 7077 (1993).

[35] E. I. Baibekov, "Decay of rabi oscillations induced by magnetic dipole interactions in dilute paramagnetic solids", JETP Letters **93**, 292 (2011).

[36] A. Morello, F. L. Mettes, F. Luis, J. F. Fernández, J. Krzystek, G. Aromí, G. Christou, and L. J. de Jongh, "Long-range ferromagnetic dipolar ordering of high-spin molecular clusters", Physical Review Letters **90**, 017206 (2003).

[37] G. Jeschke, *Einführung in die ESR-spektroskopie, ein vorlesungs-skript*, 1998.

[38] R. Shankar, *Principles of quantum mechanics*, 2nd ed (Plenum Press, New York, 1994).

[39] H. Casimir and F. du Pré, "Note on the thermodynamic interpretation of paramagnetic relaxation phenomena", Physica **5**, 507 (1938).

[40] K. S. Cole and R. H. Cole, "Dispersion and absorption in dielectrics, alternating current characteristics", The Journal of Chemical Physics **9**, 341 (1941).

[41] J. Clarke and A. I. Braginski, *Fundamentals and technology of SQUIDs and SQUID systems*, OCLC: 922799558 (2004).

[42] W. Buckel and R. Kleiner, *Supraleitung: grundlagen und anwendungen*, 6., vollst. überarb. und erw. Aufl., 1. Nachdr, Lehrbuch Physik (Wiley-VCH, Weinheim, 2007).

[43] Q. Design, *MPMS, SQUID VSM AC option user's manual*, Nov. 2010.

[44] Q. Design, *MPMS 3 user's manual, 1500-100, rev. f1*, June 2016.

[45] S. Zherlitsyn, T. Herrmannsdörfer, Y. Skourski, A. Sytcheva, and J. Wosnitza, "Design of non-destructive pulsed magnets at the HLD", Journal of Low Temperature Physics **146**, 719 (2007).

[46] S. Zherlitsyn, B. Wustmann, T. Herrmannsdörfer, and J. Wosnitza, "Magnet-technology development at the dresden high magnetic field laboratory", Journal of Low Temperature Physics **170**, 447 (2013).

[47] G. A. Bain and J. F. Berry, "Diamagnetic corrections and pascal's constants", Journal of Chemical Education **85**, 532 (2008).

[48] A. R. Harutyunyan, A. A. Kuznetsov, O. A. Kuznetsov, and O. Kaliya, "Metal-organic magnetic materials based on cobalt phthalocyanine and possibilities of their application in medicine", Journal of Magnetism and Magnetic Materials **194**, 16 (1999).

[49] M. Kobayashi and S. Shimizu, "Cobalt proteins", European Journal of Biochemistry **261**, 1 (1999).

[50] A. R. Battersby, "Biosynthesis of vitamin b12", Accounts of Chemical Research **26**, 15 (1993).

[51] M. Dennis and P. E. Kolattukudy, "A cobalt-porphyrin enzyme converts a fatty aldehyde to a hydrocarbon and CO.", Proceedings of the National Academy of Sciences **89**, 5306 (1992).

[52] E.-C. Yang, D. N. Hendrickson, W. Wernsdorfer, M. Nakano, L. N. Zakharov, R. D. Sommer, A. L. Rheingold, M. Ledezma-Gairaud, and G. Christou, "Cobalt single-molecule magnet", Journal of Applied Physics **91**, 7382 (2002).

[53] S. Gao, ed., *Molecular nanomagnets and related phenomena*, Vol. 164, Structure and Bonding (Springer Berlin Heidelberg, Berlin, Heidelberg, 2015).

[54] W. Wernsdorfer, S. Bhaduri, C. Boskovic, G. Christou, and D. N. Hendrickson, "Spin-parity dependent tunneling of magnetization in single-molecule magnets", Physical Review B **65**, 180403 (2002).

[55] M. S. Fataftah, J. M. Zadrozny, D. M. Rogers, and D. E. Freedman, "A mononuclear transition metal single-molecule magnet in a nuclear spin-free ligand environment", Inorganic Chemistry **53**, 10716 (2014).

[56] Y. Rechkemmer, F. D. Breitgoff, M. van der Meer, M. Atanasov, M. Hakl, M. Orlita, P. Neugebauer, F. Neese, B. Sarkar, and J. van Slageren, "A four-coordinate cobalt(II) single-ion magnet with coercivity and a very high energy barrier", Nature Communications **7**, 10467 (2016).

[57] M. R. Saber and K. R. Dunbar, "Ligands effects on the magnetic anisotropy of tetrahedral cobalt complexes", Chem. Commun. **50**, 12266 (2014).

[58] E. A. Suturina, D. Maganas, E. Bill, M. Atanasov, and F. Neese, "Magneto-structural correlations in a series of pseudotetrahedral [co ^{II} (XR) $_4$] $^{2-}$ single molecule magnets: an ab initio ligand field study", Inorganic Chemistry **54**, 9948 (2015).

[59] S. Vaidya, S. Tewary, S. K. Singh, S. K. Langley, K. S. Murray, Y. Lan, W. Wernsdorfer, G. Rajaraman, and M. Shanmugam, "What controls the sign and magnitude of magnetic anisotropy in tetrahedral cobalt(II) single-ion magnets?", Inorganic Chemistry **55**, 9564 (2016).

[60] J. M. Zadrozny, J. Telser, and J. R. Long, "Slow magnetic relaxation in the tetrahedral cobalt(II) complexes [co(EPh)$_4$]$^{2-}$ (EO, s, se)", Polyhedron **64**, 209 (2013).

[61] S. Tripathi, S. Vaidya, N. Ahmed, E. Andreasen Klahn, H. Cao, L. Spillecke, C. Koo, S. Spachmann, R. Klingeler, G. Rajaraman, J. Overgaard, and M. Shanmugam, "Structure-property correlation in stabilizing axial magnetic anisotropy in octahedral co(II) complexes", Cell Reports Physical Science **2**, 100404 (2021).

[62] Y.-Y. Zhu, Y.-Q. Zhang, T.-T. Yin, C. Gao, B.-W. Wang, and S. Gao, "A family of co ^{II} co ^{III} $_3$ single-ion magnets with zero-field slow magnetic relaxation: fine tuning of energy barrier by remote substituent and counter cation", Inorganic Chemistry **54**, 5475 (2015).

[63] Z.-S. Yao, S.-Q. Wu, Y. Kitagawa, S.-Q. Su, Y.-G. Huang, G.-L. Li, Z.-H. Ni, H. Nojiri, Y. Shiota, K. Yoshizawa, S. Kang, S. Kanegawa, and O. Sato, "Anisotropic change in the magnetic susceptibility of a dynamic single crystal of a cobalt(II) complex", Angewandte Chemie International Edition **56**, 717 (2017).

[64] E. A. Suturina, J. Nehrkorn, J. M. Zadrozny, J. Liu, M. Atanasov, T. Wey-hermüller, D. Maganas, S. Hill, A. Schnegg, E. Bill, J. R. Long, and F. Neese, "Magneto-structural correlations in pseudotetrahedral forms of the [co(SPh) $_4$] $^{2-}$ complex probed by magnetometry, MCD spectroscopy, advanced EPR techniques, and ab initio electronic structure calculations", Inorganic Chemistry **56**, 3102 (2017).

[65] Y. Krupskaya, A. Alfonsov, A. Parameswaran, V. Kataev, R. Klingeler, G. Steinfeld, N. Beyer, M. Gressenbuch, B. Kersting, and B. Büchner, "Interplay of magnetic exchange interactions and ni-s-ni bond angles in polynuclear nickel(II) complexes", ChemPhysChem, NA (2010).

[66] S. Stoll and A. Schweiger, "EasySpin, a comprehensive software package for spectral simulation and analysis in EPR", Journal of Magnetic Resonance **178**, 42 (2006).

[67] P. Comba, M. Großhauser, R. Klingeler, C. Koo, Y. Lan, D. Müller, J. Park, A. Powell, M. J. Riley, and H. Wadepohl, "Magnetic interactions in a series of homodinuclear lanthanide complexes", Inorganic Chemistry **54**, 11247 (2015).

[68] A. N. Vasiliev, O. S. Volkova, E. A. Zvereva, E. A. Ovchenkov, I. Munaò, L. Clark, P. Lightfoot, E. L. Vavilova, S. Kamusella, H.-H. Klauss, J. Werner, C. Koo, R. Klingeler, and A. A. Tsirlin, "1/3 magnetization plateau and frustrated ferrimagnetism in a sodium iron phosphite", Physical Review B **93**, 134401 (2016).

[69] O. Waldmann, "A criterion for the anisotropy barrier in single-molecule magnets", Inorganic Chemistry **46**, 10035 (2007).

[70] G. A. Craig and M. Murrie, "3d single-ion magnets", Chemical Society Reviews **44**, 2135 (2015).

[71] Y.-Z. Zhang, S. Gómez-Coca, A. J. Brown, M. R. Saber, X. Zhang, and K. R. Dunbar, "Trigonal antiprismatic co(ii) single molecule magnets with large uniaxial anisotropies: importance of raman and tunneling mechanisms", Chemical Science **7**, 6519 (2016).

[72] S. Kanegawa, S. Karasawa, M. Maeyama, M. Nakano, and N. Koga, "Crystal design of monometallic single-molecule magnets consisting of cobalt-aminoxyl heterospins", Journal of the American Chemical Society **130**, 3079 (2008).

[73] A. Schnegg, J. Behrends, K. Lips, R. Bittl, and K. Holldack, "Frequency domain fourier transform THz-EPR on single molecule magnets using coherent synchrotron radiation", Physical Chemistry Chemical Physics **11**, 6820 (2009).

[74] K. Ridier, B. Gillon, A. Gukasov, G. Chaboussant, A. Cousson, D. Luneau, A. Borta, J.-F. Jacquot, R. Checa, Y. Chiba, H. Sakiyama, and M. Mikuriya, "Polarized neutron diffraction as a tool for mapping molecular magnetic anisotropy: local susceptibility tensors in co ^{II} complexes", Chemistry - A European Journal **22**, 724 (2016).

[75] H.-H. Cui, J. Wang, X.-T. Chen, and Z.-L. Xue, "Slow magnetic relaxation in five-coordinate spin-crossover cobalt(ii) complexes", Chemical Communications **53**, 9304 (2017).

[76] S. Titos-Padilla, J. Ruiz, J. M. Herrera, E. K. Brechin, W. Wersndorfer, F. Lloret, and E. Colacio, "Dilution-triggered SMM behavior under zero field in a luminescent zn_2dy_2 tetranuclear complex incorporating carbonato-bridging ligands derived from atmospheric CO_2 fixation", Inorganic Chemistry **52**, 9620 (2013).

[77] C. Boskovic, R. Bircher, P. L. W. Tregenna-Piggott, H. U. Güdel, C. Paulsen, W. Wernsdorfer, A.-L. Barra, E. Khatsko, A. Neels, and H. Stoeckli-Evans, "Ferromagnetic and antiferromagnetic intermolecular interactions in a new family of mn_4 complexes with an energy barrier to magnetization reversal", Journal of the American Chemical Society **125**, 14046 (2003).

[78] Z.-B. Hu, Z.-Y. Jing, M.-M. Li, L. Yin, Y.-D. Gao, F. Yu, T.-P. Hu, Z. Wang, and Y. Song, "Important role of intermolecular interaction in cobalt(II) single-ion magnet from single slow relaxation to double slow relaxation", Inorganic Chemistry **57**, 10761 (2018).

[79] F. Habib, I. Korobkov, and M. Murugesu, "Exposing the intermolecular nature of the second relaxation pathway in a mononuclear cobalt(ii) single-molecule magnet with positive anisotropy", Dalton Transactions **44**, 6368 (2015).

[80] J. E. O'Connor and E. L. Amma, "Crystal and molecular structure of trans-dichlorotetrakis(thiourea) cobalt(II)", Inorganic Chemistry **8**, 2367 (1969).

[81] R. Herchel, L. Váhovská, I. Potočňák, and Z. Trávníček, "Slow magnetic relaxation in octahedral cobalt(II) field-induced single-ion magnet with positive axial and large rhombic anisotropy", Inorganic Chemistry **53**, 5896 (2014).

[82] R. Díaz-Torres, M. Menelaou, O. Roubeau, A. Sorrenti, G. Brandariz-de-Pedro, E. C. Sañudo, S. J. Teat, J. Fraxedas, E. Ruiz, and N. Aliaga-Alcalde, "Multiscale study of mononuclear co ^{II} SMMs based on curcuminoid ligands", Chemical Science **7**, 2793 (2016).

[83] Y.-Y. Zhu, C. Cui, Y.-Q. Zhang, J.-H. Jia, X. Guo, C. Gao, K. Qian, S.-D. Jiang, B.-W. Wang, Z.-M. Wang, and S. Gao, "Zero-field slow magnetic relaxation from single co(ii) ion: a transition metal single-molecule magnet with high anisotropy barrier", Chemical Science **4**, 1802 (2013).

[84] Y.-F. Deng, M. K. Singh, D. Gan, T. Xiao, Y. Wang, S. Liu, Z. Wang, Z. Ouyang, Y.-Z. Zhang, and K. R. Dunbar, "Probing the axial distortion effect on the magnetic anisotropy of octahedral co(II) complexes", Inorganic Chemistry **59**, 7622 (2020).

[85] T. A. Bazhenova, L. V. Zorina, S. V. Simonov, V. S. Mironov, O. V. Maximova, L. Spillecke, C. Koo, R. Klingeler, Y. V. Manakin, A. N. Vasiliev, and E. B. Yagubskii, "The first pentagonal-bipyramidal vanadium(iii) complexes with a schiff-base n$_3$o$_2$ pentadentate ligand: synthesis, structure and magnetic properties", Dalton Transactions **49**, 15287 (2020).

[86] W.-P. Chen, J. Singleton, L. Qin, A. Camón, L. Engelhardt, F. Luis, R. E. P. Winpenny, and Y.-Z. Zheng, "Quantum monte carlo simulations of a giant ni21gd20 cage with a s = 91 spin ground state", Nature Communications **9**, 2107 (2018).

[87] T. Gupta and G. Rajaraman, "Modelling spin hamiltonian parameters of molecular nanomagnets", Chemical Communications **52**, 8972 (2016).

[88] M. Idešicová, J. Titiš, J. Krzystek, and R. Boča, "Zero-field splitting in pseudotetrahedral co(II) complexes: a magnetic, high-frequency and -field EPR, and computational study", Inorganic Chemistry **52**, 9409 (2013).

[89] A. K. Mondal, M. Sundararajan, and S. Konar, "A new series of tetrahedral co(ii) complexes [CoLX$_2$] (x = NCS, cl, br, i) manifesting single-ion magnet features", Dalton Transactions **47**, 3745 (2018).

[90] S. Sottini, G. Poneti, S. Ciattini, N. Levesanos, E. Ferentinos, J. Krzystek, L. Sorace, and P. Kyritsis, "Magnetic anisotropy of tetrahedral co ^{II} single-ion magnets: solid-state effects", Inorganic Chemistry **55**, 9537 (2016).

[91] J. Krzystek, S. A. Zvyagin, A. Ozarowski, A. T. Fiedler, T. C. Brunold, and J. Telser, "Definitive spectroscopic determination of zero-field splitting in high-spin cobalt(II)", Journal of the American Chemical Society **126**, 2148 (2004).

[92] S. F. M. Schmidt, C. Koo, V. Mereacre, J. Park, D. W. Heermann, V. Kataev, C. E. Anson, D. Prodius, G. Novitchi, R. Klingeler, and A. K. Powell, "A three-pronged attack to investigate the electronic structure of a family of ferromagnetic fe_4ln_2 cyclic coordination clusters: a combined magnetic susceptibility, high-field/high-frequency electron paramagnetic resonance, and ^{57}fe mössbauer study", Inorganic Chemistry **56**, 4796 (2017).

[93] Y. Skourski, M. D. Kuz'min, K. P. Skokov, A. V. Andreev, and J. Wosnitza, "High-field magnetization of ho2fe17", Physical Review B **83**, 214420 (2011).

[94] B. Bauer, L. D. Carr, H. G. Evertz, A. Feiguin, J. Freire, S. Fuchs, L. Gamper, J. Gukelberger, E. Gull, S. Guertler, A. Hehn, R. Igarashi, S. V. Isakov, D. Koop, P. N. Ma, P. Mates, H. Matsuo, O. Parcollet, G. Pawłowski, J. D. Picon, L. Pollet, E. Santos, V. W. Scarola, U. Schollwöck, C. Silva, B. Surer, S. Todo, S. Trebst, M. Troyer, M. L. Wall, P. Werner, and S. Wessel, "The ALPS project release 2.0: open source software for strongly correlated systems", Journal of Statistical Mechanics: Theory and Experiment **2011**, P05001 (2011).

[95] A. W. Sandvik, "Stochastic series expansion method with operator-loop update", Physical Review B **59**, R14157 (1999).

[96] A. K. Bar, C. Pichon, and J.-P. Sutter, "Magnetic anisotropy in two- to eight-coordinated transition–metal complexes: recent developments in molecular magnetism", Coordination Chemistry Reviews **308**, 346 (2016).

[97] T. Kajiwara, K. Takahashi, T. Hiraizumi, S. Takaishi, and M. Yamashita, "Structural correlations between the crystal field and magnetic anisotropy of ln–cu single-molecule magnets", CrystEngComm **11**, 2110 (2009).

[98] K. L. M. Harriman, J. Murillo, E. A. Suturina, S. Fortier, and M. Murugesu, *See-saw shaped dy(III) single-molecule magnets with high anisotropy barriers*, preprint (Jan. 22, 2020).

[99] S. K. Langley, N. F. Chilton, B. Moubaraki, and K. S. Murray, "Anisotropy barrier enhancement via ligand substitution in tetranuclear co(III)2ln(III)2 single molecule magnets", Chemical Communications **49**, 6965 (2013).

[100] M. A. Palacios, J. Nehrkorn, E. A. Suturina, E. Ruiz, S. Gómez-Coca, K. Holldack, A. Schnegg, J. Krzystek, J. M. Moreno, and E. Colacio, "Analysis of magnetic anisotropy and the role of magnetic dilution in triggering single-molecule magnet (SMM) behavior in a family of co ^{II} y ^{III} dinuclear complexes with easy-plane anisotropy", Chemistry – A European Journal **23**, 11649 (2017).

[101] M. Perfetti, J. Rinck, G. Cucinotta, C. E. Anson, X. Gong, L. Ungur, L. Chibotaru, M.-E. Boulon, A. K. Powell, and R. Sessoli, "Single crystal investigations unravel the magnetic anisotropy of the "square-in square" cr4dy4 SMM coordination cluster", Frontiers in Chemistry **7**, 6 (2019).

[102] L. Escalera-Moreno, J. J. Baldoví, A. Gaita-Ariño, and E. Coronado, "Spin states, vibrations and spin relaxation in molecular nanomagnets and spin qubits: a critical perspective", Chemical Science **9**, 3265 (2018).

[103] M. J. Martínez-Pérez, S. Cardona-Serra, C. Schlegel, F. Moro, P. J. Alonso, H. Prima-García, J. M. Clemente-Juan, M. Evangelisti, A. Gaita-Ariño, J. Sesé, J. van Slageren, E. Coronado, and F. Luis, "Gd-based single-ion magnets with tunable magnetic anisotropy: molecular design of spin qubits", Physical Review Letters **108**, 247213 (2012).

[104] L. Tesi, E. Lucaccini, I. Cimatti, M. Perfetti, M. Mannini, M. Atzori, E. Morra, M. Chiesa, A. Caneschi, L. Sorace, and R. Sessoli, "Quantum coherence in a processable vanadyl complex: new tools for the search of molecular spin qubits", Chemical Science **7**, 2074 (2016).

[105] C.-J. Yu, M. J. Graham, J. M. Zadrozny, J. Niklas, M. D. Krzyaniak, M. R. Wasielewski, O. G. Poluektov, and D. E. Freedman, "Long coherence times in nuclear spin-free vanadyl qubits", Journal of the American Chemical Society **138**, 14678 (2016).

[106] M.-X. Xu, Z. Liu, B.-W. Dong, H.-H. Cui, Y.-X. Wang, J. Su, Z. Wang, Y. Song, X.-T. Chen, S.-D. Jiang, and S. Gao, "Single-crystal study of a low spin co(II) molecular qubit: observation of anisotropic rabi cycles", Inorganic Chemistry **58**, 2330 (2019).

[107] M. Atzori, L. Tesi, E. Morra, M. Chiesa, L. Sorace, and R. Sessoli, "Room-temperature quantum coherence and rabi oscillations in vanadyl phthalocyanine: toward multifunctional molecular spin qubits", Journal of the American Chemical Society **138**, 2154 (2016).

[108] R. Boča, C. Rajnák, J. Titiš, and D. Valigura, "Field supported slow magnetic relaxation in a mononuclear cu(II) complex", Inorganic Chemistry **56**, 1478 (2017).

[109] M. Ding, G. E. Cutsail III, D. Aravena, M. Amoza, M. Rouzières, P. Dechambenoit, Y. Losovyj, M. Pink, E. Ruiz, R. Clérac, and J. M. Smith, "A low spin manganese(iv) nitride single molecule magnet", Chemical Science **7**, 6132 (2016).

[110] J. M. Zadrozny, A. T. Gallagher, T. D. Harris, and D. E. Freedman, "A porous array of clock qubits", Journal of the American Chemical Society **139**, 7089 (2017).

[111] A. B. Buades, V. S. Arderiu, L. Maxwell, M. Amoza, D. Choquesillo-Lazarte, N. Aliaga-Alcalde, C. Viñas, F. Teixidor, and E. Ruiz, "Slow-spin relaxation of a low-spin $S = 1/2$ fe ^{III} carborane complex", Chemical Communications **55**, 3825 (2019).

[112] I. Bhowmick, D. W. Shaffer, J. Y. Yang, and M. P. Shores, "Single molecule magnet behaviour in a square planar $S = 1/2$ co(ii) complex and spin-state assignment of multiple relaxation modes", Chemical Communications **56**, 6711 (2020).

[113] L. Chen, J. Song, W. Zhao, G. Yi, Z. Zhou, A. Yuan, Y. Song, Z. Wang, and Z.-W. Ouyang, "A mononuclear five-coordinate co(ii) single molecule magnet with a spin crossover between the $S = 1/2$ and $3/2$ states", Dalton Transactions **47**, 16596 (2018).

[114] J. K. Stalick, P. W. R. Corfield, and D. W. Meek, "Structural isomerization and rapid interconversion of two five-coordinate cobalt(II) complexes containing chelating diphosphine ligands", Journal of the American Chemical Society **94**, 6194 (1972).

[115] J. K. Stalick, D. W. Meek, B. Y. K. Ho, and J. J. Zuckerman, "^{119m} Sn mössbauer parameters and crystal structure of the SnCl $_3$ $^-$ ion in two forms of chlorobis[bis-(1,2-diphenylphosphino)ethane]cobalt(ii) trichlorostannate(ii)", J. Chem. Soc., Chem. Commun. **0**, 630 (1972).

[116] J. K. Stalick, P. W. R. Corfields, and D. W. Meek, "Trigonal-bipyramidal and square-pyramidal five-coordinate cobalt(II). crystal and molecular structures of the red and green isomers of chlorobis [1,2-bis(diphenylphosphino)ethane] cobalt(II) trichlorostannate(II)", Inorganic Chemistry **12**, 1668 (1973).

[117] V. Malatesta and B. R. McGarvey, "Single crystal electron spin resonance of low spin co(II) and of cu(II) schiff base complexes", Canadian Journal of Chemistry **53**, 3791 (1975).

[118] C. N. Sethulakshmi and P. T. Manoharan, "EPR and electronic structural investigations of a few low-spin bis(tertiary phosphine) complexes of cobalt(II)", Inorganic Chemistry **20**, 2533 (1981).

[119] A. von Zelewsky and M. Zobrist, "EPR. spectroscopic investigations of planar cu (II)- and low-spin co (II)-complexes in nematic phases and in single crystals", Helvetica Chimica Acta **64**, 2154 (1981).

[120] D. M. Jenkins, A. J. Di Bilio, M. J. Allen, T. A. Betley, and J. C. Peters, "Elucidation of a low spin cobalt(II) system in a distorted tetrahedral geometry", Journal of the American Chemical Society **124**, 15336 (2002).

[121] C. Rajnák and R. Boča, "Reciprocating thermal behavior in the family of single ion magnets", Coordination Chemistry Reviews **436**, 213808 (2021).

[122] K. N. Shrivastava, "Theory of spin–lattice relaxation", physica status solidi (b) **117**, 437 (1983).

[123] A. Świtlicka, B. Machura, M. Penkala, A. Bieńko, D. C. Bieńko, J. Titiš, C. Rajnák, R. Boča, and A. Ozarowski, "Slow magnetic relaxation in hexacoordinated cobalt(ii) field-induced single-ion magnets", Inorganic Chemistry Frontiers **7**, 2637 (2020).

[124] I. Nemec, R. Herchel, and Z. Trávníček, "Suppressing of slow magnetic relaxation in tetracoordinate co(II) field-induced single-molecule magnet in hybrid material with ferromagnetic barium ferrite", Scientific Reports **5**, 10761 (2015).

[125] D. Sertphon, K. S. Murray, W. Phonsri, J. Jover, E. Ruiz, S. G. Telfer, A. Alkaş, P. Harding, and D. J. Harding, "Slow relaxation of magnetization in a bis- *mer* -tridentate octahedral co(ii) complex", Dalton Transactions **47**, 859 (2018).

[126] P. Cieslik, P. Comba, W. Hergett, R. Klingeler, G. F. P. Plny, L. Spillecke, and G. Velmurugan, "Molecular magnetic properties of a dysprosium(III) complex coordinated to a nonadentate bispidine ligand", Zeitschrift für anorganische und allgemeine Chemie **647**, 843 (2021).

[127] R. Mitsuhashi, S. Hosoya, T. Suzuki, Y. Sunatsuki, H. Sakiyama, and M. Mikuriya, "Zero-field slow relaxation of magnetization in cobalt(ii) single-ion magnets: suppression of quantum tunneling of magnetization by tailoring the intermolecular magnetic coupling", RSC Advances **10**, 43472 (2020).

[128] I. Bhowmick, A. J. Roehl, J. R. Neilson, A. K. Rappé, and M. P. Shores, "Slow magnetic relaxation in octahedral low-spin ni(iii) complexes", Chemical Science **9**, 6564 (2018).

[129] R. C. Poulten, M. J. Page, A. G. Algarra, J. J. Le Roy, I. López, E. Carter, A. Llobet, S. A. Macgregor, M. F. Mahon, D. M. Murphy, M. Murugesu, and M. K. Whittlesey, "Synthesis, electronic structure, and magnetism of [ni (6-mes)$_2$]$^+$: a two-coordinate nickel(i) complex stabilized by bulky n-heterocyclic carbenes", Journal of the American Chemical Society **135**, 13640 (2013).

[130] I. Ivanović-Burmazović and K. Jelković, "Transition metal complexes with bis(hydrazone) ligands pf 2,6-diacetylpyridine, hepta-coordination of 3d metals", in *Advances in inorganic chemistry*, Vol. 55 (Elsevier, 2004), pp. 315–360.

[131] C. Pichon, B. Elrez, V. Béreau, C. Duhayon, and J.-P. Sutter, "From heptacoordinated cr^{III} complexes with cyanide or isothiocyanate apical groups to 1d heterometallic assemblages with all-pentagonal-bipyramid coordination geometries: from heptacoordinated cr^{III} complexes with cyanide or isothiocyanate apical groups to 1d heterometallic assemblages with all-pentagonal-bipyramid coor", European Journal of Inorganic Chemistry **2018**, 340 (2018).

[132] M. Gerloch and L. R. Hanton, "Ligand bonding parameters in some macrocyclic, seven- coordinate complexes of nickel(II) and cobalt(II)", Inorganica Chimica Acta **49**, 37 (1981).

[133] M. Gerloch, I. Morgenstern-Badarau, and J. P. Audiere, "Magnetic and spectral properties of the pentagonal-bipyramidal complex ions chloroaqua- and diaqua[2,6- diacetylpyridinebis (semicarbazone)] cobalt(II)", Inorganic Chemistry **18**, 3220 (1979).

[134] M. Gerloch and I. Morgenstern-Badarau, "Magnetic and spectral properties of chloroaqua [2,6- diacetylpyridinebis (semicarbazone)] iron(II) and diaqua [2,6- diacetylpyridinebis (semicarbazone)] nickel(II): ligand fields and bonding in pentagonal-bipyramidal complexes", Inorganic Chemistry **18**, 3225 (1979).

[135] Y.-S. Ding, N. F. Chilton, R. E. P. Winpenny, and Y.-Z. Zheng, "On approaching the limit of molecular magnetic anisotropy: a near-perfect pentagonal bipyramidal dysprosium(III) single-molecule magnet", Angewandte Chemie International Edition **55**, 16071 (2016).

[136] Y.-C. Chen, J.-L. Liu, L. Ungur, J. Liu, Q.-W. Li, L.-F. Wang, Z.-P. Ni, L. F. Chibotaru, X.-M. Chen, and M.-L. Tong, "Symmetry-supported magnetic blocking at 20 k in pentagonal bipyramidal dy(III) single-ion magnets", Journal of the American Chemical Society **138**, 2829 (2016).

[137] E. L. Gavey and M. Pilkington, "Employing schiff-base macrocycles to probe the effect of ligand field on the relaxation dynamics of a family of DyIII SMMs", Polyhedron **108**, 122 (2016).

[138] J. Krzystek, A. T. Fiedler, J. J. Sokol, A. Ozarowski, S. A. Zvyagin, T. C. Brunold, J. R. Long, L.-C. Brunel, and J. Telser, "Pseudooctahedral complexes of vanadium(III): electronic structure investigation by magnetic and electronic spectroscopy", Inorganic Chemistry **43**, 5645 (2004).

[139] J. Krzystek, S. Zvyagin, A. Ozarowski, S. Trofimenko, and J. Telser, "Tunable-frequency high-field electron paramagnetic resonance", Journal of Magnetic Resonance **178**, 174 (2006).

[140] E. Ferentinos, C. P. Raptopoulou, V. Psycharis, A. Terzis, J. Krzystek, and P. Kyritsis, "Magnetostructural correlations in s = 1 trans- [ni {(OPPh2) EPPh2) n}2 (dmso)2], e = s, se, and related complexes", Polyhedron **151**, 177 (2018).

[141] C. E. Schäffer and C. K. Jørgensen, "The angular overlap model, an attempt to revive the ligand field approaches", Molecular Physics **9**, 401 (1965).

[142] C. E. Schäffer, "A perturbation representation of weak covalent bonding", in Structure and bonding (1968), pp. 68–95.

[143] K. A. Campbell, E. Yikilmaz, C. V. Grant, W. Gregor, A.-F. Miller, and R. D. Britt, "Parallel polarization EPR characterization of the mn(III) center of oxidized manganese superoxide dismutase", Journal of the American Chemical Society **121**, 4714 (1999).

[144] T. Matsukawa, H. Mino, D. Yoneda, and A. Kawamori, "Dual-mode EPR study of new signals from the s$_3$-state of oxygen-evolving complex in photosystem II †", Biochemistry **38**, 4072 (1999).

[145] C. Mennerich, H. .-. Klauss, A. U. B. Wolter, S. Süllow, F. J. Litterst, C. Golze, R. Klingeler, V. Kataev, B. Büchner, M. Goiran, H. Rakoto, J. .-. Broto, O. Kataeva, and D. J. Price, "High field level crossing studies on spin dimers in the low dimensional quantum spin system na2t2(c2o2)3(h2o)2 with t = ni, co, fe, mn", in *Quantum magnetism* (Springer Netherlands, Dordrecht, 2008), pp. 97–124.

[146] F. Neese, "Approximate second-order SCF convergence for spin unrestricted wavefunctions", Chemical Physics Letters **325**, 93 (2000).

[147] A. Schäfer, C. Huber, and R. Ahlrichs, "Fully optimized contracted gaussian basis sets of triple zeta valence quality for atoms li to kr", The Journal of Chemical Physics **100**, 5829 (1994).

[148] F. Neese, "The ORCA program system", WIREs Computational Molecular Science **2**, 73 (2012).

[149] F. Neese and E. I. Solomon, "Calculation of zero-field splittings, g-values, and the relativistic nephelauxetic effect in transition metal complexes. application to high-spin ferric complexes", Inorganic Chemistry **37**, 6568 (1998).

[150] F. Scarpelli, R. Bartucci, L. Sportelli, and R. Guzzi, "Solvent effect on librational dynamics of spin-labelled haemoglobin by ED- and CW-EPR", European Biophysics Journal **40**, 273 (2011).

[151] R. Cammack, D. S. Patil, and D. Linstead, "EPR spectroscopic studies of haemoglobin breakdown in malarial parasite-infected erythrocytes", Journal of the Chemical Society, Faraday Transactions **90**, 3409 (1994).

[152] A. R. Bizzarri and S. Cannistraro, "Conformational substate distribution in low spin ferric myoglobin as studied by electron paramagnetic resonance", Applied Magnetic Resonance **3**, 1033 (1992).

[153] Y. Miyajima, H. Yashiro, T. Kashiwagi, M. Hagiwara, and H. Hori, "High field and multi-frequency EPR in single crystals of sperm whale met-myoglobin: determination of the axial zero-field splitting constant and frequency dependence of the linewidth", Journal of the Physical Society of Japan **73**, 280 (2004).

[154] C. Andreini, I. Bertini, G. Cavallaro, G. L. Holliday, and J. M. Thornton, "Metal ions in biological catalysis: from enzyme databases to general principles", JBIC Journal of Biological Inorganic Chemistry **13**, 1205 (2008).

[155] T. Irrgang and R. Kempe, "3d-metal catalyzed n- and c-alkylation reactions via borrowing hydrogen or hydrogen autotransfer", Chemical Reviews **119**, 2524 (2019).

[156] C. J. Milios, A. Vinslava, W. Wernsdorfer, S. Moggach, S. Parsons, S. P. Perlepes, G. Christou, and E. K. Brechin, "A record anisotropy barrier for a single-molecule magnet", Journal of the American Chemical Society **129**, 2754 (2007).

[157] D. Maniaki, E. Pilichos, and S. P. Perlepes, "Coordination clusters of 3d-metals that behave as single-molecule magnets (SMMs): synthetic routes and strategies", Frontiers in Chemistry **6**, 461 (2018).

[158] P. King, W. Wernsdorfer, K. A. Abboud, and G. Christou, "A family of mn $_{16}$ single-molecule magnets from a reductive aggregation route", Inorganic Chemistry **43**, 7315 (2004).

[159] A. A. Kitos, C. G. Efthymiou, C. Papatriantafyllopoulou, V. Nastopoulos, A. J. Tasiopoulos, M. J. Manos, W. Wernsdorfer, G. Christou, and S. P. Perlepes, "The search for cobalt single-molecule magnets: a disk-like CoIIICoII6 cluster with a ligand derived from a novel transformation of 2-acetylpyridine", Polyhedron **30**, 2987 (2011).

[160] N. Ishikawa, M. Sugita, T. Okubo, N. Tanaka, T. Iino, and Y. Kaizu, "Determination of ligand-field parameters and f-electronic structures of double-decker bis(phthalocyaninato)lanthanide complexes", Inorganic Chemistry **42**, 2440 (2003).

[161] N. Ishikawa, M. Sugita, T. Ishikawa, S.-y. Koshihara, and Y. Kaizu, "Lanthanide double-decker complexes functioning as magnets at the single-molecular level", Journal of the American Chemical Society **125**, 8694 (2003).

[162] A. Dey, P. Kalita, and V. Chandrasekhar, "Lanthanide(III)-based single-ion magnets", ACS Omega **3**, 9462 (2018).

[163] M. Feng and M.-L. Tong, "Single ion magnets from 3d to 5f: developments and strategies", Chemistry - A European Journal **24**, 7574 (2018).

[164] S. G. McAdams, A.-M. Ariciu, A. K. Kostopoulos, J. P. Walsh, and F. Tuna, "Molecular single-ion magnets based on lanthanides and actinides: design considerations and new advances in the context of quantum technologies", Coordination Chemistry Reviews **346**, 216 (2017).

[165] J. Tang and P. Zhang, *Lanthanide single molecule magnets* (Springer Berlin Heidelberg, Berlin, Heidelberg, 2015).

[166] D. N. Woodruff, R. E. P. Winpenny, and R. A. Layfield, "Lanthanide single-molecule magnets", Chemical Reviews **113**, 5110 (2013).

[167] S. K. Gupta and R. Murugavel, "Enriching lanthanide single-ion magnetism through symmetry and axiality", Chemical Communications **54**, 3685 (2018).

[168] C. R. Ganivet, B. Ballesteros, G. de la Torre, J. M. Clemente-Juan, E. Coronado, and T. Torres, "Influence of peripheral substitution on the magnetic behavior of single-ion magnets based on homo- and heteroleptic tb^{III} bis (phthalocyaninate)", Chemistry - A European Journal **19**, 1457 (2013).

[169] S. T. Liddle and J. van Slageren, "Improving f-element single molecule magnets", Chemical Society Reviews **44**, 6655 (2015).

[170] S.-D. Jiang, S.-S. Liu, L.-N. Zhou, B.-W. Wang, Z.-M. Wang, and S. Gao, "Series of lanthanide organometallic single-ion magnets", Inorganic Chemistry **51**, 3079 (2012).

[171] M.-E. Boulon, G. Cucinotta, J. Luzon, C. Degl'Innocenti, M. Perfetti, K. Bernot, G. Calvez, A. Caneschi, and R. Sessoli, "Magnetic anisotropy and spin-parity effect along the series of lanthanide complexes with DOTA", Angewandte Chemie International Edition **52**, 350 (2013).

[172] S. K. Langley, D. P. Wielechowski, V. Vieru, N. F. Chilton, B. Moubaraki, L. F. Chibotaru, and K. S. Murray, "Modulation of slow magnetic relaxation by tuning magnetic exchange in cr_2dy_2 single molecule magnets", Chem. Sci. **5**, 3246 (2014).

[173] L. Rosado Piquer and E. C. Sañudo, "Heterometallic 3d–4f single-molecule magnets", Dalton Transactions **44**, 8771 (2015).

170

[174] J. D. Rinehart and J. R. Long, "Exploiting single-ion anisotropy in the design of f-element single-molecule magnets", Chemical Science **2**, 2078 (2011).

[175] A. Upadhyay, S. K. Singh, C. Das, R. Mondol, S. K. Langley, K. S. Murray, G. Rajaraman, and M. Shanmugam, "Enhancing the effective energy barrier of a dy(iii) SMM using a bridged diamagnetic zn(ii) ion", Chem. Commun. **50**, 8838 (2014).

[176] A. Watanabe, A. Yamashita, M. Nakano, T. Yamamura, and T. Kajiwara, "Multi-path magnetic relaxation of mono-dysprosium(III) single-molecule magnet with extremely high barrier", Chemistry - A European Journal **17**, 7428 (2011).

[177] N. F. Chilton, S. K. Langley, B. Moubaraki, A. Soncini, S. R. Batten, and K. S. Murray, "Single molecule magnetism in a family of mononuclear beta-diketonate lanthanide(iii) complexes: rationalization of magnetic anisotropy in complexes of low symmetry", Chemical Science **4**, 1719 (2013).

[178] S. Biswas, K. S. Bejoymohandas, S. Das, P. Kalita, M. L. P. Reddy, I. Oyarzabal, E. Colacio, and V. Chandrasekhar, "Mononuclear lanthanide complexes: energy-barrier enhancement by ligand substitution in field-induced dy ^{III} SIMs", Inorganic Chemistry **56**, 7985 (2017).

[179] P. Kalita, J. Goura, J. Manuel Herrera Martínez, E. Colacio, and V. Chandrasekhar, "Homodinuclear {ln $^{III}_2$} (ln ^{III} = gd ^{III} , tb ^{III} , ho ^{III} , and dy ^{III}) complexes: field-induced SMM behavior of the dy ^{III} and tb ^{III} analogues", European Journal of Inorganic Chemistry **2019**, 212 (2019).

[180] P. Kalita, N. Ahmed, A. K. Bar, S. Dey, A. Jana, G. Rajaraman, J.-P. Sutter, and V. Chandrasekhar, "Pentagonal bipyramidal ln(III) complexes containing an axial phosphine oxide ligand: field-induced single-ion magnetism behavior of the dy(III) analogues", Inorganic Chemistry **59**, 6603 (2020).

[181] A. A. Athanasopoulou, J. J. Baldoví, L. M. Carrella, and E. Rentschler, "Field-induced slow magnetic relaxation in the first dy(iii)-centered 12-metallacrown-4 double-decker", Dalton Transactions **48**, 15381 (2019).

[182] S. She, X. Gu, and Y. Yang, "Field-induced single molecule magnet behavior of a three-dimensional dy(III)-based complex", Inorganic Chemistry Communications **110**, 107584 (2019).

[183] R. Marx, F. Moro, M. Dörfel, L. Ungur, M. Waters, S. D. Jiang, M. Orlita, J. Taylor, W. Frey, L. F. Chibotaru, and J. van Slageren, "Spectroscopic determination of crystal field splittings in lanthanide double deckers", Chemical Science **5**, 3287 (2014).

[184] P. Comba, L. J. Daumann, R. Klingeler, C. Koo, M. J. Riley, A. E. Roberts, H. Wadepohl, and J. Werner, "Correlation of structural and magnetic properties in a set of mononuclear lanthanide complexes", Chemistry - A European Journal **24**, 5319 (2018).

[185] P. Ma, F. Hu, R. Wan, Y. Huo, D. Zhang, J. Niu, and J. Wang, "Magnetic double-tartaric bridging mono-lanthanide substituted phosphotungstates with photochromic and switchable luminescence properties", Journal of Materials Chemistry C **4**, 5424 (2016).

[186] Y. Peng, V. Mereacre, C. E. Anson, and A. K. Powell, "The role of coordinated solvent on co(ii) ions in tuning the single molecule magnet properties in a co(II)2dy(III)2 system", Dalton Transactions **46**, 5337 (2017).

[187] K. C. Mondal, A. Sundt, Y. Lan, G. E. Kostakis, O. Waldmann, L. Ungur, L. F. Chibotaru, C. E. Anson, and A. K. Powell, "Coexistence of distinct single-ion and exchange-based mechanisms for blocking of magnetization in a co(II)2dy(III)2 single-molecule magnet", Angewandte Chemie International Edition **51**, 7550 (2012).

[188] A. Castro-Alvarez, Y. Gil, L. Llanos, and D. Aravena, "High performance single-molecule magnets, orbach or raman relaxation suppression?", Inorganic Chemistry Frontiers **7**, 2478 (2020).

[189] A. A. Patrascu, M. Briganti, S. Soriano, S. Calancea, R. A. Allão Cassaro, F. Totti, M. G. F. Vaz, and M. Andruh, "SMM behavior tuned by an exchange coupling LEGO approach for chimeric compounds: first 2p–3d–4f heterotrispin complexes with different metal ions bridged by one aminoxyl group", Inorganic Chemistry **58**, 13090 (2019).

[190] Y.-N. Guo, L. Ungur, G. E. Granroth, A. K. Powell, C. Wu, S. E. Nagler, J. Tang, L. F. Chibotaru, and D. Cui, "An NCN-pincer ligand dysprosium single-ion magnet showing magnetic relaxation via the second excited state", Scientific Reports **4**, 5471 (2015).

[191] R. J. Blagg, L. Ungur, F. Tuna, J. Speak, P. Comar, D. Collison, W. Wernsdorfer, E. J. L. McInnes, L. F. Chibotaru, and R. E. P. Winpenny, "Magnetic relaxation pathways in lanthanide single-molecule magnets", Nature Chemistry **5**, 673 (2013).

[192] L. Ungur, J. J. Le Roy, I. Korobkov, M. Murugesu, and L. F. Chibotaru, "Finetuning the local symmetry to attain record blocking temperature and magnetic remanence in a single-ion magnet", Angewandte Chemie International Edition **53**, 4413 (2014).

[193] J. Li, M. Kong, L. Yin, J. Zhang, F. Yu, Z.-W. Ouyang, Z. Wang, Y.-Q. Zhang, and Y. Song, "Photochemically tuned magnetic properties in an erbium(III)-based easy-plane single- molecule magnet", Inorganic Chemistry **58**, 14440 (2019).

[194] E. Lucaccini, L. Sorace, M. Perfetti, J.-P. Costes, and R. Sessoli, "Beyond the anisotropy barrier: slow relaxation of the magnetization in both easy-axis and easy-plane ln(trensal) complexes", Chem. Commun. **50**, 1648 (2014).

[195] E. Lucaccini, J. J. Baldoví, L. Chelazzi, A.-L. Barra, F. Grepioni, J.-P. Costes, and L. Sorace, "Electronic structure and magnetic anisotropy in lanthanoid single-ion magnets with C_3 symmetry: the ln(trenovan) series", Inorganic Chemistry **56**, 4728 (2017).

172

[196] R. Rakhimov, H. Horton, D. Jones, G. Loutts, and H. Ries, "Spin dynamics of the triplet cr4+ in the vicinity of energy level anti-crossing", Chemical Physics Letters **319**, 639 (2000).

[197] W. R. Hagen, "EPR spectroscopy as a probe of metal centres in biological systems", Dalton Transactions, 4415 (2006).

[198] B. G. Wyborne, *Spectroscopic properties of rare earths* (New York, 1965).

[199] S. Hüfner, *Optical spectra of transparent rare earth compounds* (Academic Press, New York, 1978), 237 pp.

[200] L. Eyring and K. A. Gschneidner, *Handbook on the physics and chemistry of rare earths* (1999).

[201] D. J. Newman, *The orbit-lattice interaction for lanthanide ions. i. determination of empirical parameters*, 1975.

[202] D. J. Newman and B. Ng, "The superposition model of crystal fields", Reports on Progress in Physics **52**, 699 (1989).

[203] C. Bungenstock, T. Tröster, and W. B. Holzapfel, "Effect of pressure on free-ion and crystal-field parameters of pr3 + in l OCl (l = l a , p r , gd)", Physical Review B **62**, 7945 (2000).

[204] C. Benelli and D. Gatteschi, "Magnetism of lanthanides in molecular materials with transition-metal ions and organic radicals", Chemical Reviews **102**, 2369 (2002).

[205] A. Rohde, S. T. Hatscher, and W. Urland, "Crystal structure and magnetic behaviour of a new lanthanide acetate gd(HF2ccoo)3(h2o)2·h2o in comparison to gd(h3ccoo)3(h2o)2·2h2o", Journal of Alloys and Compounds **374**, 137 (2004).

[206] S. T. Hatscher and W. Urland, "Unexpected appearance of molecular ferromagnetism in the ordinary acetate [{gd(OAc)3(h2o)2}2]4 h2o", Angewandte Chemie International Edition **42**, 2862 (2003).

[207] T. Shimada, A. Okazawa, N. Kojima, S. Yoshii, H. Nojiri, and T. Ishida, "Ferromagnetic exchange couplings showing a chemical trend in cu–ln–cu complexes (ln = gd, tb, dy, ho, er)", Inorganic Chemistry **50**, 10555 (2011).

[208] R. Watanabe, K. Fujiwara, A. Okazawa, G. Tanaka, S. Yoshii, H. Nojiri, and T. Ishida, "Chemical trend of ln–m exchange couplings in heterometallic complexes with ln = gd, tb, dy, ho, er and m = cu, v", Chem. Commun. **47**, 2110 (2011).

[209] Y. Ida, S. Ghosh, A. Ghosh, H. Nojiri, and T. Ishida, "Strong ferromagnetic exchange interactions in hinge- like dy(o$_2$cu)$_2$ complexes involving double oxygen bridges", Inorganic Chemistry **54**, 9543 (2015).

[210] T. Ishida, R. Watanabe, K. Fujiwara, A. Okazawa, N. Kojima, G. Tanaka, S. Yoshii, and H. Nojiri, "Exchange coupling in TbCu and DyCu single-molecule magnets and related lanthanide and vanadium analogs", Dalton Transactions **41**, 13609 (2012).

[211] R. Gopalan, *Inorganic chemistry for undergraduates*, OCLC: 708645565 (Universities Press, Hyderabad, 2009).

[212] A.-L. Barra, L.-C. Brunel, D. Gatteschi, L. Pardi, and R. Sessoli, "High-frequency EPR spectroscopy of large metal ion clusters: from zero field splitting to quantum tunneling of the magnetization", Accounts of Chemical Research **31**, 460 (1998).

[213] C.-C. Wu, S. Datta, W. Wernsdorfer, G.-H. Lee, S. Hill, and E.-C. Yang, "Studies of magnetic properties and HFEPR of octanuclear manganese single-molecule magnets", Dalton Transactions **39**, 10160 (2010).

[214] R. Baggio, R. Calvo, M. T. Garland, O. Peña, M. Perec, and A. Rizzi, "Gadolinium and neodymium citrates: evidence for weak ferromagnetic exchange between gadolinium(III) cations", Inorganic Chemistry **44**, 8979 (2005).

[215] A. Bencini, C. Benelli, A. Caneschi, R. L. Carlin, A. Dei, and D. Gatteschi, "Crystal and molecular structure of and magnetic coupling in two complexes containing gadolinium(III) and copper(II) ions", Journal of the American Chemical Society **107**, 8128 (1985).

[216] F. Luis, P. J. Alonso, O. Roubeau, V. Velasco, D. Zueco, D. Aguilà, J. I. Martínez, L. A. Barrios, and G. Aromí, "A dissymmetric [gd2] coordination molecular dimer hosting six addressable spin qubits", Communications Chemistry **3**, 176 (2020).

[217] V. N. Glazkov, M. E. Zhitomirsky, A. I. Smirnov, H.-A. Krug von Nidda, A. Loidl, C. Marin, and J.-P. Sanchez, "Single-ion anisotropy in the gadolinium pyrochlores studied by electron paramagnetic resonance", Physical Review B **72**, 020409 (2005).

[218] A. Caneschi, A. Dei, D. Gatteschi, C. A. Massa, L. A. Pardi, S. Poussereau, and L. Sorace, "Evaluating the magnetic anisotropy in molecular rare earth compounds. gadolinium derivatives with semiquinone radical and diamagnetic analogues", Chemical Physics Letters **371**, 694 (2003).

[219] A. J. Shuskus, "Electron spin resonance of gd 3 + and eu 2 + in single crystals of CaO", Physical Review **127**, 2022 (1962).

[220] A. Okazawa, T. Nogami, H. Nojiri, and T. Ishida, "Exchange coupling and energy-level crossing in a magnetic chain [dy $_2$ cu $_2$] $_n$ evaluated by high-frequency electron paramagnetic resonance", Chemistry of Materials **20**, 3110 (2008).

[221] D. Komijani, A. Ghirri, C. Bonizzoni, S. Klyatskaya, E. Moreno-Pineda, M. Ruben, A. Soncini, M. Affronte, and S. Hill, "Radical-lanthanide ferromagnetic interaction in a t b III bis-phthalocyaninato complex", Physical Review Materials **2**, 024405 (2018).

174

[222] L. Quintanar and L. Rivillas-Acevedo, "Studying metal ion–protein interactions: electronic absorption, circular dichroism, and electron paramagnetic resonance", in *Protein-ligand interactions*, Vol. 1008, edited by M. A. Williams and T. Daviter, Series Title: Methods in Molecular Biology (Humana Press, Totowa, NJ, 2013), pp. 267–297.

[223] S. K. Singh and G. Rajaraman, "Decisive interactions that determine ferro/ antiferromagnetic coupling in {3d–4f} pairs: a case study on dinuclear v(iv)–gd(iii) complexes", Dalton Transactions **42**, 3623 (2013).

[224] M. Andruh, I. Ramade, E. Codjovi, O. Guillou, O. Kahn, and J. C. Trombe, "Crystal structure and magnetic properties of [ln2cu4] hexanuclear clusters (where ln = trivalent lanthanide). mechanism of the gadolinium(III)-copper(II) magnetic interaction", Journal of the American Chemical Society **115**, 1822 (1993).

[225] Y. Rechkemmer, J. E. Fischer, R. Marx, M. Dörfel, P. Neugebauer, S. Horvath, M. Gysler, T. Brock-Nannestad, W. Frey, M. F. Reid, and J. van Slageren, "Comprehensive spectroscopic determination of the crystal field splitting in an erbium single-ion magnet", Journal of the American Chemical Society **137**, 13114 (2015).

[226] G. Peng, G. E. Kostakis, Y. Lan, and A. K. Powell, "Body-wing swapping in butterfly {fe $^{III}_2$ ln $^{III}_2$ } coordination clusters with triethylene glycol as ligand", Dalton Trans. **42**, 46 (2013).

[227] A. S. R. Chesman, D. R. Turner, K. J. Berry, N. F. Chilton, B. Moubaraki, K. S. Murray, G. B. Deacon, and S. R. Batten, "Ln(III)2mn(III)2 heterobimetallic "butterfly" complexes displaying antiferromagnetic coupling (ln = eu, gd, tb, er)", Dalton Transactions **41**, 11402 (2012).

[228] K. C. Mondal, G. E. Kostakis, Y. Lan, W. Wernsdorfer, C. E. Anson, and A. K. Powell, "Defect-dicubane ni $_2$ ln $_2$ (ln = dy, tb) single molecule magnets", Inorganic Chemistry **50**, 11604 (2011).

[229] S. K. Langley, L. Ungur, N. F. Chilton, B. Moubaraki, L. F. Chibotaru, and K. S. Murray, "Single-molecule magnetism in a family of {co $^{III}_2$ dy $^{III}_2$ } butterfly complexes: effects of ligand replacement on the dynamics of magnetic relaxation", Inorganic Chemistry **53**, 4303 (2014).

[230] A. V. Funes, L. Carrella, Y. Rechkemmer, J. van Slageren, E. Rentschler, and P. Alborés, "Synthesis, structural characterization and magnetic behaviour of a family of [co(III)2ln(III)2] butterfly compounds", Dalton Transactions **46**, 3400 (2017).

[231] D. Tu, D. Shao, H. Yan, and C. Lu, "A carborane-incorporated mononuclear co(ii) complex showing zero-field slow magnetic relaxation", Chemical Communications **52**, 14326 (2016).

[232] W. Huang, T. Liu, D. Wu, J. Cheng, Z. W. Ouyang, and C. Duan, "Field-induced slow relaxation of magnetization in a tetrahedral co(ii) complex with easy plane anisotropy", Dalton Transactions **42**, 15326 (2013).

[233] J. Vallejo, M. Viciano-Chumillas, F. Lloret, M. Julve, I. Castro, J. Krzystek, M. Ozerov, D. Armentano, G. De Munno, and J. Cano, "Coligand effects on the field-induced double slow magnetic relaxation in six-coordinate cobalt(II) single-ion magnets (SIMs) with positive magnetic anisotropy", Inorganic Chemistry **58**, 15726 (2019).

[234] J.-J. Liu, S.-D. Jiang, P. Neugebauer, J. van Slageren, Y. Lan, W. Wernsdorfer, B.-W. Wang, and S. Gao, "Magnetic and HFEPR studies of exchange coupling in a series of mu-cl dicobalt complexes", Inorganic Chemistry **56**, 2417 (2017).

[235] N. Lazarov, V. Spasojevic, V. Kusigerski, V. Matić, and M. Milić, "Magnetic susceptibility calculation of the dinuclear cobalt complex [co2(ox)tpmc] (ClO4)2· 3h2o", Journal of Magnetism and Magnetic Materials **272-276**, 1065 (2004).

[236] C. J. Pedersen, "Cyclic polyethers and their complexes with metal salts", Journal of the American Chemical Society **89**, 7017 (1967).

[237] S. Shinkai, T. Nakaji, T. Ogawa, K. Shigematsu, and O. Manabe, "Photoresponsive crown ethers. 2. photocontrol of ion extraction and ion transport by a bis(crown ether) with a butterfly-like motion", Journal of the American Chemical Society **103**, 111 (1981).

[238] K. H. Wong, K. Yagi, and J. Smid, "Ion transport through liquid membranes facilitated by crown ethers and their polymers", The Journal of Membrane Biology **18**, 379 (1974).

[239] J. Gao, J. Fu, C. Lin, J. Lin, Y. Han, X. Yu, and C. Pan, "Formation and photoluminescence of silver nanoparticles stabilized by a two-armed polymer with a crown ether core", Langmuir **20**, 9775 (2004).

[240] M. M. Pyrch, J. M. Williams, and T. Z. Forbes, "Exploring crown-ether functionalization on the stabilization of hexavalent neptunium", Chemical Communications **55**, 9319 (2019).

[241] Y. Han, Z. Meng, Y.-X. Ma, and C.-F. Chen, "Iptycene-derived crown ether hosts for molecular recognition and self-assembly", Accounts of Chemical Research **47**, 2026 (2014).

[242] B. Zheng, F. Wang, S. Dong, and F. Huang, "Supramolecular polymers constructed by crown ether-based molecular recognition", Chem. Soc. Rev. **41**, 1621 (2012).

[243] M. Zhang, D. Xu, X. Yan, J. Chen, S. Dong, B. Zheng, and F. Huang, "Self-healing supramolecular gels formed by crown ether based host-guest interactions", Angewandte Chemie **124**, 7117 (2012).

[244] G. Mezei, C. M. Zaleski, and V. L. Pecoraro, "Structural and functional evolution of metallacrowns", Chemical Reviews **107**, 4933 (2007).

[245] M. S. Lah and V. L. Pecoraro, "Isolation and characterization of {MnII[MnIII (salicylhydroximate)] 4(acetate) 2(DMF)6}. cntdot. 2dmf: an inorganic analog of m2+(12-crown-4)", Journal of the American Chemical Society **111**, 7258 (1989).

176

[246] C. M. Zaleski, E. C. Depperman, J. W. Kampf, M. L. Kirk, and V. L. Pecoraro, "Synthesis, structure, and magnetic properties of a large lanthanide–transition-metal single-molecule magnet", Angewandte Chemie International Edition **43**, 3912 (2004).

[247] T. T. Boron, J. W. Kampf, and V. L. Pecoraro, "A mixed 3d-4f 14-metallacrown-5 complex that displays slow magnetic relaxation through geometric control of magnetoanisotropy", Inorganic Chemistry **49**, 9104 (2010).

[248] A. Deb, T. T. Boron, M. Itou, Y. Sakurai, T. Mallah, V. L. Pecoraro, and J. E. Penner-Hahn, "Understanding spin structure in metallacrown single-molecule magnets using magnetic compton scattering", Journal of the American Chemical Society **136**, 4889 (2014).

[249] J. Wang, Q.-W. Li, S.-G. Wu, Y.-C. Chen, R.-C. Wan, G.-Z. Huang, Y. Liu, J.-L. Liu, D. Reta, M. J. Giansiracusa, Z.-X. Wang, N. F. Chilton, and M.-L. Tong, "Opening magnetic hysteresis by axial ferromagnetic coupling: from mono-decker to double-decker metallacrown", Angewandte Chemie International Edition **60**, 5299 (2021).

[250] M. S. Muravyeva, G. S. Zabrodina, M. A. Samsonov, E. A. Kluev, A. A. Khrapichev, M. A. Katkova, and I. V. Mukhina, "Water-soluble tetraaqua ln(III) glycinehydroximate 15-metallacrown-5 complexes towards potential MRI contrast agents for ultra-high magnetic field", Polyhedron **114**, 165 (2016).

[251] M. A. Katkova, G. S. Zabrodina, M. S. Muravyeva, A. S. Shavyrin, E. V. Baranov, A. A. Khrapichev, and S. Y. Ketkov, "Facile one-pot route toward water-soluble lanthanide-copper-glycinehydroximate 15-metallacrown-5 complexes: lanthanide-copper glycinehydroximate 15-metallacrown-5 complexes", European Journal of Inorganic Chemistry **2015**, 5202 (2015).

[252] M. A. Katkova, G. S. Zabrodina, E. V. Baranov, M. S. Muravyeva, E. A. Kluev, A. S. Shavyrin, G. Y. Zhigulin, and S. Y. Ketkov, "New insights into water- soluble and water- coordinated copper 15- metallacrown-5 gadolinium complexes designed for high-field magnetic resonance imaging applications: 15-metallacrown-5 complexes designed for high-field MRI applications", Applied Organometallic Chemistry **32**, e4389 (2018).

[253] N. F. Chilton, R. P. Anderson, L. D. Turner, A. Soncini, and K. S. Murray, "PHI: a powerful new program for the analysis of anisotropic monomeric and exchange-coupled polynuclear d - and f -block complexes", Journal of Computational Chemistry **34**, 1164 (2013).

[254] Y. Song, J.-C. Liu, Y.-J. Liu, D.-R. Zhu, J.-Z. Zhuang*, and X.-Z. You*, "Preparation, crystal structures and magnetic properties of 12-metallacrown-4 complexes with the donors on the organic periphery of molecule", Inorganica Chimica Acta **305**, 135 (2000).

[255] A. V. Pavlishchuk, S. V. Kolotilov, M. Zeller, O. V. Shvets, I. O. Fritsky, S. E. Lofland, A. W. Addison, and A. D. Hunter, "Magnetic and sorption properties of supramolecular systems based on pentanuclear copper(II) 12-metallacrown-4 complexes and isomeric phthalates: structural modeling of the different stages of alcohol sorption", European Journal of Inorganic Chemistry **2011**, 4826 (2011).

[256] C. McDonald, T. Whyte, S. M. Taylor, S. Sanz, E. K. Brechin, D. Gaynor, and L. F. Jones, "Progressive decoration of pentanuclear cu(ii) 12-metallacrown-4 nodes towards targeted 1- and 2d extended networks", CrystEngComm **15**, 6672 (2013).

[257] X.-M. Liu, X.-Q. Li, Q.-L. Wang, Q.-Y. Liu, Y.-Z. Tong, X.-P. Jia, and C. Yang, "Crystal structure and magnetic properties of a pentanuclear copper(II) 12-metallacrown-4 complex derived from glutaroimide-dioxime", Inorganic Chemistry Communications **118**, 107985 (2020).

[258] I. Heckelmann, "Elektronenspinresonanzspektroskopie und magnetisierungsmessungen an metallacrown- cu4cu- komplexen", Bachlorarbeit (Universität Heidelberg, 2019).

[259] C. P. Poole, *Electron spin resonance: a comprehensive treatise on experimental techniques* (Dover Publications, Mineola, N.Y, 1996), 780 pp.

[260] C. P. Slichter, *Principles of magnetic resonance*, 3rd enl. and updated ed, Springer series in solid-state sciences 1 (Springer, Berlin ; New York, 1996), 655 pp.

[261] G. Ilangovan, J. L. Zweier, and P. Kuppusamy, "Mechanism of oxygen-induced EPR line broadening in lithium phthalocyanine microcrystals", Journal of Magnetic Resonance **170**, 42 (2004).

[262] T. I. Smirnova, A. I. Smirnov, R. B. Clarkson, and R. Linn Belford, "Accuracy of oxygen measurements inT2 (line width) EPR oximetry", Magnetic Resonance in Medicine **33**, 801 (1995).

[263] P. R. Spackman, M. J. Turner, J. J. McKinnon, S. K. Wolff, D. J. Grimwood, D. Jayatilaka, and M. A. Spackman, "*CrystalExplorer* : a program for hirshfeld surface analysis, visualization and quantitative analysis of molecular crystals", Journal of Applied Crystallography **54**, 1006 (2021).

List of Partial Publications

1 S. Tripathi, S. Vaidya, K.U. Ansari, N. Ahmed, E. Rivière, **L. Spillecke**, C. Koo, R. Klingeler, T. Mallah, G. Rajaraman, M. Shanmugam: *Influence of a Counteranion on the Zero-Field Splitting of Tetrahedral Cobalt(II) Thiourea Complexes*
In: Inorganic Chemistry 58, 9085–9100. (2019)
DOI: 10.1021/acs.inorgchem.9b00632

2 T.A. Bazhenova, L.V. Zorina, S.V. Simonov, V.S. Mironov, O.V. Maximova, **L. Spillecke**, C. Koo, R. Klingeler, Y.V. Manakin, A.N. Vasiliev, E.B. Yagubskii: *The first pentagonal-bipyramidal vanadium(III) complexes with a Schiff-base N_3O_2 pentadentate ligand: synthesis, structure and magnetic properties*
In: Dalton Transactions 49, 15287–15298. (2020)
DOI: 10.1039/D0DT03092A

3 S. Tripathi, S. Vaidya, N. Ahmed, E. Andreasen Klahn, H. Cao, **L. Spillecke**, C. Koo, S. Spachmann, R. Klingeler, G. Rajaraman, J. Overgaard, M. Shanmugam: *Structure-property correlation in stabilizing axial magnetic anisotropy in octahedral Co(II) complexes*
In: Cell Reports Physical Science 2, 100404. (2021)
DOI: 10.1016/j.xcrp.2021.100404

4 P. Cieslik, P. Comba, W. Hergett, R. Klingeler, G.F.P. Plny, **L. Spillecke**, G. Velmurugan: *Molecular magnetic properties of a dysprosium(III) complex coordinated to a nonadentate bispidine ligand*
In: Zeitschrift für Anorganische und Allgemeine Chemie 647, 843–849. (2021)
DOI: 10.1002/zaac.202000475

5 **L. Spillecke**, S. Tripathi, C. Koo, M. Ansari, S. Vaidya, A. Rasamsetty, T. Mallah, G. Rajaraman, M. Shanmugam, R. Klingeler: *A high-frequency EPR study of magnetic anisotropy and intermolecular interactions of Co(II) ions*
In: Polyhedron 208, 115389. (2021)
DOI: 10.1016/j.poly.2021.115389

Danksagung

Als Abschluss dieser Arbeit möchte ich die Gelegenheit nutzen, mich hiermit ganz herzlich bei allen zu bedanken, die mich bei meiner Doktorarbeit, aber auch im gesamten Verlauf meines Studiums unterstützt haben. Herrn Prof. Dr. Rüdiger Klingeler danke ich, mir zum einen die Möglichkeit gegeben zu haben, meine Doktorarbeit am Kirchhoff-Institut für Physik in Heidelberg schreiben zu dürfen, zum anderen für eine hervorragende Betreuung meiner Arbeit mit vielen Diskussionen. Für die Übernahme des Zweitgutachtens dieser Arbeit möchte ich Herrn Prof. Dr. Maurits Haverkort danken.

Herrn Dr. Changhyun Koo danke ich für die viele Hilfe und Unterstützung während der HF-EPR Messungen sowie die vielen aufschlussreichen Gespräche zu molekularen Magneten im allgemeinen. Ebenfalls für die große Unterstützung bei technischen EPR Fragen möchte ich Herrn Dr. Johannes Werner danken. Frau Dr. Marion Kerscher danke ich für die Unterstützung bei den X-band EPR Messungen. Weiterhin danke ich den Chemikern unserer indischen, russischen und deutschen Kollaborationen für die Synthese der molekularen Materialien, welche mir für meine Untersuchungen zur Verfügung gestellt wurden.

Den Mitglieder und ehemaligen Mitgliedern der Gruppe F25 danke ich für die wunderbare Arbeitsatmosphäre und die große Hilfsbereitschaft untereinander sowie eine schöne Zeit am KIP Heidelberg. Insbesondere danke ich Herrn Martin Jonak für seine zuverlässige Hilfe beim Heliumfüllen und anderen technische Schwierigkeiten sowie Herrn Dr. Kaustav Dey als gesprächigen und hilfsbereiten Bürokollegen.

Für das Korrekturlesen dieser Arbeit möchte ich Herrn Changhyun Koo, Herrn Prof. Dr. Rüdiger Klingeler sowie Herrn Dr. Johannes Stoldt danken.

Meinen Eltern Antje und Jörg Spillecke danke ich für die Unterstützung während meines Studiums und in allen Lebenslagen. Zum Schluss möchte ich meinem Mann Johannes Stoldt für seinen steten Zuspruch und seine Geduld danken, und dafür mich während meines gesamten Studiums und meiner Promotion in der Lösung aller (meist programmiertechnischen Probleme) unterstützt zu haben.

Eigenständigkeitserklärung

Hiermit erkläre ich, dass ich die vorliegende Dissertation selbst verfasst habe ohne unzulässige Hilfe Dritter und alle verwendeten Quellen als solche gekennzeichnet sind.

_____

Ort, Datum   Unterschrift